

UNCLASSIFIED

AD NUMBER
ADB001103
NEW LIMITATION CHANGE
TO Approved for public release, distribution unlimited
FROM Distribution authorized to U.S. Gov't. agencies only; Test and Evaluation; OCT 1974. Other requests shall be referred to Air Force Rocket Propulsion Lab., AFSC, Edwards AFB, CA 93523.
AUTHORITY
AFRPL ltr, 15 May 1986

THIS PAGE IS UNCLASSIFIED

L

1

SIMULATED AIR LAUNCH ENVIRONMENT  
FINAL REPORT FOR PERIOD SEPT. 72 THROUGH MAY 74

ADBO01103

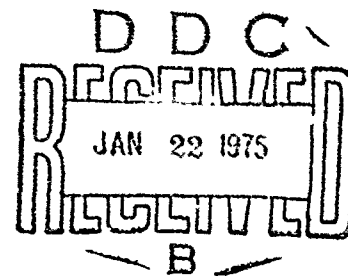
D. R. PRITTS, ET AL

THIOL CORPORATION  
HUNTSVILLE DIVISION  
HUNTSVILLE, ALABAMA 35807

OCTOBER 1974

DISTRIBUTION LIMITED TO U.S. GOV'T AGENCIES  
ONLY; TEST AND EVALUATION, 11 SEPTEMBER 74.  
OTHER REQUESTS FOR THIS DOCUMENT MUST BE RE-  
REFERRED TO AFRPL (STINFO/DOZ), EDWARDS, CA.  
93523

VOLUME I: TECHNICAL REPORT



AIR FORCE ROCKET PROPULSION LABORATORY  
DIRECTOR OF SCIENCE AND TECHNOLOGY  
AIR FORCE SYSTEMS COMMAND  
EDWARDS, CALIFORNIA 93523

NOTICE

"When U. S. Government drawings, specifications, or other data are used for any purpose other than a definitely related government procurement operation, the Government thereby incurs no responsibility nor any obligation whatsoever, and the fact that the Government may have formulated, furnished, or in any way supplied the said drawings, specifications or other data, is not to be regarded by implication or otherwise, or in any manner licensing the holder or any other person or corporation, or conveying any rights or permission to manufacture, use, or sell any patented invention that may in any way be related thereto."

FOREWORD

This program was sponsored by AFRPL. Dr. J. L. Trout, AFRPL/MKPB, was the Program Monitor. Mr. G. F. Mangum was Project Director and Mr. D. B. Turner was Program Manager for the Thiokol Corporation. Mr. O. R. Pritts was Principal Investigator. Significant contributions were made by Mr. J. M. Nelson in Stress Analysis and Physical Properties Testing, Mr. G. A. Collingwood in Stress Analysis, and Mr. J. D. Marlin, III who acted as Test Engineer. The contract was performed over the period September 1972 to May 1974.

This report has been read and is approved.

  
CHARLES R. COOKE, Chief  
Solid Rocket Division

**UNCLASSIFIED**

SECURITY CLASSIFICATION OF THIS PAGE (When Data Entered)

REPORT DOCUMENTATION PAGE		READ INSTRUCTIONS BEFORE COMPLETING FORM
1. REPORT NUMBER AFRPL-TR-74-47	2. GOVT ACCESSION NO.	3. RECIPIENT'S CATALOG NUMBER
4. TITLE (and Subtitle) FINAL REPORT - Simulated Air Launch Environment		5. TYPE OF REPORT & PERIOD COVERED Final - Sept 72 - May 1974
		6. PERFORMING ORG. REPORT NUMBER U-74-30
7. AUTHOR(s) Mr. O. R. Pritts, et al		8. CONTRACT OR GRANT NUMBER(s) F04611-73-C-0015
9. PERFORMING ORGANIZATION NAME AND ADDRESS Thiokol/Redstone Division Redstone Arsenal Huntsville, Alabama 35807		10. PROGRAM ELEMENT, PROJECT, TASK AREA & WORK UNIT NUMBERS BPSN-62302F Project - 3417
11. CONTROLLING OFFICE NAME AND ADDRESS Air Force Rocket Propulsion Laboratory/AFSC Edwards, California 93523		12. REPORT DATE October 1974
14. MONITORING AGENCY NAME & ADDRESS (if different from Controlling Office)		13. NUMBER OF PAGES Volume I - 280; Volume II - 315
		15. SECURITY CLASS. (of this report) Unclassified
		13a. DECLASSIFICATION/DOWNGRADING SCHEDULE N/A
16. DISTRIBUTION STATEMENT (of this Report) Distribution limited to U. S. Gov't agencies only; Test and Evaluation 11 September 1974. Other requests for this document must be referred to AFRPL(STINFO/DOZ), Edwards, CA 93523		
17. DISTRIBUTION STATEMENT (of this abstract entered in Block 20, if different from Report) Approved for Public Release: Distribution Unlimited		
18. SUPPLEMENTARY NOTES		
19. KEY WORDS (Continue on reverse side if necessary and identify by block number) Air Launch Environment, Aeroheat Analysis, THVINC, Uninstrumented Motor Test, Instrumented Motor Test, Gage Calibration, Failure Criteria, Propellant Characteristics, Temperature		
20. ABSTRACT (Continue on reverse side if necessary and identify by block number) A program was conducted in which the response and failure characteristics of solid propellant rocket motors when subjected to transient thermal conditions representing air launch operational environments were recorded and analyzed. Future Air Force mission profiles were used. The Maverick motor, AGM-65A, was used as a test bed on the program.		

## CONTENTS

	<u>Page</u>
INTRODUCTION	1
OBJECTIVE AND BACKGROUND	1
SCOPE	1
PROGRAM ORGANIZATION	2
TECHNICAL ACCOMPLISHMENTS	5
AIR LAUNCH ENVIRONMENT ANALYSIS	5
Requirements	5
Mission Review and Selection	5
Mission Severity Analysis	9
Aeroheat Schedule Selection	20
INSTRUMENTED MOTOR DESIGN AND MANUFACTURE	24
Instrumented Motor Design Rationale	24
Instrumented Motor Design	24
Instrumentation Selection and Location	31
Gage Manufacture and Calibration	37
Gage Installation	43
Motor Manufacture	43
TESTING	58
Test Facility	58
Hardware and Procedures	68
Uninstrumented Motor Aeroheat Testing	74
Instrumented Motor Testing	88
Instrumented Motor Aeroheat Testing	102
Aeroheat Simulation Testing	161
MOTOR DISSECTION AND PROPELLANT PROPERTY TESTING	170
IM#2 Dissection and Propellant Testing	170
IM#2 Propellant Testing	170
IM#1 & 3 Dissection and Propellant Testing	179
Uninstrumented Motor Propellant Testing	187
Gage Recovery and Recalibration	188
INTERPRETATION OF DATA	193
PROGRAM EVALUATION - CONCLUSIONS AND RECOMMENDATIONS	227
AEROHEAT SIMULATION METHODS AND PROCEDURES	227
AEROHEAT FAILURE CRITERIA	230
CONCLUSIONS	233
Aeroheat Environment and Simulation	233
Motor Instrumentation and Data Acquisition	234
Structural Response Analyses	235
Failure Criteria	235
Program	236
RECOMMENDATIONS	237
REFERENCES	238
APPENDIX A- GAGE RESPONSE	

## TABLES

<u>No.</u>	<u>Title</u>	<u>Page</u>
1	Missions Considered	7
2	Material Properties Used in the Analysis	27
3	P-14EA 150 Normal Gage Pre- and Post Installation Calibration Data	41
4	JIB-1 Clip Gage Calibration Data	44
5	Shear Gage Post Installation Zero Load Data	45
6	Summary of Uniaxial Test Results	52
7	Uninstrumented Motor Test Summary	75
8	Summary of Instruments Installed in Motors	92
9	Instrumented Motor Test Summary	96
10	Instrumented Motor Test Summary - Aeroheat Tests	103
11	Hardness Measurements from IM#3, Section #3	180
12	Summary of Gage Calibrations for Gages in IM#1	190
13	Summary of Gage Calibrations for Gages in IM#2	191
14	Summary of Gage Calibrations for Gages in IM#3	192

## FIGURES

1	Program Overview	3
2	Typical Mass Flux and Recovery Temperature Schedules	8
3	Results of THVINC Analysis of Selected Mission Profiles	11
4	Results of THVINC Analysis of Selected Mission Profiles	12
5	Results of THVINC Analysis of Selected Mission Profiles	13
6	Results of THVINC Analysis of Selected Mission Profiles	14
7	Results of THVINC Analysis of Selected Mission Profiles	15
8	Hoop Stress at Inner Bore as Function of Heat Transfer Coefficient and Adiabatic Wall Temperature	17
9	Hoop Stress and Strains at Inner Bore for Selected Missions	18
10	Failure Boundary for UM#1 Propellant	19
11	Typical Radial Stress and Strain Relationships at Propellant Bond Line	21
12	Aeroheat Time - Temperature Schedule Sequence for a Two-Motor Program	23
13	Sketch of Selected Cylindrical Bore Configuration and Maverick Web Configuration	25
14	Finite Element for Cylindrical Core Configuration	26
15	Hoop Strain Contours in Cylindrical Bore Configuration at -75°F	28
16	Maximum Strain Contours in R-Z Plane at a Storage Temperature of -75°F	29
17	Maximum Stress Contours at -75°F in Cylindrical Core Configuration	30
18	Maximum Strain Contours in Maverick Web Configuration at -75°F	33

Figures (continued)

No.	Title	Page
19	Maximum Stress Contours in Maverick Web Configuration at Storage Temperature of $-75^{\circ}\text{F}$	33
20	Preliminary Grain Instrumentation Layout for SALE Motor	34
21	Normal Stress Gage (Konigsberg P-14)	36
22	Shear Stress Cube Configuration	36
23	Clip Bore Strain Gage	36
24	Potted Normal Stress Gage	39
25	Normal Stress Gage Calibration Data	39
26	Shear Gage Calibration Fixture	39
27	Shear Stress Gages Mounted in Shear Frame	40
28	Shear Gage Master Sensitivity Plot	39
29	Thermocouple Slab Design	46
30	IM#1 Gage Locations	48
31	IM#2 Gage Locations	49
32	IM#3 Gage Locations	50
33	Failure Boundary for Mix L-198	53
34	Temperature and Strain Rate Reduce Master Stress - Strain Curve for TP-L8006 Propellant (Mix L-198)	54
35	Relaxation Modulus for TP-L8006 Propellant	55
36	Comparison of Calibration Modulus Data from Mix L-198	57
37	Schematic Layout of Aeroheat Facility	59
38	Main Compressor	60
39	Air Storage Tanks	61
40	Typical Test Duration	62
41	Main Pressure Regulator Manifold - Process Air Piping	63
42	Capacitance Heater	65
43	SEL Data Acquisition	66
44	Data Acquisition Sequencer Panel	67
45	Drawing of Motor Mounted in Aeroheat Chamber (R50548)	69
46	UM#1 Being Stalled in Test Chamber	71
47	Test Instrumentation Layout	72
48	Typical Test Schedule for a SFPI Mission - Source Test No. 7	76
49	Comparison of Predicted and Measured Motor Case Temperatures	77
50	Temperature Distribution on the Motor Case at Three Selected Times	79
51	Typical Test Conditions for TS Mission - Test 12	80
52	Motor Case Temperature Histories for the TS Series	82
53	Typical Test Conditions for DMP-3 Mission - Test 17	83
54	Comparison of Predicted and Measured Motor Case Temperature for the DMP-3 Mission Test No. 14, UM#2	84
54A	Typical Test Conditions for HSMH Test Mission	86

Figures (continued)

No.	Title	Page
55	Stress Transducer Schematic	89
56	Bridge Completion Unit	90
57	Relationship Between S(t) and (o) for Data Reduction	94
58	Motor Ready for Gage Checkout Testing	97
59	Normal Stress in IM#2 as Measured by Gage N2-51	99
60	Normal Stress Elastic Analysis Results	100
61	Measured Normal Stress Results for Motor and Bench Calibration of Gage N2-51	101
62	Location of the Unbond Failure on IM#2	105
63	Schematic Showing Location of Failure	106
64	Gage N2-51 Output as a Function of Motor Temperature	107
65	Gage N2-48 Output as a Function of Motor Temperature	108
66	Gage N2-51 Response for the SFPI Tests	109
67	Gage N2-48 Response for the SFPI Tests	110
68	Comparisons of Gage N2-51 Response for Tests A-2 and A-20 and Tests A-5 and A-21	112
69	Normal Stress Induced by SFPI Mission as Measured by N2-51	114
70	Normal Stress Induced by the SFPI Mission as Measured by N2-42	115
71	Normal Stress Induced by the SFPI Mission as Measured by N2-46	116
72	Shear Stress Induced by the SFPI Mission as Measured by S2-111	117
73	Shear Stress Induced by the SFPI Mission as Measured by S2-105	118
74	Shear Stress Induced by the SFPI Mission as Measured by S2-110	119
75	Temperature Profile Histories for Various Aeroheat Loads (Test No. A-1)	123
76	Temperature Profile Histories for Various Aeroheat Loads (Test No. A-4)	124
77	Temperature Profile Histories for Various Aeroheat Loads (Test No. A-6)	125
78	Temperature Profile Histories for Various Aeroheat Loads (Test No. A-7)	126
79	Temperature Profile Histories for Various Aeroheat Loads	127
80	Temperature Profile Histories for Various Aeroheat Loads	128
81	Temperature Profile Histories for Various Aeroheat Loads	129
82	Temperature Profile Histories for Various Aeroheat Loads Test A-3	131
83	Temperature Profile Histories for Various Aeroheat Loads Test A-4	132
84	IM#3 Mid Motor Normal Stress, Tests A1 through A-3	133

Figures (continued)

<u>No.</u>	<u>Title</u>	<u>Page</u>
85	Comparison of HSMH and SFPI Test Results at an Initial Motor Temperature of 60°F	134
86	Effect of Decreasing Initial Motor Temperature - Gage N3-43, SFPI Profile	135
87	Comparison of Results from Successive SFPI Tests - Gage N3-43	136
88	Comparison of Results from Successive SFPI Test-Gage N3-47	137
89	Effect of Aeroheat Testing on DMP-3 Profile Response	138
90	Baseline Stress Data for Gage N3-44	141
91	Baseline Stress Data for Gage N3-43	142
92	Baseline Stress Data for Gage N3-47	143
93	Baseline Stress Data for Gage N3-45	144
94	Change in Stress in IM#3 at -65°F Due to Aeroheat Cycling	145
95	Aft End Motor Stress Relaxation Rate Increase Observed by Gage N3-45	146
96	S3-104 Test A-12	148
97	Change in Bore Hoop Strain in IM#3 at -65°F Due to Aeroheat Cycling	149
98	Baseline Bore Strain Data from Gage C3-18	150
99	Baseline Bore Strain Data from Gage C3-19	151
100	Baseline Bore Strain Data from Gage C3-30	152
101	Comparison of Results from Successive SFPI Tests - Gage C3-19	153
102	Comparison of Gage Measured Strain with Adjacent Bore Diameter Measurements - Gage C3-19	154
103	Change in Gage N1-49 Response for Various Tests	157
104	Mid Motor Stress Response to Aeroheat Loads - Gage N1-40 (Test No. A-1)	158
105	Change in Measured Stress in IM#1 at -65°F Due to Aeroheating Cycling	159
106	Difference in Stress Levels between Aeroheat and Equilibrium Cycles	162
107	Comparison between Aeroheat and Simulation Cycle for Gage N3-47	164
108	History of IM#3 Normal Gage Response Changes at -65°F	165
109	History of IM#3 Clip Gage Response Changes at -65°F	166
110	History of IM#1 Normal Gage Response Changes at -65°F	167
111	History of IM#1 Clip Gage Response Changes at -65°F	168
112	Motor in Lathe	171
113	Propellant Grain Being Severed Using Butcher Knife	172

Figures (continued)

No.	Title	Page
114	IM#1 with Head End Removed	173
115	IM#2 After Dissection	174
116	IM#2 After Dissection (Aft Section)	175
117	TP-L8006 Propellant Removed from SALE IM#2, Segment 2	177
118	TP-L8006 Propellant Removed from SALE IM#2, Segment 3	178
119	Cut Interface Between Sections 1 and 2 of IM#1	181
120	Segments of IM#3	182
121	Cracking in IM#3	183
122	Maximum Stress Versus Radius, Motor IM#3	184
123	Strain at Maximum Stress Versus Radius, Motor IM#3	185
124	Nodal Point Modeling of Problem (one dimensional) THVINC	194
125	Element Modeling for Problem (one dimensional) THVINC	195
126	Relaxation Modulus Curve, TP-L8006 Propellant	197
127	Calculated and Measured Normal Stresses N2-51 for Aeroheat DMP-3, A-1, IM#2, Using Different Modulus Curves	198
128	THERMVINC Results Using Different Modulus Curves for Aeroheat DMP-3, A-1, IM#2	199
129	Relaxation Modulus Curve for Aged and Unaged TP-L8006 Propellant	200
130	THVINC Prediction of Radial Stress at the Bondline for DMP-3 Aeroheat Mission with Aged and Unaged Propellant	202
131	THVINC Prediction of Hoop Stress at the Inner Bore for DMP-3 Aeroheat Mission with Aged and Unaged Propellant	203
132	Relaxation Modulus Curve for TL-H706A Liner and TA-H727B Adhesive	204
133	THVINC Prediction of Radial Stress at the Bondline for the SFPI Aeroheat Mission Using Different Modulus Curves	205
134	THVINC Prediction of Hoop Stress at the Inner Bore for the SFPI Aeroheat Mission Using Different Modulus Curves	206
135	THVINC Prediction of Radial Stress at the Bondline for DMP-3 Aeroheat Mission with Different Liner Thicknesses	207
136	THVINC Prediction of Hoop Stress at the Inner Bore for DMP-3 Aeroheat Mission with Different Liner Thickness	208
137	Comparison of THVINC Predictions and Aeroheat Results	209
138	Temperature Profile Histories for Various Aeroheat Loads Test A-1	210
139	THVINC Axisymmetric Mathematical Element Model	212
140	Temperature Profile Histories for Various Aeroheat Loads	213
141	THVINC Prediction of Radial Stress at the Bondline for SFPI Aeroheat Mission	214
142	THVINC Prediction of Radial Stress at the Bondline for SFPI Aeroheat Mission	215

Figures (continued)

No.	Title	Page
143	THVINC Prediction of Hoop Stress at the Bondline for SFPI Aeroheat Mission	216
144	THVINC Prediction of Maximum Principal Stress at the Bondline for SFPI Aeroheat Mission	217
145	THVINC Prediction of Axial Stress at the Bondline for SFPI Aeroheat Mission	218
146	THVINC Prediction of Shear Stress at the Bondline for SFPI Aeroheat Mission	219
147	Head End Normal Stress Gage Output and Axisymmetric THVINC Results at the Bondline	220
148	THVINC Prediction of Hoop Strain at the Inner Bore for SFPI Aeroheat Mission	222
149	THVINC Prediction of Radial Stress at the Bondline for SFPI Aeroheat Mission	223
150	Comparison between Normal Gage Data and THVINC Prediction for a SFPI Aeroheat Mission with IM#2 and IM#3	224
151	Comparison between Normal Stress Gage Data and THVINC Predictions for Test A-2, IM#2, and Test A-1, IM#3, DMP-3 Aeroheat Mission	225

## INTRODUCTION

### OBJECTIVE AND BACKGROUND

The objective of this program is to define the response and failure characteristics of solid propellant rocket motors when subjected to transient thermal conditions representing air launched operational environments. A further goal of this program is to provide data useful for aiding in the establishment of procedures for air launched rocket surveillance programs.

This program was conducted by Thiokol Corporation, Huntsville Division, Huntsville, Alabama, for the Air Force Systems Command, Air Force Rocket Propulsion Laboratory, Edwards Air Force Base, California, under Contract F04611-73-C-0015.

Traditionally, the effects of temperature on a solid propellant rocket motor are evaluated for conditions that correspond to storage at various ambient conditions (e. g. , -65 to 165°F). Propellant ballistics, grain structural integrity, bond systems, etc. , are investigated by conditioning the motor to specified temperatures and then performing inspections and/or static firings. Effects of transporting the motor from one temperature environment to another are simulated by cycling the temperature in the conditioning device between specified limits at a certain rate of change. With the advent of new high speed aircraft that carry missiles externally and exposed to aerodynamic heating, a new dimension of temperature extremes has been introduced. The velocities of these new aircraft are sufficient to produce air recovery temperatures as high as 700°F. Since these high velocities may be encountered at both high and low altitudes, resulting in vastly different local air pressures (and thus heat transfer coefficients), it becomes more involved to simulate the heating environments to which a motor might be exposed. An additional complication is the fact that the motor is returned to its original storage environment, (a cycle that can be repeated several times before the motor is fired), whereas the normal temperature evaluation permits the motor to be exposed to a given environment for several hours.

### SCOPE

Air launched operational environments normally consist of four parts: transportation, ground storage, flight line readiness storage, and air carry during flight on the airplane. This program was primarily concerned with actual flight on the airplane, but also considered the varying starting and end temperatures from two storage conditions, i. e. , ground and flight line readiness. The reason that this program was concerned with the air carry regime was the current inability to mathematically analyze the structural behavior of a propellant grain under transient thermal conditions.

## UNCLASSIFIED

The Maverick motor, AGM-65A, was used as a test bed on this program. No time-temperature schedule derived from Maverick mission profiles would cause motor failure. Therefore, future Air Force mission profiles for other motor designs which would cause failure in the Maverick motor were used on this program. One motor with a slightly modified mandrel, to allow location of strain gages, was instrumented and cast. In addition, a second and third motor with simple grain geometries were instrumented and cast with the Maverick case and propellant.

### PROGRAM ORGANIZATION

An overview of the program is shown on Figure 1. As shown, the program was basically divided into four areas of investigation; Aeroheat Analysis, Testing, Data Analysis, and Program Evaluation. To accomplish the program in a logical manner, these areas of investigation were further divided into seven basic tasks as follows:

#### Task One - Mission Profile Analysis and Aeroheat Severity Study

Time-temperature schedules will be selected from present and projected Air Force mission profiles. A non-instrumented motor will be subjected to these schedules to determine when failure occurs.

#### Task Two - Motor Manufacture and Propellant Characterization

Three Maverick motors will be instrumented and cast. The propellant will be characterized.

#### Task Three - Aeroheat Mission Simulation (Motor #1)

The first instrumented motor will be subjected to the five schedules selected in Task One and cycled to failure.

#### Task Four - Simulation of Aeroheat Conditions (Motors #2 and #3)

The maximum stresses and strains encountered in the aerodynamic heating schedules on the first instrumented motor will be reproduced in the second and third instrumented motors by equilibrium temperature cycling.

#### Task Five - Failure Verification (Motors #2 and #3)

The second and third instrumented motors will be cycled to failure using equilibrium temperature cycling. The remaining non-instrumented motors will also be cycled to failure, to obtain a failure distribution curve.

#### Task Six - Dissection and Stress Analyses

The motors will be dissected, propellant tested and stress analyses run. Margins of safety for this motor will be computed.

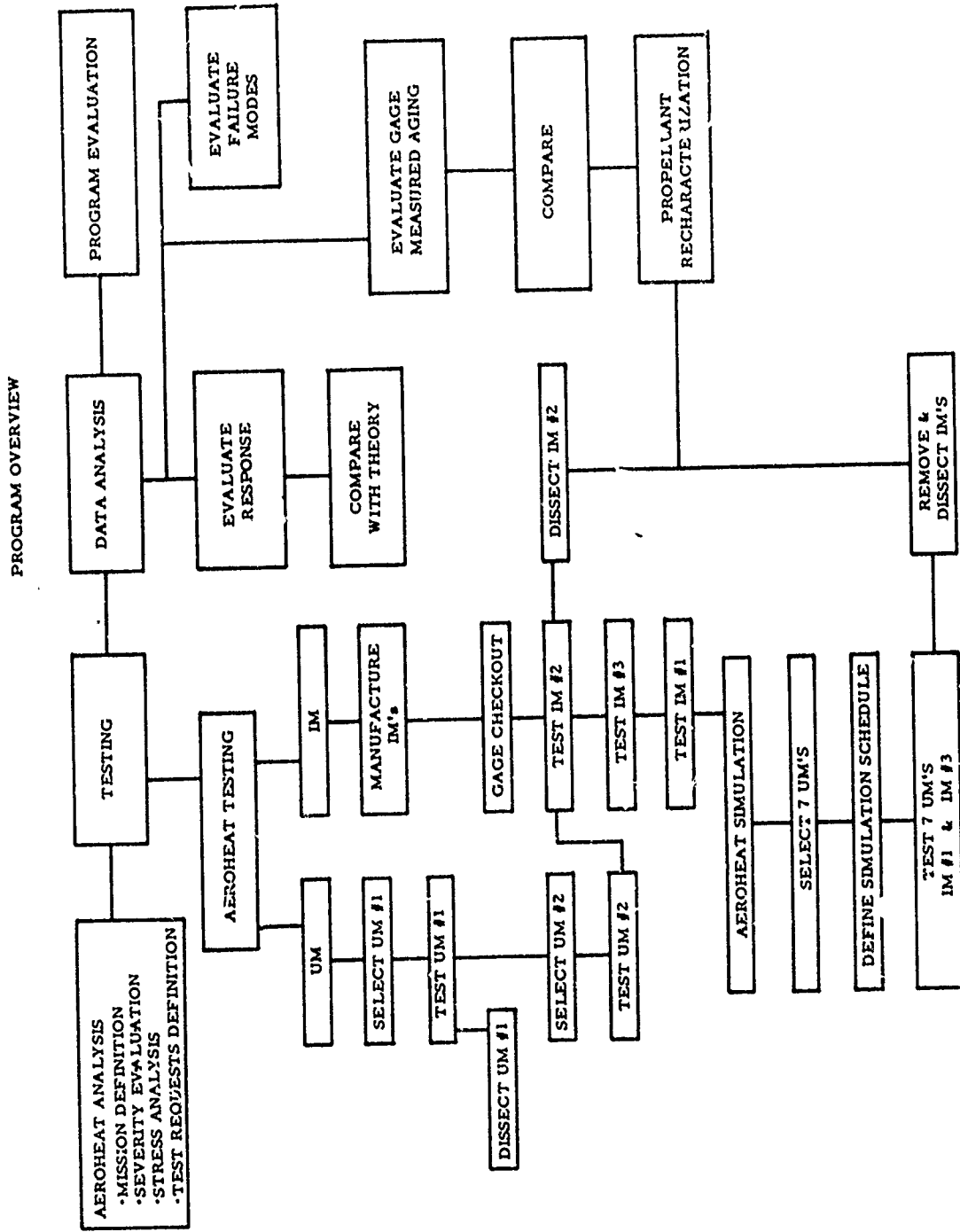


Figure 1. Program Overview

## Task Seven - Program Evaluation

The status of the simulation of the air launch environment will be assessed.

Thus, the program consisted of initially defining and selecting appropriate mission profiles. Each profile was analyzed with respect to the thermal environment it imposes which was then used to conduct a stress analysis to determine the severity of that profile. Six missions were selected for further evaluation to determine not only which missions were the most severe in relation to each other, but also how they rank with respect to propellant capability. The transient thermal viscoelastic computer code (THVINC) was used to generate predictions of stress and strain levels characteristic of the selected mission profiles. Five time-temperature schedules were selected, in order of increasing severity, as a result of the analysis of the mission profiles. To guard against a failure occurring within the first several cycles with only a limited amount of information being obtained, a two motor test program was initiated. The first uninstrumented was subjected to only thirteen tests since a possible liner failure by high temperature reversion was suspected. The second uninstrumented motor was then tested. This motor was subjected to 37 aeroheat tests without failure. Three instrumented motors were then tested. A total of 50 aeroheat tests was conducted on instrumented motors. An unbond failure was detected in IM#2 in the early phases of its testing. This prompted a deviation from the original test program plan and IM#3 was tested to fully obtain the structural response of the CP configuration to the aeroheat loads. The third motor (IM#1) was also aeroheat tested to determine the structural response of the star configuration.

An analysis of the aeroheat data indicated that the aeroheat induced stress and strains were short duration phenomena and a function of initial motor temperature. It was obvious that these data could not be reproduced through equilibrium temperature cycling and it was, therefore, decided to establish a simulated cycle which could possibly produce a similar stress level as a function of temperature without an appreciable compromise on the strain level. Two of the motors (IM#1 and IM#3) were tested using the selected cycle. The instrumented motors were removed from this test series after the twelfth test and were then dissected, the propellant tested, and stress analysis run. Considerable changes in the output of the normal and clip gages were seen to occur near the end of the simulation tests which could indicate significant degradation of the motor. The results of the dissection of these motors indicated that much of the changes were due to changes within themselves.

At this time, the data gathered during the program were interpreted which required consideration of each aspect that could induce errors or shifts in those data. The overall program was then evaluated with respect to methodology and procedure used and assessments made as to necessity and worth of aeroheat simulation.

## TECHNICAL ACCOMPLISHMENTS

### AIR LAUNCH ENVIRONMENT ANALYSIS

#### Requirements

Before proceeding into a discussion of the mission profiles selected and analyzed for relative severity levels, a review of the requirements imposed upon this study by the program objectives is in order. Inasmuch as the prime objective is to define response and failure characteristics under conditions relating to air launched operational environments, some definition of air launched operational environments is necessary. As previously stated, these environments consist of four parts: transportation, ground storage, flight readiness storage, and air carry during flight on the airplane. These environments are considered and incorporated into the missile surveillance plans in terms of standard tests. Of course, all standardized testing can come under some degree of scrutinization with respect to their relevance with real life environments. This is particularly true of thermal testing, since the stress and strain fields set up under an aeroheat environment may not remotely resemble the stress and strain fields under equilibrium conditions at the two extremes of an aeroheat cycle.

Of the four aforementioned air launched environments, the least is known about the mechanical behavior of the propellant grain during air carry. Some work had, of course, been done in this area; however, attempts to relate types of missions in terms of severity with response and failure characteristics are meager. This is the area then in which this program concentrated by attempting to define failure probability as function of the number of air carry missions.

To define structural response and failure characteristics as a function of air carry, one must first define plausible aircraft mission profile for which a motor might be subjected. Then these must be analyzed with respect to the transient thermal conditions which are produced in the motor as the missions progresses. To accomplish this, special computer codes are required such as THVINC which performs stress and strain calculations for transient thermal conditions. The results of analyzing the severity level of selected mission profiles by use of the THVINC code is discussed in the next few sections followed by a discussion of the initial result of the aeroheat testing of an uninstrumented motor.

#### Mission Review and Selection

Essentially, two sources of projected Air Force mission profiles are available. The first is information generated by the Severe Environmental Air Launch Study (SEALS), Reference 1, which projects extremely high recovery temperatures and heating rates on pylon mounted missiles. These missions can be considered as extremes since it is unlikely that higher aircraft velocities will be efficiently achieved with a "dirty" aircraft configura-

tion. The second source is the "Determination of Aircraft Missile Environment" (DAME), Reference 2, study which is a current study related to F-111 aircraft capability. These two sources coupled with consultation with AFRPL have provided the information necessary to select the required five mission profiles.

Although the mission profiles as defined in those studies appear to show a great degree of variance from one to another, they have little meaning until converted into missile skin recovery temperature and heating rate coefficient schedules with time. The schedules are included in the DAME report and will not be reproduced here. In the SEALS report, these are not given; however, they can be simply calculated. The total heat flux to the missile skin due to convective heating is defined as:

$$q = h (T_{aw} - T_w)$$

Where  $h$  is the heat transfer coefficient,  $T_{aw}$  is the recovery temperature number, and altitude can be calculated using either the Schmidt, Reference 3, and/or Eckert, Reference 4, techniques which are based on Reynolds analogy and an empirical skin friction coefficient. These methods are well recognized and need no further explanation. The value of  $T_{aw}$  is obtained from the expression:

$$T_{aw} = T_{\infty} + r (T_o - T_m)$$

Where  $T_{\infty}$  is static temperature,  $T_o$  is total temperature, and  $r$  is the recovery factor which is equal to the cubic root of the Prandtl number for turbulent flow. Note that the heat transfer coefficient is proportional to the mass flux (i. e., density times velocity) at the outer edge of the boundary layer to the 0.8 power. Thus, a most meaningful method for expressing the heat transfer coefficient is in terms of mass flux. Therefore, this becomes the logical method for reducing the mission profiles and it also relates directly to facility flow requirements. The recovery temperature schedule becomes the desired facility air temperature schedule.

The mission profiles described in the SEALS and DAME study are depicted in terms of local adiabatic wall temperature and mass flux on Figure 2. In addition to these profiles, another which will be referred to as HSM was added to the list by the AFRPL. This profile is also presented on the same figure for comparison purposes. In reviewing these missions, it is obvious that the DAME Mission 4 (DMP-4) is basically an aerocool profile or perhaps a very mild aeroheat profile and can be dropped from consideration.

Six missions were then selected for further evaluation in terms of structural severity. These missions are: DMP-2, DMP-3, DMP-5, HSM, SLRI, and SFPI and are defined in Table 1. These six missions become many more when variations in initial motor storage temperatures and atmospheric conditions are considered. For example, consideration of hot day,

TABLE 1

MISSIONS CONSIDERED

SOURCE

DAME - Determination of Aircraft Missile Environment

- DMP -2 - Climb to 50K feet, accelerate & cruise at M=2.5
- DMP -3 - Climb to 35K feet, accelerate & cruise at M=2.0
- DMP -5 - Cruise M=0.9 at 500 feet

SEALS - Severe Environmental Air Launched Study

- SFPI - High speed chase followed by low speed cruise - high altitude
- SLRI - High altitude, high speed cruise

OTHERS - AFRPL

- HSM - Moderate speed, low altitude cruise

Note: DMP = Dame Mission Profile  
 SFPI = Seals Fighter Point Interceptor  
 SLRI = Seals Long Range Interceptor

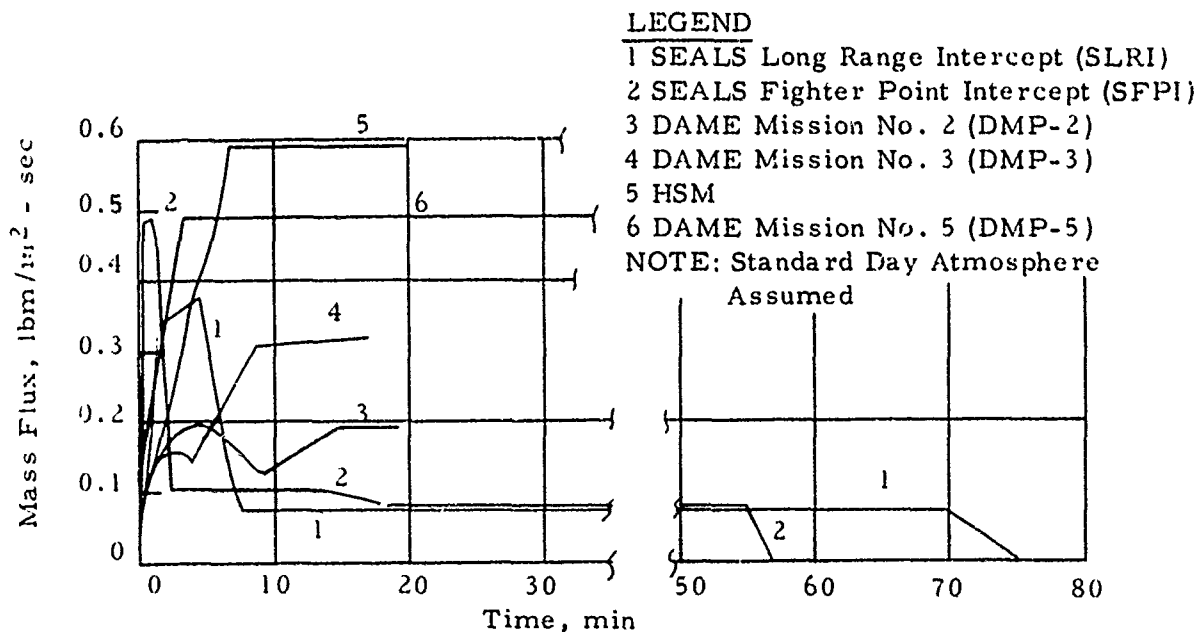
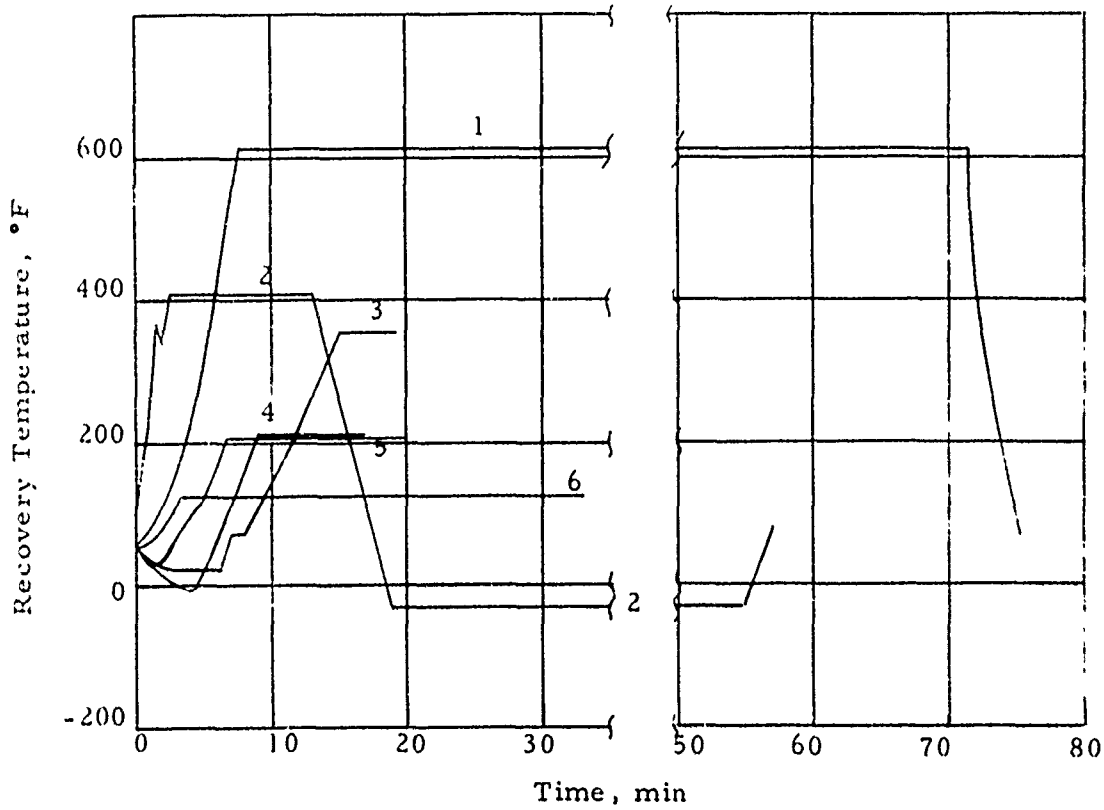


Figure 2. Typical Mass Flux and Recovery Temperature Schedules

standard day, and cold day atmospheric conditions increase the number to 18. Consideration of, for instance, three initial motor storage temperatures further increase this number to 54. Many can be eliminated as being unrealistic while many others eliminated as being thermally similar. Although this is possible, however, there is some question of practicality. The simple facts are that a motor is initially at some temperature and is then heated or cooled at a given rate. The temperature and rate of change of temperature throughout the motor are then the two important variables to be considered. For a given mission, changes in either  $T_{aw}$  because of assumed different atmospheric conditions or changes in initial motor temperatures are reflected in changes in heating rate. This then can result in any number of heating rates for a given flight profile. A further complication is, of course, that the thermally induced stresses and strains in the propellant are not linearly dependent upon the temperature level or heating rate because of viscoelastic effects. Therefore, it was decided to analyze the basic mission profiles and determine not only which missions were the most severe in relation to each other but also how they ranked with respect to propellant capability. Based on this information, aeroheat schedules can be derived.

#### Mission Severity Analysis

The transient thermal viscoelastic computer code (THVINC), Reference 5, was used to generate predictions of stress and strain levels characteristic of the selected mission profiles. THVINC was developed by Dr. R. L. Taylor and G. L. Goudreau at the University of California for the Air Force under the STV program. Thiokol/Huntsville obtained THVINC from the Air Force for the SALE program, however, the computer code received was not operational. With the assistance of Dr. R. S. Dunham at the University of Texas, THVINC was made operational.

The reason for developing THVINC was to determine temperature, deformations, stress, and strains in solids of revolution loaded axisymmetrically as a function of time and temperature. The effects of arbitrary time dependent temperature, heat flux, displacement, or stress boundary conditions are included. The present version is reformulated to handle the incompressibility of solid propellant. The program uses a viscoelastic shear modulus specifying the viscoelastic properties of isotropic linear viscoelastic material. The use of a viscoelastic shear modulus with a constant Poisson's ratio forces a dependent viscoelastic bulk modulus. The effect of temperature on the shear modulus is determined for thermorheologically simple materials through the use of a shift function  $a_T$ . Variable time steps may be used in the step forward integration. A Prony series curve fit is used on the master relaxation modulus curve to obtain the viscoelastic shear modulus.

THVINC has been modified to incorporate strain calculations, stress-time accumulation damage logic which is calculated at every nodal point and for every element, and a plot program. The plot program was written to better compare analytical results with instrument motor gage readout data. Our instrumented motor gage readout data reduction program plots stress and

strain as a function of time and temperature. With both analytical and test data plotted, faster and more accurate comparisons are available. The cumulative damage logic used in THVINC is the same logic used in the Aerojet one and two-dimensional thermoviscoelastic computer codes.

To obtain good results from THVINC, it is essential to have good thermal properties and relaxation modulus inputs for the propellant. The essential input parameters for THVINC are the viscoelastic shear modulus curve, the  $a_T$  curve, the mass density, the thermal conductivity, the specific heat, the heat transfer coefficient or a specified temperature history. The accuracy of THVINC is a function of the size of the time steps used in specifying temperature history. Long time steps in the range of 10 seconds were used in these calculations after comparisons made with RECAP-- a finite difference type transient heating code - showed no more than 3 degrees difference in the temperature profiles.

For this program, the geometry used in the calculation was selected as a cylindrical perforated core of infinite length with the web thickness being equivalent to that of the Maverick motor design with the star points removed. Although such a selection is not fully representative of the finite and more complex grain geometry which will be tested under this program, it does provide the most efficient and inexpensive method for determining the relative severity levels of the missions.

Perhaps the most informative aspects of these results are found by comparing the tangential or hoop stress time histories at the inner bore and the radial or normal stress time histories at the bond line with time for the mission profiles. These comparisons along with comparisons of bond line temperature-time histories and both inner bore hoop and bond line radial strain time histories are presented on Figure 3 through 7. Because of the rapid rate of increase of temperature at the bond line with time, one might expect high values of radial stress and strain to be induced at the bond line. Inspection of Figures 4 and 5 refute this expectation. Because the motor has been cooled to a temperature below cure temperature, a negative or compressive strain is induced in the radial direction. Although aeroheating has induced a tensile stress (Figure 4) which is relatively small, we find that the effect is one of strain relief. Therefore, it would appear that the effects of aeroheat are relatively mild from a structural standpoint at the bond line; however, such a conclusion would be premature since a large degradation in propellant capability may be exhibited if the propellant were repeatedly cycled through this high temperature range.

The hoop stresses and strains at the inner bore (Figures 6 and 7) do show a considerable effect from aeroheating. Although these values do not seem large, they do represent a relatively severe stress condition when a stress concentration factor of three is introduced. This factor represents the relationship between the cylindrical core case and a star point design of the Maverick type. Therefore, increasing the values of hoop stress and strain in the figures by a factor of three, does represent a relatively severe

<u>Mission</u>	<u>Curve</u>
DMP-2	1
DMP-3	2
DMP-5	3
HSM	4
SLRI	5
SFPI	6

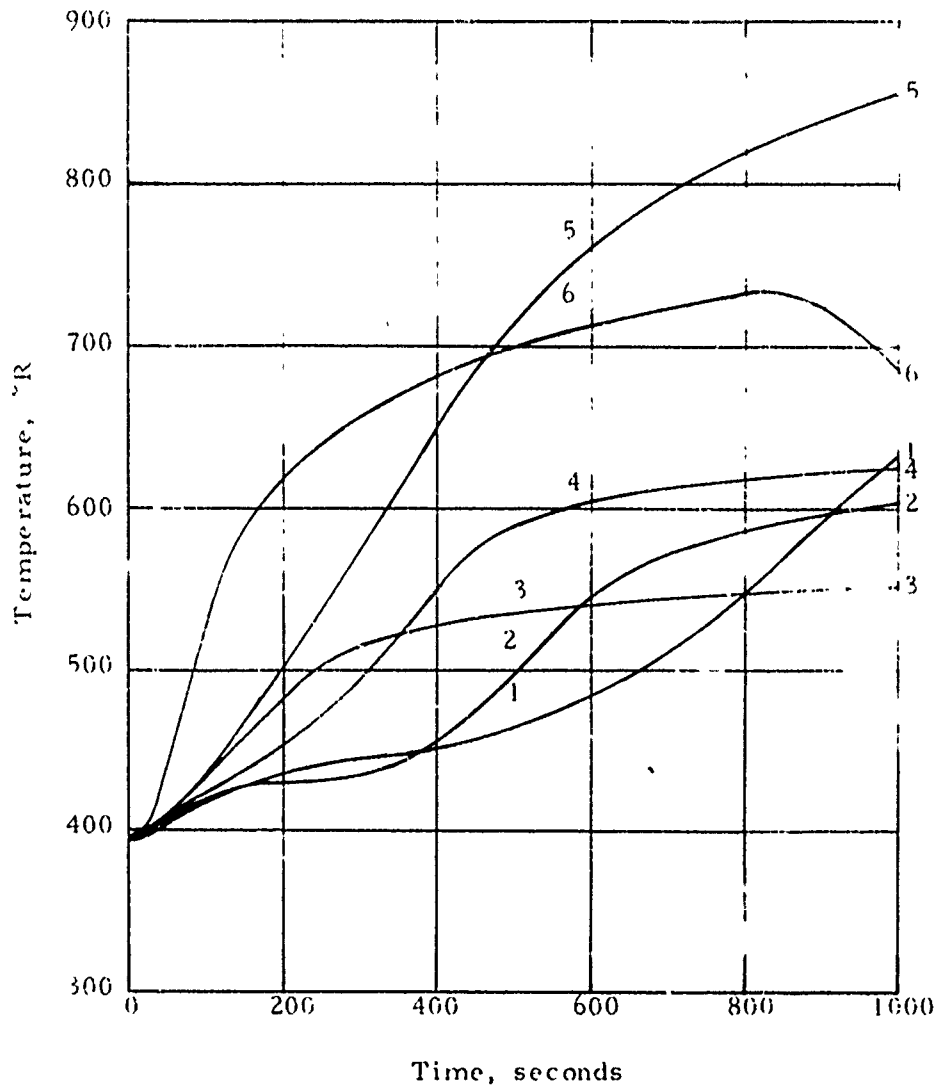


Figure 3. Results of THVINC Analysis of Selected Mission Profiles, Temperature at Propellant Bond Line

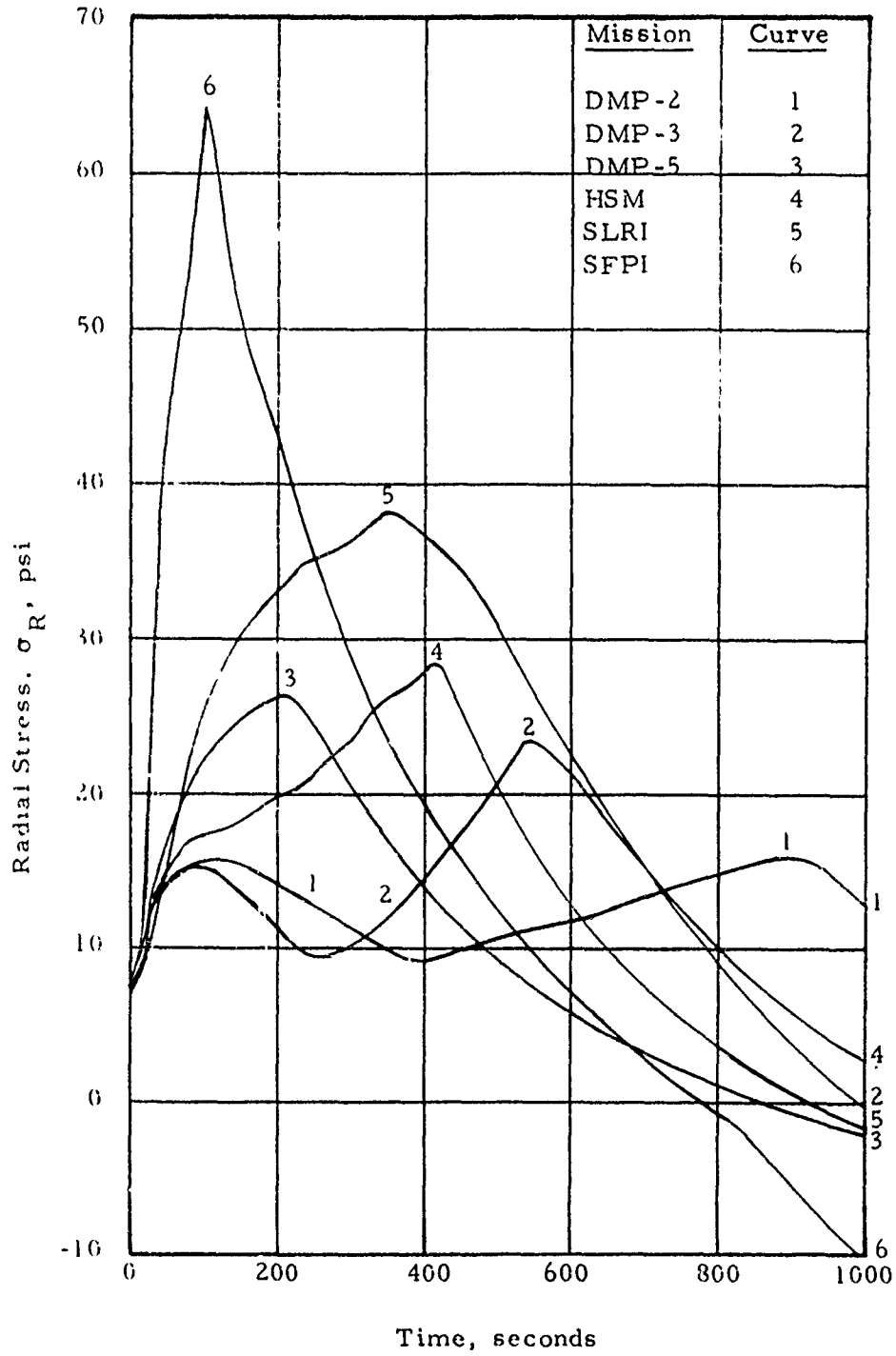


Figure 4. Results of THVINC Analysis of Selected Mission Profiles, Radial Stress at Propellant Bond Line

<u>Mission</u>	<u>Curve</u>
DMP-2	1
DMP-3	2
DMP-5	3
HSM	4
SLRI	5
SFPI	6

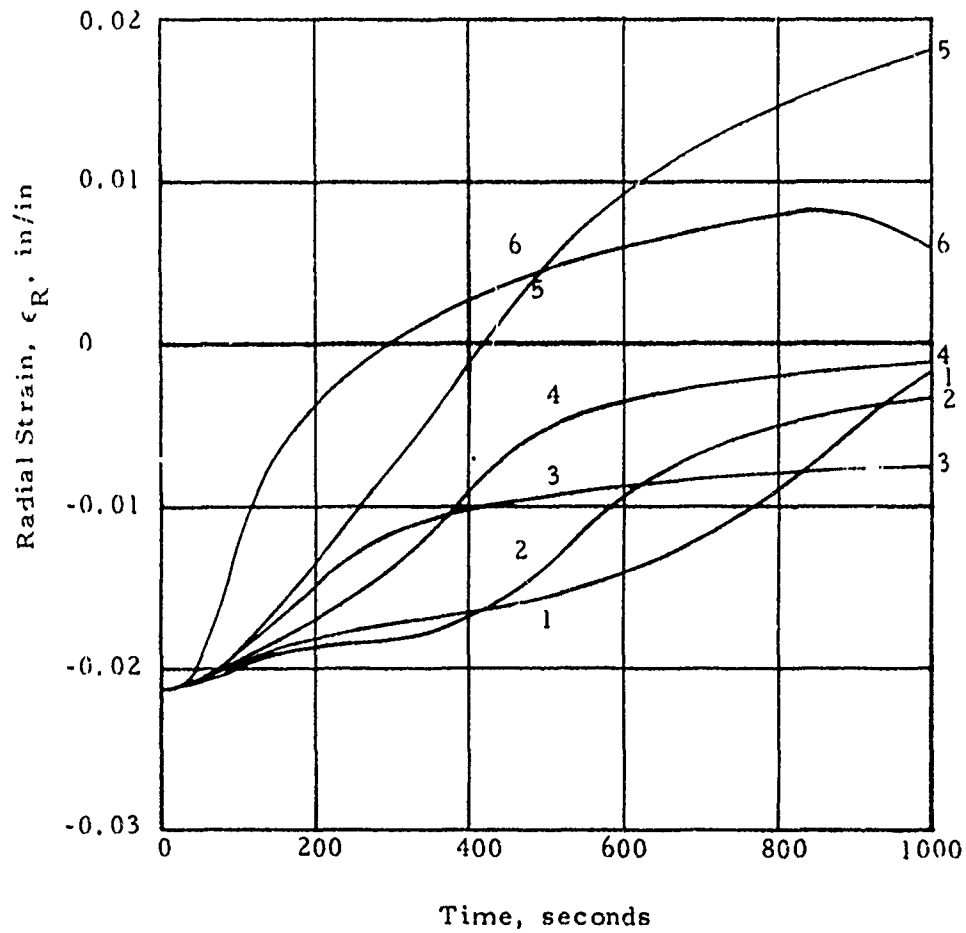


Figure 5. Results of THVINC Analysis of Selected Mission Profiles, Radial Strain at Propellant Bond Line

<u>Mission</u>	<u>Curve</u>
DMP-2	1
DMP-3	2
DMP-5	3
HSM	4
SLRI	5
SFPI	6

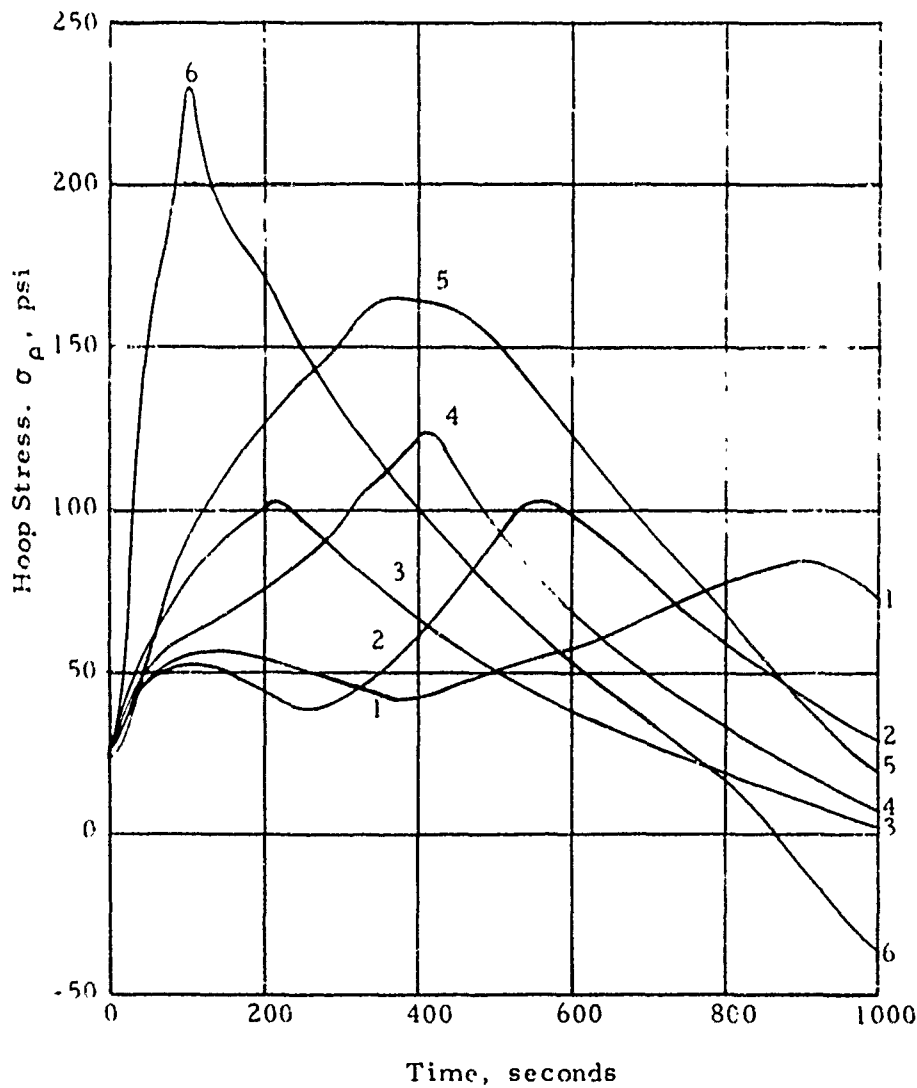


Figure 6 Results of THVINC Analysis of Selected Mission Profiles, Hoop Stress at Inner Bore

<u>Mission</u>	<u>Curve</u>
DMP-2	1
DMP-3	2
DMP-5	3
HSM	4
SLRI	5
SFPI	6

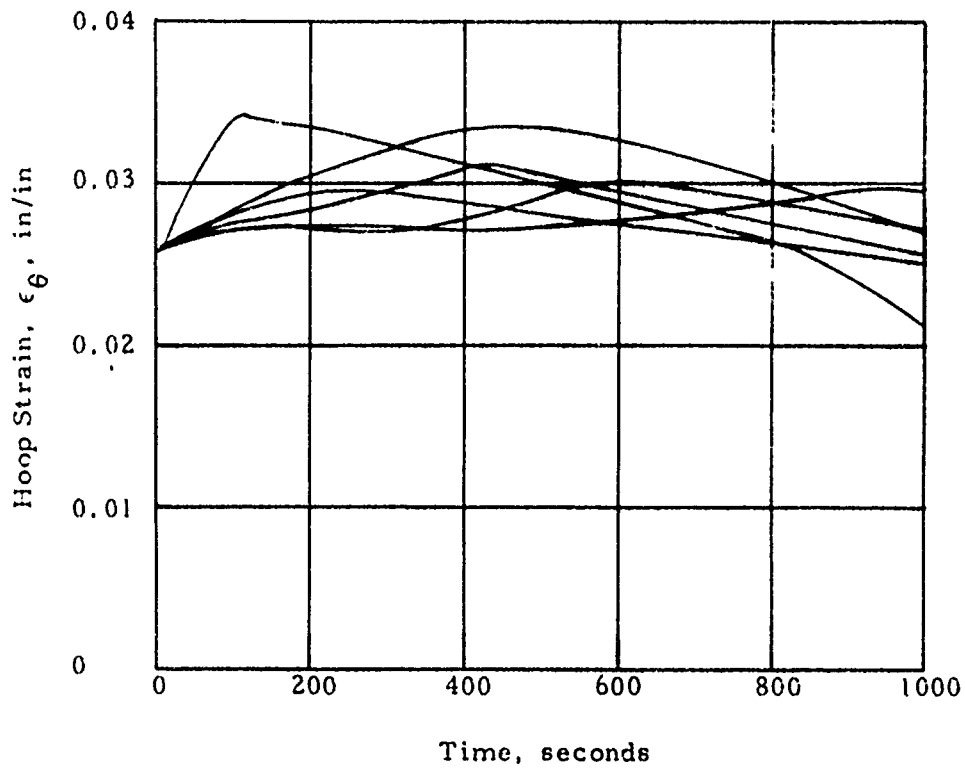


Figure 7. Results of THVINC Analysis of Selected Mission Profiles, Hoop Strain at Inner Bore

condition.

Because the stress and strain levels do not explicitly show the effects of any perturbation upon a given mission, it was decided to do a parametric analysis to see if a relationship between peak stress, heat transfer coefficient,  $h$ , and adiabatic wall temperature  $T_{aw}$  did exist. In making these calculations, it was assumed that the motor was at an initial temperature of  $-65^{\circ}\text{F}$  and then suddenly immersed in a medium characterized by a given value of  $h$  and  $T_{aw}$ . The results of these calculations are shown on Figure 8. As shown, the peak hoop stress at the inner bore increases as both temperature and heat transfer coefficient increases. It is interesting to compare the values obtained in this analysis with those from the HSM case. As shown on Figure 6, the peak hoop stress for the HSM is 125 psi which when multiplied by the stress concentration factor becomes 375 psi. The corresponding value from Figure 8 is 558 ( $h = 0.032 \text{ Btu/ft}^2\text{-sec-}^{\circ}\text{R}$  and  $T_{aw} = 670^{\circ}\text{R}$ ). The vast difference in these levels is due to the fact that the initial heating rate for the HSM case is reduced by the effect of acceleration and climb to the cruise conditions as compared to a hypothetical start at cruise conditions.

The above tends to confirm that there is considerable difference in the hoop stress histories set up on the inner bore as a function of the initial portion of the mission. Whether or not this is of significant importance is another question. The fact that this is of little significance is shown on Figure 9. Here the inner bore hoop stress and strain profiles are presented in the same manner that is used to show failure boundary curves. The more severe missions along with one termed "Case 11", (this represents the point on Figure 8 where  $h = 0.060 \text{ Btu/ft}^2\text{-sec-}^{\circ}\text{R}$  and  $T_{aw} = 820^{\circ}\text{R}$ ) are shown for an initial grain temperature of  $-65^{\circ}\text{F}$ . As shown, all missions fall on the same line. Of course, all start at the same point and move forward with the distance moved being a function of severity. Note that a failure can occur; that is, the superimposed failure boundary curve is crossed by the mission labeled "Case 11" and the SFPI case is not far behind. Such a failure would result from an over stress condition as opposed to an excessive-strain failure which is more characteristic of most rocket motor failures. The effect of starting from a higher initial motor temperature is also shown. As expected, this eases the situation by reducing both the stress and strain levels at the starting point thus moving the entire curve further from the failure boundary.

The propellant properties and failure characteristics referred to above and used throughout this analysis was obtained from uniaxial tests conducted as part of this study. The failure boundary curve generated from these data is shown on Figure 10. The propellant tested was cut from ice cream cartons cast from the same mix as the motor selection for use as UN #1. Early in the program it was found that certain production motors had been rejected for delivery because minor flaws such as voids in the star points were found. It was determined that flaws in the star points would have no effect on the failure characteristics of the motor under aeroheat environments and thus could be utilized in this program. Therefore, such a motor,

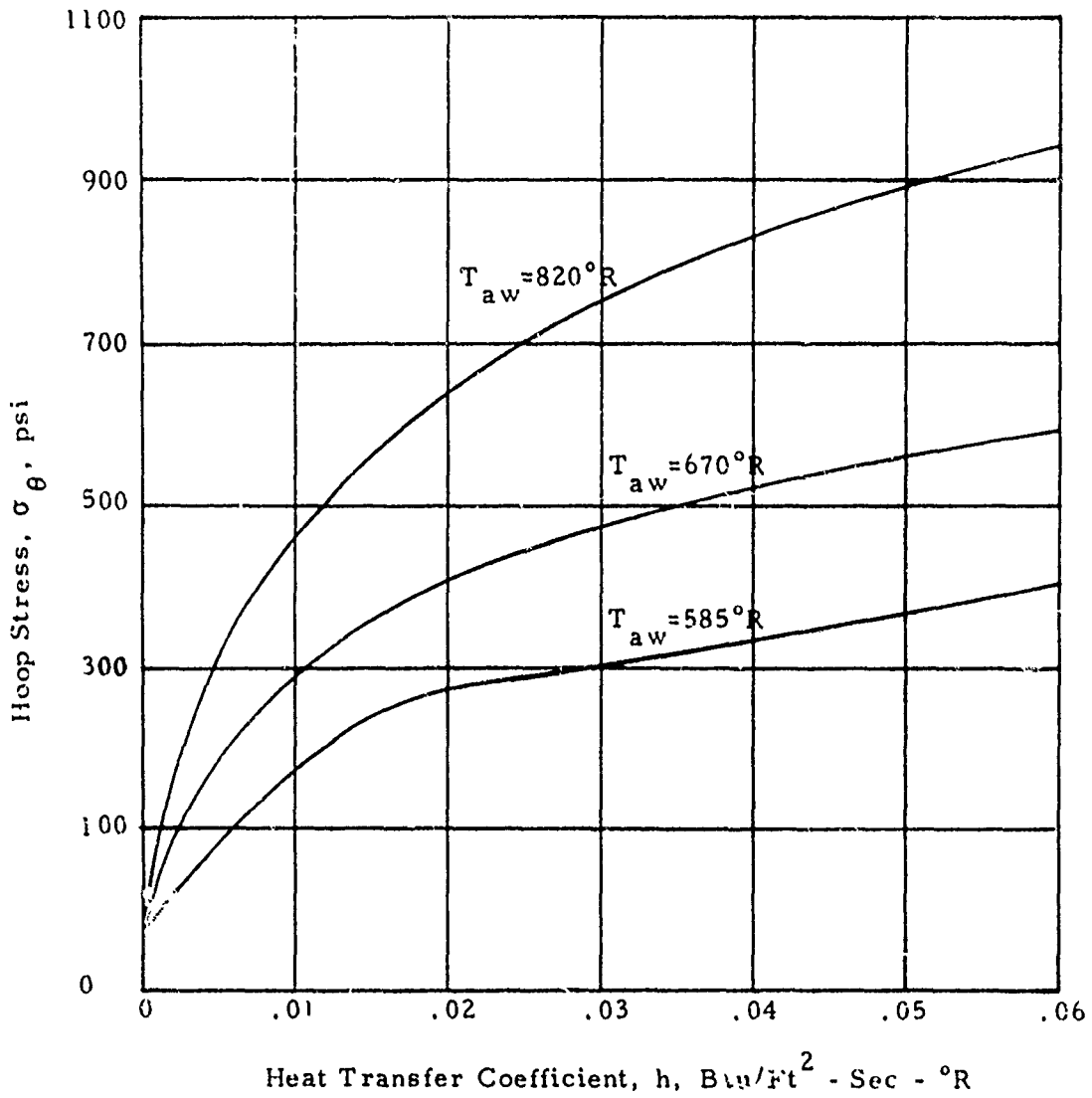


Figure 8. Hoop Stress at Inner Bore as Function of Heat Transfer Coefficient and Adiabatic Wall Temperature

Thiokol

- HSM
- DMP-3
- ◇ SLRI
- ◊ SFPI
- ◻ Case 11

Note: Corrected for Star Point Stress and Strain Concentrations.

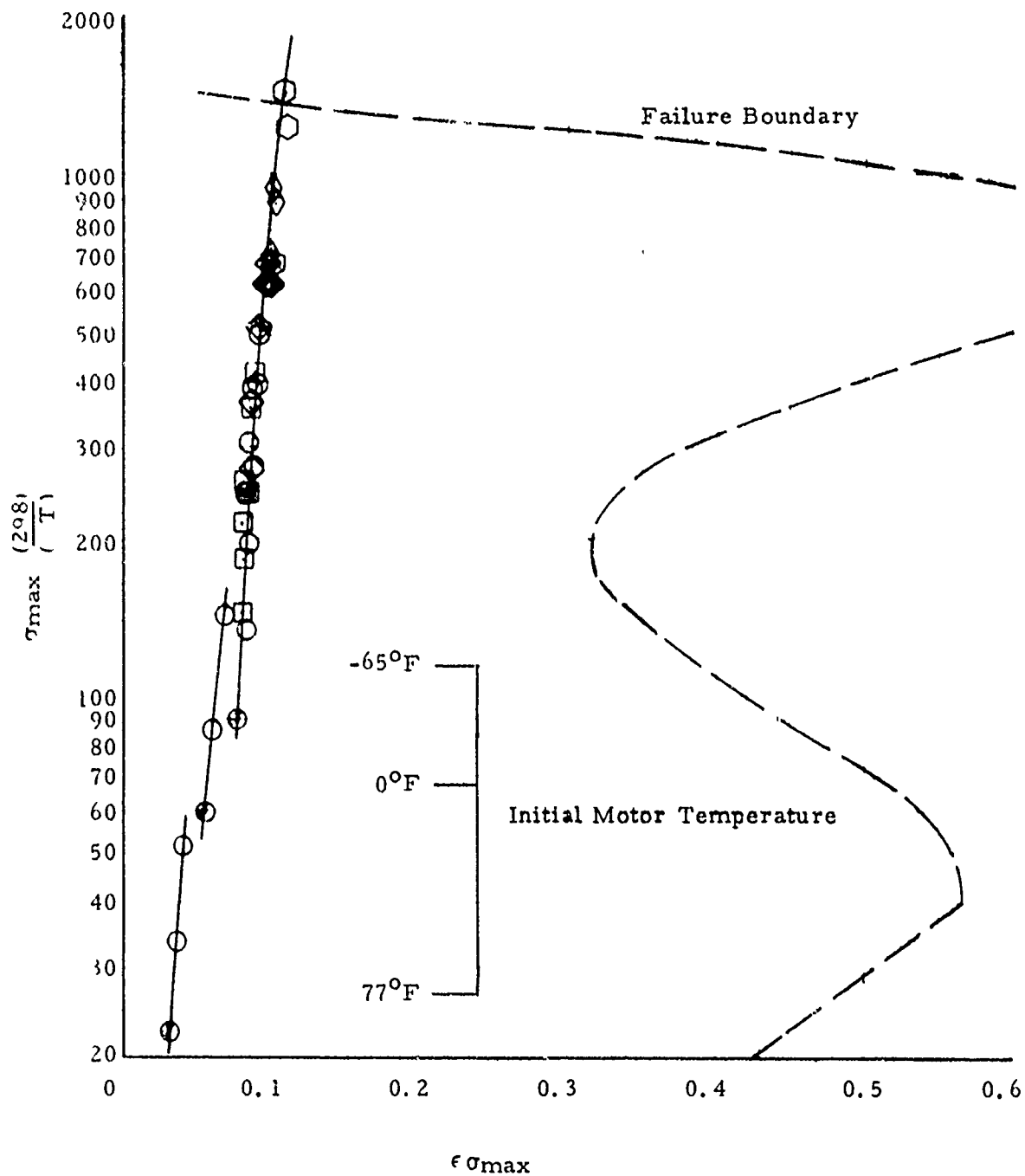


Figure 9. Hoop Stress and Strains at Inner Bore for Selected Missions

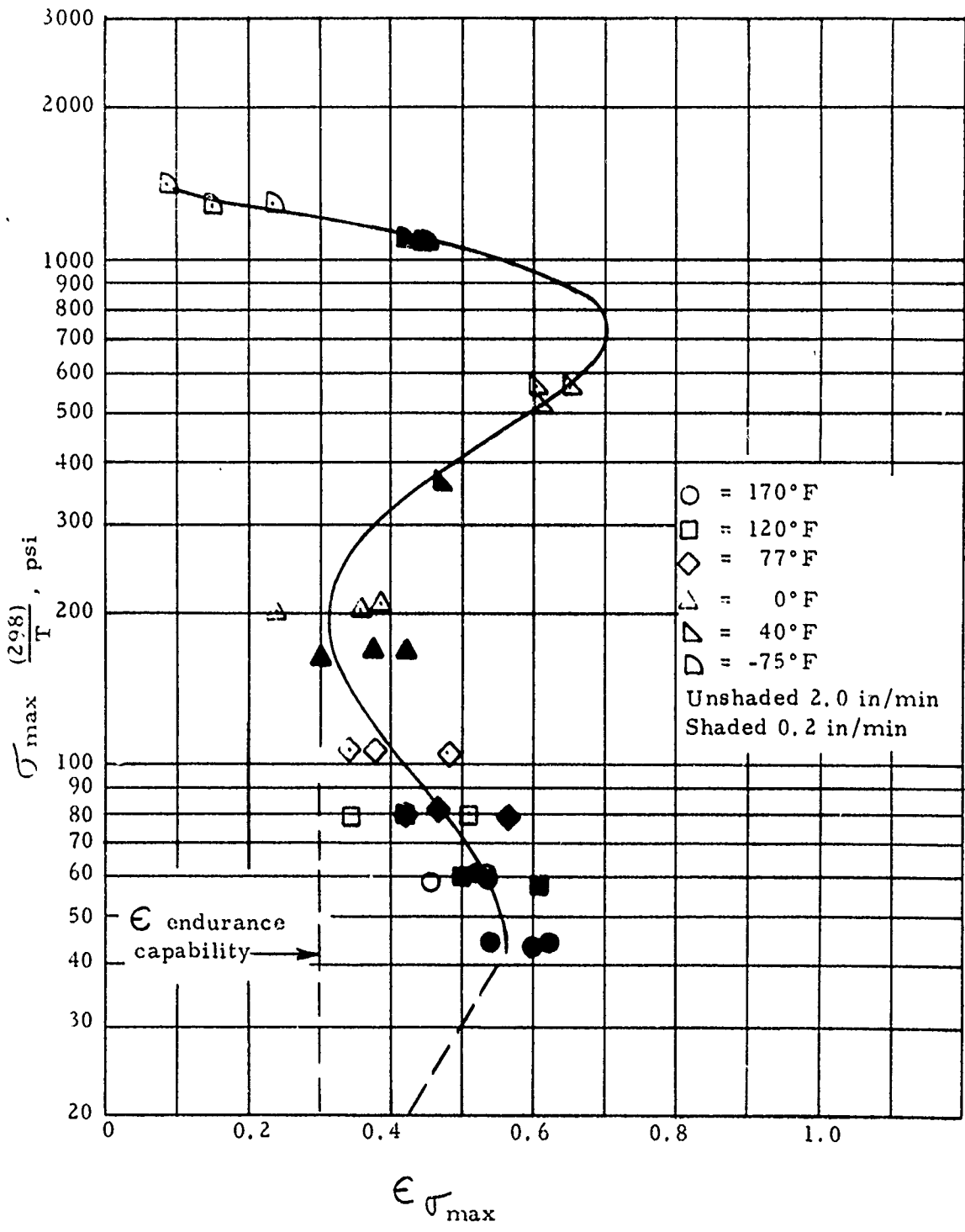


Figure 10 . Failure Boundary for UM #1 Propellant (Mix L158-54)

designated L-158-15, was selected and obtained along with an ice cream carton of propellant for use in determining properties of that mix.

It was mentioned earlier that the effect of aeroheat on the bond line stresses and strains was one of strain relief. This is illustrated on Figure 11 where the radial stresses and strains are plotted in the same manner as the hoop stresses and strains were on Figure 9. In this instance, only the data from the HSM and "Case 11" missions are plotted since they represent a nominal range of interest. As shown, these curves do not collapse into a single curve due principally to the vast difference in bond line temperature experience between missions. The strains approach zero as the mission progresses and can reflect off the boundary (that is the strain is going positive) if the heating is sufficiently rapid. This is also shown on Figure 5. Noting the expanded scales as compared to Figure 9, it can be seen that a very large degradation must occur in propellant capabilities to induce a bond line failure.

The effect of an "aero cool" mission was also investigated. It was assumed that the motor at ambient temperature had been suddenly exposed to Mach = 0.8 flight at an altitude of 35,000 feet (a much more severe cooling than actually possible). The results of this analysis showed a peak hoop stress at the inner bore of -10.0 psi (concentration factor included) and a normal stress at the bond line of -1.0 psi. From this, it can be concluded that this "aero cool" mission produces minimal mechanical loading; consequently, the effect of this type of mission would be essentially confined within the area attributed to temperature cycling effects.

It appears that two possible modes of failure can be attributed to aeroheat -- (1) overstress of the inner bore with probable corresponding degradation of propellant stress capability and (2) degradation of propellant and/or liner properties and ultimate failure by separation or unbond at the bond line because of the effects of temperature cycling. The ranking of the severity of the six missions is obvious from the results presented above. The DMP-2 is, of course, the least severe from a mechanical loading standpoint; although, the temperature level at the bond line does increase quite rapidly near the end of the mission. The DMP-3 and DMP-5 appear comparable in severity level being slightly less severe than the HSM in both mechanical loading and temperature levels. As expected, the SLRI and SFPI are the most severe. In comparing these mechanical loading levels with the propellant capability as shown on Figure 9, it may be safe to say that the degree of severity on the DMP-2, DMP-3 and DMP-5 seem so low that failure induced by any of these may require an excessive number of cycles.

#### Aeroheat Schedule Selection

The results of the severity study have produced more than a ranking of various missions with respect to severity of aeroheat induced stresses. These results have also shown the dependency of the stresses on the rate of change of motor temperature and such propellant properties as relaxation modulus. Of course, none of these effects could have been evaluated without

Thiokol

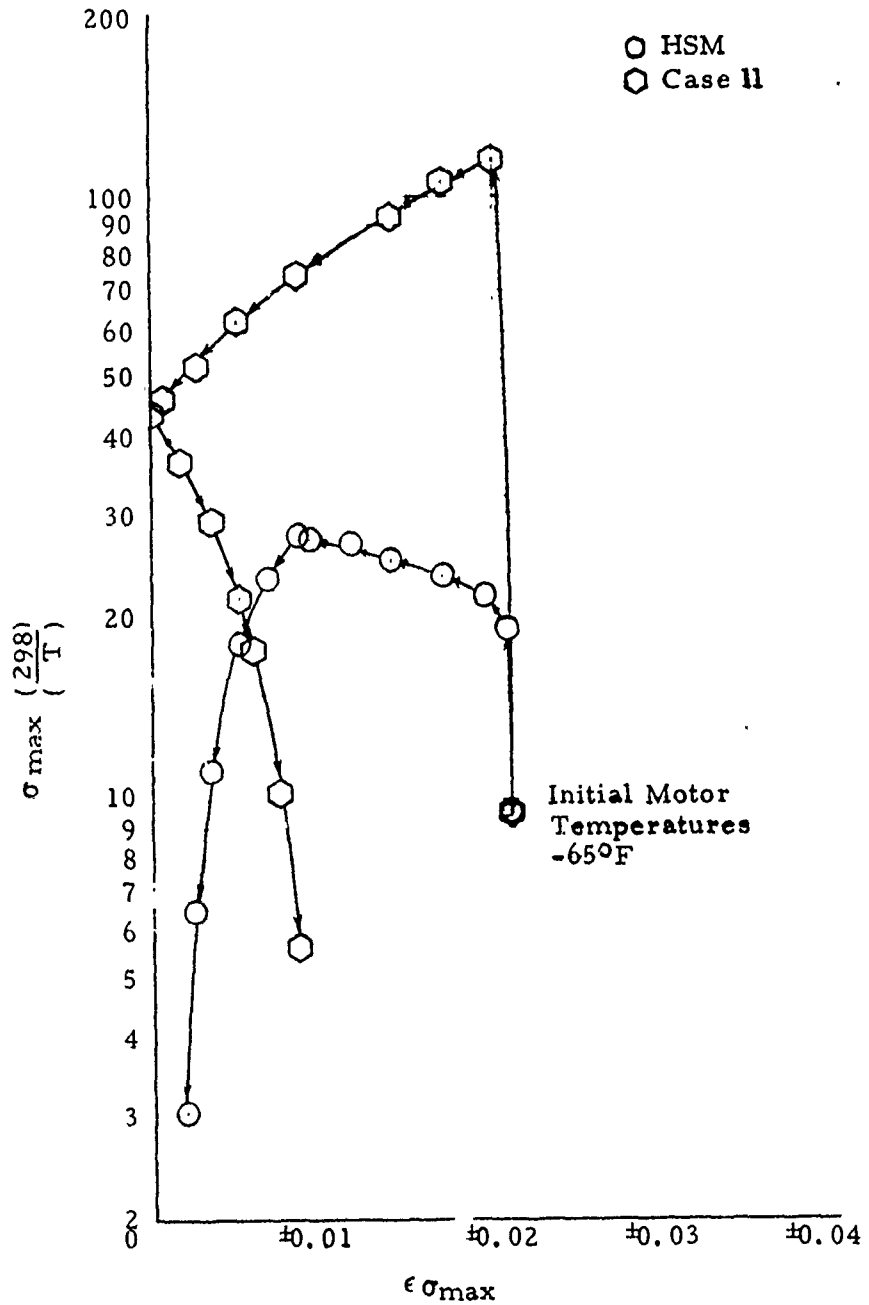


Figure 11. Typical Radial Stress and Strain Relationships at Propellant Bond Line

such computer codes as THVINC. Although, the calculations were quite simplified (i. e. , plain strain) and some question exists as to how accurate the values used for relaxation modulus were; the fact remains that one now has an understanding of what occurs in a motor undergoing aeroheat. However, how such damage may accumulate as the motor is repeatedly cycled through the aeroheat mission is unknown. This is, of course, the purpose here - to determine the failure characteristics under such loading conditions. A determination of failure characteristics infers that failure must occur and be directly attributable to the aeroheat cycling. Therefore, the selection of the aeroheat test schedules should be made based on one schedule being of sufficient severity to induce failure within that schedule of ten cycles.

To assure failure, the failure schedule should transgress beyond the failure boundary curve such as "Case 11" as shown on Figure 10. Based on the results shown on Figure 9, it would appear that either the DMP-2, DMP-3, or both missions could be selected as a schedule comparable to the DAME environment. The HSM mission could be used as the second schedule, the SLRI as the third, the SFPI as the fourth, and the "Case 11" or equivalent as the fifth schedule. This selection assumes that little damage is accumulated through each of the schedules and that the fifth schedule must be capable of causing immediate failure, even if tested as the initial schedule.

Fortunately, aeroheat testing of an uninstrumented motor (UM) was included in scope of this study to allow the selection of schedules to be fully checked out without worry of premature failure of an expensive instrumented motor (IM). To preclude premature failure in the IM's, it is imperative that the UM be failed. After reviewing these results, various approaches were considered for establishing the aeroheat test schedule for the UM #1 tests. Because of the relatively low level of stress and strains exhibited for the DMP missions when compared to the overall propellant capability, there was considerable uncertainty as to whether the motor could be failed in a reasonable number of cycles if these profiles were used. To be fully confident that both a failure can be achieved and premature failure can be avoided, it is desirable to attempt to achieve an early failure. Therefore, it is logical to subject the motor to the most severe mission or schedule which is, of course, the SFPI mission.

Initiating UM #1 testing with the most severe cycle does provide the danger of failure occurring within the first several cycles. If this happens only a limited amount of information is gained. To guard against this occurring, the idea of a second UM was conceived. By using a two motor test program, one of the motors can be subjected to the most severe cycles first in an attempt to force an early failure. The second motor provides a contingency for backing off to a less severe schedule if failure is achieved on the SFPI schedule or to continue a series if the failure is achieved on the second or third schedule. The test sequence using the two test motor concept is shown on Figure 12.

Thickol

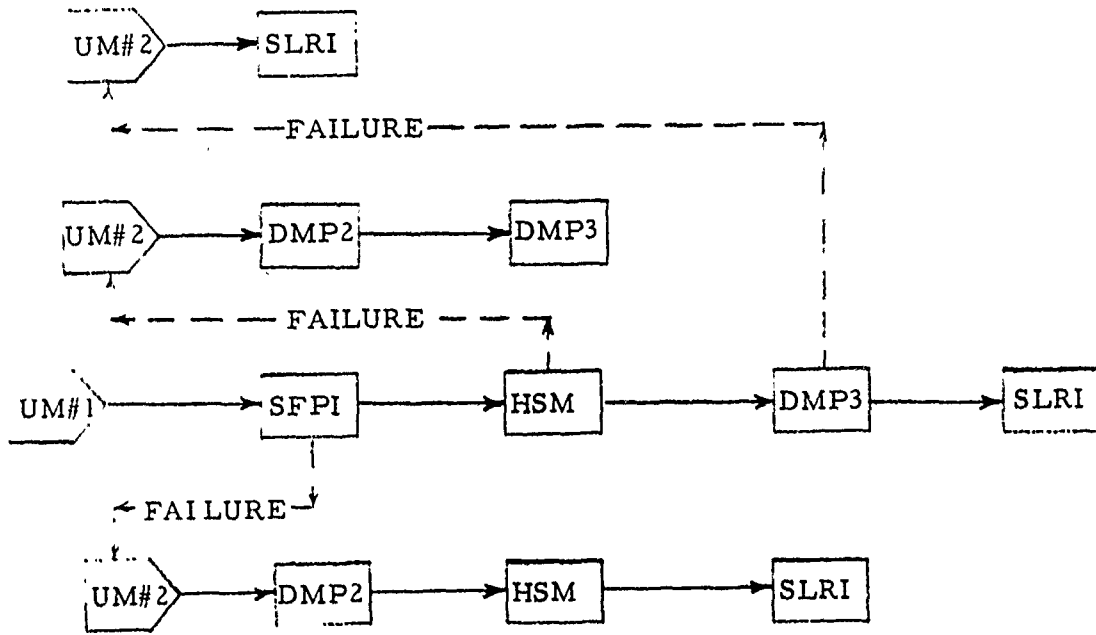


Figure 12. Aeroheat Time-Temperature Schedule Sequence for a Two-Motor Program

## INSTRUMENTED MOTOR DESIGN AND MANUFACTURE

### Instrumented Motor Design Rationale

Design of the instrumented motors were based on several considerations. The scope of the program included three motors, one of which was to be a CP analogue of the Maverick grain. The purpose of including this CP analogue was basically to have a grain configuration that could be more readily analyzed, particularly under aeroheat conditions than the Maverick configuration. Early in the program, it was decided to change the original scope and manufacture two CP motors and one Maverick as opposed to one CP and two Maverick configurations. The reason for this change was to provide a greater degree of continuity in the test program leading to the development of the failure schedule. The original plan was to use a CP motor for aeroheat testing. Since this motor was to have failed as a result of the test series, the motor would no longer be available for use in the simulation testing. The purpose of the simulation tests was to reproduce the same stress and strain levels as induced by aeroheat but using an equilibrium temperature cycle. Since a true analogue in which all stress and strain levels are duplicated cannot be made, it was felt that a second CP tested in conjunction with the Maverick configuration in simulation tests would be the only way to assure that these tests were true simulation of the aeroheat tests.

### Instrumented Motor Design

The philosophy for selecting the cylindrical grain design is to duplicate as near as practical, the maximum strain in the fillets of the Maverick configuration and at the aft grain termination. In selecting the bore diameter, several axisymmetric sections were analyzed with a finite element computer program. Several different web fractions were analyzed to select the bore diameter, the head-end configuration and the aft configuration. A stress relief fillet was employed in the head-end to avoid failure in this area. In the aft end, a transition was made to a lower web fraction configuration to simulate the bond stresses and strains in the aft end of the Maverick motor. A sketch of the configuration selected is shown in Figure 13 as well as an axisymmetric section of the Maverick web configuration.

The grid used for analyzing the selected configuration is shown on Figure 14. This grid was used for calculating the thermal stresses and strains at a storage temperature of  $-75^{\circ}\text{F}$ . The properties used in this analysis are shown in Table 2. The calculated hoop strain contours are shown on Figure 15. The maximum calculated hoop strain is 9.3% compared to a maximum strain of 9.8% in the Maverick motor. Contours of the maximum strain in the R-Z plane are shown on Figure 16. It can be seen that the areas of maximum strain in this plane occur in the head-end and aft end at the grain termination points. The web fraction near the aft end was adjusted to approximate the bond stresses and strains in the Maverick motor. Contours of the maximum stress in the R - Z plane are shown on Figure 17.

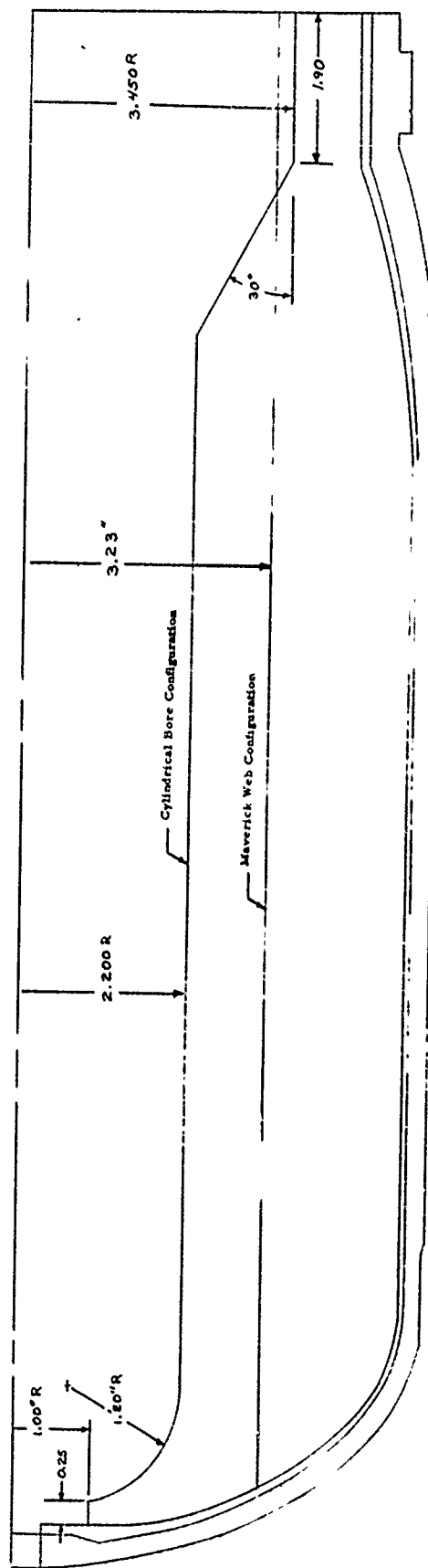


Figure 13. Sketch of Selected Cylindrical Bore Configuration and Maverick Web Configuration

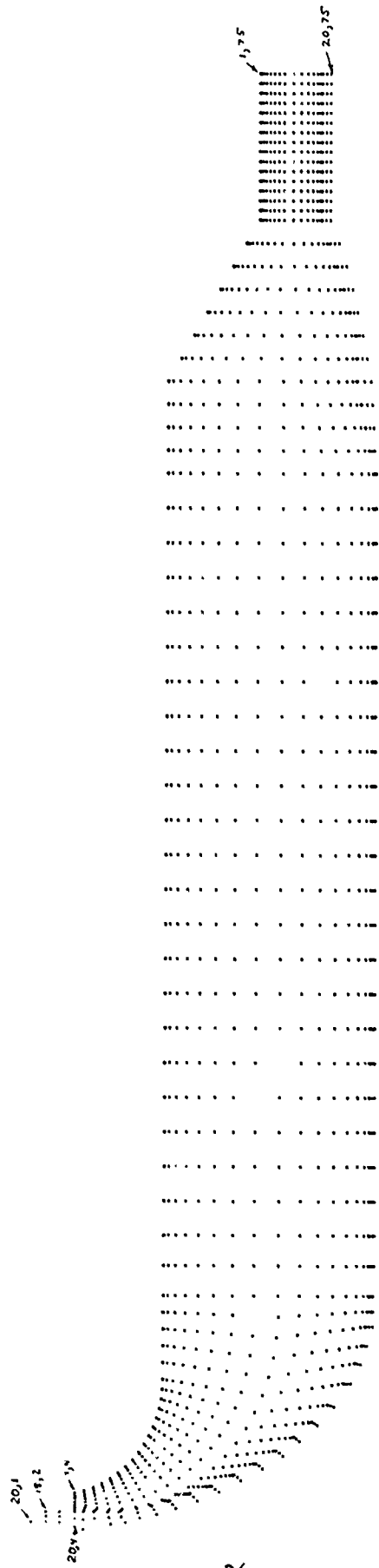


Figure 14. Finite Element Grid for Cylindrical Core Configuration

TABLE 2  
MATERIAL PROPERTIES  
USED IN THE ANALYSES

PROPELLANT

Modulus	= 300 psi
Poisson's Ratio	= 0.499
Coefficient of Expansion	= $5.0 (10)^{-5}$ in/in/°F
Cure Shrinkage	= $0.006 \text{ in}^3/\text{in}^3$
Cure Temperature	= 170°F
Specific Heat	= 0.2643 BTU/lb-°F
Density	= 0.0628 lbs/in <sup>3</sup>
Thermal Conductivity	= $7.04 (10)^{-6}$ BTU/sec-in <sup>2</sup> -°F/in

CASE

Modulus	= $10.5 (10)^6$ psi
Poisson's Ratio	= 0.3
Density	= 0.100 lbs/in <sup>3</sup>
Specific Heat	= 0.214 BTU/lb °F
Thermal Conductivity	= $1.68 (10)^{-3}$ BTU/sec-in <sup>2</sup> -°F/in

LINER

Modulus	= 300 psi
Poisson's Ratio	= 0.499
Density	= 0.0469 lbs/in <sup>3</sup>
Specific Heat	= 0.30 BTU/lb-°F
Thermal Conductivity	= 2.80 BTU/sec-in <sup>2</sup> -°F/in

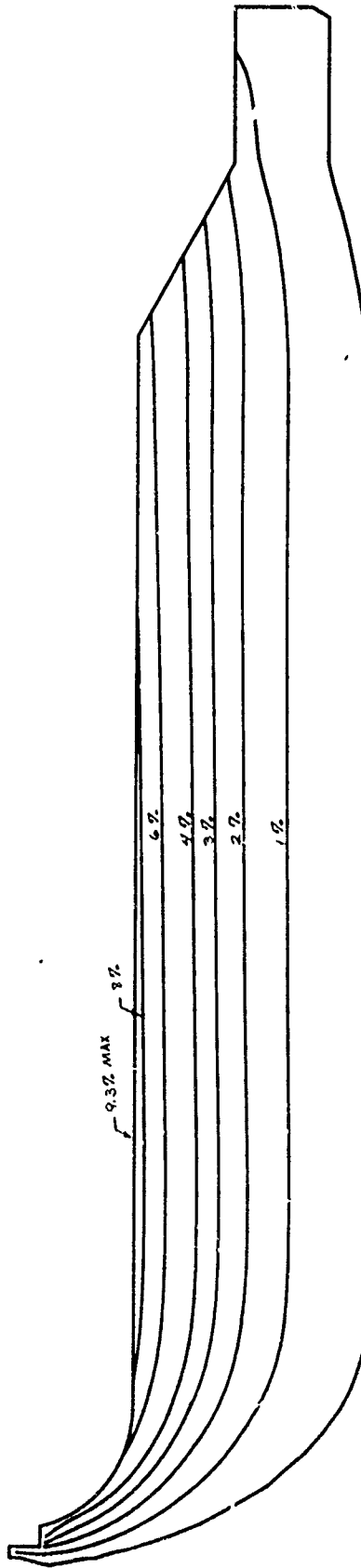


Figure 15. Hoop Strain Contours in Cylindrical Bore Configuration at  $-75^{\circ}\text{F}$

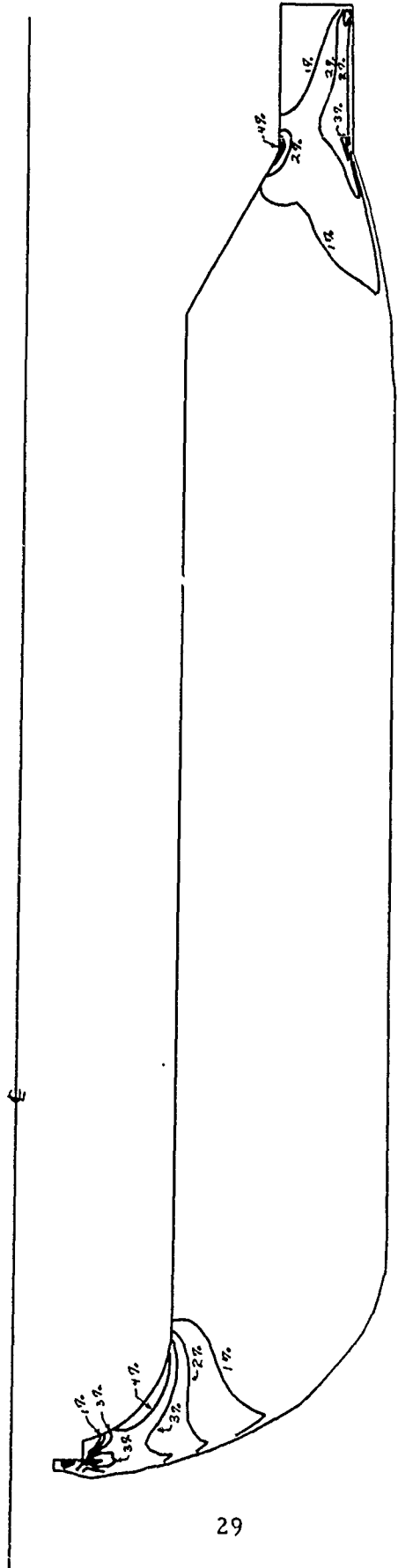


Figure 16. Maximum Strain Contours in R - Z Plane at a Storage Temperature of  $-75^{\circ}\text{F}$

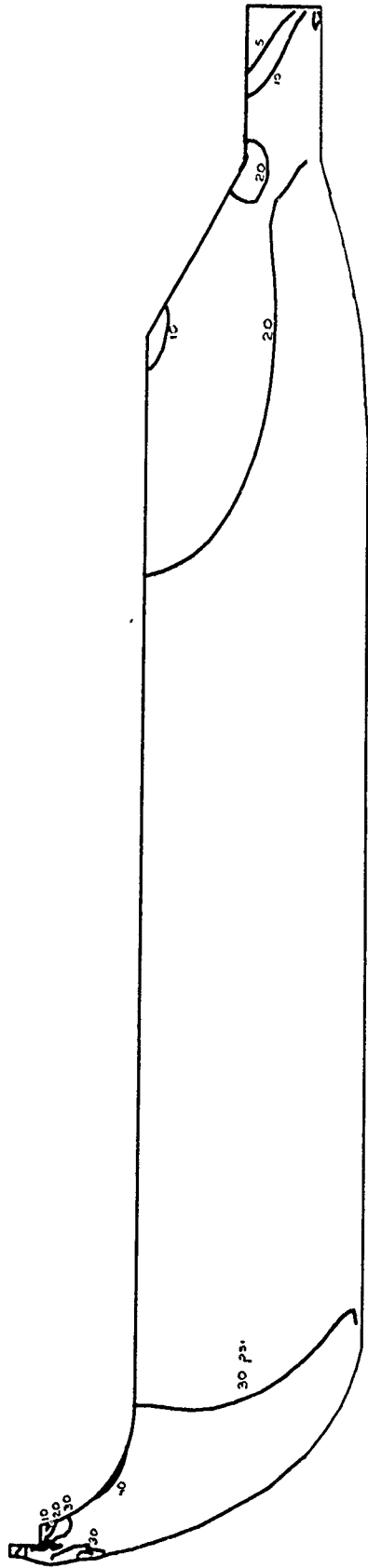


Figure 17. Maximum Stress Contours at  $-75^{\circ}\text{F}$  in Cylindrical Core Configuration

For comparative purposes, an axisymmetric cross-section of the Maverick motor was analyzed. Contours of the maximum strain in the R - Z plane are shown on Figure 18 for a storage temperature of  $-75^{\circ}\text{F}$ . The maximum stress in the R - Z plane for the Maverick web configuration are shown on Figure 19.

Based on this investigation, the selected cylindrical bore configuration should produce strains at the inner bore approximately equal to the strains in the Maverick configuration. Also, the bond stresses and strains near the aft end of the motor should be approximately equal to the bond stresses and strains in the Maverick grain configuration. The bond stresses and strains near the center of the motor will be higher in the cylindrical grain configuration than in the Maverick configuration. However, it was not possible to select a cylindrical grain configuration which would provide stresses and strains similar to those in the Maverick motor for all areas of interest.

#### Instrumentation Selection and Location

The selection of the type and quantity of instrumentation to be used in this program was made by the AFRPL prior to the initiation of the program. The types of instruments selected included clip strain gages for measuring bore strain, embedded normal stress gages, shear stress gages, and thermocouples. All instrumentation except thermocouples were provided GFE by the AFRPL and included:

- 12 P-14EA - 150 psi normal stress gages
- 9 Ruggedized shear gages
- 9 Clip strain gages

The thermocouples selected were copper-constantan type. They were to be used for both monitoring gage temperature and defining the temperature gradient through the web.

The gages selected had been developed under AFRPL sponsorship by Dr. Harold Leeming or Leeming Ph. D. and Associates and Konigsberg Instruments. The gage supplied by the AFRPL to this program were manufactured and calibrated by these two firms. In addition, Dr. Leeming was retained as a Consultant to the program and to install the gages in the motors and do the necessary post installation gage calibrations. A general description of these gages is given in the following section.

A preliminary grain instrumentation layout is shown on Figure 20. This basic instrumentation plan will be used for two cylindrical grain configurations and one Maverick configuration. In locating the grain instrumentation primary consideration was given to the center section and the aft strain termination since these are the areas in which failure is anticipated. Failure is not anticipated in the head-end of the motors but instrumentation has been included in this region to monitor the bond stresses in case failure should occur in this region for some unknown reason.

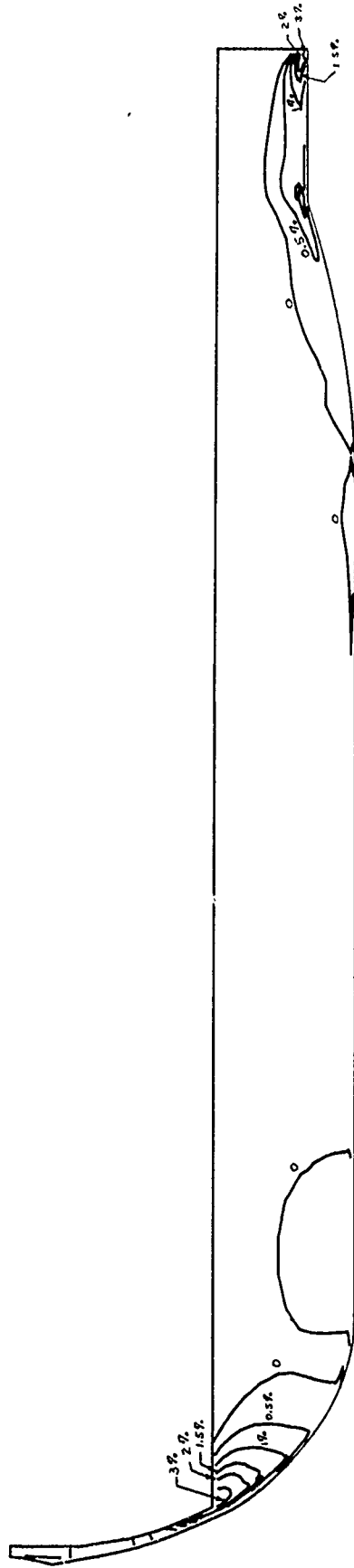


Figure 18. Maximum Strain Contours in Maverick Web Configuration at  $-75^{\circ}\text{F}$

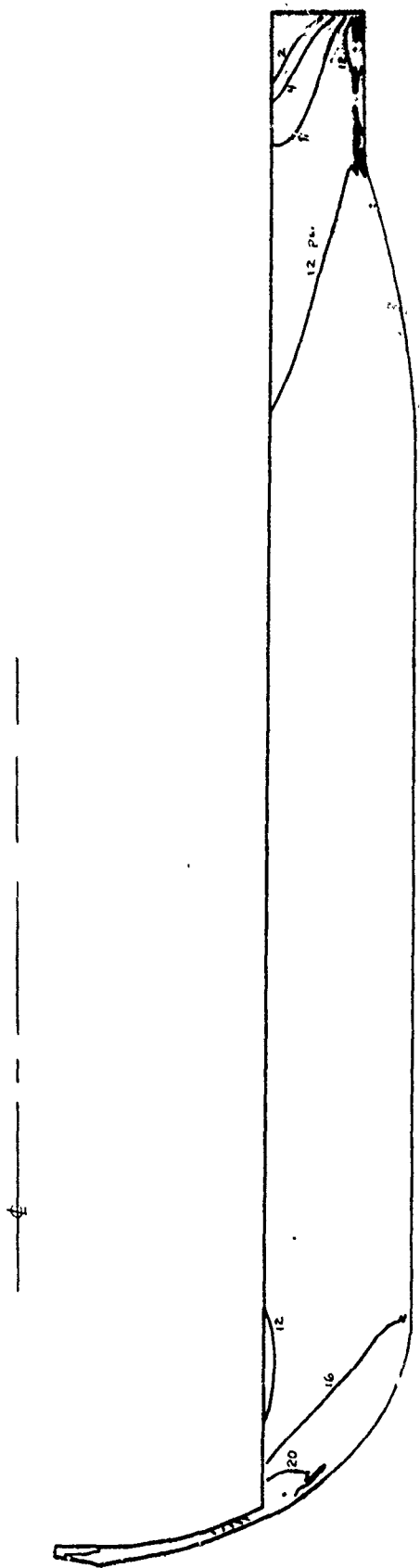


Figure 19. Maximum Stress Contours in Maverick Web Configuration at Storage Temperature of  $-75^{\circ}\text{F}$

Thiokol

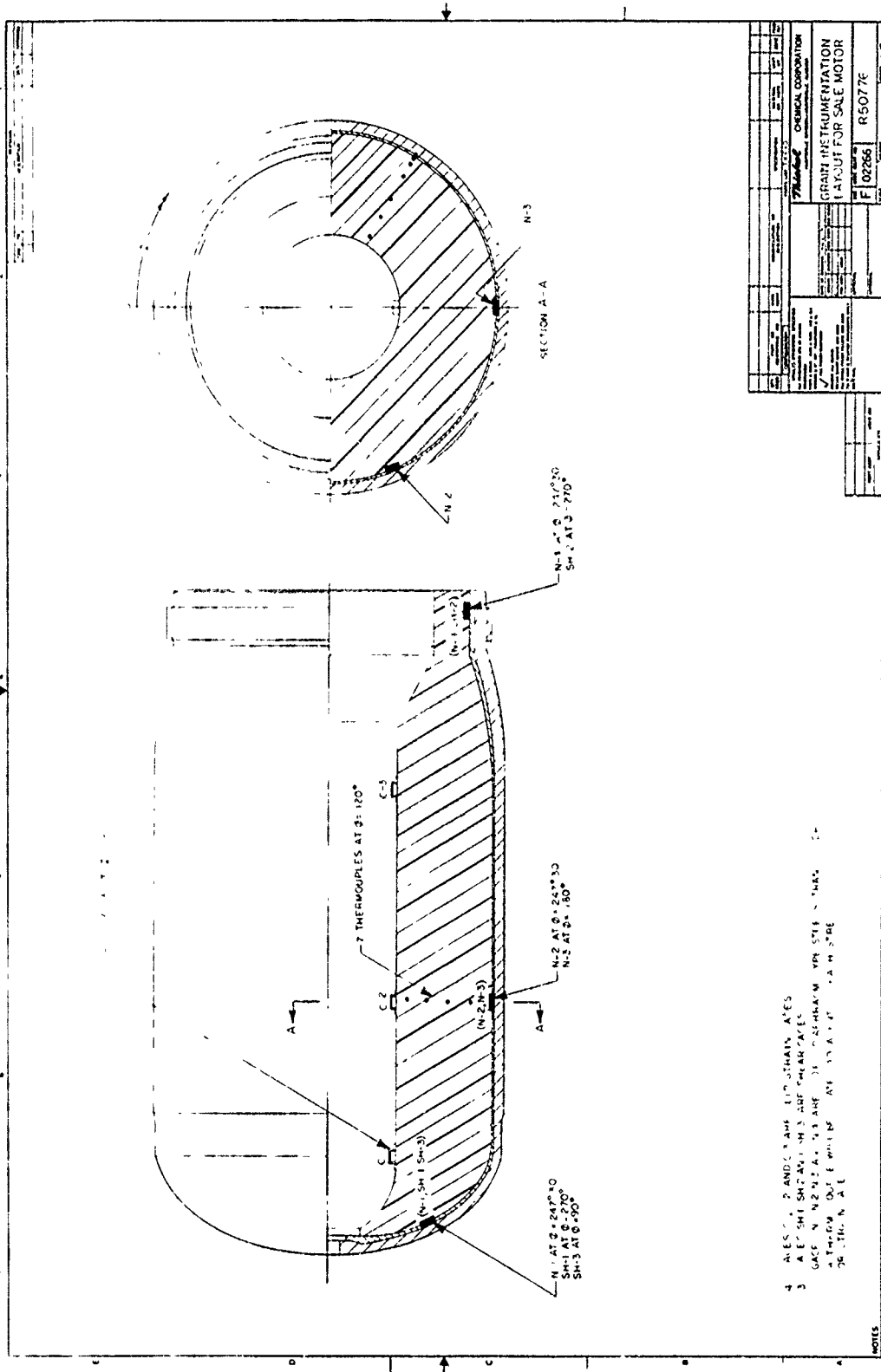


Figure 20. Preliminary Grain Instrumentation Layout for SALE Motor

### Embedded Miniature Diaphragm Normal Stress Transducer

The embedded miniature diaphragm normal stress transducer was developed for fluid or gaseous pressure measurements. The gage consists of a circular metallic diaphragm supported by a rigid metal ring with a metal back sealing the cavity. Semiconductor strain gages are mounted on the diaphragm to measure its deflection under pressure. By making use of both the compressive stresses and the tensile stresses generated during flexing of the diaphragm, a temperature-compensated gage is produced. The diaphragm pressure transducer was developed at LPC. Subsequent analytical work by Professors Pister and Fitzgerald resulted in the Konigsberg 150 psi gage design shown on Figure 21. . This new type of 150-psi diaphragm transducer was evaluated during the STV and Bomb Dummy Unit Programs at LPC. Past experience with these gages suggests that they can measure stresses to within  $\pm 1$  psi, or within  $\pm 2$  percent of the reading under isothermal conditions. The error band increases to about  $\pm 10$  percent of the reading when thermal stresses are considered.

### Embedded Shear Gage

The embedded shear gage shown on Figure 22 was developed at LPC from the shear transducer manufactured by Gulton Industries for the Hercules Powder Company. The transducer is simple, containing a pair of semiconductor strain gages mounted perpendicularly to each other and at a 45-degree angle to the mounting surface of the cube. In operation, the two gages are connected in a Wheatstone bridge circuit, to measure either the shear strain in the shear mode of connection, or the normal strain in the normal mode of connection. When the gages are connected in the shear mode, changes in gage resistance caused by temperature effects are largely self-compensating, providing that the two gage elements are well matched. This type of embedded shear strain measuring device has been used with considerable success in the development of motors such as SRAM and in the flight tests of motors for high acceleration conditions, e.g., Hibex and Sprint.

### Clip-Type Surface Strain Gages

The clip gage illustrated in Figure 23 was developed for the measurement of surface strains at the bore of a propellant grain. The problem with conventional surface strain gages is the fact that they can be used only on a rigid surface, such as a metal motor case, if precise strain values are required. They cannot be used as strain gages in conjunction with soft elastomeric materials such as propellant. The gage consists of a small clip made from thin metallic foil to which are attached two resistance gages, as shown. When the two feet of the clip gage are displaced relative to each other, the central beam of the clip is subjected to bending, which produces a tensile strain in one of the strain gages and a corresponding compressive strain in the other gage. This type of gage has proved extremely accurate in the laboratory for small displacement measurement, and it has also given good

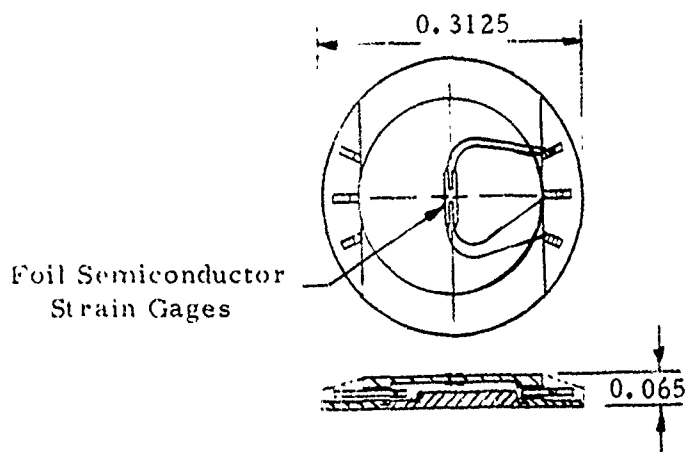


Figure 21. Normal Stress Gage (Königsberg P-14)

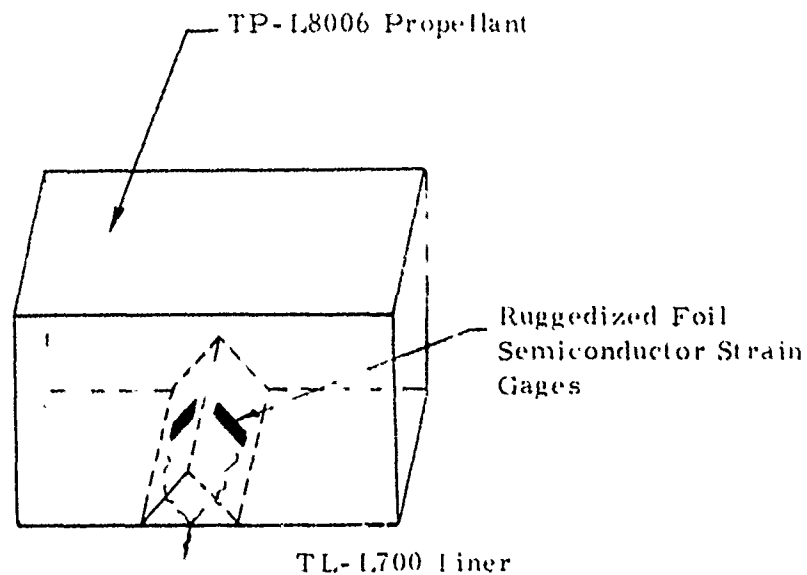


Figure 22. Shear Stress Cube Configuration

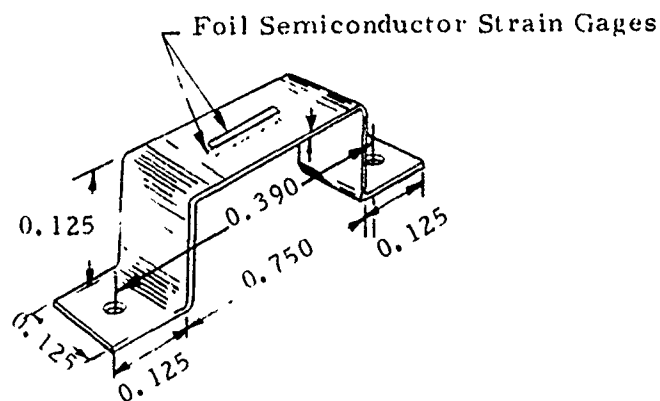


Figure 23. Clip Bore Strain Gage

results in motor tests, such as those of the Structural Test Vehicle program (STV) at Lockheed Propulsion Company (LPC).

The major problem with the clip gage is the method of attaching the gage to the surface of the propellant grain. Apart from the obvious difficulty of being able to reach far enough inside the grain to place the gage in the desired location, it was found that simply bonding the tabs to the grain surface was unreliable. In fact, the gages became unbonded during thermal cycling tests of the STV's. A method devised to solve this problem utilized metal pins pushed into the propellant surface. The clip gage, with holes drilled in the tabs, is then fitted in place onto the pins and small amounts of epoxy adhesive are placed on the top surface of the tabs to prevent the clip gage from falling off. While this is the most positive technique available for attaching the surface clip gages, it cannot be used in a situation of very high strain because of insertion of the pins could cause cracking of the propellant grain. This approach is, therefore, not suitable for the measurement of surface strains up to failure conditions.

#### Gage Manufacture and Calibration

Although the gages used in this program are GFE to the program, consideration of gage-motor interface design, gage calibration, and gage acquisition require direct involvement with the gage manufacturer - Konigsberg Instruments. Early in the program, three decisions were made which established the directions of gage manufacture and calibration. These were:

- (1) The temperature range over which the gages were to be calibrated was from  $-65^{\circ}\text{F}$  to  $300^{\circ}\text{F}$ .
- (2) The normal stress gages would be potted in liner material (TL-L700) which Thiokol will mix and supply to the gage manufacturer.
- (3) Thiokol will manufacture and supply the triangular shaped blocks (wedges) of liner for mounting the shear gages. After the gages are mounted on the wedges, they will be returned to Thiokol mounted on shear frames in which Thiokol will cast propellant. Dr. Leeming will then calibrate the shear gages at Thiokol.

The first decision caused some problems inasmuch as these calibration requirements were over and above the scope of the basic gage supply contract with Konigsberg Instruments. The extra calibration points and gage modification necessary to assure operation at the high temperatures were purchased by this program as separate items of modification for the GFE gages.

Gage calibration refers to the operation of determining the sensitivity and zero load reading of an embedded gage in an environment as close as

possible to that found in the grain. To this end, the miniature normal stress gages are encapsulated in "potting material" (either insulation, liner or propellant) as shown in Figure 24 and pressure calibration tests are performed to determine sensitivity at several temperatures over the range of interest.

During calibration of the normal stress gages at the 300°F point, Konigsberg Instruments noted that the liner material that was potted around the gages became tacky and appeared to degrade. Three of the 12 gages appeared to be quite bad whereas the other nine appeared to be acceptable. Separate laboratory checks at Thiokol were conducted on this liner and showed that prolonged exposure of the liner material at 300°F caused it to revert. Thus, it appeared that this was what occurred on the three gages. Check calibrations of the other nine were made at ambient and good repeatability was found; therefore, these gages were deemed acceptable. The other three gages were repotted and recalibrated with an upper temperature limit of 250°F now imposed. This limit was also imposed upon the shear gage calibration temperature levels. Calibration of the shear gages was scheduled to be accomplished immediately before installation into the motor. No problems were encountered with the clip strain gages.

The potted gages are then bonded in place in the motor and the zero load readings are measured at the various temperatures of interest. Thus, the 150 psi normal stress gage embedded within its hemisphere of potting is treated as an elastic system. Linear gage output versus pressure records are obtained; any viscoelastic effects due to the propellant are small enough to be ignored. Typical calibration data are shown in Figure 25. In general the gage sensitivity changes vary slightly with temperature (and this change is usually ignored in data analysis). Changes in gage output due to thermal stresses are measured from the corresponding zero load gage reading with the gage bonded in place in the motor. It should be noted that once the grain is cast there is then no means of checking the zero stress gage readings although the gage sensitivity value may be verified approximately by pressure testing the grain. The data for both the factory calibrations (potted in liner) and the effect of thermal stresses from bonding in the motor on the zero load output of the gages are shown on Table 3. It is interesting to note the magnitude and the wide disparity in magnitude from gage to gage of the thermal stresses at the low temperatures. These post installation gage readings are assumed as the zero gage reading in the motor and are used accordingly in reducing the data.

Because of the very strong interaction between the shear gage and the propellant, calibration of these devices is performed in a shear fixture (Figure 26) and a viscoelastic type calibration has to be employed. In this program the shear stress gages were manufactured by Konigsberg Instruments Inc. from small wedges of cured liner material provided by Thiokol. This manufacturing process consisted of bonding ruggedized semi-conducted strain gages to a wedge of liner. (See Figure 22). The shear stress gages were mounted in the shear frame by Dr. Leeming and shipped to Thiokol. TP-L8006

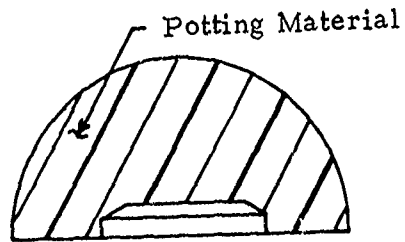


Figure 24 - Potted Normal Stress Gage

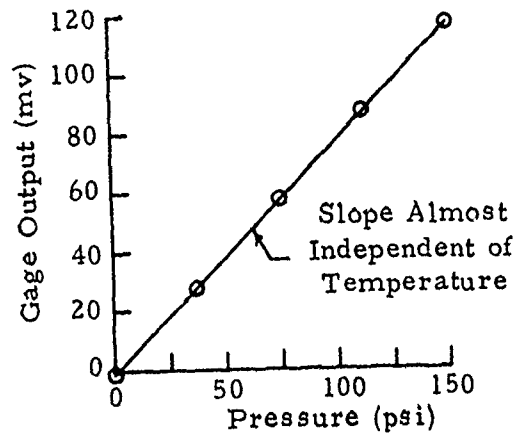


Figure 25 - Normal Stress Gage Calibration Data

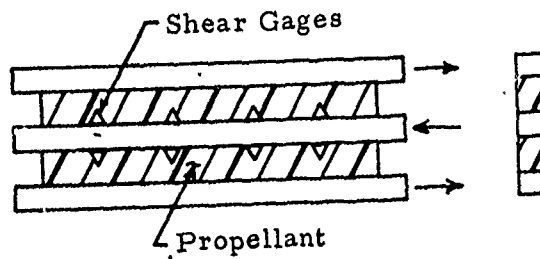


Figure 26 - Shear Gage Calibration Fixture

Figure 27 - shown on page 40

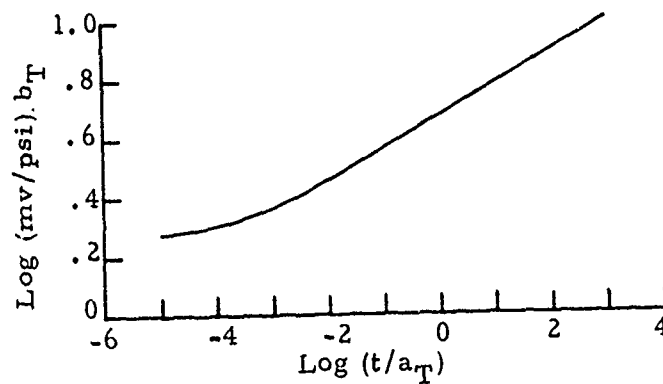


Figure 28 - Shear Gage Master Sensitivity Plot

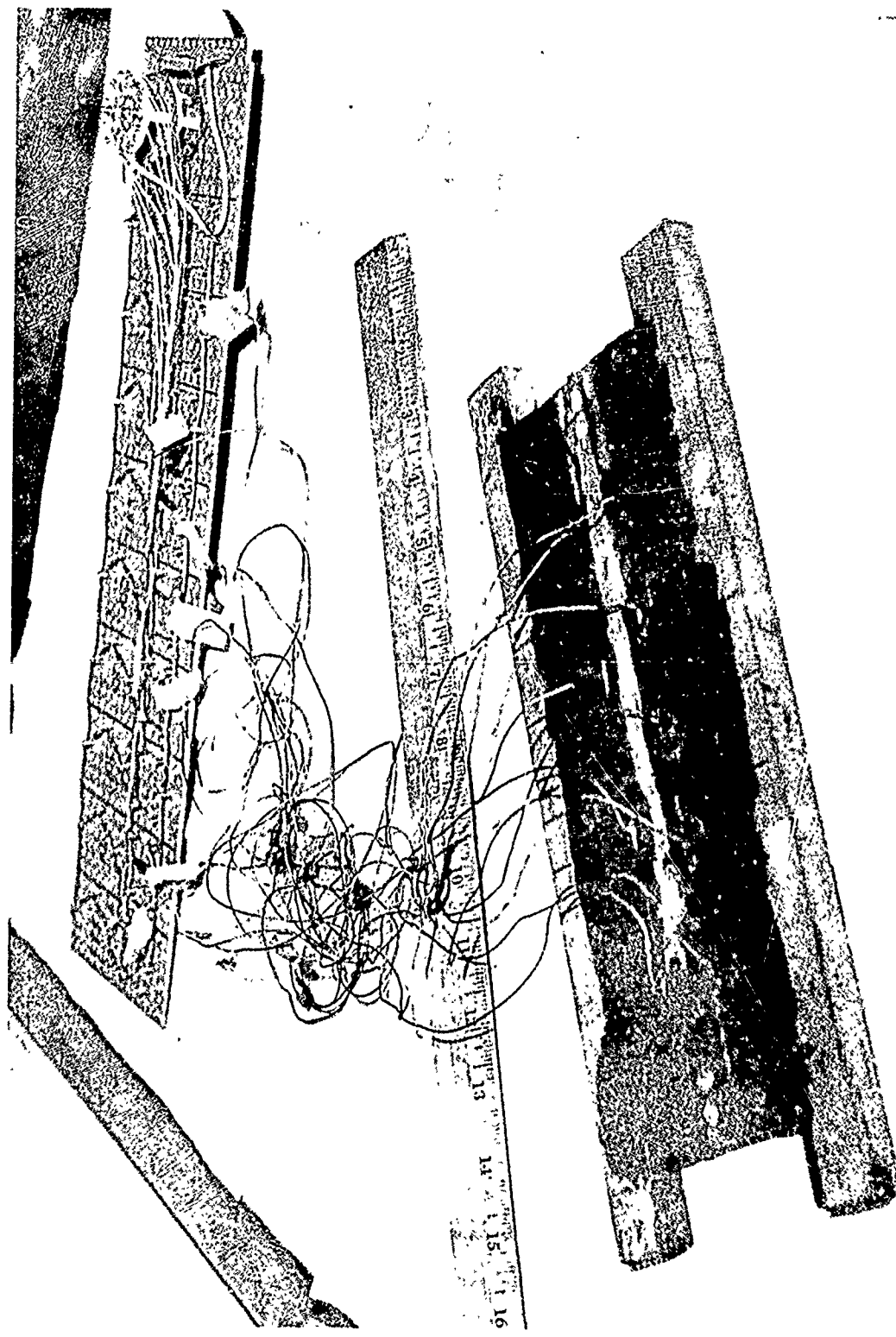


Figure 27. Shear Stress Gages Mounted in Shear Frame

Table 3

## P-14EA 150 Normal Gage Pre- and Post Installation Calibration Data

Gage S/N	Code	Gage Zero Load Output/Sensitivity (mv)/(mv/psi)						
		Temperature, °F						
		-65	0	80	150	170	250	300
40	1	5.65	0.47	0.12	0.60	---	---	-3.02
	2	-9.66	-4.16	-3.1	---	1.8	---	----
	3	---	0.781	0.771	0.768	---	---	0.756
41	1	4.77	1.49	1.81	2.74	---	---	0.86
	2	-25.14	-4.94	-5.1	---	-4.2	---	----
	3	---	0.825	0.827	0.827	---	---	0.819
42	1	1.67	0.78	1.48	2.24	---	---	2.69
	2	-12.45	-4.42	-5.0	---	-2.1	---	---
	3	---	0.717	0.723	0.725	---	---	0.727
43	1	2.36	0.97	1.09	1.86	---	---	1.70
	2	-4.01	-2.38	-2.1	---	0.2	---	----
	3	---	0.757	0.764	0.765	---	---	0.761
44	1	1.94	-0.48	-0.24	0.22	---	---	0.06
	2	-3.69	-2.62	-2.6	---	-2.9	---	---
	3	---	0.800	0.301	0.800	---	---	0.797
45	1	5.65	-1.25	-0.68	1.61	---	---	5.44
	2	-9.50	-2.02	-1.7	---	-52	---	---
	3	---	0.715	0.730	0.738	---	---	0.734
46	1	1.60	-0.90	-1.46	0.16	---	----	2.80
	2	-1.94	2.22	2.3	---	5.3	---	---
	3	---	0.725	0.731	0.727	---	---	0.735
47	1	8.60	-0.31	-1.48	3.02	---	---	7.80
	2	-15.77	-3.83	-3.0	---	-1.6	---	----
	3	---	0.713	0.711	0.707	---	---	0.705
48	1	-1.10	0.35	-0.19	0.58	---	---	-1.55
	2	3.30	0.5	-0.4	---	4.6	---	----
	3	---	0.708	0.718	0.718	---	---	0.722
49	1	-1.60	-1.05	0.21	---	3.33	1.27	---
	2	-38.36	-2.96	-4.1	---	-3.4	---	---
	3	---	0.731	0.731	---	0.734	0.733	---
50	1	-1.00	-0.14	-0.15	---	0.49	-0.73	----
	2	18.25	-2.04	-1.7	---	4.8	---	----
	3	---	0.763	0.768	---	0.778	0.777	----
51	1	-1.97	-2.61	-1.34	---	0.44	0.77	----
	2	-8.09	-5.84	-6.6	---	-0.8	---	----
	3	---	0.793	0.787	---	0.793	0.785	----

## Code

- 1 Zero load gage output, factory calibration, mv
- 2 Zero load gage outputs, installed in motor, mv
- 3 Gage sensitivity, factory calibration, mv/psi

propellant from a 5 gallon characterization mix was then cast in the shear frame. After normal cure, the shear frame was returned to a 170°F oven for thermal conditioning for 3 days. It was decided to only condition for about one half the normal seven day period since the propellant would undergo additional temperature conditioning during motor cure. The frame was then stored at ambient until Dr. Leeming was available to calibrate the gages. The frame is shown on Figure 27.

Calibration of the shear gages was done by Dr. Leeming at Thiokol during the period of 12 - 14 March 1973. Nine shear gages were mounted in the frame and calibrated; however, upon removal of the gages from the frame, two were irreparably damaged. Seven shear gages were then available to be installed in the motor. The calibration involved placing the shear frame in a tensile testing machine and applying either a constant load (creep) calibration or a constant strain (relaxation) calibration test is used, simultaneous values of gage output and specimen load at discrete time points being noted over a 10-minute period. From these data gage sensitivity, i. e. gage output/applied stress, is plotted against log time and these data are translated along the log time axis by the propellant log  $a_T$  shift factors and then vertically to produce a smooth curve by the log  $b_T$  factor [ $\log (mv/psi)$ ] resulting in a viscoelastic gage calibration curve as shown in Figure 28. Note that this single curve combines the effects of viscoelasticity (due to the embedding propellant) and temperature changes (due to gage imperfections and propellant changes). The corresponding log  $a_T$  versus temperature and log  $b_T$  versus temperature plots are, however, required to interpret the gage output data.

Once the shear gages have been calibrated for sensitivity in the shear fixtures they are removed from the fixture together with some of the propellant surrounding the gage. The calibrated shear gage is then bonded in place in the motor and its new zero load reading as a function of temperature must be determined (as with the normal stress gage).

When a shear gage is to be employed for measuring large shear stresses up to failure, it is useful to ensure that the response curve is reasonably linear to some high stress level. Although most of the calibration tests may be performed at low shear stress levels (1 to 5 psi) a linearity check up to 25 or even 50 psi may be considered if it is felt necessary. The absolute stress levels are greatly dependent upon the gage material and the shear fixture material.

Another calibration test which should be performed on the shear gages while still mounted in the shear fixture is a normal stress test. The shear specimen is gripped along the wooden sides and is pulled in tension normal to the shear direction. The purpose of this test is to ascertain the response of the shear gages to normal stress. A good gage properly installed will exhibit virtually zero response to normal stress but a poor gage, in which the two sensing elements are not well matched will exhibit a fair response to normal stress.

The normal stress response of the shear gage may be used in the analysis of shear gage data from complex stress fields where the normal stress is known. In some cases, the effects of the normal stress component can be comparable to the shear stress effects and considerable care must be employed in analysis of the data.

Strain measuring clip gages used to determine bore strains are calibrated by determining the output of the bridge circuit for different displacements of the clip arms. Again, these measurements are made at several temperatures over the range of interest. Calibration of these devices is comparatively straightforward because there is essentially no interaction effects to worry about. A summary of the clip gage calibrations are presented in Table 4.

### Gage Installation

Gage installation was accomplished on 15 - 16 March 1973. The case had been fully lined prior to this time. The liner system used in these motors is a fully cured system, thus fresh liner can be placed on old liner and re-cured to obtain a new fully cured system. Thermocouples (Cu-Const) were installed at each gage location.

A thermocouple slab was fabricated and installed in the center of the motor (at the same longitudinal location as the normal gages) to provide a measure of temperature gradient through the web. These slabs were made by sandwiching thermocouples between two slabs of propellant each one-half inch thick as shown on Figure 29. These slabs were then bonded into the motor. The leads from the gages and the thermocouple wire were routed back and out through the aft end of the case. These leads were bonded to the liner by fresh liner material in the same manner as the gages. The cases then were placed into ovens and the fresh liner cured at 170°F. Following this, additional liner was painted over the lead wires until they were completely embedded. After another cure cycle, the cases were ready for loading.

Gage outputs were recorded for each gage for four temperature levels, 170, 70, 0 and -65°F. The normal stress gages seemed to react constantly with the output decreasing with decreasing temperature (See Table 3). Three shear gages seemed to exhibit extreme sensitivity to temperature and one (S/N 108) was finally removed from the motor as being bad. These data are presented on Table 5.

### Motor Manufacture

The three instrumented motors were cast with TP-L8006 propellant on 22 March 1973 from Mix L-198. The motors were vacuum cast and vibrated during casting. Two of the three motors were made with the CP geometry while the third was the Maverick configuration (TX-481) with a simple star point removed in order to provide a suitable surface to install the bore strain clip gages. These motors are designated as follows:

Table 4.

JIB-1 CLIP GAGE CALIBRATION DATA

FACTORY CALIBRATION

Gage S/N	Zero Load Output, mv Temperature			Sensitivity mv/% $\epsilon$ Temperature		
	-65	80	300	-65	80	300
12	0.30	0.06	0.38	---	14.62	---
13	0.52	0.35	0.26	---	15.21	---
14	0.43	0.42	0.56	---	14.40	---
15	0.39	0.15	0.16	---	16.04	---
16	0.80	0.76	0.71	---	14.59	---
17	0.30	0.59	0.34	---	15.80	---
18	0.39	0.49	0.70	---	16.12	---
19	0.59	0.60	0.79	---	14.92	---
20	0.40	0.37	0.45	---	15.99	---

Table 5.  
Shear Gage Post Installation Zero Load Data

Gage S/N	Gage Zero Load Output, mv			
	Temperature, °F			
	-65	0	80	170
104	-26.7	-46.5	-24.9	0
105	-50.3	-27.0	-13.2	2.7
107	-135.4	-93.4	-71.5	-5.9
108	-272.4	-141.2	-115.8	-9.6
109	6.09	1.76	-0.8	-0.2
110	2.4	1.2	-0.2	-0.6
111	-47.4	-35.8	-27.4	3.5

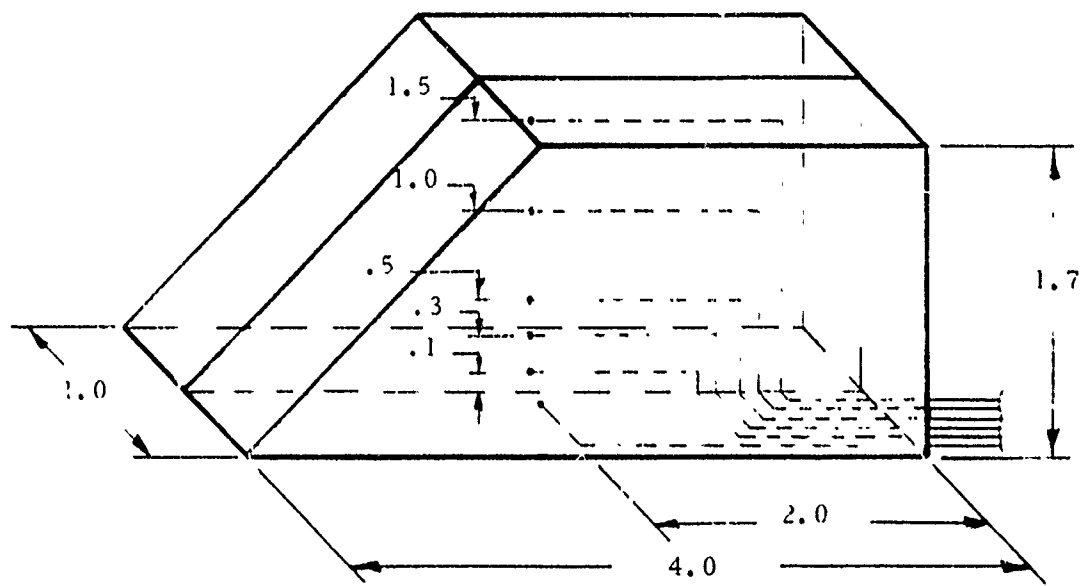


Figure 29. Thermocouple Slab Design

IM #1 - TX-481 with a single star point removed  
IM #2 - cylindrical bore  
IM #3 - cylindrical bore (same as IM #2)

Each of the motors were subjected to standard quality control inspection requirements during manufacture and after core removal. X-ray inspections indicated a few small voids near the aft end of IM #1 and IM #2. These voids were within the specification limits of the TX-481 motors. The X-rays were also used to define gage locations within the motor. Neither the 0.005-inch-diameter thermocouple wire nor the shear gages were visible on the X-rays. The normal gages and the location of the propellant slab was visible, however, and did provide the needed location data. Gage and thermocouple locations as determined for each motor are presented on Figures 30, 31, and 32 for Motors IM #1, IM #2, and IM #3, respectively.

During the same casting operation, forty-five strain evaluation cylinders (SEC) consisting of three sets of fifteen each were manufactured. Each set consists of three each of five core sizes for later testings. Also, twenty ice cream cartons and twenty slabs of propellant were cast for use in subsequent propellant characterization studies. Unfortunately, both the SEC's and biaxial slabs were found to contain excessive voids sufficient to render them useless to the program.

Following case removal and X-ray inspection, three bore clip gages were placed in each motor by Dr. Leeming as part of his consultation agreement with Thiokol on this program. Locations of the clip gages in the two CP motors were changed somewhat from those originally planned. Instead of placing all three clip gages in the small bore of the CP motors, two were placed there and one placed on the aft CP segment. Theoretically, this aft location should show very little strain; however, end effects from nonuniform aeroheating could possibly induce strain levels grossly different than anticipated so it was determined that this aspect should be checked by installing a gage at this location.

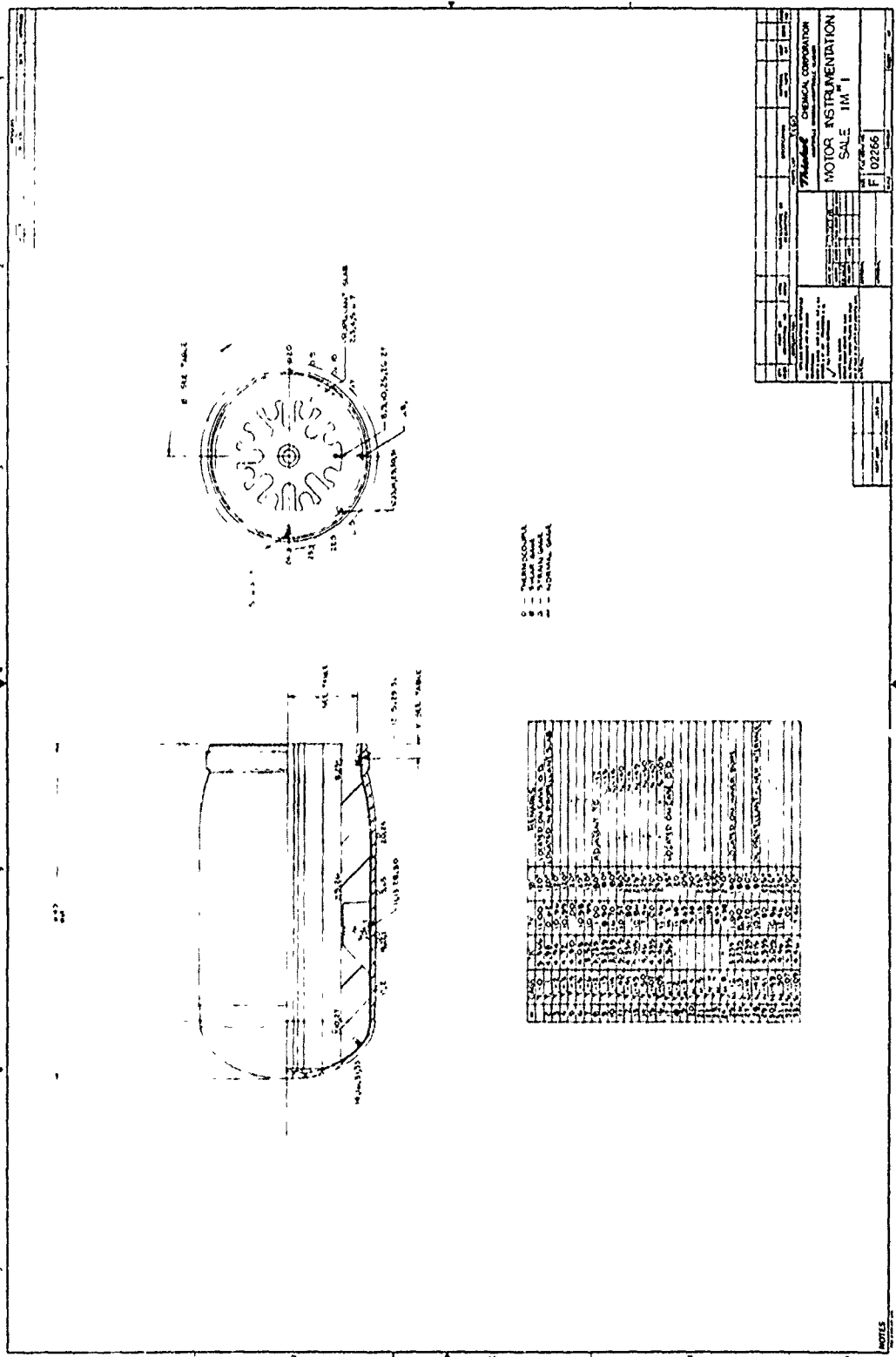


Figure 30. IM #1 Gage Locations

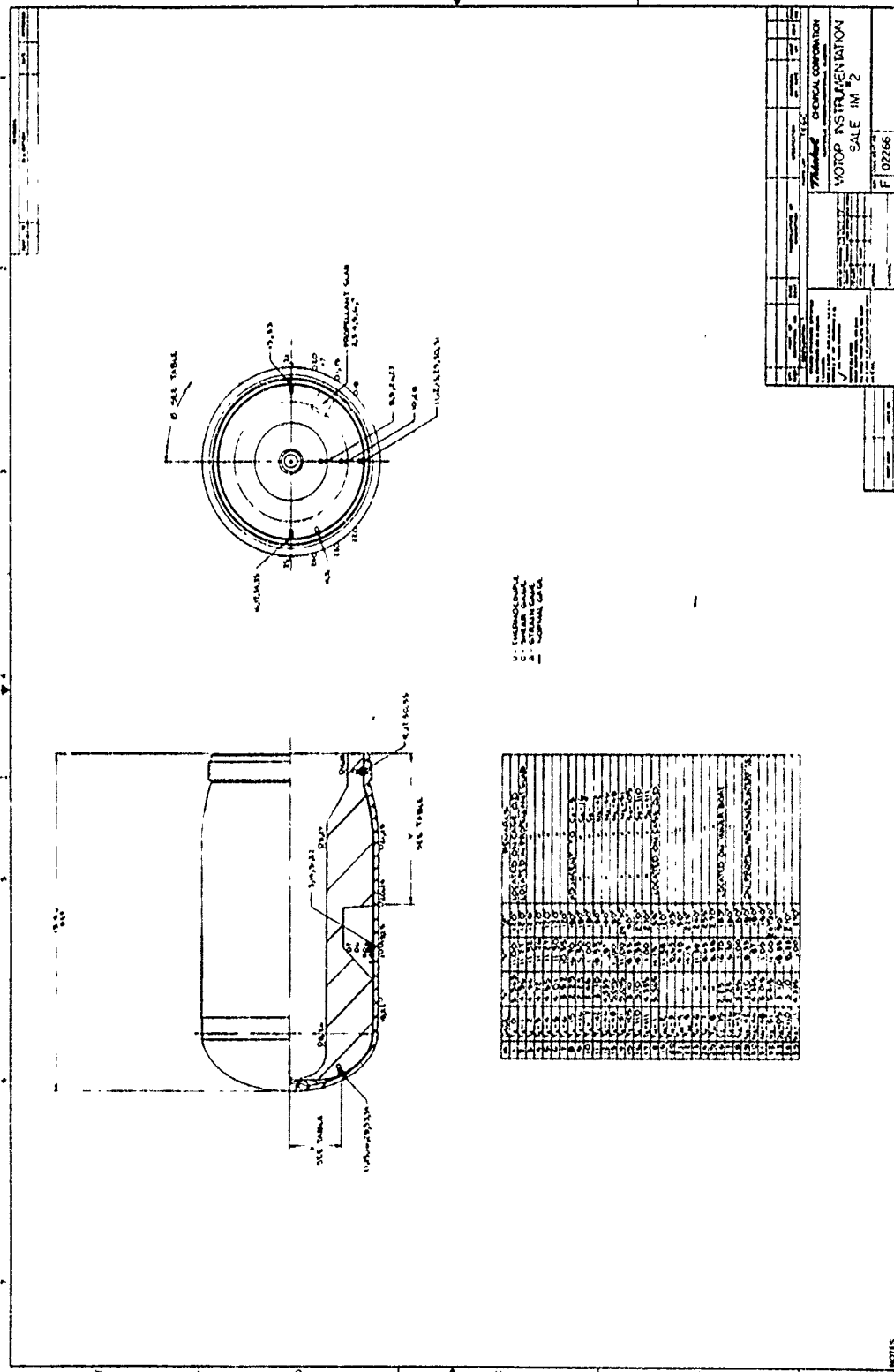


Figure 31. IM #2 Gage Location



### Propellant Testing

Uniaxial tensile properties were measured from Mix L-198 of TP-L8006 propellant (used to cast the three instrumented motors) to evaluate mechanical response of the propellant needed for analyzing the stresses and strains during aeroheat cycling. The failure characteristics were also measured for the purpose of predicting when failure could be expected in the instrumented motors. JANNAF uniaxial tensile specimens with a plastic gage for measuring strain were used in these tests. The tests were conducted at nine temperatures and three crosshead speeds with three specimens tested at each condition. The results of these tests are summarized in Table 6.

Strain endurance was measured for Mix L-198 by subjecting specimens to constant strains of 36, 34, and 32%. Specimens at the 36 and 34% levels failed and all three of the specimens at the 32% level showed no indications of cracking after 21 days. Therefore, the strain endurance of this propellant mix is 32%.

The failure boundary for this propellant mix is shown in Figure 33. The shape of the failure boundary is in general agreement with previous failure boundaries established for this propellant. Also, the magnitude stresses and strains at each temperature are comparable to those obtained from previous mixes of TP-L8006 propellant. Therefore, this mix is considered to be typical of Maverick production propellant.

A specific heat of 0.2747 cal/g °C at +77°F and a propellant density of 1.7376 g/cc were measured for Mix L-198.

The relaxation modulus for TP-L8006 (Mix L-198) was determined from constant strain rate uniaxial tensile tests. Die-cut JANNAF tensile specimens were tested with a plastic gage for measuring strain at temperatures of 200, 170, 120, 77, 20, -10, -40, -65 and -75°F. Measurements were made at cross-head speeds of 10.0, 2.0 and 0.2 in/min. Three specimens were tested at each test condition.

By time - temperature superposition of tests conducted at the various strain rates and temperatures, the master stress-strain curve shown on Figure 34 was obtained by the technique of Smith<sup>(1)</sup>. The slope of this curve was then used to obtain the relaxation modulus of TP-L8006 propellant. This relaxation modulus curve was fitted with the modified power law suggested by Blatz. The glassy modulus was determined from constant strain tests at -150°F; which is well below the measured glass transition temperature of -105°F. The equilibrium modulus was taken as the reciprocal of the creep compliance measured after three months at +77°F. The relaxation modulus measured for TP-L8006 is shown in Figure 35 (July 1973 data).

---

(1) T. L. Smith, Viscoelastic Behavior of Polyisobutylene Under Constant Rates of Elongation, J. Polymer Science, 20, 89-100 (1956).

TABLE 6  
Summary of Uniaxial Test Results

<u>Temp.</u> of	<u>Crosshead</u> <u>Speed</u> in/min	<u>Modulus</u> psi	<u>Ult.</u> <u>Strain</u> %	<u>Strain at</u> <u>Max. Stress</u> %	<u>Max.</u> <u>Stress</u> psi
200	10.0	1270	43.4	39.9	77
200	2.0	730	46.0	42.6	61
200	0.2	400	53.2	50.3	46
170	10.0	1725	35.0	34.3	85
170	2.0	940	45.1	40.0	70
170	0.2	450	48.9	47.2	54
120	10.0	2260	36.2	33.0	100
120	2.0	1060	41.0	39.2	83
120	0.2	600	50.4	48.4	65
77	10.0	2710	30.7	27.3	122
77	2.0	1430	41.0	37.5	104
77	0.2	921	44.8	43.0	80
20	10.0	5870	39.4	29.7	182
20	2.0	4170	40.1	28.0	150
20	0.2	2430	40.6	35.8	117
-10	10.0	7850	54.7	45.3	272
-10	2.0	5587	45.7	38.2	225
-10	0.2	3390	31.6	26.7	169
-40	10.0	13300	63.1	60.7	617
-40	2.0	9200	63.0	54.4	470
-40	0.2	6500	40.0	35.3	310
-65	10.0	21100	27.4	26.0	828
-65	2.0	14400	40.8	38.2	720
-65	0.2	11850	43.1	38.9	550
-75	10.0	34300	12.0	7.7	1070
-75	2.0	21600	20.9	16.5	905
-75	0.2	14700	30.2	27.4	722

# FAILURE BOUNDARY

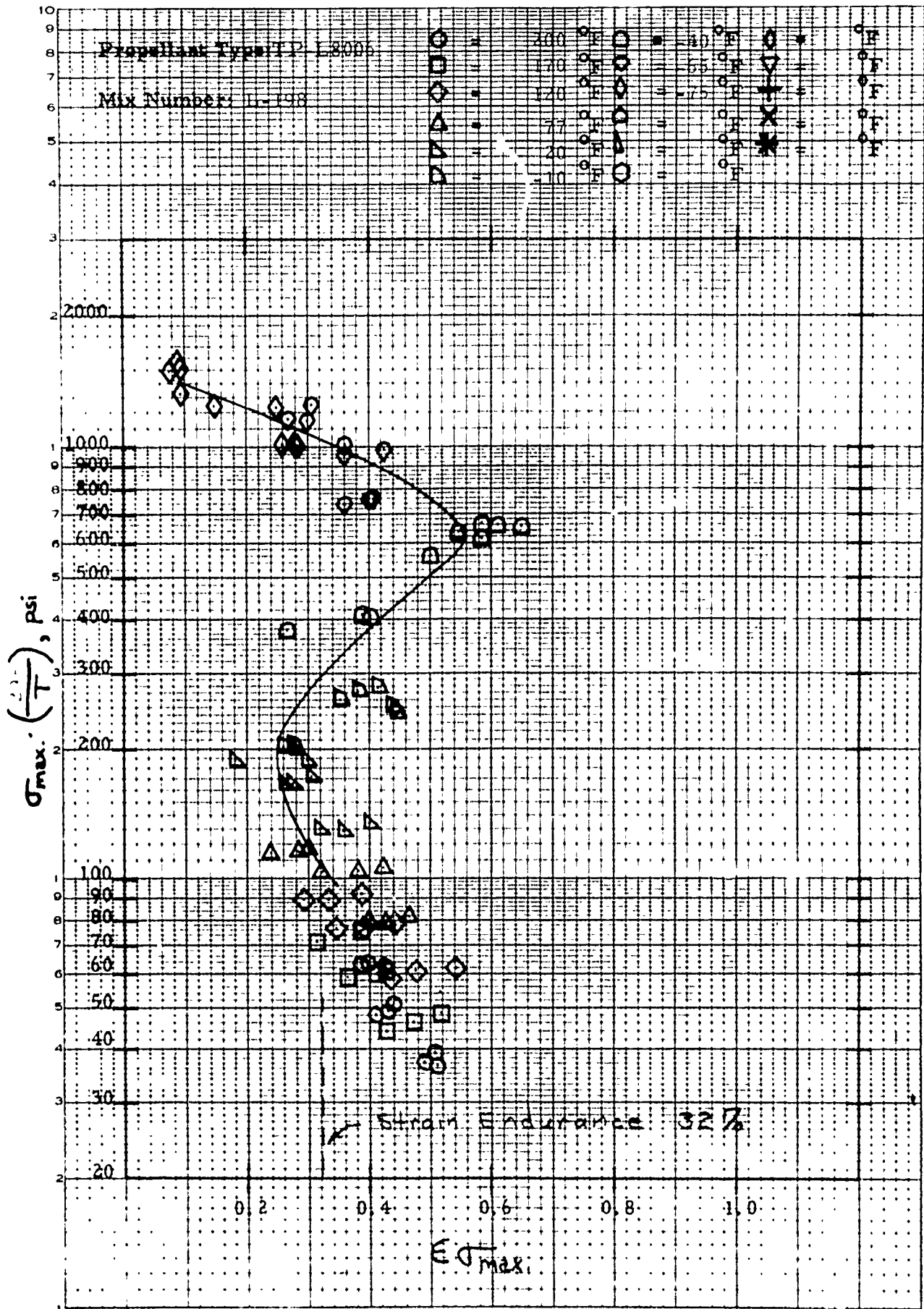


Figure 33. Failure Boundary for Mix 1-198

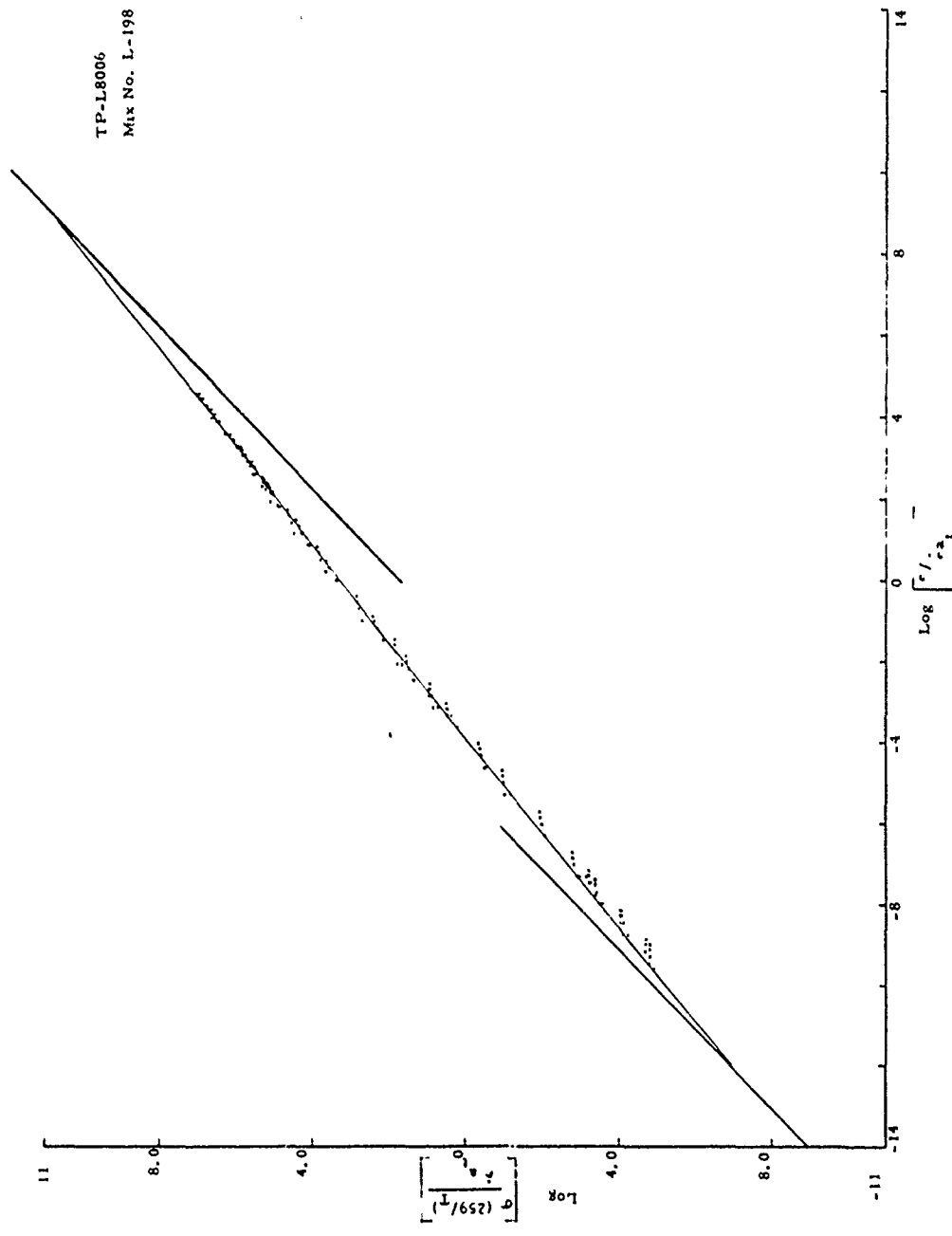


Figure 34. Temperature and Strain Rate Reduce Master Stress - Strain Curve for TP-L8006 Propellant (Mix L-198)

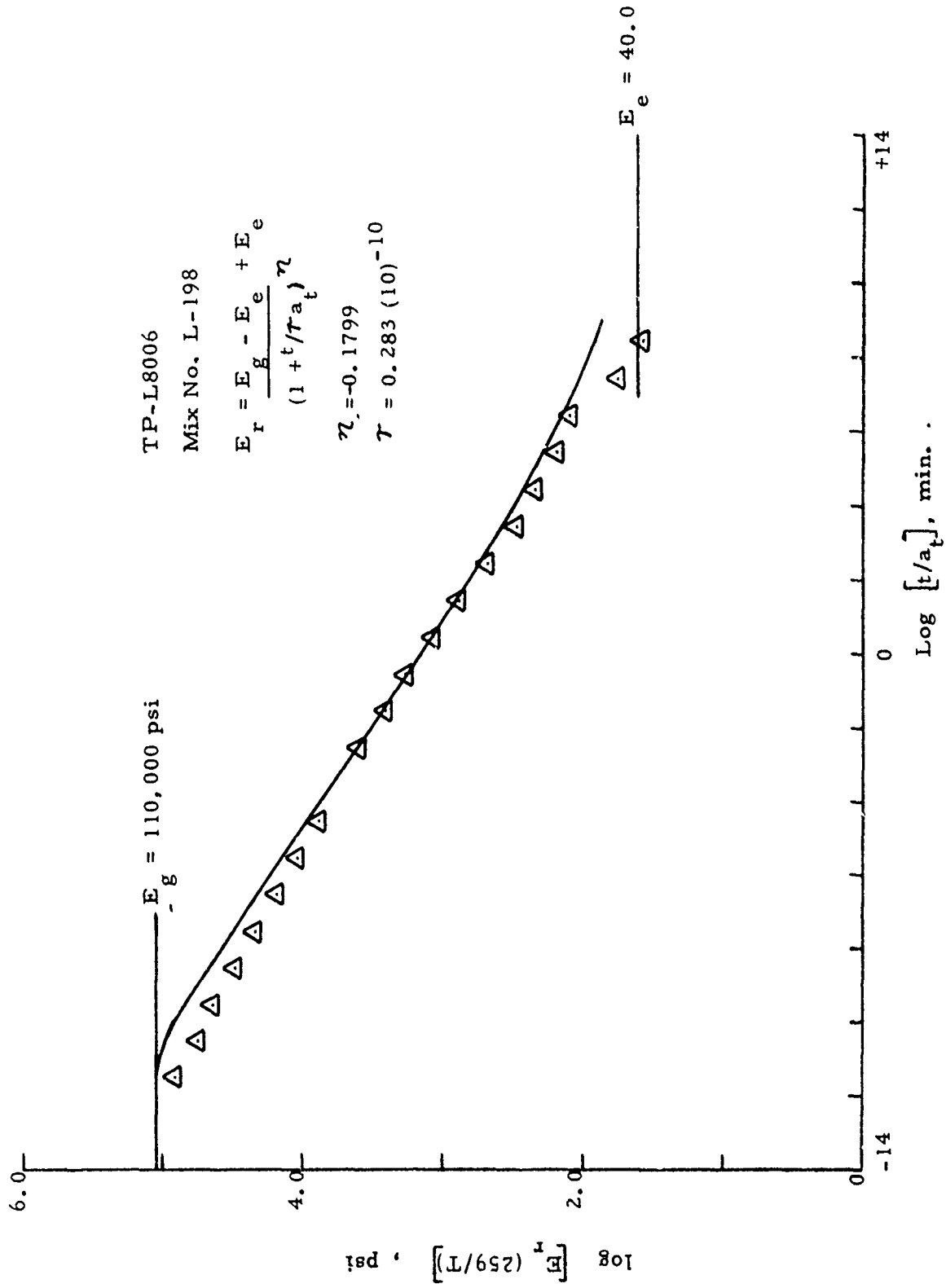


Figure 35. Relaxation Modulus for TP-L8006 Propellant

As shown on Figure 35, the modified power law equation does not quite fit the experimental data in the glassy or equilibrium modulus regions. In previous tests of other propellants much better agreement has been obtained.

A modified test technique was then used to obtain additional relaxation modulus data for TP-L8006 propellant. This modified technique was based on the direct measurement of relaxation load versus time at constant strain increments. It was thought that this method would give more accurate values of relaxation modulus than the original method, which was based on slope measurements of a master stress-strain curve obtained from constant strain rate test data. End-bonded tensile specimens were strained to 2.5% at a cross-head speed of 2.0 in/min. Load readings were taken at 1.0, 2.0, 4.0, 7.0, and 10.0 minutes; and values for relaxation modulus were calculated at each time. Relaxation modulus data from both methods are shown on Figure 36. In general, the agreement of the relaxation modulus obtained by the two different methods is considered good in the time range of general interest. For very short times or low temperatures there is a substantial difference. For long-term storage at a constant temperature, the calculated stresses are expected to be approximately the same when either relaxation modulus curve is used in the calculation.

The constant strain test results were shifted to account for the different test temperatures based on the reference temperature ( $T_s$ ) determined from the constant strain uniaxial test and the WLF shift factor ( $a$ ) with the usual constants. That is:

$$\log a_t = \frac{-8.86 (T - T_s)}{101.6 + (T - T_s)}$$

$$T_s = 259^\circ\text{K}$$

The reference temperature ( $T_s$ ) in the shift factor equation was determined by shifting the maximum stress values measured in the constant strain rate test. The use of this ultimate tensile property in establishing the shift factor could account for the relative poor shift in the constant strain data at the low temperatures. As stated previously, the constant strain data were obtained at a strain of 2.5%.

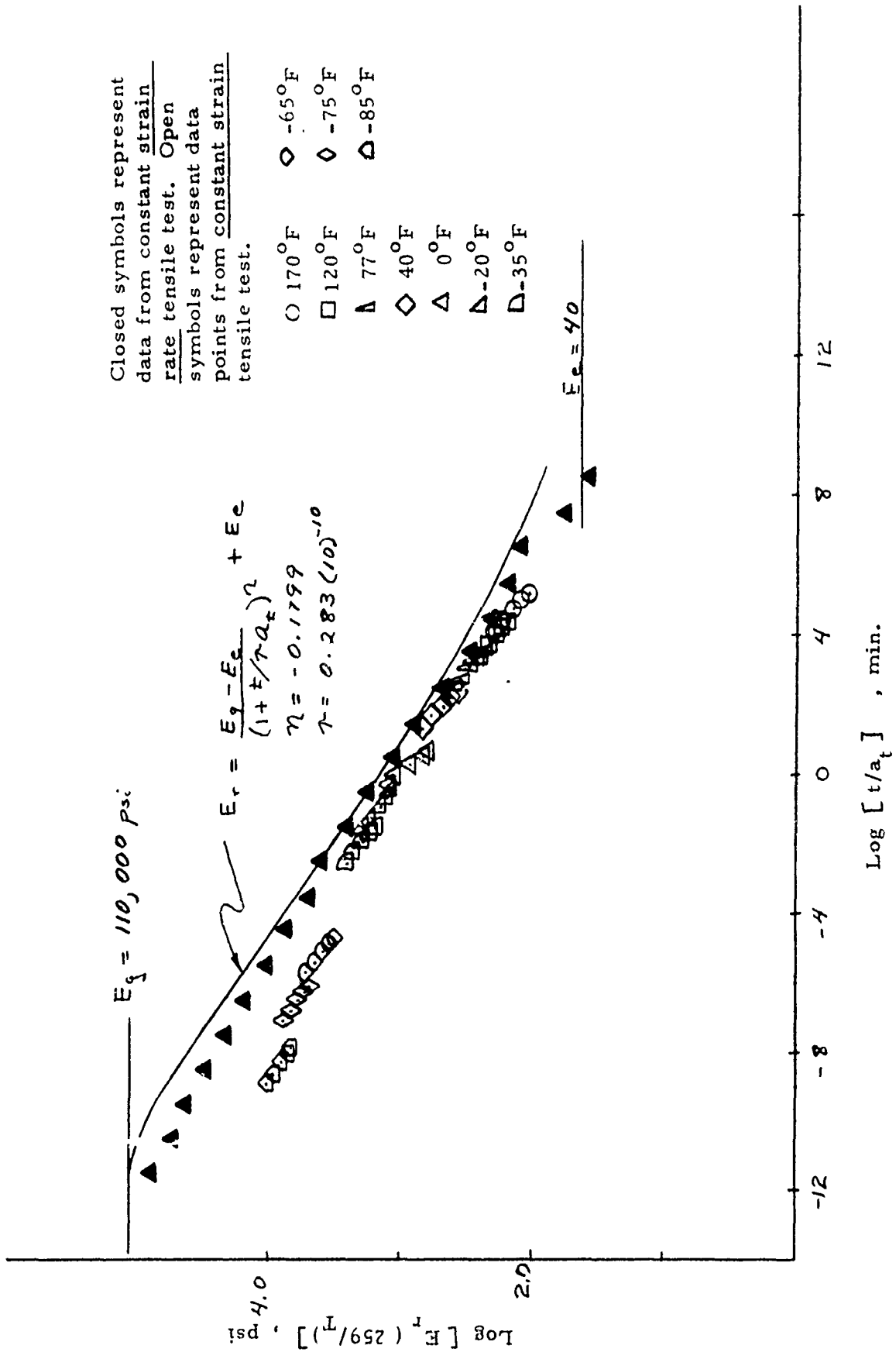


Figure 36. Comparison of Calibration Modulus Data From Mix L-198

## TESTING

### Test Facility

All testing including the gage checkout cycling was conducted in the aeroheat test facility. This Thiokol developed facility was designed and built primarily for full-scale direct connect and subscale free jet testing of air breathing propulsion systems. Because of the general arrangement and overall capability, the facility can be adapted for testing most applications requiring high temperature and high pressure air. This facility was adapted and used for the aeroheat testing in this program. The facility, as adapted for this program, consisted of air compressors, air storage tanks, air piping and regulating equipment, a capacitance air heater, a test chamber, and data acquisition and control equipment. A schematic layout of the facility as adapted for this program is shown on Figure 37. Descriptions of the capabilities of this equipment are presented in the following sections.

### Air Compressor System

An electric motor driven, stationary-type compressor (see Figure 38) with a capacity of 280 SCFM (standard cubic feet per minute) or 21 lb/min at 5,000 psia is used to pressurize the storage tanks. This compressor is capable of satisfying all the requirements of the air facility. However, two auxiliary truck mounted compressors are available as a back-up system. These units have a combined capacity of 170 SCFM (12 lb/min) at 3,500 psia.

### Air Storage

Air is stored in three tanks (see Figure 39) having a total volume of 1,875 cubic feet. The tanks are rated for operation at a pressure 3,500 psia. Total storage capacity is approximately 33,500 pounds at 530°R. Usable air depends upon the pressure to which the tanks can be depleted. Typical operating times are shown on Figure 40 for various air flow rates.

### Process Air Piping

The process air piping delivers air from the storage tanks to the test chamber. Immediately downstream of the tanks, pressure is dropped through a manifold of three pressure regulators (see Figure 41) from tank level to an intermediate level. As shown on Figure 37, the air is then passed through a critical flow venturi which is used to monitor the mass flow rate of air flowing through the system. The pressure immediately upstream of the venturi is measured and used as the controlling parameter for maintaining a mass flow/time schedule. Control of the pressure at this point is accomplished by the three aforementioned pressure regulators. After the flow passes through the venturi it is split with a portion being dissected through the capacitance heater with the rest bypassing the heater. Just upstream of the test chamber, the two streams are merged with the heated air mixing with the unheated air. The mixed air temperature is monitored just upstream of the test article. Control of the temperature is accomplished.

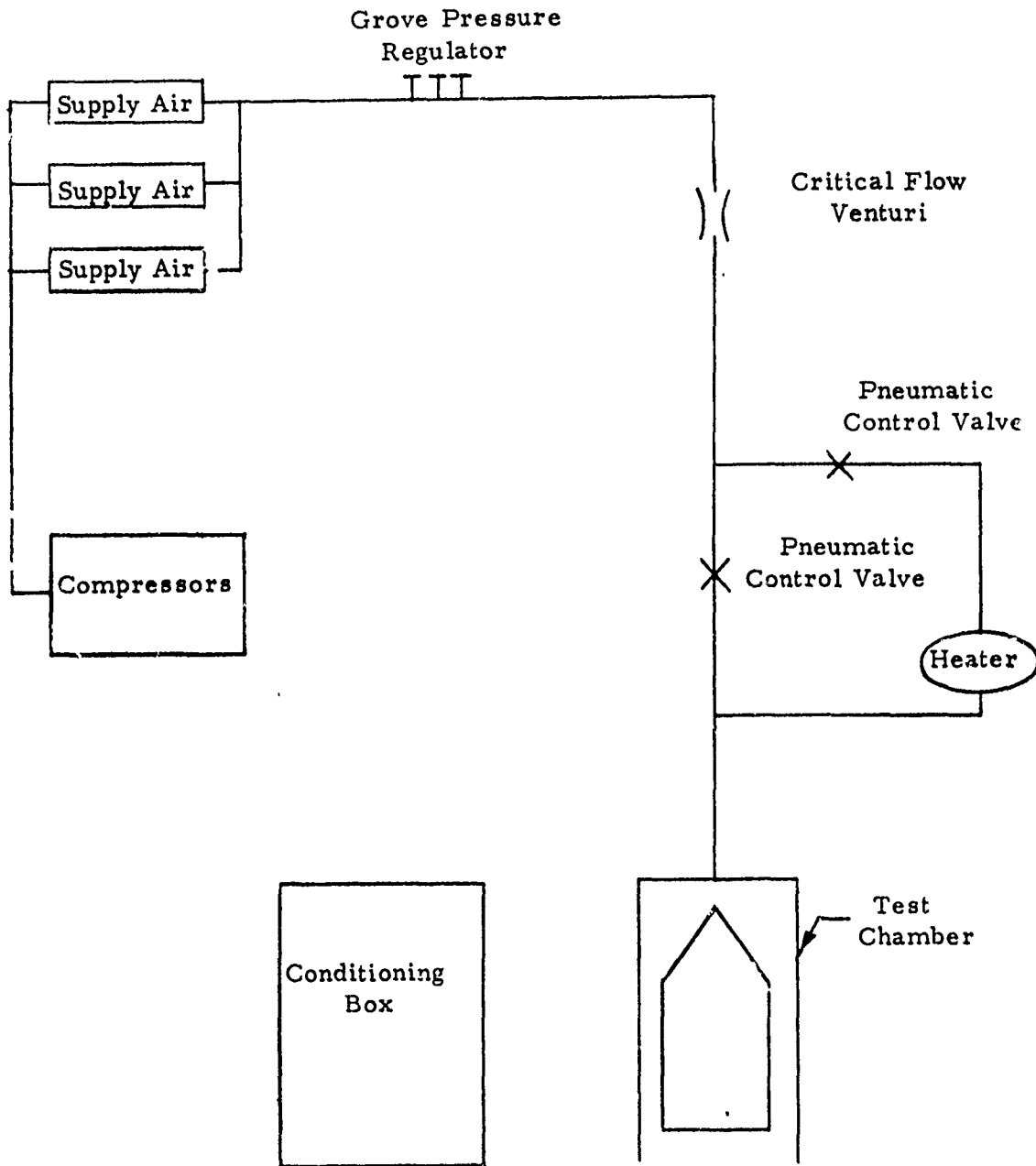


Figure 37. Schematic Layout of Aeroheat Facility

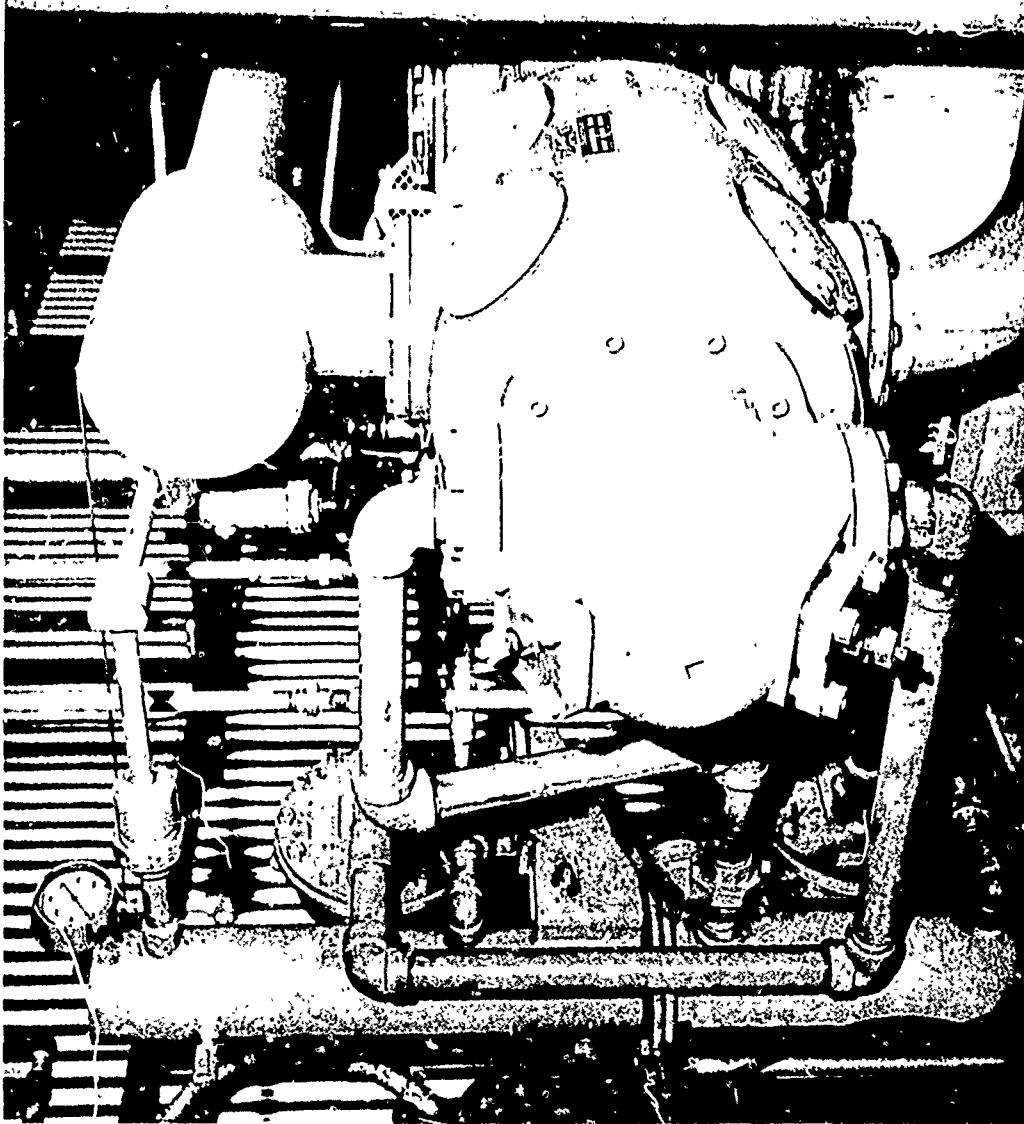
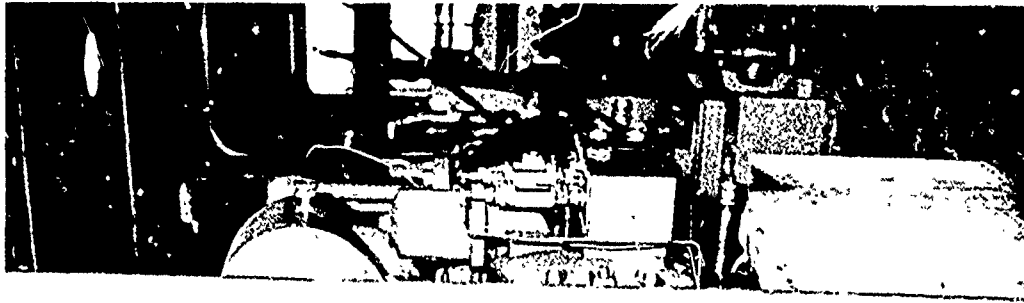


Figure 38. Main Compressor

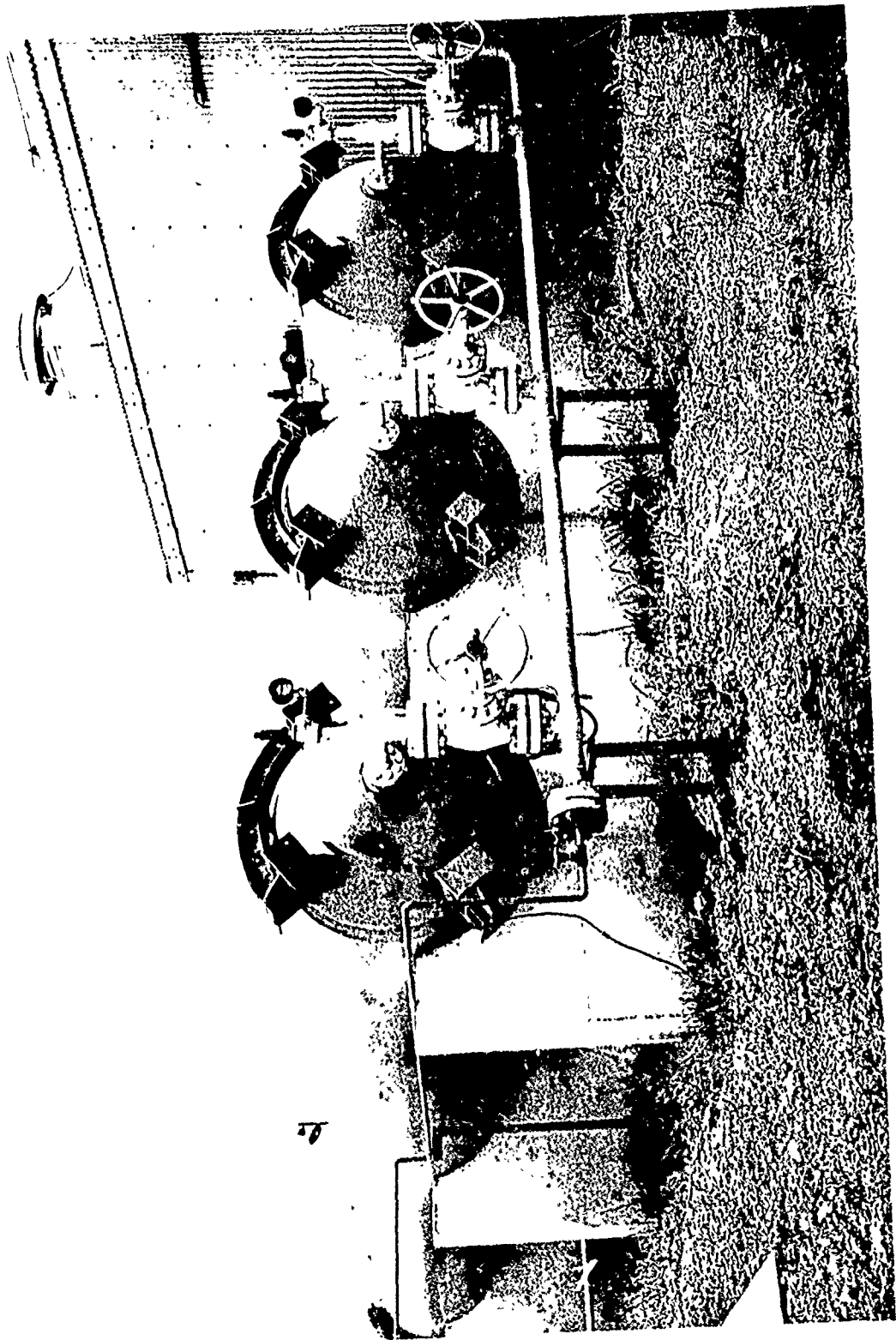


Figure 39. Air Storage Tanks

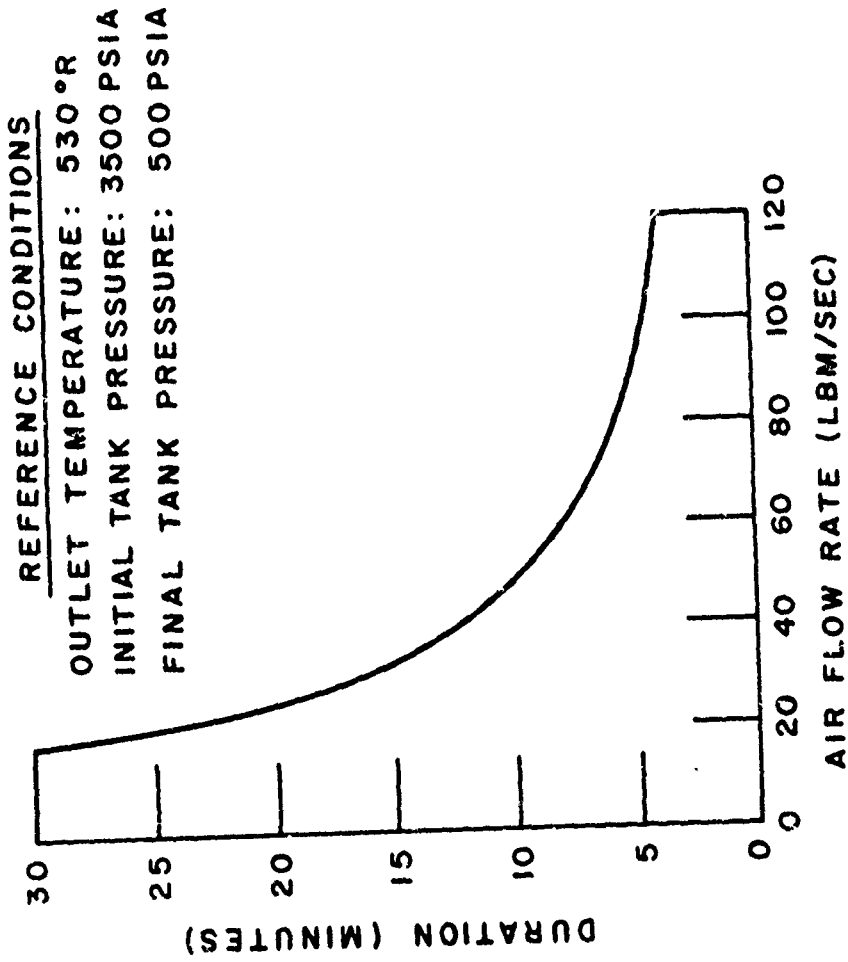


FIGURE 40. TYPICAL TEST DURATION

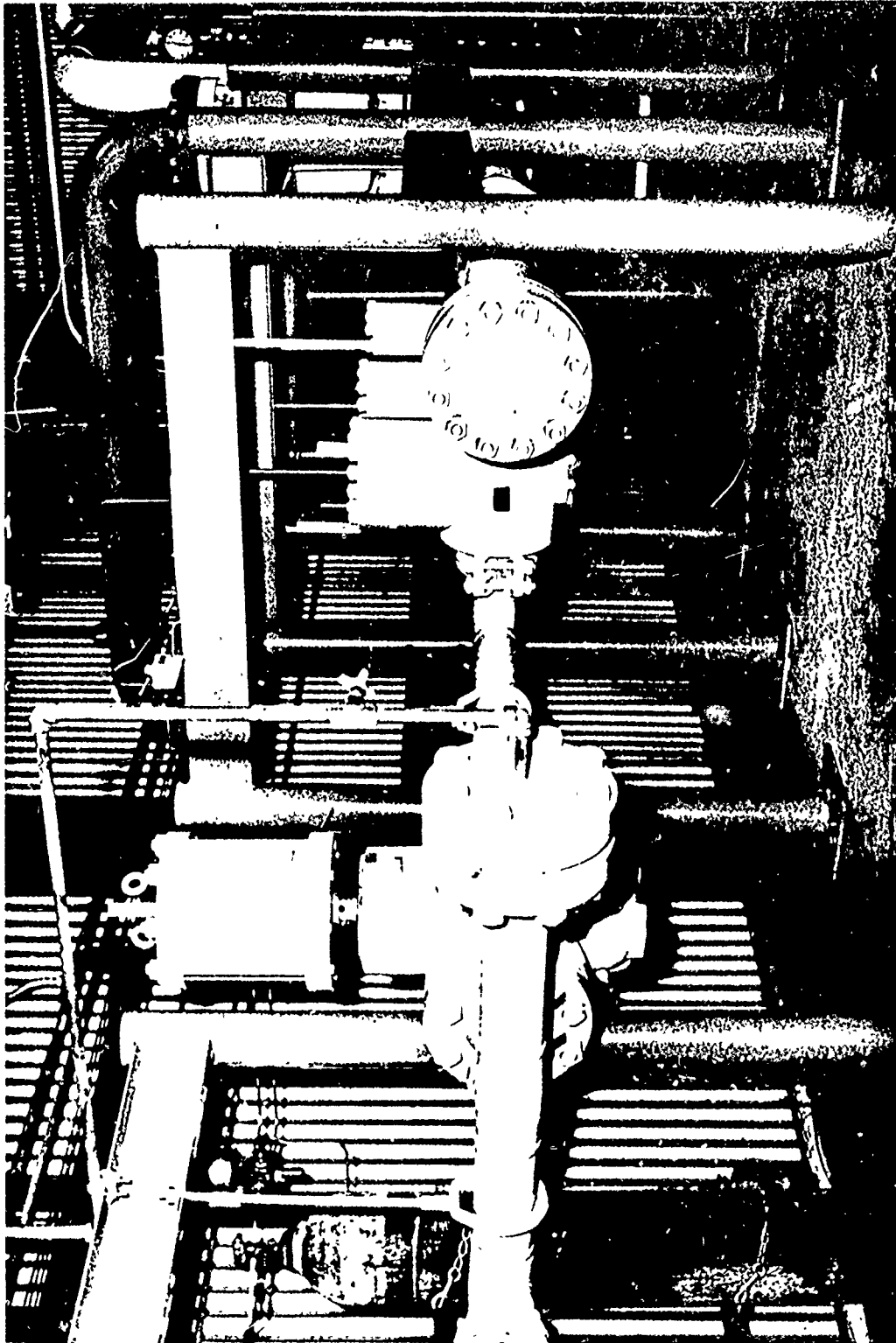


Figure 41. Main Pressure Regulator Manifold - Process Air Piping

## Heaters

The capacitance heater is a single-pass, tube-type heat exchanger (see Figure 42) with heavy-wall tubes to provide heat storage capacity for limited runs at high temperatures. The propane-fired gas burner has a maximum output of 12,000,000 Btu/hr. The heater is capable of sustaining 1,400° R at a flow rate of 15 lb/sec for a period of 30 seconds. At flow rates up to 7 lb/sec, the heater is capable of continuous operation at 1,400° R and 1,000 psia. A temperature controller and cold air bypass separate from that described above are located at the heater. For operating temperatures less than maximum, the desired temperature is set on the temperature controller and the necessary amount of cold air is mixed with the heated air to maintain the temperature at the desired level. For these tests, the heater was set at a constant firing level and the amount of air passing through it was varied as necessary to meet the required temperature history.

## Test Chamber

The test chamber consisted of a section of 14 inch standard pipe with a flange on the upstream end to attach it to the standard facility piping. The details of how the test article was placed and held in the test section will be discussed in a later section.

## Conditioning Box

A standard double wall 82 inch long by 32 inch wide by 48 inch deep (inside measurements) was located next to the test chamber. This box was adapted to accommodate raw liquid CO<sub>2</sub> being dumped directly into the box to provide low temperature capability to -100°F. Heating capability was provided by the use of steam coil mounted within the box.

## Data Acquisition and Control Equipment

Data acquisition and recording are done by a Systems Engineering Laboratories (SEL) Model 600, 96-channel low-level digital data acquisition system. This system shown on Figure 43 contains signal conditioning and electrical calibration equipment, a 96-channel multiplexer, analog-to-digital converter, tape recorders, a six-channel digital-to-analog converter, and tape processor. The system was designed for continuous data recording, but a sequencing device designed and built by Thiokol for use on this program was added which also allows data to be acquired and recorded at any time interval (between one second and 10 hours) for any desired duration. Minimum data sampling time is 120 milliseconds (one data record). A photograph of the sequencer panel as well as the closed circuit TV screen displaying the end of the test section is presented on Figure 44.

The data acquisition system samples and records data, while automatically controlling countdown sequencing. The primary multiplexer samples up to 95 analog inputs. The 96th channel is sub-multiplexed for 30 additional

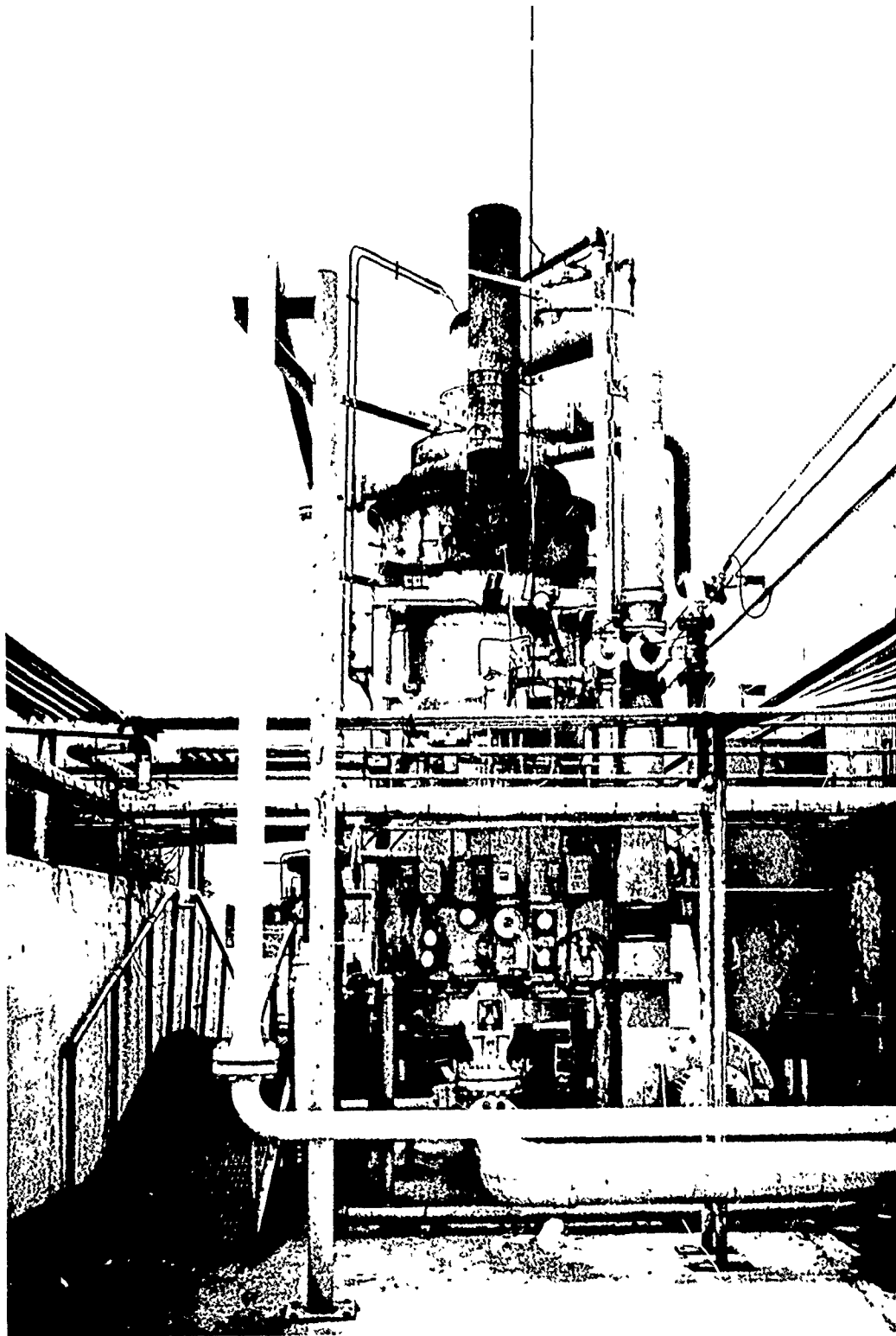


Figure 42. Capacitance Heater

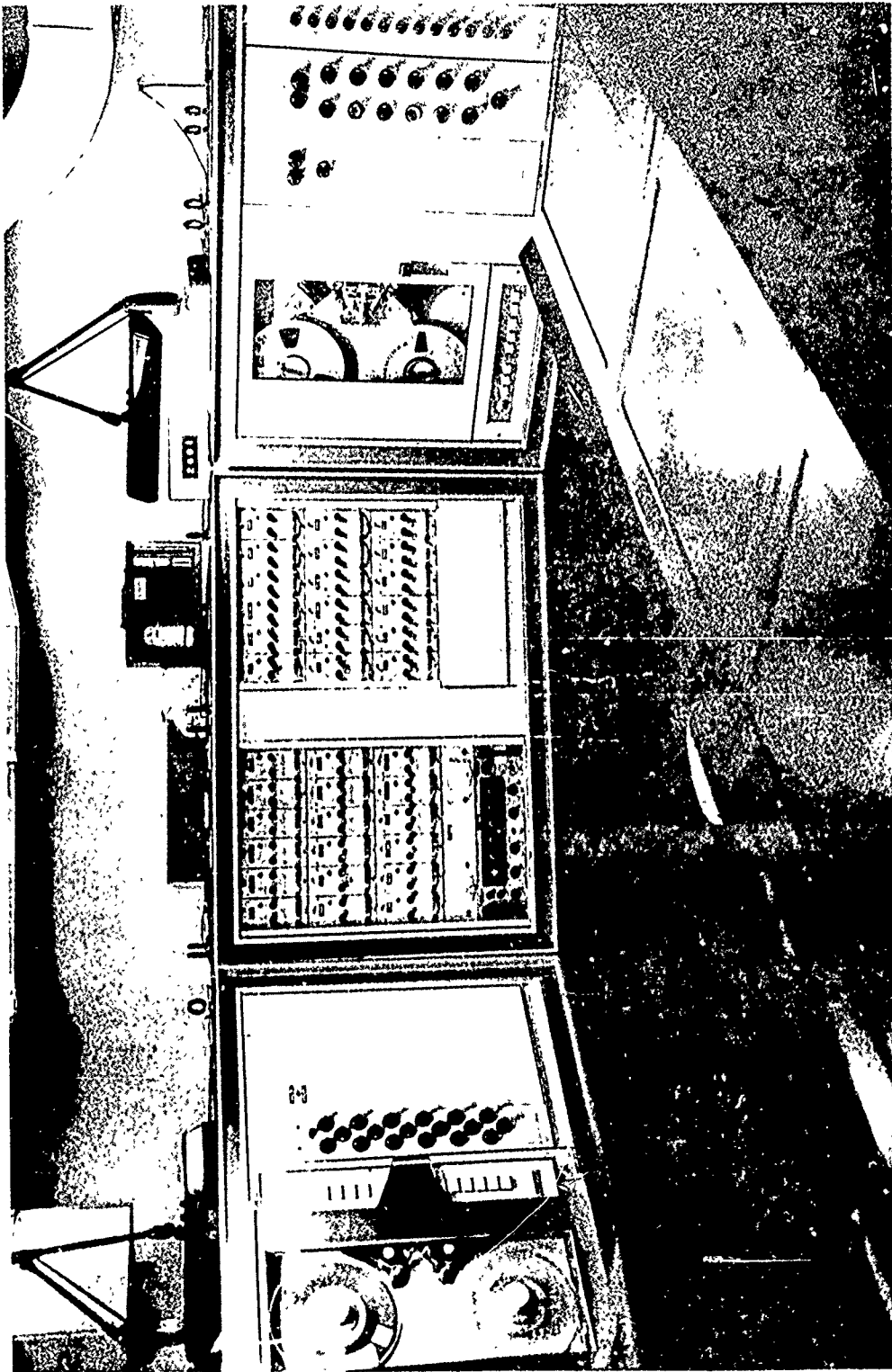


Figure 43. SEL Data Acquisition

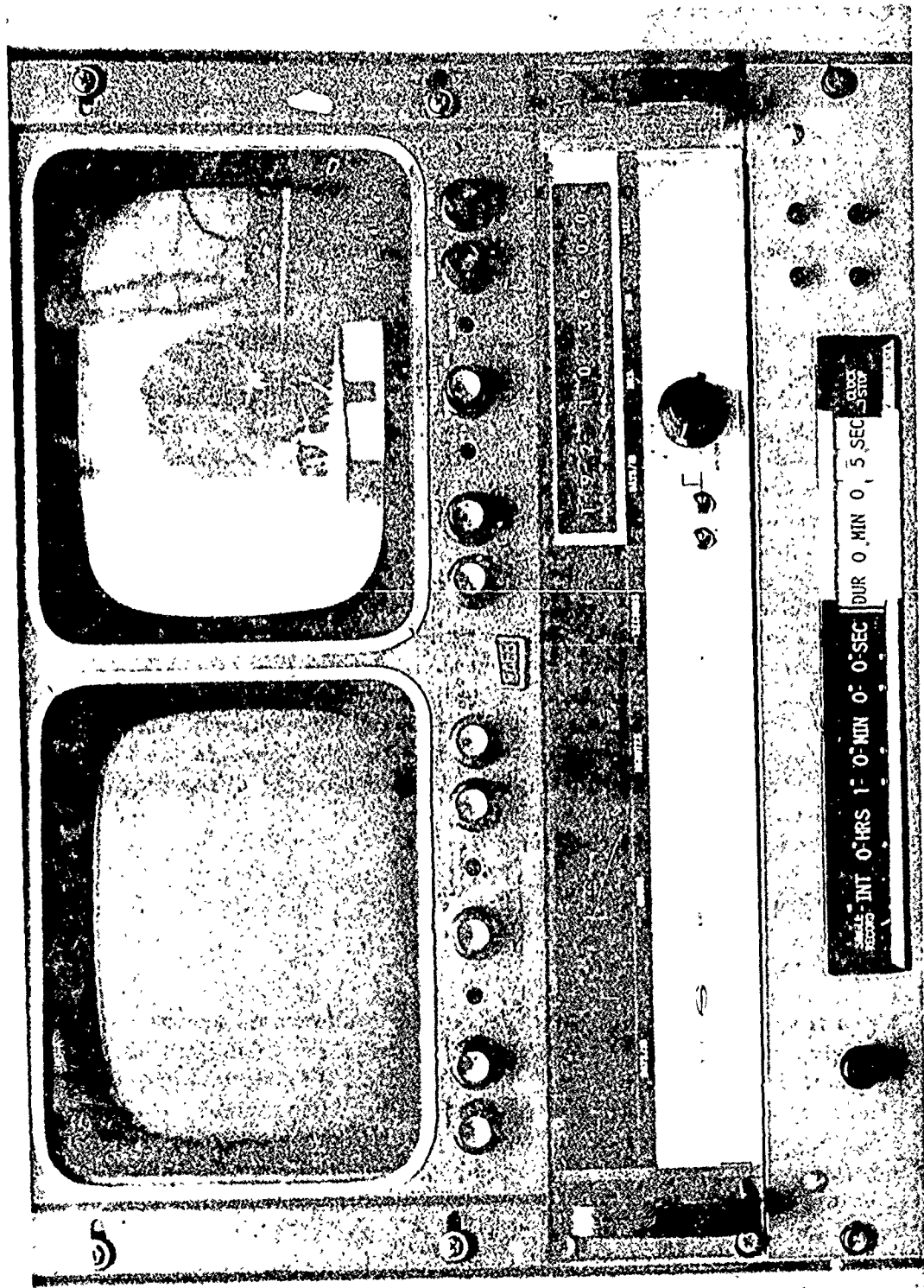


Figure 44. Data Acquisition Sequencer Panel

inputs giving a total capability of 125 channels. The 96-channel multiplexer can be programmed to sample 6, 12, 48 or 96 inputs during each cycle. At the start of each cycle of the primary multiplexer, the 30-channel sub-multiplexer samples one input. Each sample of data from the two multiplexer is presented to the analog-to-digital converter, where it is converted into a 12-bit binary word. The sample rate to the analog-to-digital converter is always 24,000 words/sec and the individual input sampling rate is dependent on the program of the 95-channel multiplexer. For example, in the 96-channel mode, each primary channel is sampled every four milliseconds. In the six-channel mode, each primary channel is sampled every 250 microseconds.

All data are recorded in real time on one inch, sixteen-track magnetic tape. Up to six channels of data can be converted from the digital encoded value to an analog reconstruction of the original signal and recorded in real time on an oscillograph. Any number of analog records can be obtained in groups of six by playing back the one-inch tape. After the test has been completed, the data from the one-inch tape are processed and recorded on a nine track, one-half inch magnetic tape in gapped format for direct entry into an IBM 360 computer.

Complete ten step electrical calibration equipment is provided within the system. Automatic electrical calibration of each input transducer is accomplished during each countdown sequence. A final pre-test calibration sequence is performed automatically immediately prior to each test. A post-test calibration sequence is performed on command immediately after the test. Calibrations can also be entered directly into the computer relating digital counts to the corresponding engineering units output of the transducer. This method is used with the normal stress, shear stress, and clip-type strain gages used in the SALE program.

## Hardware and Procedures

### Motor Geometry

A drawing of a motor in the test chamber is shown on Figure 45. As shown, a fairing or nose cone is attached to the head end of the motor. This fairing provides a smooth, uniform flow over the outside motor case and also protects the head end of the grain from direct aeroheating which, if allowed, would be nonrepresentative of actual missile heating. The fairing is fabricated from thin sheet metal and is attached to a center body that is fastened to a boss bolted to the motor case through the igniter port. Similarly, an aft fairing is used to maintain a smooth flow over the aft end of the motor. This fairing is attached to the normal Maverick aft motor closure and blast tube assembly with the blast tube removed.

The motor is mounted in the chamber by two rods which extend through a special mounting plate which forms part of the chamber wall. The forward mount is attached to the boss that extends through the nose fairing skin. The



aft mount is attached to the aft closure assembly. The motor is secured to this special mounting plate prior to testing and remains attached until the aeroheat testing of the motor is completed. A photograph of the test motor being installed into the test chamber is shown on Figure 46. The corner of the conditioning box is visible in the left center of the photograph.

### Test Instrumentation

Instrumentation in terms of pressure and temperature sensors was incorporated into the test hardware to provide a record of the actual test conditions. Flow rate and the temperature of the air ahead of the motor in the test chamber were monitored and used as the basis for control. As stated previously, the flow rate was measured using a critical flow venturi. The pressure and temperature upstream of venturi throat was measured and monitored in the control room. These values were also recorded on the SEL system. Since the air temperature change upstream of the venturi during a test was small, only the pressure was actually used in the control of flow rate. The air temperature control was based on the air temperature measure by Chromel-Alumel probes in the test chamber. The location of these probes as well as other instrumentation on the test chamber is shown on Figure 47. The purpose of measuring the static pressure along the edge of the aeroheat chamber adjacent to the motor was to define the local velocity field. A pitot probe was, as shown, also employed to measure total pressure at aft end of the flow passage. The measurements along with the static pressure ahead of the motor were used basically in the early portion of the test program to check out the simulation method. Since the simulation compared well with flight predictions (discussed in the next section) many of these pressure measurements were discontinued during the IM testing.

In addition to the test chamber instrumentation, thermocouples were also installed on the test motor. Ten copper-Constantan thermocouples were installed on the outside of the motor case as shown on Figure 47. This arrangement was maintained for all the UM and IM's tested. The location of these thermocouples on the IMs are also given in Figures 30, 31, and 32. The purpose of these thermocouples was to determine the nature of the heating gradients that existed along and around the motor. Grain bore temperatures were also measured. These served as a guide to determine if the heating rate produced the same bore temperature rise as predicted by the THVINC analysis.

Other instrumentation and electronic systems unique to the instrumented motor are discussed under Instrumented Motor Testing.

### Aeroheat Test Plan and Procedures

The general test plan at the onset of this program was to subject an uninstrumented motor to fifty aeroheat cycles prior to testing the instrumented motors. As stated before, the purpose of testing an UM was to guarantee that the aeroheat schedules were not so severe as to fail the IM's prematurely while insuring that the sequence of tests would result in eventual, and timely

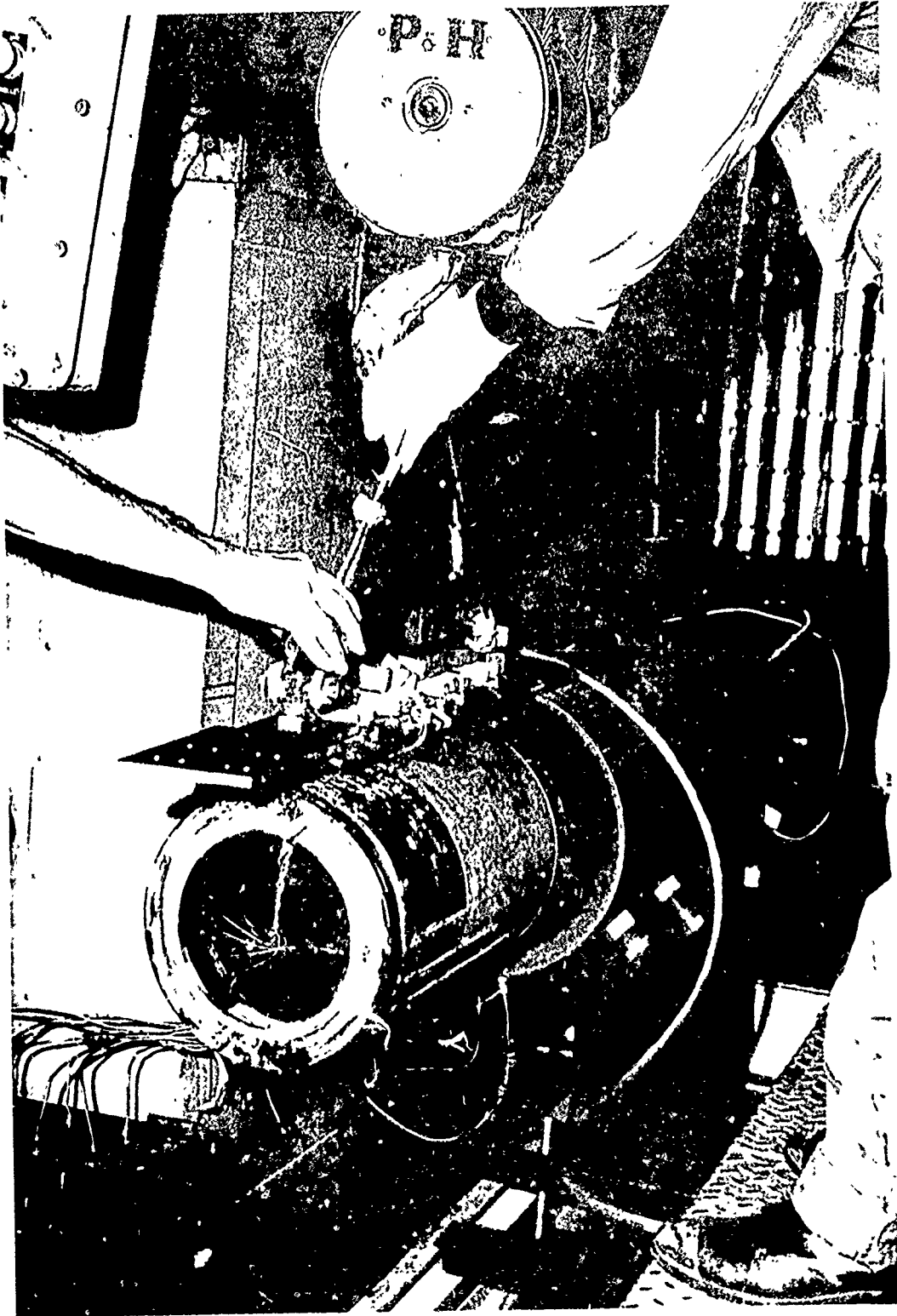
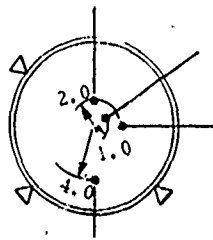
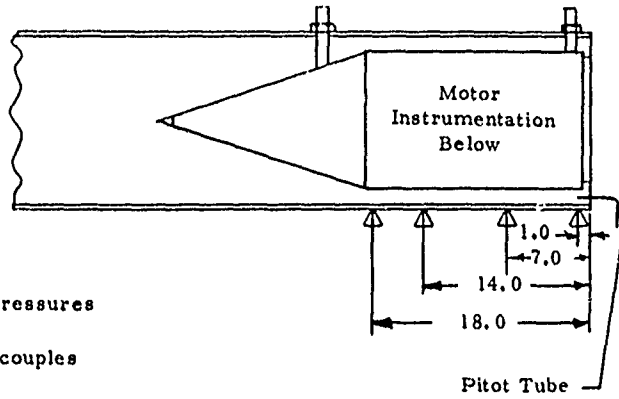


Figure 39. U.M. 1 Being Stalled in Test Chamber



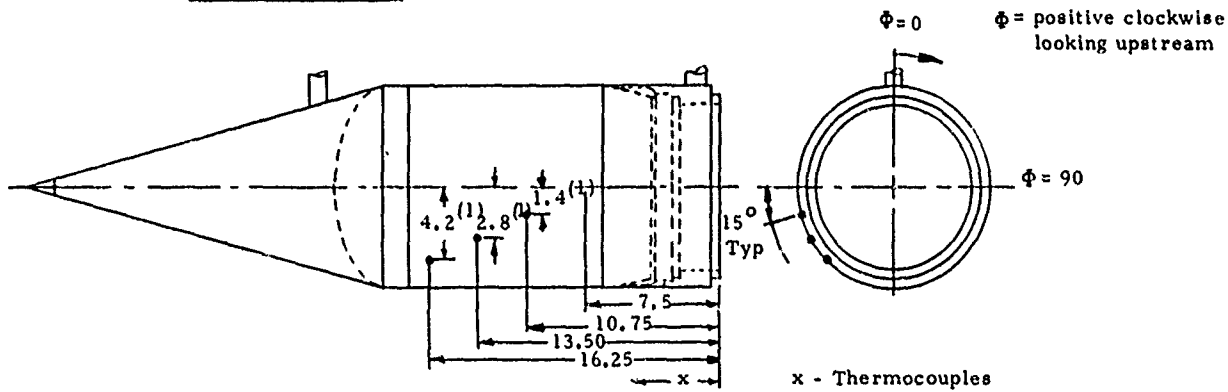
▽ Static Pressures  
 • Thermocouples



Exterior Thermocouples		
TC	X	$\Phi$
1	16.25	145
2	13.50	120
3	10.75	105
4	7.50	90
5	16.25	225
6	13.50	240
7	10.75	255
8	7.50	270

Interior* Thermocouples		
TC	X	$\Phi$
9	13.50	~180
10	7.50	~180

\*Interior Thermocouples to be Located in Valley at  $\Phi$  Near 180



All Dimensions in Inches  
 (1) Surface Distance

Figure 47. Test Instrumentation Layout

failure of the IM's. The sequence of test schedules planned for UM #1 were as outlined on Figure 12. Each test schedule consists of ten cycles of a given motor time-temperature profile. This time-temperature profile relates to the environment that the motor is in at a given time. In general, this consists of simulating the heat transfer coefficient (h) and adiabatic wall temperature ( $T_{aw}$ ) profiles as a function of time for a given mission through the duration of that mission; after which, the storage at a specified temperature is simulated. For test purposes, the values of h and  $T_{aw}$  are converted into terms of venturi pressure (from required flow rate) and aeroheat chamber temperature histories. For this series of these tests the ambient storage temperature was selected at  $-65^{\circ}\text{F}$ . Therefore, the motor is conditioned to this temperature for a minimum prescribed length of time prior to aeroheat testing.

The procedure used in conducting these tests is basically as follows. Initially, the motor was conditioned to a temperature of  $-65^{\circ}\text{F}$ . Heat transfer calculations made for motors of this type have shown that a period of at least 20 hours of exposure in a forced convection environment are required to bring the motor to an equilibrium temperature of  $-65^{\circ}\text{F}$  from an initial temperature of  $77^{\circ}\text{F}$ . This period of time was adopted as the minimum time between tests. Once this prescribed period of time had been achieved, the motor was removed from the conditioning box and installed in the aeroheat chamber. This operation took, on the average, three minutes to complete. Upon installation, the area was cleared with all personnel going to the block house. Data were being recorded during this time at one minute intervals. To assure repeatability from cycle to cycle, airflow was not started until the ten-minute mark had been reached. This is a reference time from about one minute before the conditioning box was opened. During the period of airflow, data were recorded manually every ten seconds for the first 180 seconds, and then at 30-second intervals until the test was completed at about 1020 seconds. Following the test, the inner bore was inspected for cracks, etc. and the motor placed back into conditioning.

## Uninstrumented Motor Aeroheat Testing

Uninstrumented motor testing was begun with the SFPI mission as planned (Figure 12) in an attempt to achieve an early failure. As discussed earlier, the modes of failure expected was bore cracking although the possibility of unbond between liner and case or liner and propellant was not ruled out because of the high temperatures encountered. Upon completion of this schedule there was some question as to whether the liner had failed or not - that is, a possible failure by reversion under high temperature. Because of this possibility, testing deviated from the original test plan and a short series of three very severe tests was conducted; after which the motor was dissected. The following discussion pertains to the results of UM #1 and UM #2 testing. A summary of the tests conducted on these two motors is included as Table 7.

The SFPI mission profile when translated into test conditions is shown on Figure 48. Here the flow rate and air temperature just upstream of the motor is presented as a function of test time. The test actually begins just prior to opening the conditioning box to remove the motor. Air flow is initiated at the 600 second (10 minutes) time point and continues until shut down at approximately 1400 seconds (23.3 minutes). By comparing these profiles with those shown on Figure 2, one can see that the actual test condition compares well with those planned. The expanded time scale over the first 180 seconds on Figure 48 should be noted in making such a comparison. The difference in the values between the mass flux level shown on Figure 2 and the flow rate values shown here in Figure 48 is because flow rates is equal to mass flux times the flow area. The flow area in this case would be the cross sectional area between the motor and the test chamber wall.

Although this motor is referred to as an uninstrumented motor, thermocouples were attached to the case and the inner bore of the grain as shown on Figure 49. The purpose of the thermocouples was to provide data to check whether the motor case was responding to the aeroheat cycle as predicted in the severity analysis. The temperature-time profiles of the case as predicted using THVINC were based on the flight recovery temperature and heat transfer coefficient profiles. If the flight conditions are being properly simulated in the facility, then the case should respond as predicted. This comparison is shown on Figure 49. The symbols represent the mean of the ten cycles. The comparison is excellent, thus confirming proper simulation of the SFPI mission.

Sufficient thermocouple data were measured to provide the temperature distribution over the motor as shown on Figure 31. The distribution shown is, of course, expected. The temperature near the head-end of the motor is lower than near the mid-point because of three-dimensional conduction effects. The nose cone fairing protects the head end from direct exposure, thus providing a large heat sink area. The same is true at the aft end where the large steel fairing provides a considerable heat sink. One would, of course, expect similar gradients to exist on an actual wing carried missile.

TABLE 7  
UNINSTRUMENTED MOTOR TEST SUMMARY

MOTOR	TEST NUMBER	MISSION PROFILE	INITIAL MOTOR TEMPERATURE, °F	REMARKS
UM #1 ↓	1-10	SFPI	-65	Liner failure feared, but not detected.
	11-13	TS	-75	Attempt to overstress, case temperature raised from -65 to 300 in 20 seconds.
UM #2 ↓	14-23	DMP-3	-65	No detectable degradation of motor.
	24-25	HSMH	-65	Hot day conditions assumed.
	25-33	HSMH	-65	Shortened mission duration - no detectable degradation.
	34-43	SFPI	-65	No detectable degradation noted.
	44-50	TS	-75	No failures induced.

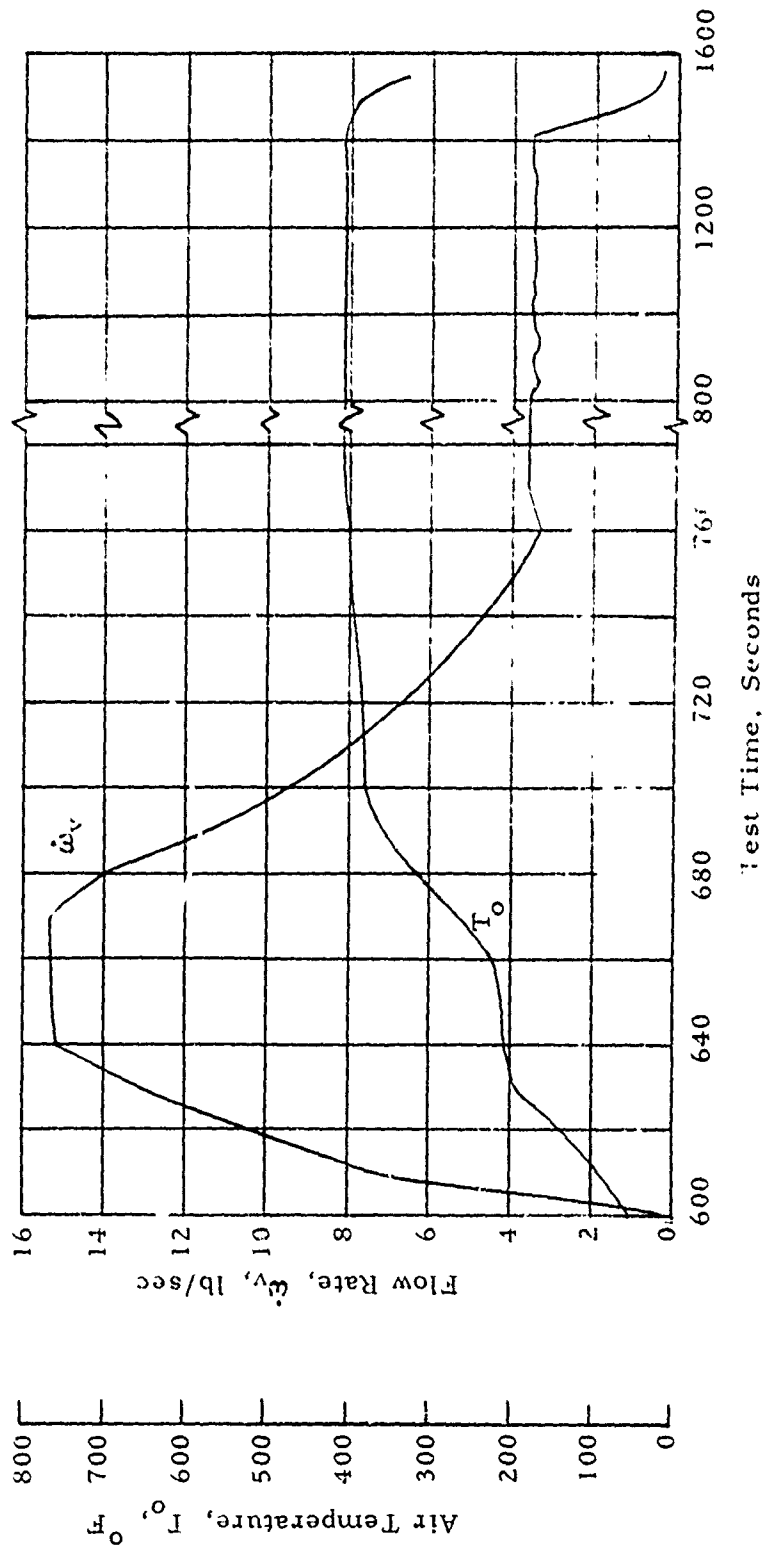


Figure 48. Typical Test Schedule for a SFPI Mission - Source Test No. 7

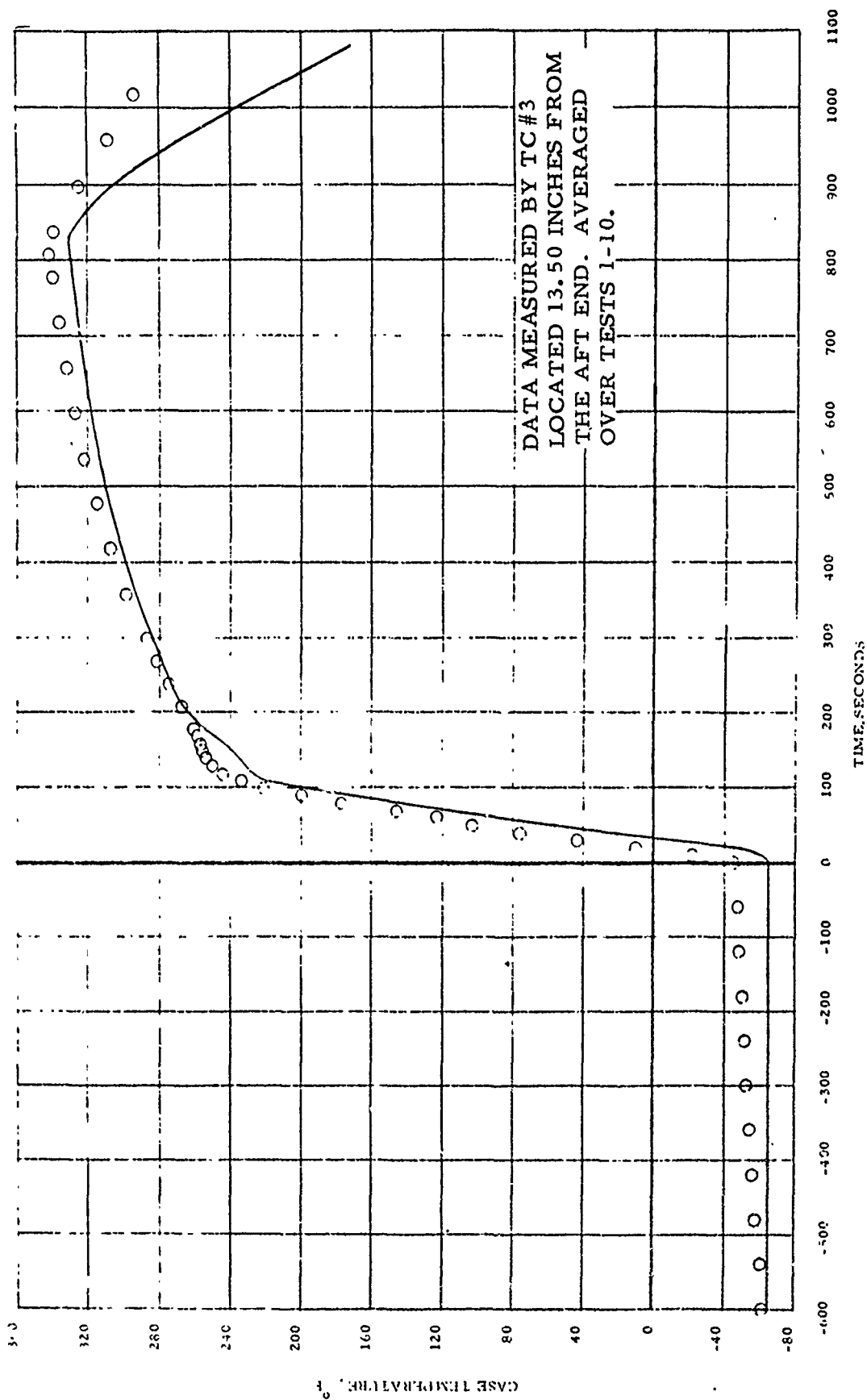


Figure 49. Comparison of Predicted and Measured Motor Case Temperatures

The temperatures at Sta. 13.50 would show a minimum effect of end losses and thus would be more representative of simple aerodynamic heating on a cone cylinder body. This station is the source for those data presented on Figure 50.

UM #1 was checked for bore cracking after each test and X-rayed for damage at the completion of the 10 SFPI test series. No failure was detected; however, this did not rule out liner failure. Inasmuch as this motor had been subjected to case temperature levels of 300°F and greater for a period of approximately nine minutes per test (as seen in Figure 50) for an accumulation of 90 minutes, the possibility of a liner failure due to material reversion was suspected. Evidence of the liner reverting to a tar-like material was seen during calibration of the normal stress gages. Reversion was evident in three of the liner-potted gages when exposed for a long period of time at 300°F. Separate laboratory tests have shown that significant weight loss and complete reversion occurs when a strip of liner is placed in a 300°F oven for a period of one hour in the presence of air. Whether the same occurs when the liner is confined within a motor is not known. However, if such a reversion were to occur, the structural response in terms of inducing high hoop stresses by aeroheating the motor would be changed. A complete reversion of the liner in that section directly exposed to the high temperatures would in effect isolate the grain from the case, and it would be impossible to induce the level of hoop stresses at the inner bore as shown in Figure 8.

Because of the suspected liner reversion, the testing sequence originally outlined for UM #1 was suspended and a special 3-test schedule was selected. The purpose here was to attempt an immediate failure by subjecting the grain to as severe a thermal shock (TS) as possible. Therefore, it was desirable to produce stress levels within the grain that would exceed by considerable margin the failure boundary criteria for the propellant. To accomplish this, it was necessary to determine if the test facility in the present configuration could provide a sufficiently fast start up to induce the high stress levels in the grain. A shakedown run of the facility (without UM #1 installed) was conducted with resulting pressure and temperature histories input into THVINC to determine the stress level. The initial temperature on the motor was also dropped to -75°F to increase the severity of the cycle. The results from the THVINC calculations indicated that the desired high stress levels could be produced. The failure boundary curve presented as Figure 9 shows that the typical aeroheat mission moves upward and would push out through the boundary curve for a value of  $\sigma_{max} (298/T)$  of approximately 1400. For this cycle, the value of  $\sigma_{max} (298/T)$  predicted by THVINC was 2300. This cycle then should be of sufficient severity to cause a failure, if the liner were still structurally sound.

Three of the TS designated tests were conducted using this cycle and the bore was visually inspected after each test. The test conditions typical of the TS cycle are illustrated in terms of flow rate and air temperature on Figure 51. The extremely expanded time scale should be noted when comparing these conditions with the SFPI test conditions. Results of these tests in

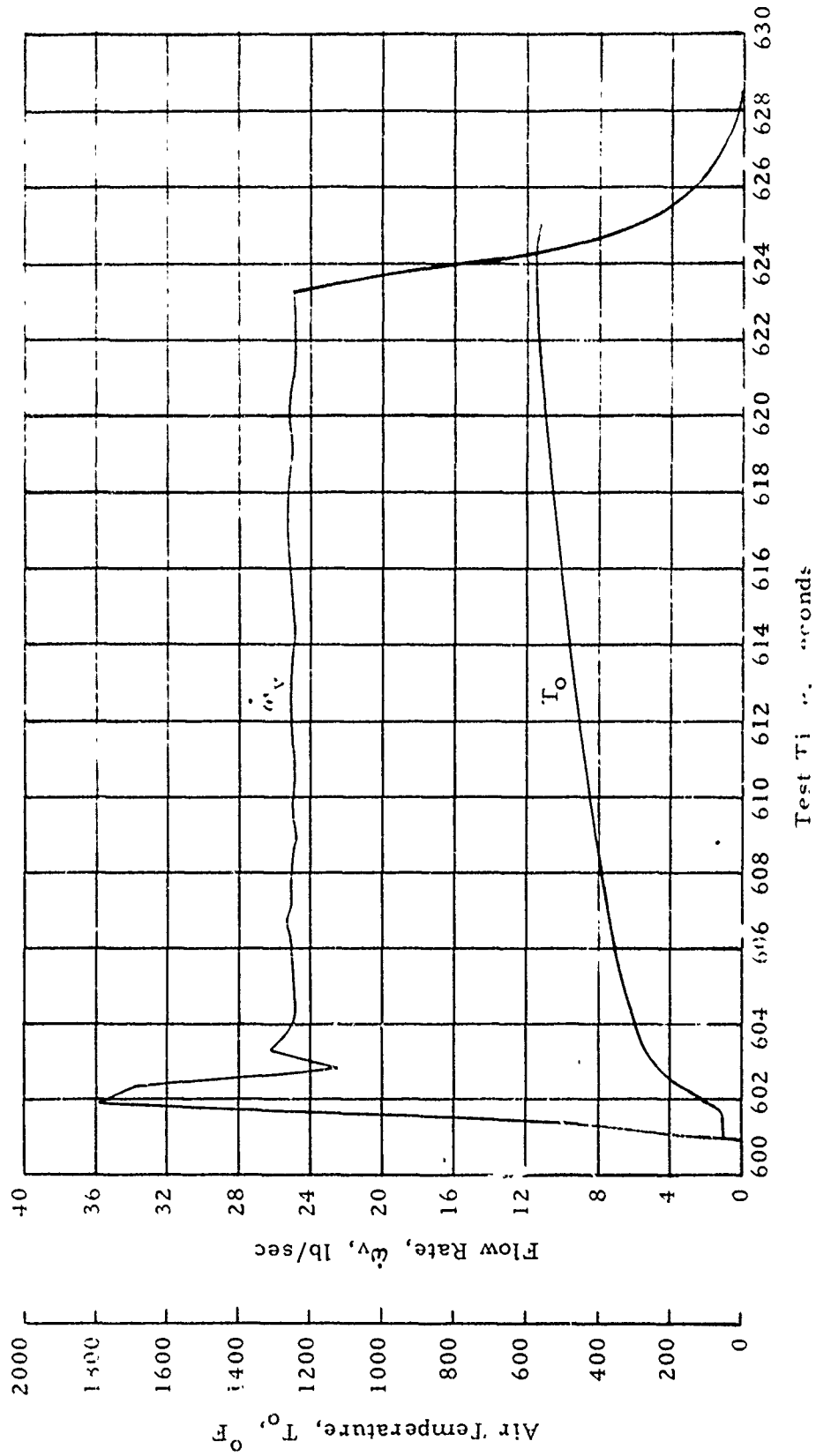


Figure 51. Typical Test Conditions for TS Mission Test 12

terms of case temperature histories are presented on Figure 52. After the third test, the motor was replaced in conditioning for 24 hours and then X-rayed. Again no evidence of any failure, either at the bond interfaces or the inner bore, was found. Inasmuch as a detectable failure was not found after such severe testing does not deny the hypothesis that the liner had reverted. Based on this evidence, it was decided to (1) suspend further testing of UM #1, (2) dissect this motor to see if the liner had really reverted, (3) obtain a new motor (UM #2) instrumented in the same manner as UM #1, and (4) resume testing.

As with UM #1, the inventory of reject production motors was checked to determine if any were available which could be used in this program as UM #2. This check resulted in Motor L-186-52 being selected. This motor was originally rejected as had UM #1 (Motor L-158-15) because of a slightly oversized void in one of the star points. Since a void in the star point does not affect the failure characteristics and the remainder of the grain was in near perfect condition, this motor was obtained for use as UM #2.

Testing of UM #2 was initiated using the DMP-3 mission profile as the schedule. This particular schedule was chosen because it is one of the least severe in terms of both stress levels and temperature levels. Consequently, testing was continued with the effects of aeroheat induced stresses being accumulated without fear of adverse temperature effects on the liner until after UM #1 could be dissected and the state of the liner reviewed.

The dissection of UM #1 was accomplished by use of a remotely operated lathe to cut the motor into three sections forward, center, and aft which are 5.4, 8.5 and 5.4 inches long, respectively. The procedure used in this operation is illustrated in a later section dealing with motor dissection. Basically, the center section is that part between the foremost and aftmost thermocouples shown on Figure 47. The liner was in excellent condition at both the cut locations showing no sign of damage due to high temperature exposure. Soft X-rays were made of the center section; but no evidence was found of any defects over and above those shown on the original motor X-rays. Since no failure was found, it appeared that perhaps either the theoretical calculations were in error or the uniaxial failure boundary is not appropriate for this loading condition. Further insight into this was felt to be gained from the UM #2 tests and the IM #1 tests.

Testing of UM #2, as shown on Table 7 began with the DMP-3 mission schedule. The corresponding test conditions in terms of flow rate and air temperature are shown on Figure 53. It is of interest to compare the actual case temperature histories with that predicted by THVINC for UM #2. Such a comparison is shown on Figure 54. Inasmuch as the comparison appears rather poor, we have taken the liberty to also show the cause on the same figure by presenting a comparison between actual and desired test air temperatures. The heat transfer coefficients have been matched very closely (i. e.  $h_{flight} \approx h_{test}$ ) and it is obvious that the case wall temperature mismatch corresponds very closely to the air temperature mismatch. The reason that

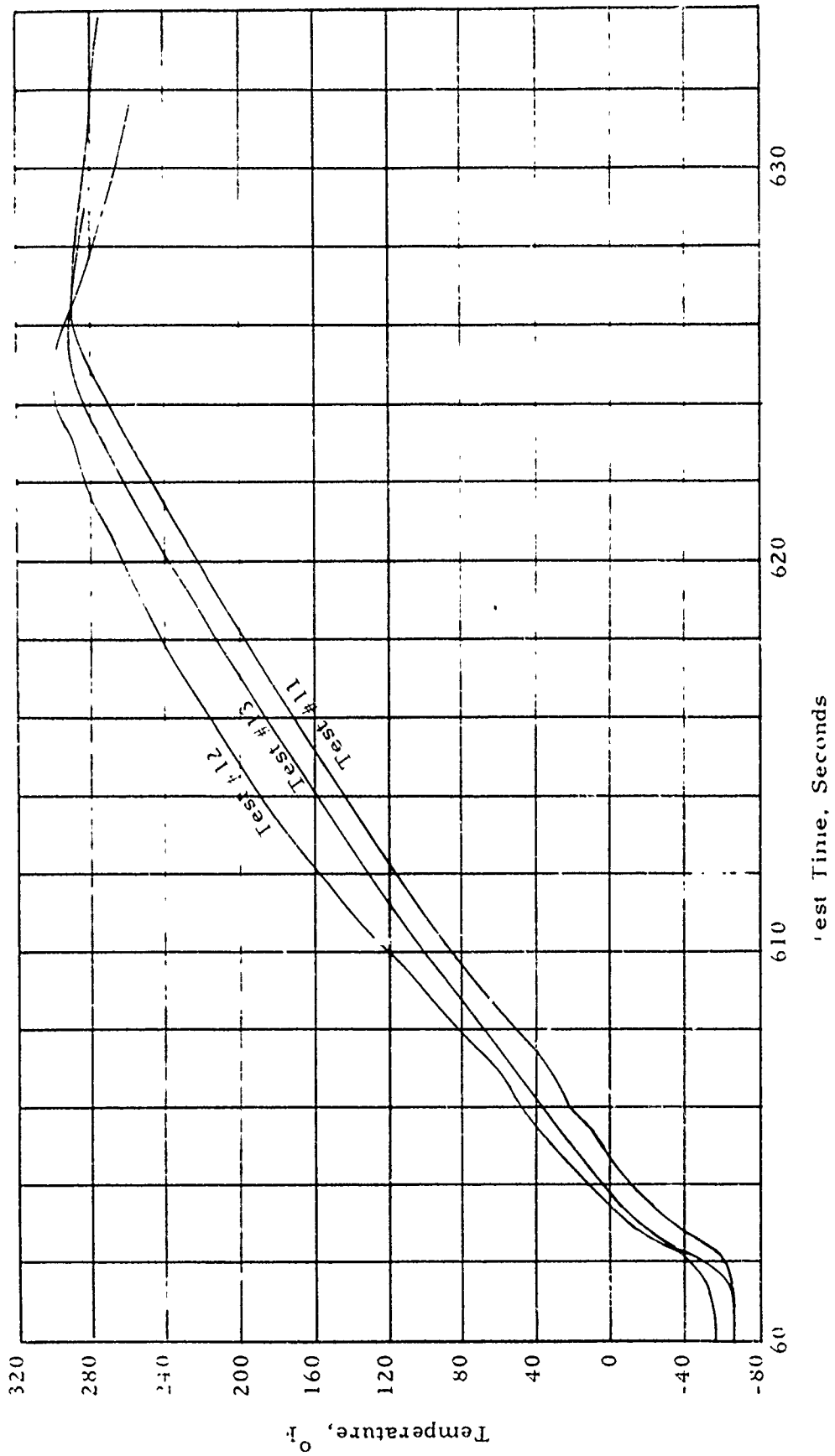


Figure 52. Motor Case Temperature Histories for the IS Series

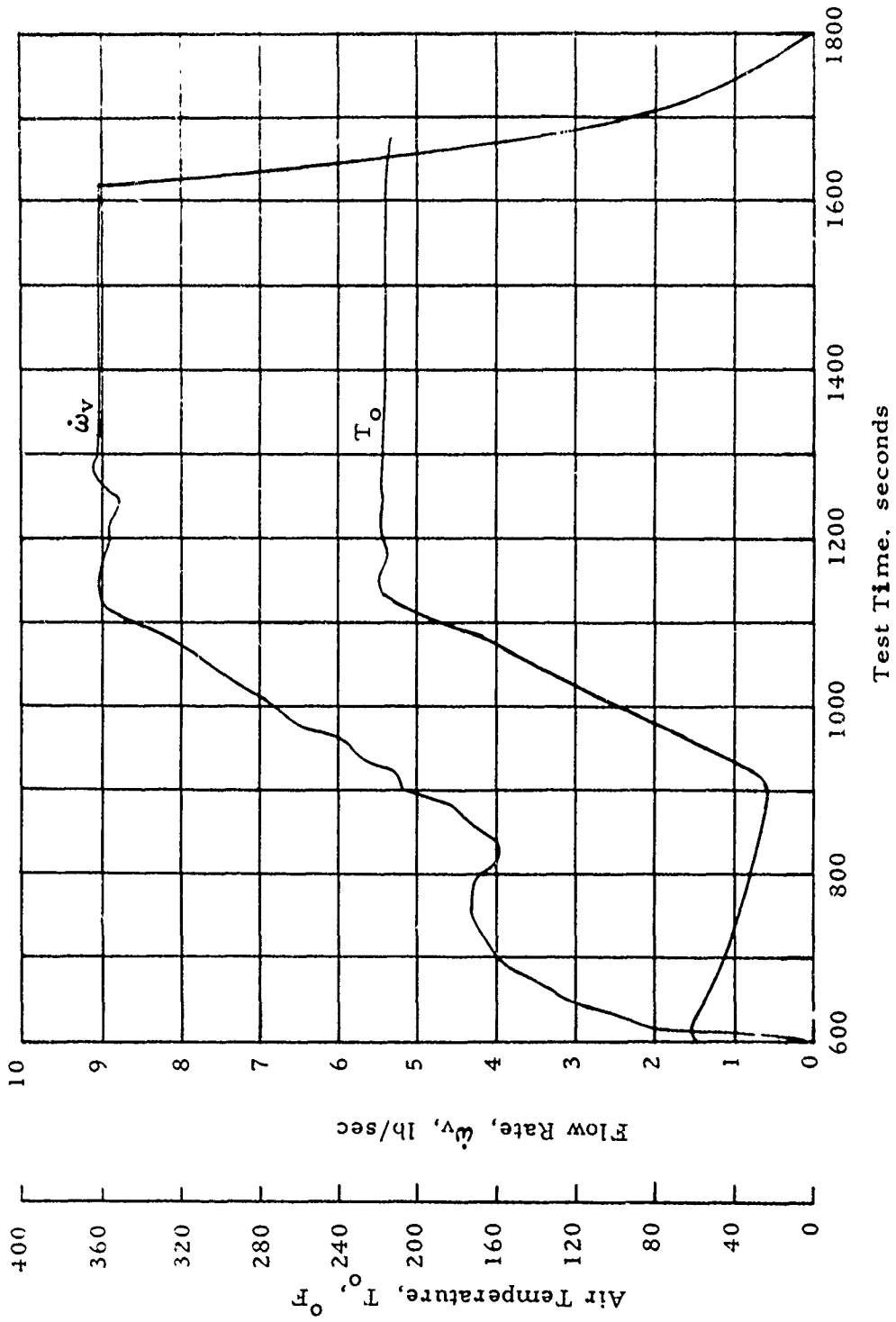


Figure 53. Typical Test Conditions for DMP-3 Mission - Test 17

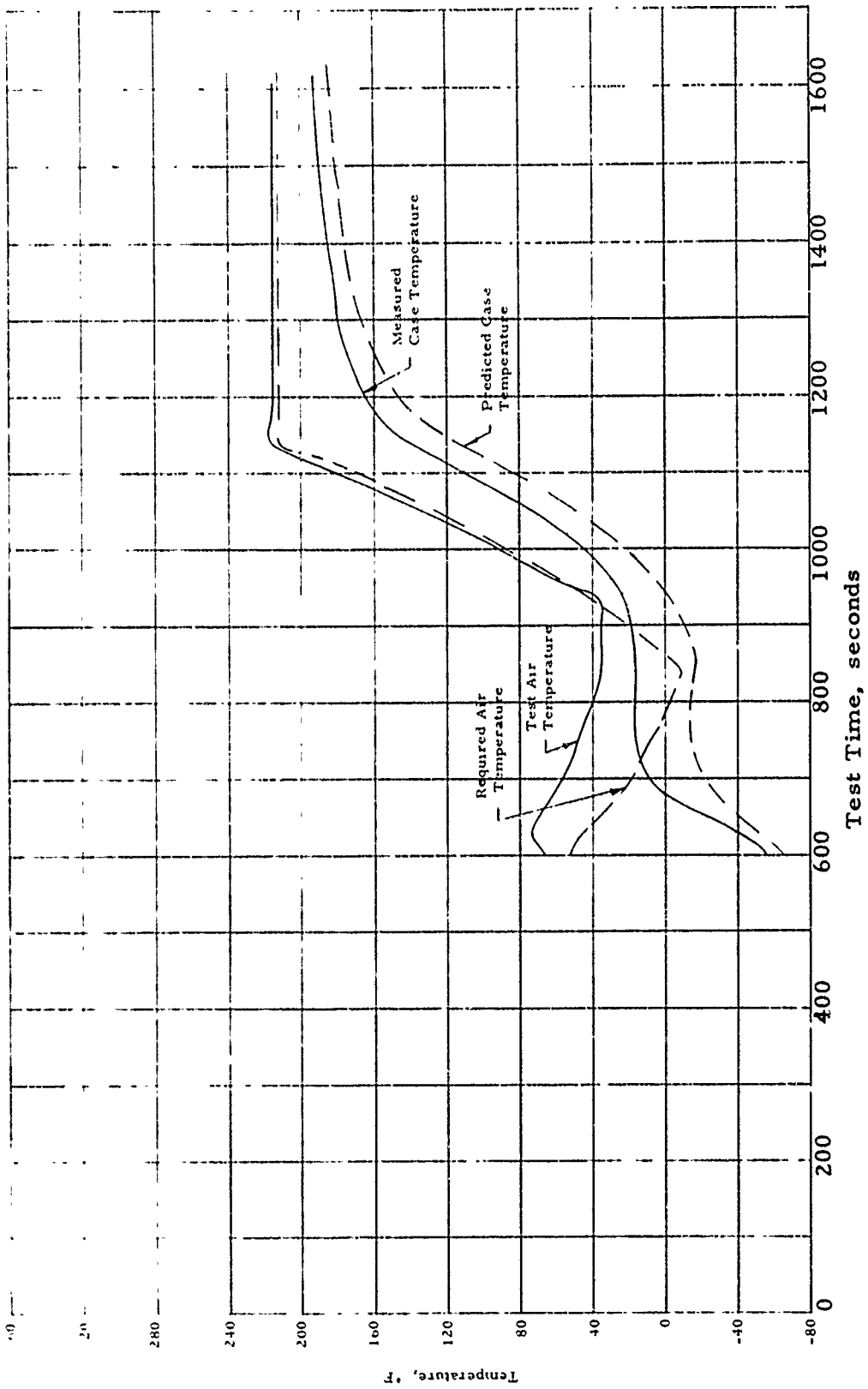


Figure 54. Comparison of Predicted and Measured Motor Case Temperature for the DMP-3 Mission Test No. 14, JM #2

a mismatch exists between actual and desired air temperature is the inability to cool the air being introduced into the aeroheat chamber without going to a rather expensive effort of injecting a coolant such as liquid nitrogen into the air stream. The effort that this mismatch has on severity level is rather slight and certainly not sufficient to justify the cost of cooling.

Following completion of the DMP-3 schedule, the decision was made to test a hot day version of the HSM mission profile. (This schedule is designated HSMH). This decision was made jointly by Thiokol and AFRPL during a meeting at Thiokol on 73 March 15, in which the test schedule for the remaining UM tests was outlined. Following a ten cycle test series of HSMH, a ten cycle test series of SFPI schedule and then a seven cycle test series of the TS schedule would be conducted. This would then complete the original test program scheduled for 50 total tests on uninstrumented motors. Selection of these remaining schedules was based upon the fact that the liner in UM #1 was found to be in excellent condition when that motor was dissected. Therefore, the remaining schedules had the purpose of providing an accumulation of at least twenty cycles of damage prior to loading at the same level that UM #1 was loaded by the SFPI and TS schedules.

Typical test conditions for the HSMH series are shown on Figure 54A. The motor case temperature case history is also shown on this figure to present comparison with the air temperature history. The effect of shortening the schedule is, of course, essentially the same as terminating these curves at a value of test time of 1200 seconds.

After the ten cycles of the HSMH schedule were completed, the SFPI schedule used in the UM #1 tests was implemented. Ten cycles of the SFPI were completed. Visual inspections made of the inner bore at the end of each test did not revealed any evidence of failure through completion of this schedule. At this point, this motor, UM #2, had undergone 30 cycles of aeroheat tests--10 each of the DMP-3, HSMH, and SFPI schedules.

The aeroheat testing of UM #2 was completed with a series of seven TS type tests. Such a test should induce hoop stresses at the inner bore much greater than propellant capability if THVINC calculations are to be believed; and a motor subjected to seven of these cycles should exhibit some cracking of the inner bore. But as was the case with UM #1 which was subjected to three such cycles, no evidence of cracking was found. A possible reason for the lack of cracking on UM #1 was attributed to propellant surface softening because of moisture damage. However, this could not have been the case in the UM #2 tests, since the propellant grain was kept under a dry nitrogen atmosphere during testing. The evidence, at this time, seems to point more and more toward overly conservative prediction by THVINC. This is quite possible since only meager data was available from which to construct a relaxation modulus curve as a function of reduced time. If the effective relaxation modulus in the motor was lower than used in the calculation, then the actual motor stresses would be much lower. The existence of the thick liner which should exhibit much lower modulus values than the propellant

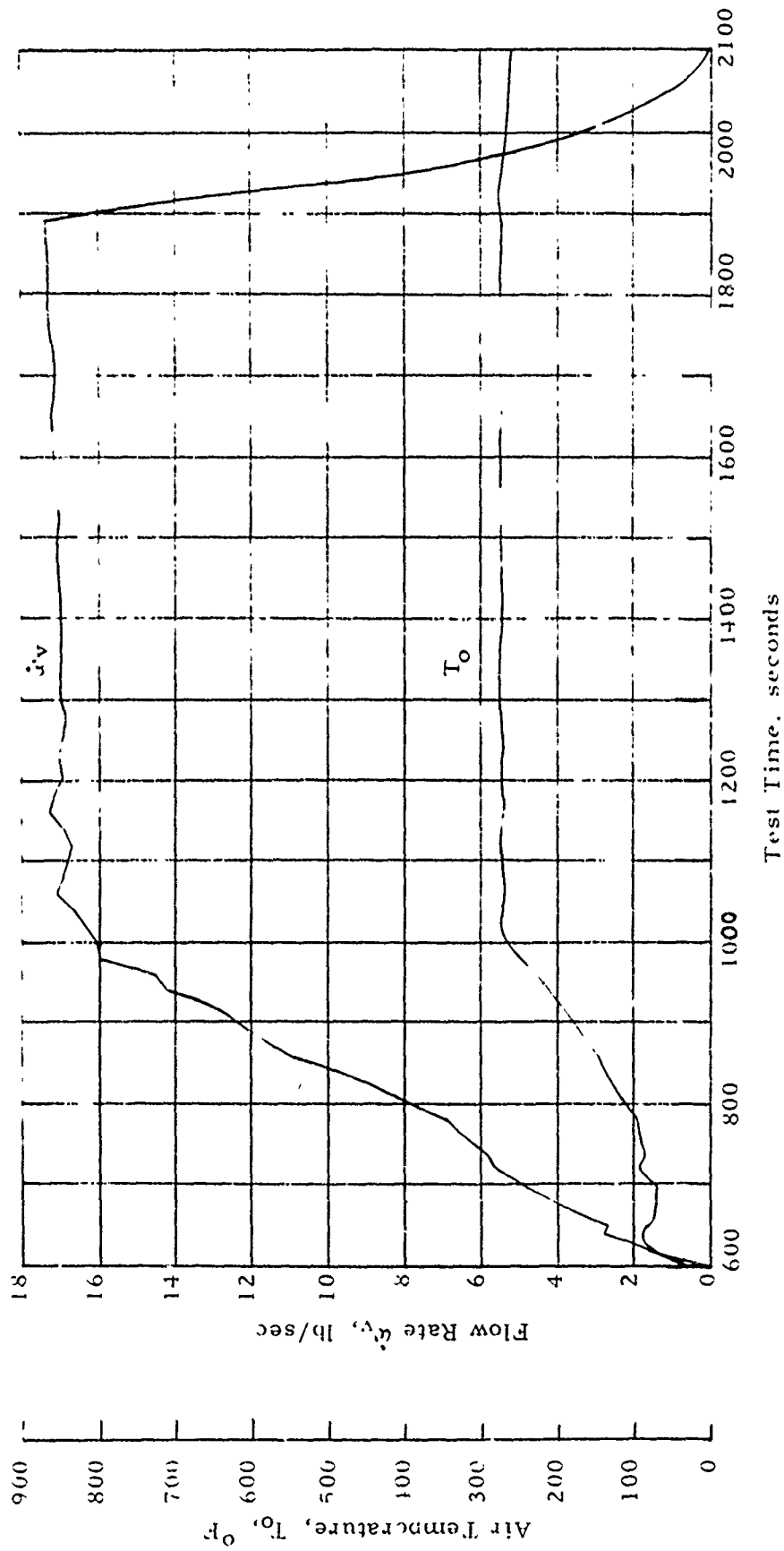


Figure 54A. Typical Test Conditions for HSMH Test Mission

would keep the stresses at a lower level than predicted. In the predictions, the liner was assumed to have the same modulus as the propellant, an obvious overprediction. Further, the calculations were based on plane strain--an assumption which would cause some overprediction of stresses. These aspects have been considered in the IM testing and analysis and the results are discussed in the subsequent sections.

## Instrumented Motor Testing

### Gage Checkout Testing

#### Gage Completion and Identification

Prior to aeroheat testing of the instrumented motors, they underwent a specialized temperature cycle to check out the behavior of the gages and establish appropriate data acquisition and reduction procedures. Before any of this could begin, it was necessary to complete considerable electronic circuitry and cabling work in order to tie the motors into the SEC data acquisition system. Since the circuitry contained in the gages represent only half of a Wheatstone bridge as shown on Figure 55, a circuit must be constructed external to the gage --- preferably near the data acquisition system --- to complete this bridge. For this program, a printed circuit (pc) board was designed capable of accommodating twelve gages. This allowed all the gages in a motor (10 maximum) to be handled on one pc board with two spare circuits available in case we might later want to add additional clip gages. A rack mount panel box was designed and fabricated to house each pc board. The assembly is referred to as the Bridge Completion Unit (BCU). A top view of this unit is shown on Figure 56. The circuitry on the pc board is easily identifiable. The resistors used to complete the circuit are on the under side of the board with only the solder terminations visible in this view. All twelve circuits are hooked in parallel with power from a 28 volt power supply fed to the terminal strip visible on the left side of the photograph. The 8-pin connectors visible at the top of the photograph accommodate the standard test facility cabling from the test bay to the control room by which the gages are connected to the BCU. The cables exiting the box in three locations tie the BCU into the SEC data acquisition system. These units are portable and easily transported with the motors. Readouts can then be made across the pins of the output cables with a digital voltmeter.

These units were used to hook up the gages following the clip gage installation to get the first check of the embedded gage readouts since casting. All normal gages with the exception of S/N 44 seemed to function as expected. It was found that the wiring diagram for the bridge circuits on the normal gages provided by Dr. Leeming was reversed in terms of gage polarity. That means an increasing positive voltage signifies tensile loads rather than the customary compressive loads.

A code was developed for use in identifying the particular gage with respect to type, location (that is, which motor; 1, 2, or 3), and a factory serial number. For example, C1-12 is the identifying code for a clip gage installed in IM #1. The factory serial number of this gage is 12. Similarly, the prefix N refers to Normal gages, S refers to the shear gages, and T refers to thermocouple. This code is used in all subsequent discussions

Shaded Area Represents that  
 Portion of the Circuit Housed  
 Within the Transducer

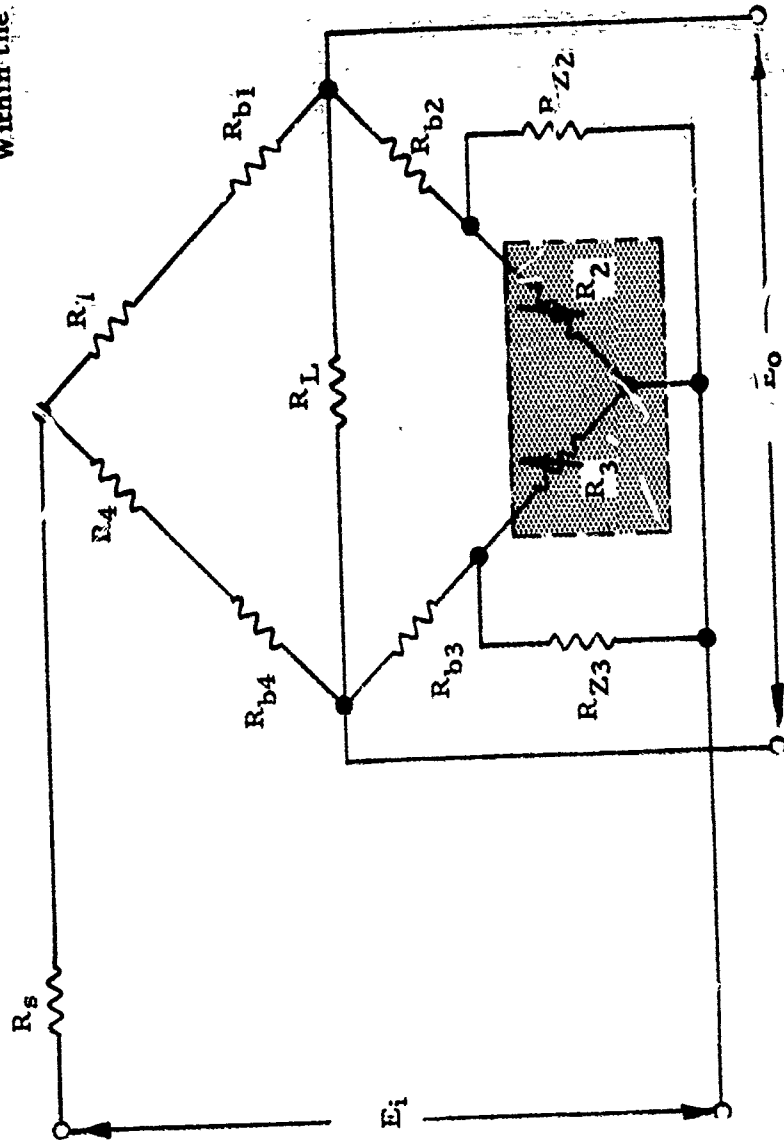


Figure 55. Stress Transducer Schematic

Shaded Area Represents that  
 Portion of the Circuit Housed  
 Within the Transducer

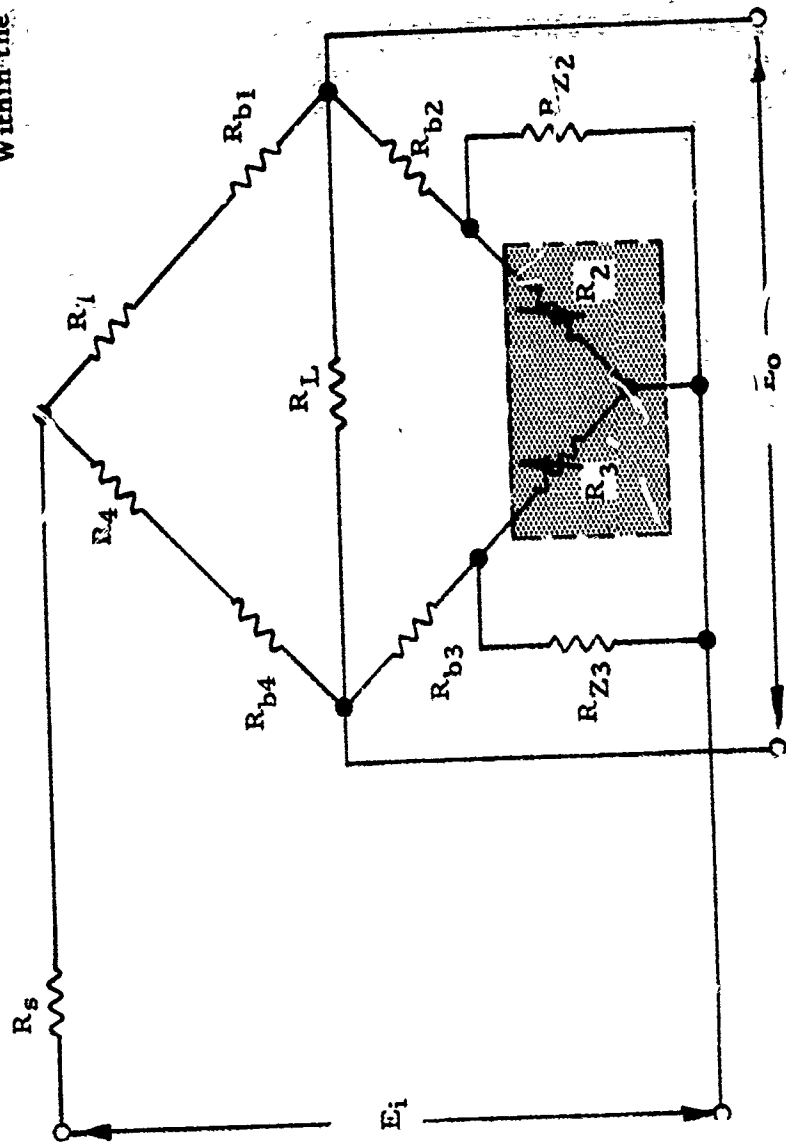


Figure 55. Stress Transducer Schematic

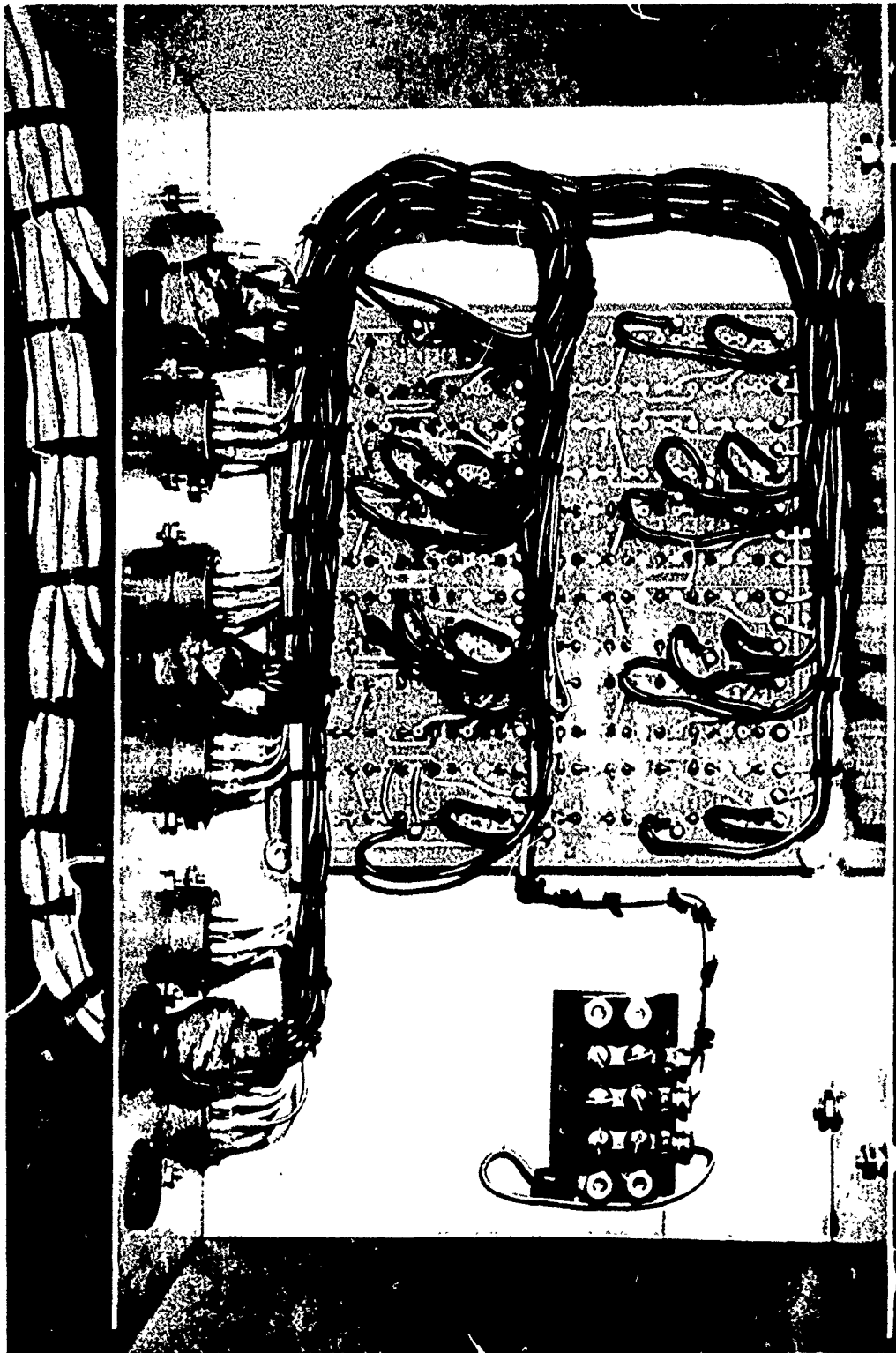


Figure 56. Bridge Completion Unit

concerning the different gages. The locations of these gages and thermocouples in terms of head end, center or aft end of each motor are summarized in Table 8. The exact locations were shown on Figures 30, 31, and 32. The thermocouples carrying the same numbers as the gage means that thermocouple was installed next to that gage. For example TI-50 refers to the thermocouple next to gage N1-50. The thermocouple number 1-6 refers to those in the thermocouple slab. As shown, a considerable number of these thermocouples including all in the thermocouple slab installed in IM #1 were found to be open after core removal. The copper and constantan thermocouple wire used was 0.005-inch diameter. On a few couples which were separable the breaks were found outside the motor and always in the copper wire. Upon closer examination the copper wire was seen to be quite brittle and would break when kinked --- a condition not normally found with this wire. This problem can be alleviated in the future by the use of chromel-alumel thermocouples which will provide considerably more strength.

### Data Reduction Procedures

Reduction of digital data into stresses and strains was accomplished in two steps. First the digital data in terms of digital counts were processed through the computer and converted into millivolts for the gages and temperature in degrees F. for the thermocouples. These data in this format were printed out by the computer and also recorded on magnetic tape. A computer code was written which utilized this data tape as input and converted the millivolt values into stress in psi or strain into percent. Output of this program included printed tabulations with printer plots, punched cards for machine plots, and magnetic tape for high density storage.

The basis for reducing the stress gage data was based on the principles given in the Gage User's Manual.

As shown in the Gage User's Manual<sup>1</sup>, if the output of a gage embedded in a viscoelastic material (propellant) is considered, then the general equation relating the gage output and the stress is as follows:

$$\sigma = \int_0^t \frac{\phi(\zeta - \zeta')}{b_T} \frac{dS(\tau)}{d\tau} d\tau$$

where:

$b_T$  = Vertical shift factor for gage

$\phi(t)$  = Inverse gage sensitivity (psi/mv)

$S(t)$  = Gage Output as function of time

$\zeta$  = Reduced time =  $\int_0^t \frac{dt'}{a_T}$

<sup>1</sup>LPC Gage User's Manual AFRPL-TR-71-131.

TABLE 8

## SUMMARY OF INSTRUMENTS INSTALLED IN MOTORS

Motor	Location		
	Head End	Center	Aft End
IM #1	N1-50	N1-40	N1-41
	T1-50	T1-50	S1-107
	S1-109	N1-49	T1-107
	T1-109	C1-13	C1-14
	C1-12	C1-13	C1-14
	T1-12		
IM #2	N2-42	N2-48	N2-46
	S2-105	T2-48	T2-46
	T2-105	N2-51	S2-111
	S2-110	T2-51	C2-17
	C2-15	C2-16*	T2-17
	T2-15	T2-16*	
		T2-1	
		T2-2	
		T2-3	
		T2-4	
		T2-5	
IM #3	N3-44	N3-43	N3-45
	T3-44	T3-43	T3-108
	S3-104	N3-47	C3-20
	T3-104	T3-47	T3-20
	C3-18	C3-19*	
	T3-18	T3-19*	
		T3-1	
		T3-2	
		T3-3	
		T3-4	
		T3-5	
		T3-6	

Approximately 5.7 inches aft of center

This equation must be used if the elastic gage response is found to change significantly with temperature, i.e. if the shape of the calibration curves is temperature dependent.

In many cases, the "potted" normal gage is compensated such that the sensitivity is essentially constant with temperature. In this case,  $\frac{1}{b_T}$  becomes a constant,  $K_2$ , and the above equation reduces to:

$$\sigma = K_1 K_2 \int_0^t \frac{dS(\tau)}{d\tau} d\tau = K_1 K_2 [S(t) - S(0)]$$

This simple equation is the one used for normal gage data interpretation with the provision that the  $S(t)$  and  $S(0)$  are the changes in gage output reading from the zero load gage readings at that temperature, as defined below:

$$S(t) = S'(t) - S'(t)_{\text{zero load}} \quad T = \text{const}$$

$$S(0) = S'(0) - S'(0)_{\text{zero load}} \quad T = \text{const}$$

where  $S'$  is the uncorrected gage output as in a function of time in the loaded motor. These may be graphically illustrated as shown on Figure 57. For the normal gage in this program, the value of  $S(0)$  was selected as gage output measured at a temperature of 170°F during the gage checkout tests. All subsequent data was referenced to this point in both time and temperature.

This simple equation is the one used for normal gage data interpretation with the provision that the  $S(t)$  and  $S(o)$  are the changes in gage output reading from the zero load gage readings at that temperature, as defined below:

$$S(t) = \left[ S'(t) - S'(t)_{\text{zero load}} \right]_{T = \text{const}}$$

$$S(o) = \left[ S'(o) - S'(o)_{\text{zero load}} \right]_{T = \text{const}}$$

where  $S'$  is the uncorrected gage output as a function of time. These may be graphically illustrated as:

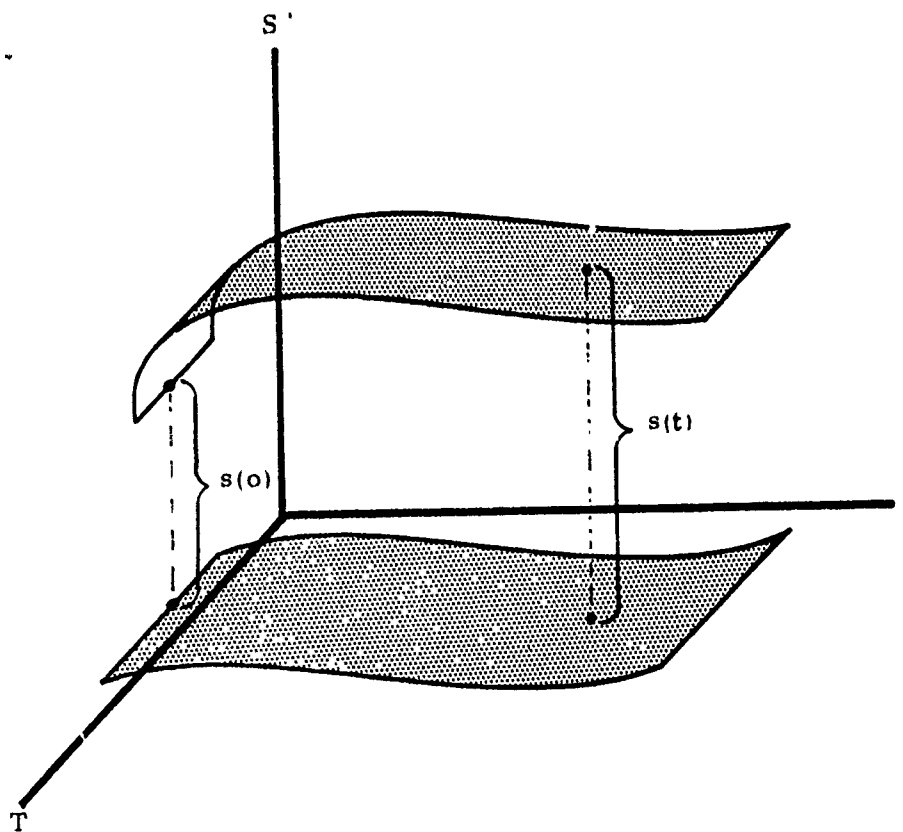


Figure 57. Relationship Between  $S(t)$  and  $S(o)$  for Data Reduction

## Temperature Cycling

The checkout of the gages installed in each of the three IM motors was accomplished by subjecting all three motors simultaneously to slow step-wise temperature changes between the extremes in temperature anticipated during subsequent testing. The motors setting in the conditioning box with all electronic cabling hooked up are shown on Figure 58 just prior to temperature cycling. The purpose of these tests was, of course, to determine if each gage was functioning properly by considering changes in the level of the output as temperature is changed and repeatability as the temperature was cycled. The temperature steps and time at which the motors were exposed to that temperature are summarized in Table 9. The response of the gages in terms of millivolt output as a function of local gage temperature are presented on a series of graphs compiled in Appendix A.

In discussing the results of the gage checkout tests, the gages have been grouped according to type as opposed to motor location. The clip gages are discussed first. In general, the response of the clip gages have been satisfactory. Two gages, C2-16 and C3-19, appear to have undergone some change during testing that resulted in huge shifts in output. Both of these gages were located in the high strain region near the aft end of the smaller bore of the two CP motors.

The normal gages responded relatively well over the temperature range except N2-48 which did not have a reasonable degree of repeatability. Since this gage was calibrated at 300°F, the problem could have originated there. It is obvious from inspection of these data that repeatability was difficult to define, inasmuch as there seems to be considerable hysteresis effects. These effects were not unanticipated; and, it is now quite evident that the reading of a gage at any particular temperature is a very strong function of the rate of temperature change that had occurred in reaching this temperature. The large offsets in normal gage output at 170°F was not believed to be realistic but probably due to some type of zero shift. This was the reason for defining the term S(o) at that condition.

The shear gages were for the most part questionable. Gage S1-109 appeared to be bad with the output wandering between -100 and -200 millivolts. The other gage S1-107 in IM #1 appeared to be functioning normally. All three gages in IM #2 appeared to be functioning normally. The only shear gage, S3-104, in IM #3 did not appear to be measuring much of a load, and thus was considered questionable at the time.

Millivolt output data of the gages, which were recorded as motor temperature was varied, were reviewed with the project officer and were used as the basis for selecting a motor to be used in aeroheat testing. Motor IM #2 was selected because all three shear gages were functioning; even

TABLE 9  
**INSTRUMENTED MOTOR TEST SUMMARY**  
**GAGE CHECKOUT TESTS\***

Test Number	Initial Temperature T <sub>L</sub> °F	Final Temperature T <sub>F</sub> °F	Time At T <sub>F</sub> Hrs	Total Time of Test Hrs
1	86	117	12	24
2	117	148	12	24
3	148	174	60	72
4	174	117	12	24
5	117	67	12	24
6	67	-5	12	24
7	-5	-44	12	24
8	-44	-67	60	72
9	-67	-83	12	24
10	-83	-40	12	24
11**	-40	0	--	24
12***	0	---	--	--
13	82	-36	9	24
14	-36	169	48	72
15	168	83	8	24

\*All three IM's tested simultaneously  
 \*\*Data Acquisition System Malfunction - no data recorded  
 \*\*\*Test Scheduled, but Canceled

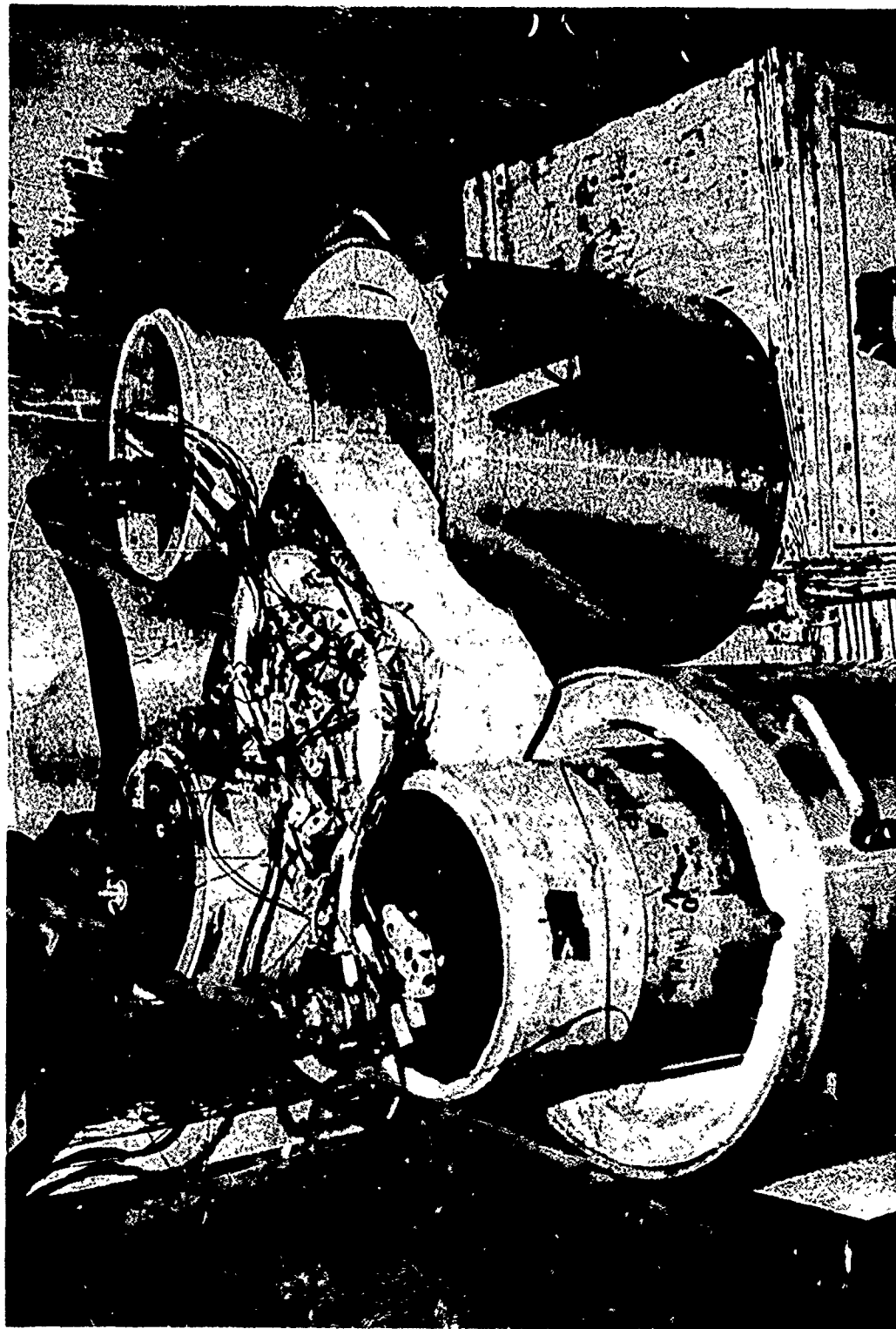


Figure 58. Motor Ready for Gage Checkout Testing

though some questions existed in the interpretation of the data from gage number S2-105. This gage located in the head end of the motor, ninety degrees from S2-110, showed a much greater sensitivity to motor temperature change than S2-110. However, both gages showed the same trends and when the output of S2-105 was attenuated by a factor of three, a reasonable comparison existed.

Inasmuch as IM #2 was selected for aeroheat testing, the millivolt data was reduced into stresses and strains and compared with theory. The normal stress variation with temperature measured by gage N2-51 is shown on Figure 59. A linear elastic axisymmetric analysis was performed modeling the whole propellant grain at 180°F, 75°F, 0°F, and -75°F which are also shown on Figure 59 for comparison. Note that the general tendency of the gage output and analysis results respond in the same manner. However, in an elastic analysis the solution is very dependent upon the selection of relaxation time for calculating the propellant modulus from the relaxation modulus curve. Based upon this fact, a comparative study was performed at different relaxation times to determine the normal stress response as a function of temperature. As shown on Figure 60, the relaxation time has a substantial effect at low temperature. The high stress at low temperature seems to be a realistic response for this motor.

The time history of the stress levels measured by gage N2-51 during the overall period of these tests is shown along with the corresponding temperature on Figure 61. As a matter of interest, two stress levels are shown--- one referred to as bench and the other as motor. The difference in these are based on whether the post gage installation calibration data are used or not. The motor calibration is based on the post installation zero load data shown on Table 3 and the data reduction equation discussed previously and illustrated on Figure 57. The bench calibration assumes use of the factory gage zero readings which basically set the value of  $S(o)$  equal to zero. The difference, as expected, is considerable at low temperature.

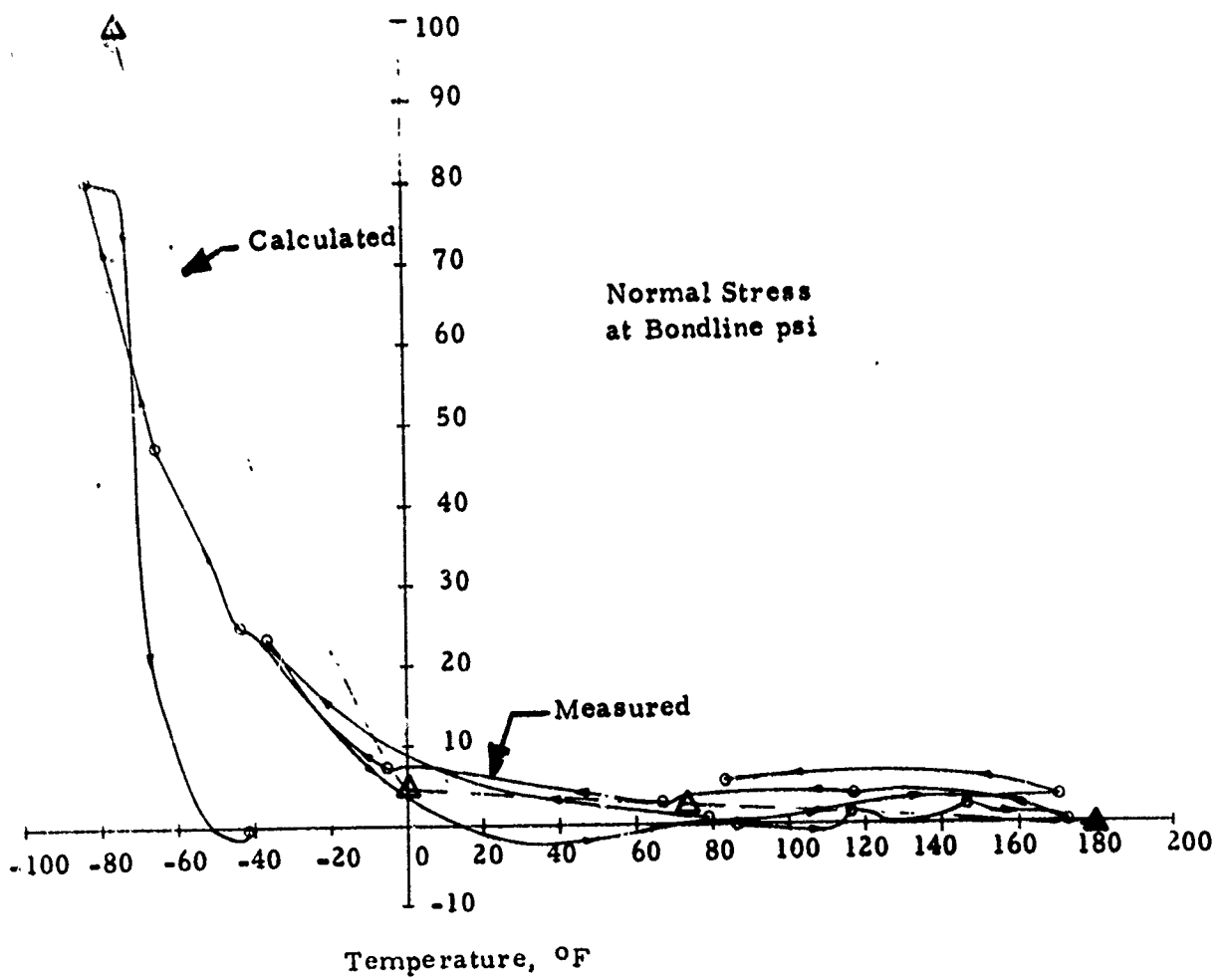


Figure 59. Normal Stress in IM #2 as Measured by Gage N2-51

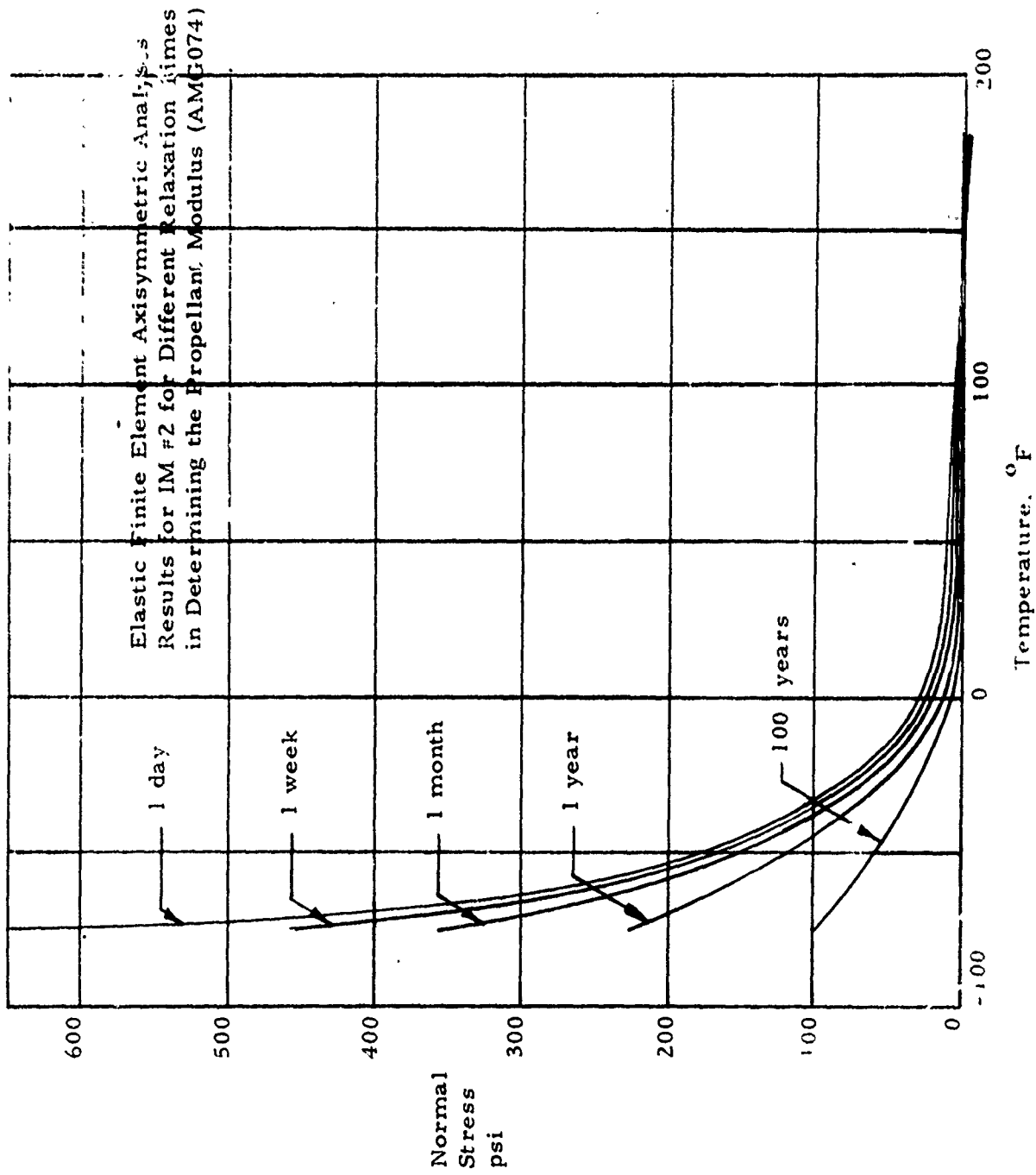


Figure 60. Normal Stress Elastic Analysis results

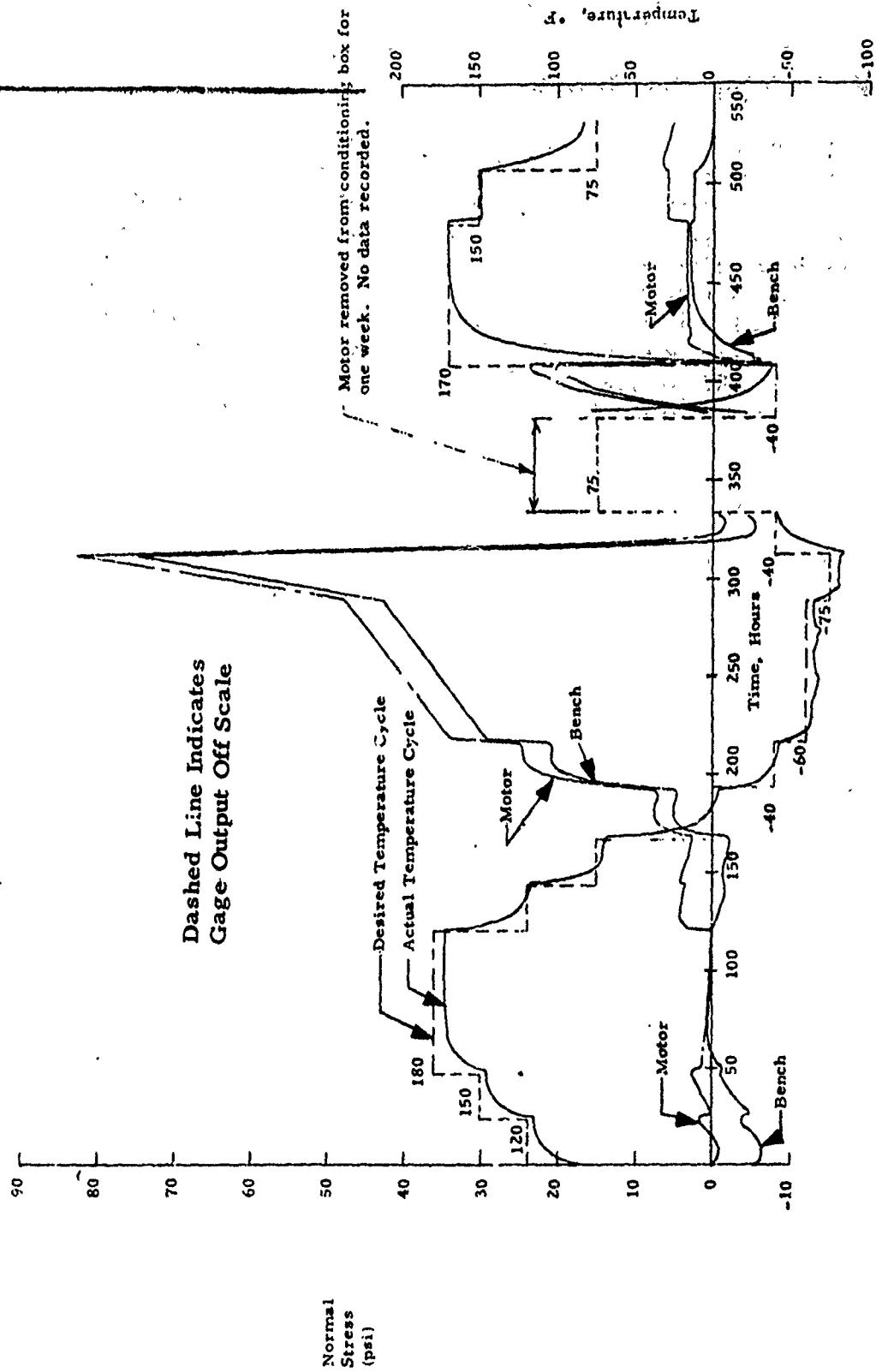


Figure 61. Measured Normal Stress Results for Motor and Bench Calibration of Gage N2-51

## Instrumented Motor Aeroheat Testing

Fifty aeroheat tests were conducted on instrumented motors as illustrated in Table 10. As shown, all three motors were subjected to aeroheat testing, a deviation from the original program plan brought on by an unbond failure in IM #2 in the early phases of its testing. Because of this failure, IM #3 was tested in order to fully obtain the structural response of the CP configuration to the aeroheat loads. Since, however, this did not leave a CP motor without a test history to evaluate the aeroheat simulation tests, it was decided to also aeroheat IM #1 to determine the structural response of that configuration. This then would allow direct comparison of the structural response between the aeroheat tests and the equilibrium temperature cycle simulation tests on a single motor.

### IM #2 Aeroheat Test Results

Aeroheat testing of IM #2 consisted of a total of 21 aeroheat tests being conducted as illustrated in Table 10. The first six tests were conducted to provide baseline motor response data for the three aeroheat temperature-time schedules representative of light, moderate, and severe aeroheat missions. Inasmuch as failure had not been induced by a cycle as severe as the TS series in the UM aeroheat testing, it was felt that these six tests could be conducted without fear of a motor failure. This conclusion was based on the fact that the SFPI mission on the CP configuration would not be as severe as the TS cycle on the star configuration. Based on this UM experience, the SFPI missions were tested after the DMP-3 missions rather than having the HSMH mission between them as one would expect. The reason for doing this was based primarily on logistics to minimize the facility changeouts necessary to accommodate the higher flow rate HSMH mission.

Upon completion of these initial six tests, the HSMH tests were continued (Tests 7-9) to investigate the effect of changing the initial motor temperature on the stress level induced by aeroheating at this moderate level. At a motor temperature of 140°F, the initial portion of the aeroheat mission actually aerocools the motor which tends to nullify the stress buildup during the later heating phase. Thus, very little stress increase is found for this condition. The next two tests (Tests 10-11) centered on the SFPI mission to determine the effect of initial motor temperature on that cycle. The tests at -40°F and 80°F were also baseline tests to provide a comparison for tests such as Tests 13-16, which is an aerocool followed by an aeroheat cycle. The idea here was to take a motor at ambient temperature and rapidly cool it in a cold box until the skin reached a temperature of -40°F, then subject the motor to a SFPI mission. This essentially simulates a motor being exposed to wing carry at high altitude-low Mach number for a period of time followed by a dash to target. Test 17 was a repeat as was Test 12 to determine if the intermediate tests had resulted in any damage which may have effected the structural response of the motor.

TABLE 10  
INSTRUMENTED MOTOR TEST SUMMARY  
AEROHEAT TESTS

Motor	Grain Configuration	Test Number	Mission Profile	Initial Motor Temperature °F
IM #2 ↓	CP ↓	1-2 3-4 5-6 7 8 9 10 11 12 13-14 15-16 17-19 20 21	DMP-3 SFPI HSMH ↓ SFPI ↓ DMP-3 HSMH	-65 ↓ +80 +140 0 -40 +80 -65 +80 → -40* +140 → -40* -65 ↓
IM #3 ↓	CP ↓	1-3 4 5-6 7 8 9-10 11 12-16 17	DMP-3 HSMH ↓ SFPI ↓ DMP-3 SFPI DMP-3	-65 +55 -65 60 0 -40 -65 ↓
IM #1 ↓	STAR ↓	1-2 3 4 5 6 7-11 12	DMP-3 HSMH SFPI ↓ DMP-3 SFPI DMP-3	-65 ↓ 0 -40 -65 ↓

\*Thermally equilibrated to higher temperature, then rapidly cooled until skin reached lower temperature, then aeroheated.

Following Test 17, a sonic and ultrasonic inspection of the motor was made. The results of this inspection showed an area of liner-to-case unbond located near the forward end of the motor as shown on Figure 62. The areas marked as shown on this figure represent the areas of unbond. It is interesting to note that the ultrasonic inspection shows unbond extending beyond that found using sonic techniques. The relationship of the unbonded area to location of the embedded instrumentation is shown on Figure 63. The fact that the unbond area is seen to be directly under the thermocouple slab could lead to speculation that the instrumentation contributed to the failure; however, this is not felt to be the cause because the liner was in place and completely cured prior to installation of the gages.

The failure was confirmed by additional sonic inspections and X-ray inspections with the motor at  $-65^{\circ}\text{F}$ . Tests 18 and 19 were then conducted to determine if the area of unbond would grow with repeated cycling. Post test sonic and ultrasonic inspections revealed essentially no increase in the unbond area.

Following the detection of the failure, the principal effort was in determining if the time at which failure occurred could be detected by the gages. Throughout testing, a graphical history of gage output in millivolts prior to an aeroheat test and when the motor was in temperature equilibrium was maintained for gages N2-51 and N2-48 such as shown on Figures 64 and 65. The data were continuously compared to the comparable data from the gage checkout tests as each test was made. Inspection of these data show that essentially no deviation as a function of test number until Test 19 when gage N2-48 showed a huge decrease in response. (The numbers shown on Figures 64 and 65 represent the actual gage output just prior to that aeroheat test.) Even though Gage N2-48 is near the edge of the unbond area, the data from this and the N2-51 opposite from the unbond do not show sufficient deviation from initial gage data to indicate that a failure occurred. Based on these data alone, one might conclude that the failure could have occurred during gage checkout; however, X-ray inspections made of the motor following gage checkout did not indicate an unbond failure.

Since gage output under an equilibrium temperature loading does not indicate failure, it was decided to evaluate gage response during highly transient loading. These results in millivolts for gages N2-51 and N2-48 showing induced response for the SFPI mission as a function of time are shown on Figures 66 and 67. Inspection of these data shows a drastic decrease in response from Test 3 to 4 to 12 and so on. It is unfortunate that the peak data for Tests 3 and 4 were lost because of their imposed data acquisition limitations; however, it is obvious that high normal stresses were induced on Test 3 and most probably on Test 4. Therefore, Test 3 or Test 4 became the most likely time of failure.

A program technical review meeting was held at the AFRPL on 4 October 1973 and, as a result of this meeting, the following action items were delineated and agreed to by the AFRPL and Thiokol:



Figure 62. Location of the Unbend Failure on IM#2

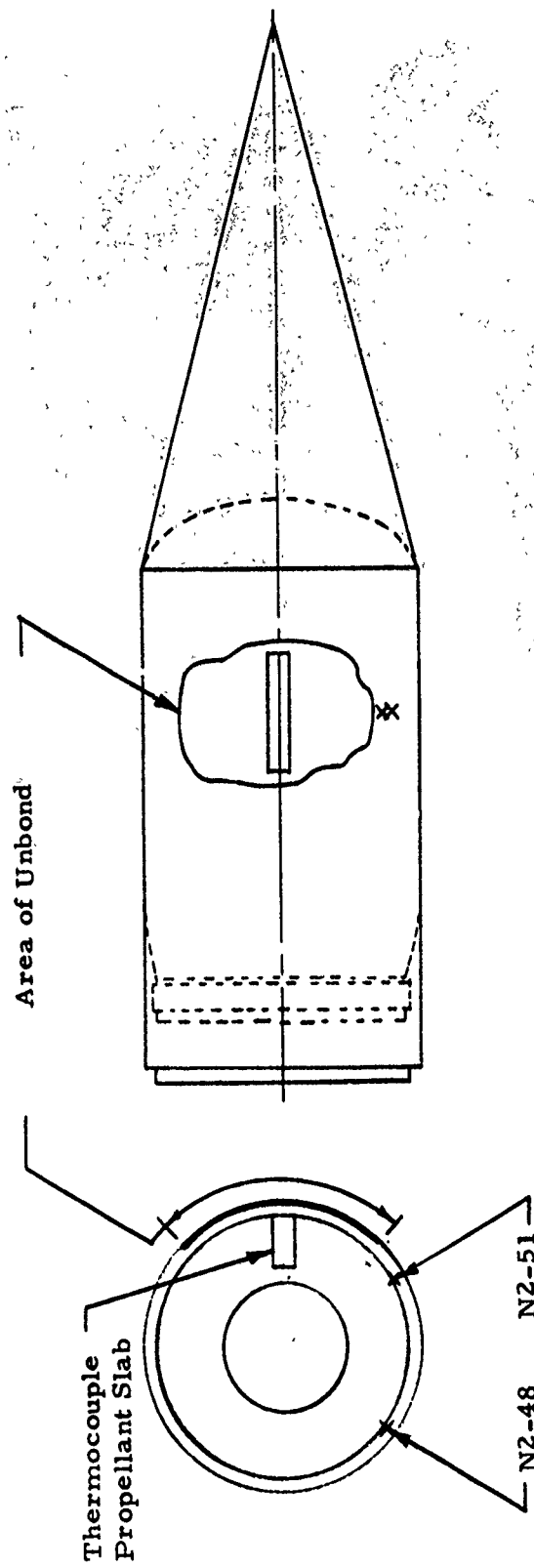


Figure 63. Schematic Showing Location of Failure

TEMPERATURE EFFECT ON MOTOR RESPONSE

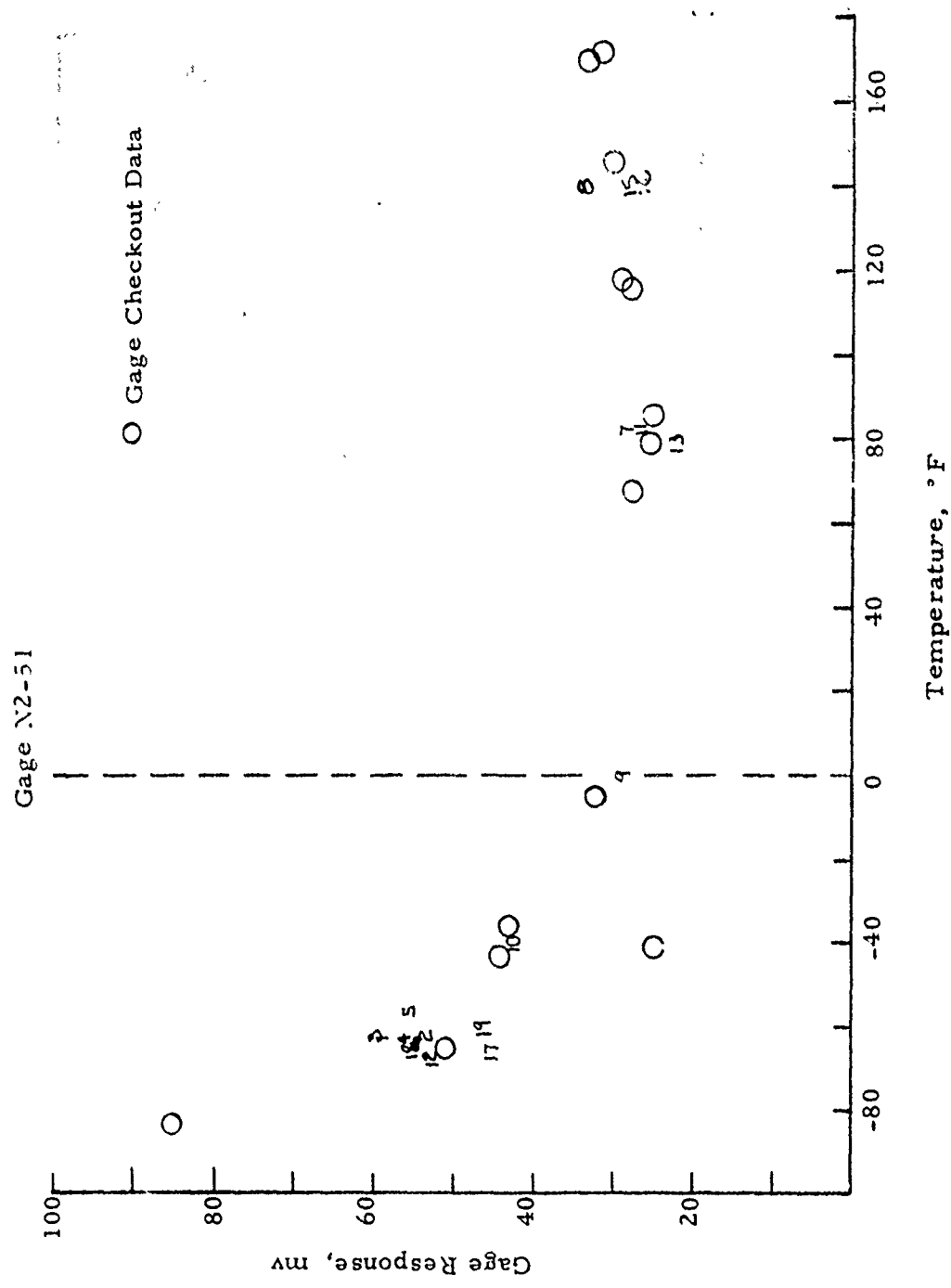


Figure 64. Gage N2-51 Output as a Function of Motor Temperature

TEMPERATURE EFFECT ON MOTOR RESPONSE

GAGE N2-48

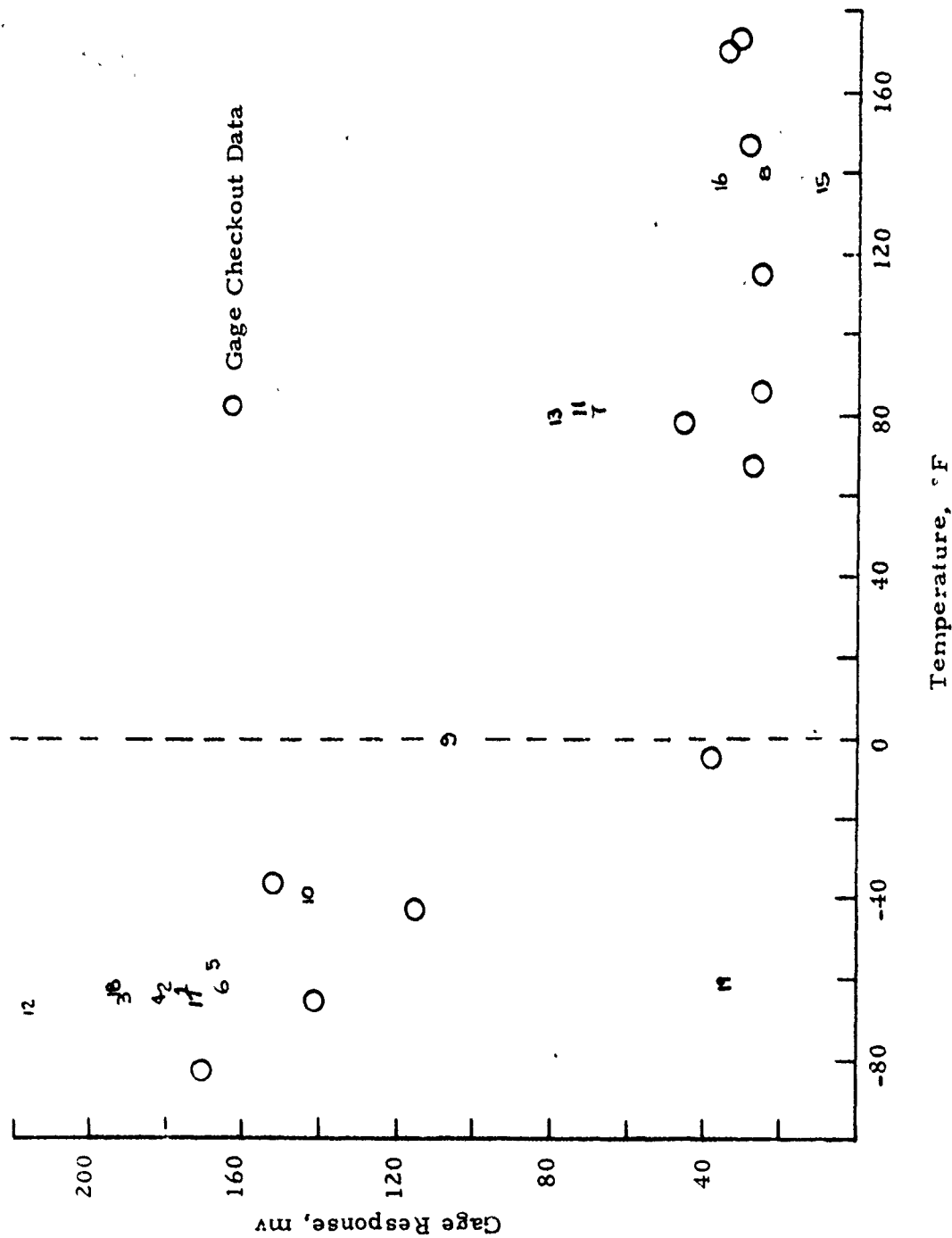


Figure 65. Gage N2-48 Output as a Function of Motor Temperature

INDUCED GAGE RESPONSE

SFPI Mission  
Gage N2-51

Numbered curves represent response for that test.

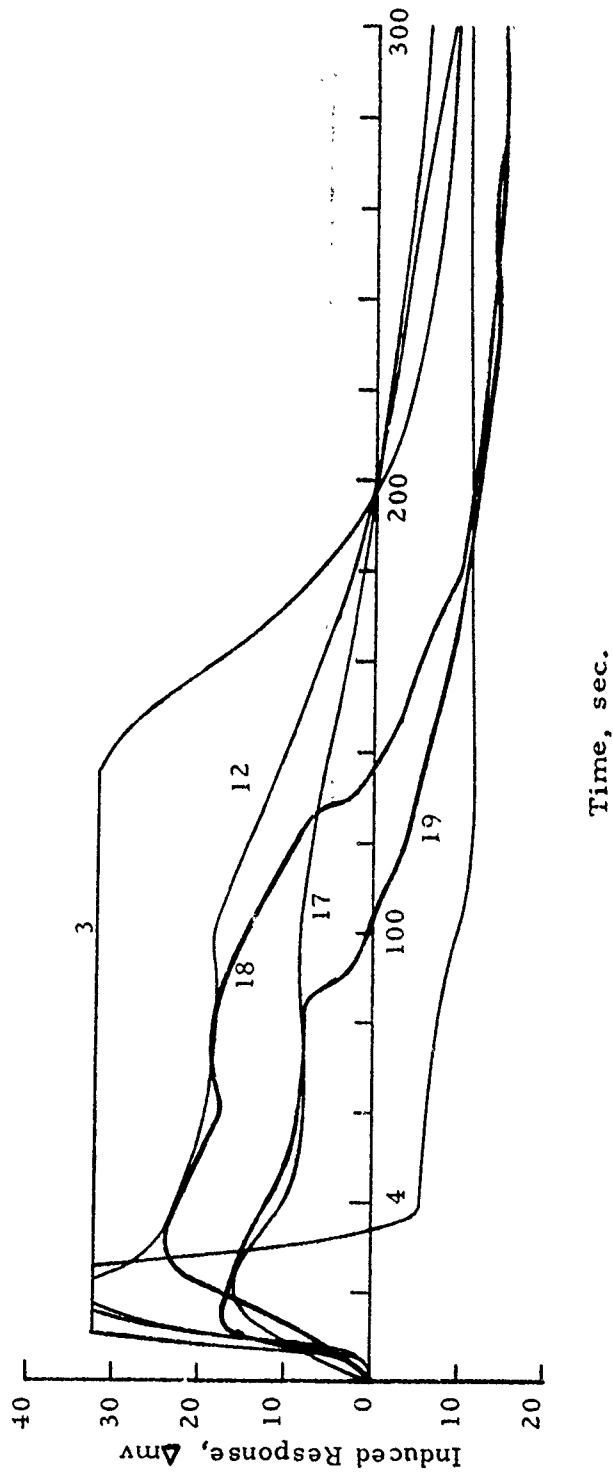


Figure 66. Gage N2-51 Response for the SFPI Tests

INDUCED GAGE RESPONSE  
SFPI Mission  
Gage N2-48

Numbered Curves Represent Response for that Test.

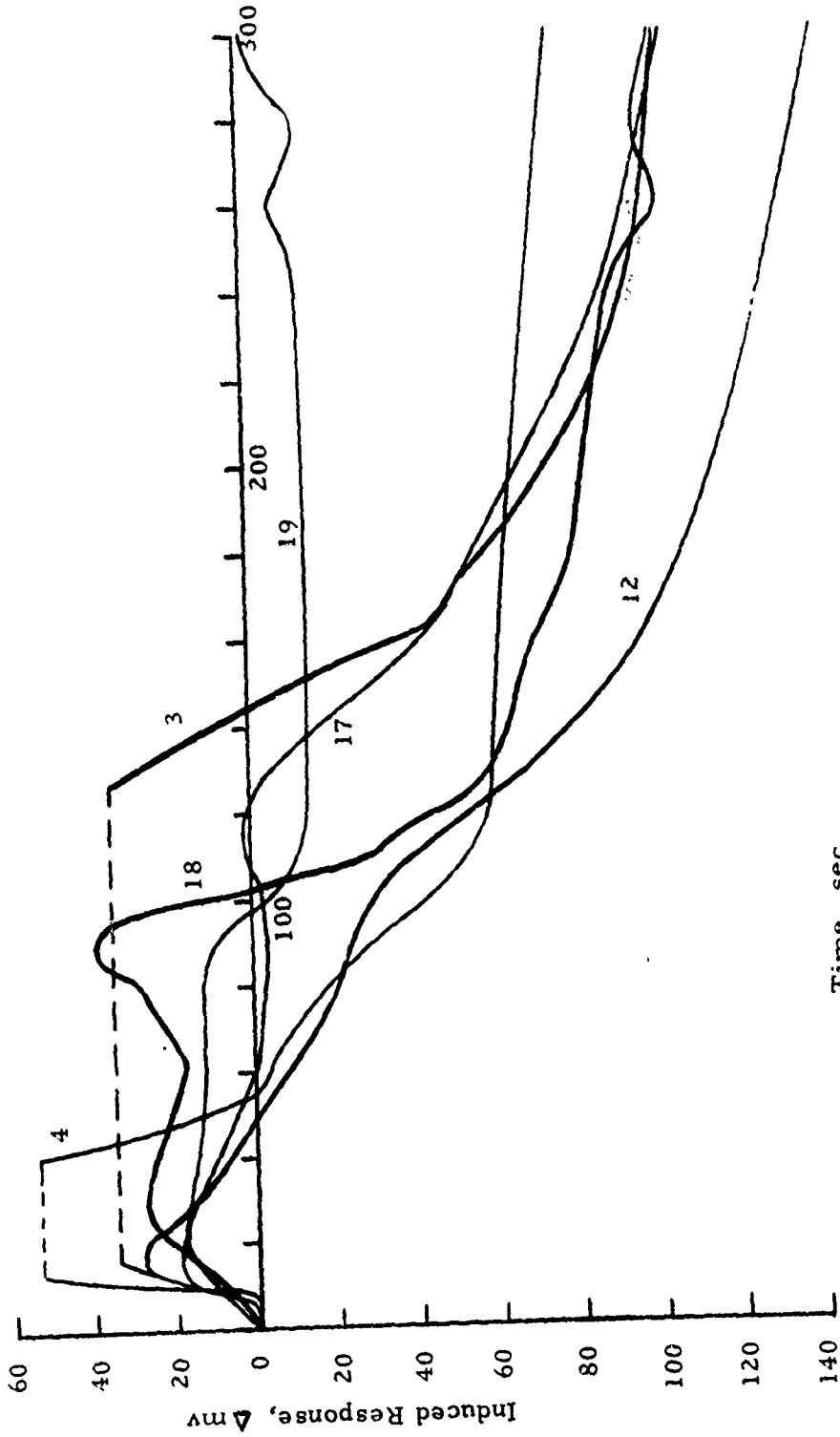


Figure 67. Gage N2-48 Response for the SFPI Tests

1. Conduct two additional aeroheat tests on IM #2 - one DMP-3 and one HSMH.
2. Dissect IM #2 by lathe (cut into 4 pieces). The sections were to be (1) head end dome, (2) 4-inch-thick segment containing unbond, (3) 4-inch-thick segment aft of unbond and (4) aft section. Section 2 was to be cut on the edges of the unbond.
3. Cut propellant from Sections 2 and 3 and manufacture "mini-samples" for uniaxial testing. The purpose was to determine if a change or gradient exists in the propellant properties in the radial direction near the bondline. This was to be done for samples made from propellant taken from under the unbond on Section 2. Similar samples were to be cut and tested from Section 3.
4. Assemble aeroheat hardware on IM #3 (a twin of IM #2) and initiate aeroheat testing with two DMP-3 missions, followed by several HSMH missions. The SFPI mission which failed UM #2 was not tested until after the data from the less severe tests were reviewed. It was assumed that approximately 10-12 tests would be conducted using IM #3.
5. Set up and run the same tests on IM #1 (Maverick grain) as conducted on IM #3.

The two tests specified in Item 1 were conducted and designated as tests 20 and 21. Test 20 was of the DMP-3 type and a duplicate of Test 2; whereas Test 21 was of the HSMH type and a duplicate of Test 5. The purpose of conducting these two additional tests was to determine if the failure did occur during the initial SFPI tests, Tests 3-4, or subsequent to the HSMH tests. The thought here was that the motor or gage response would be significantly different between tests made before and after failure for the same loading condition; therefore, the repeat of Test 2 as Test 20. Similarly, little change in gage output would be effected if any tests made after the suspected time of failure were repeated. This condition was satisfied by making Test 21 a repeat of Test 5.

The results of these two tests as compared to their appropriate counterparts are shown on Figure 68. These data offer no conclusive proof that failure occurred or did not occur on the initial SFPI tests. Certainly there are no significant difference between the two DMP-3 tests. Somewhat faster response is found on Test 2; however, this is offset by the higher output levels induced in Test 20. On the other hand, Test 21 (HSMH) shows essentially little response as compared to Test 5 and even more surprising less response than Test 20. It almost appears that the motor had reached a point

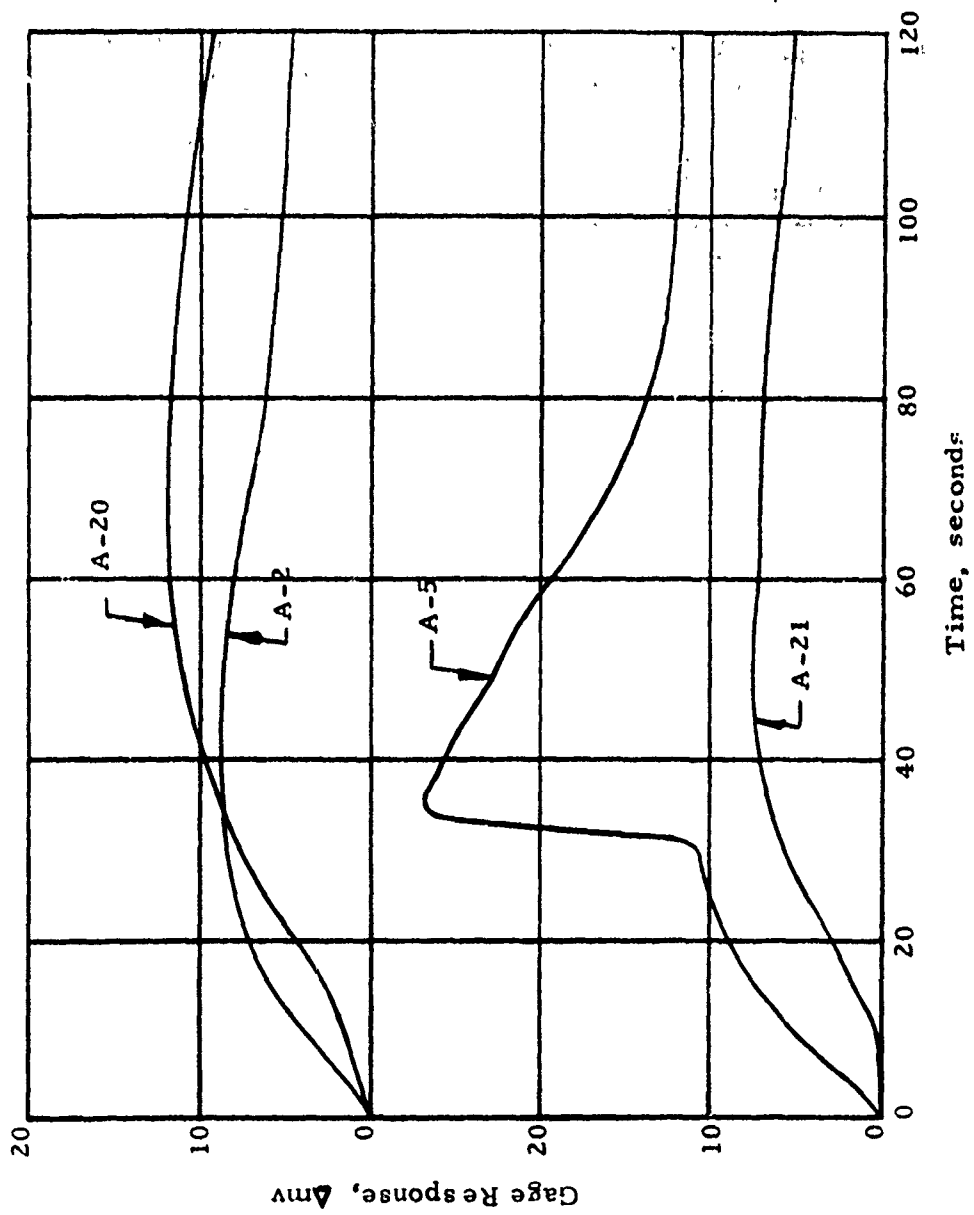


Figure 68. Comparison of Gage N2-51 Response for Tests A-2 and A-20 and Tests A-5 and A-21.

of structural degradation wherein the response had become independent of the severity of the load. That is, the more severe the load, the more relief offered by the unbond so that only a certain level of stress could be introduced in the grain.

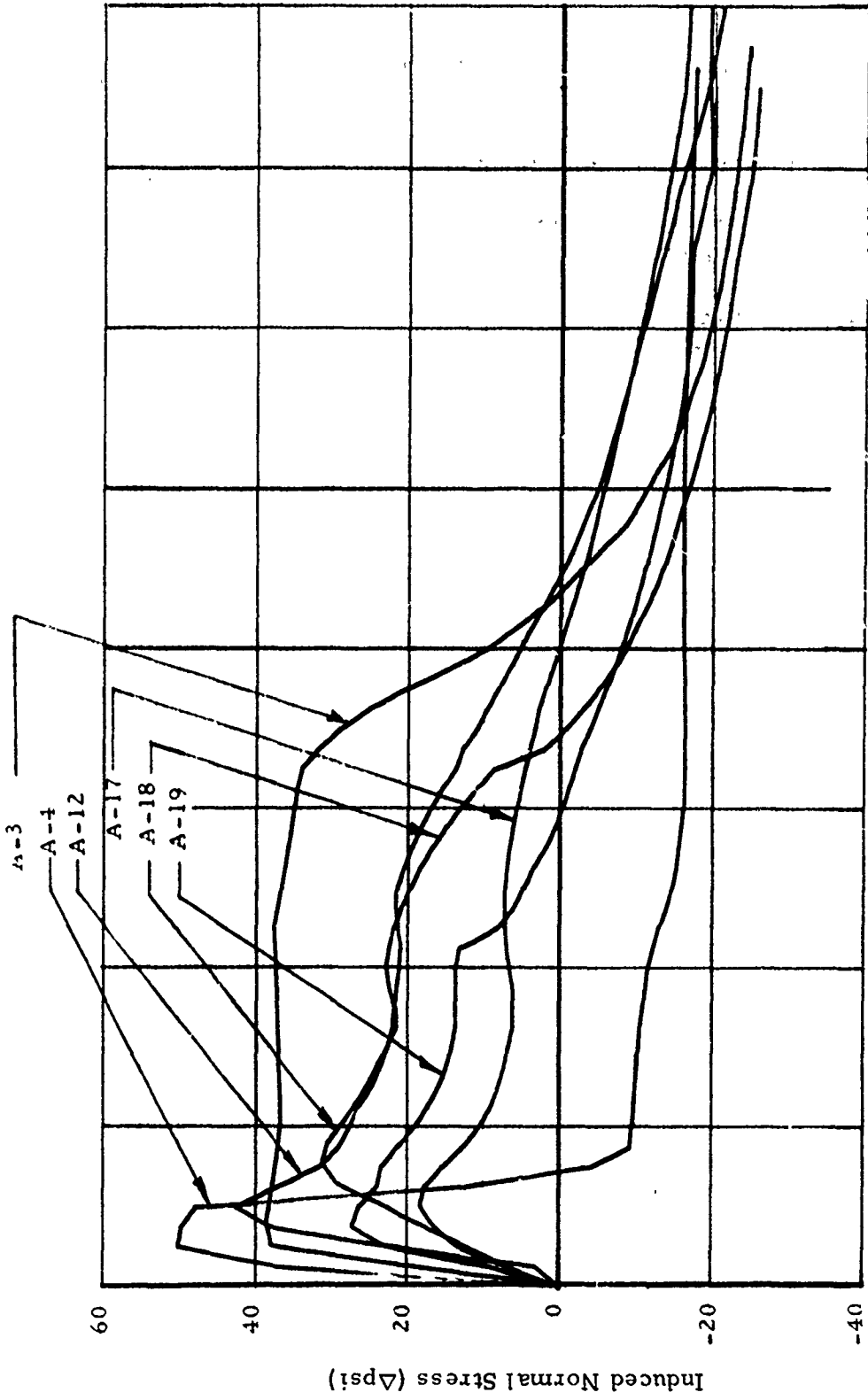
The above premise seemed more viable based on the results of further investigation into the state of the motor following these tests. These results are discussed in detail in the section entitled, Motor Dissection and Propellant Property Testing. However, they do show significant unbond over the entire aft end of the case with the grain actually being pulled forward into the case and cocked. At this point in the investigation, it certainly appeared that a massive unbond failure occurred during Test 4 and the area of unbond grew progressively during subsequent testing to its final proportions. Further, the aft shear gages indicate that a high shear stress acting forward is generated by aeroheat loading. Apparently, the act of rapidly expanding the grain and case in the middle results in a force attempting to pull the aft end of the grain forward in the case. Therefore, it became apparent that aeroheating this motor induced a very complex stress field within the propellant which was not readily amenable to theoretical reconciliation.

It became obvious that the only two methods were available for use in attempting to correlate gage response with motor condition. The first method was one in which we looked at the relationship between gage output and motor temperature when the motor was in thermal equilibrium (Figures 64 and 65). It was obvious that the failure had to be massive to effect a change in gage output. Actually it was found that the only indication of motor failure was seen by the reduced response of the motor/gage to an aeroheat load. This effect was illustrated by the data from the two normal gages located at the center of the motor (Figures 66 and 67). During the critical portion of this investigation, the comparisons were made using only the millivolt output data because of some difficulty in getting the data reduction program operational. Once it became operational, the test data for all the SFPI tests initiated from a motor temperature of  $-65^{\circ}\text{F}$  were reduced into the appropriate values of stress and strain. These data are presented for all the stress gages in terms of induced stress on Figures 69-74.

The stress measured by gage N2-51 located in the center of the motor is illustrated on Figure 69 for the various tests. On Test 3, it can be seen that gage went off-scale for a considerable period of time (10-140 seconds); consequently, the magnitude of stress that the motor actually experienced is not known. The same problem of being off-scale also exists on Test 4; however, here we see a very narrow stress peak with very rapid relaxation. Since the stress rise was much quicker, it would seem that this test was more severe than Test 3 and was probably the time that the unbond failure occurred. This conclusion was partially borne out by the fact that the measured motor response shows a decrease with each succeeding test.

Examination of results measured by the other normal gages (N2-42 located at the head end of the motor, Figure 70, and N2-46 located at the aft end of the motor, Figure 71, show similar results. This is particularly true

SFPI Mission Profile (Aeroheating) IM #2  
Normal Stress Gage #51 Located at the Center of the Motor



Time, seconds

GAC 12/7/73

Figure 69. Normal Stress Induced by the SFPI Mission as Measured by N2-51

SFPI Mission Profile (Acroheating) IM = 2

Normal Stress Gage #42 Located in the Head End of the Motor

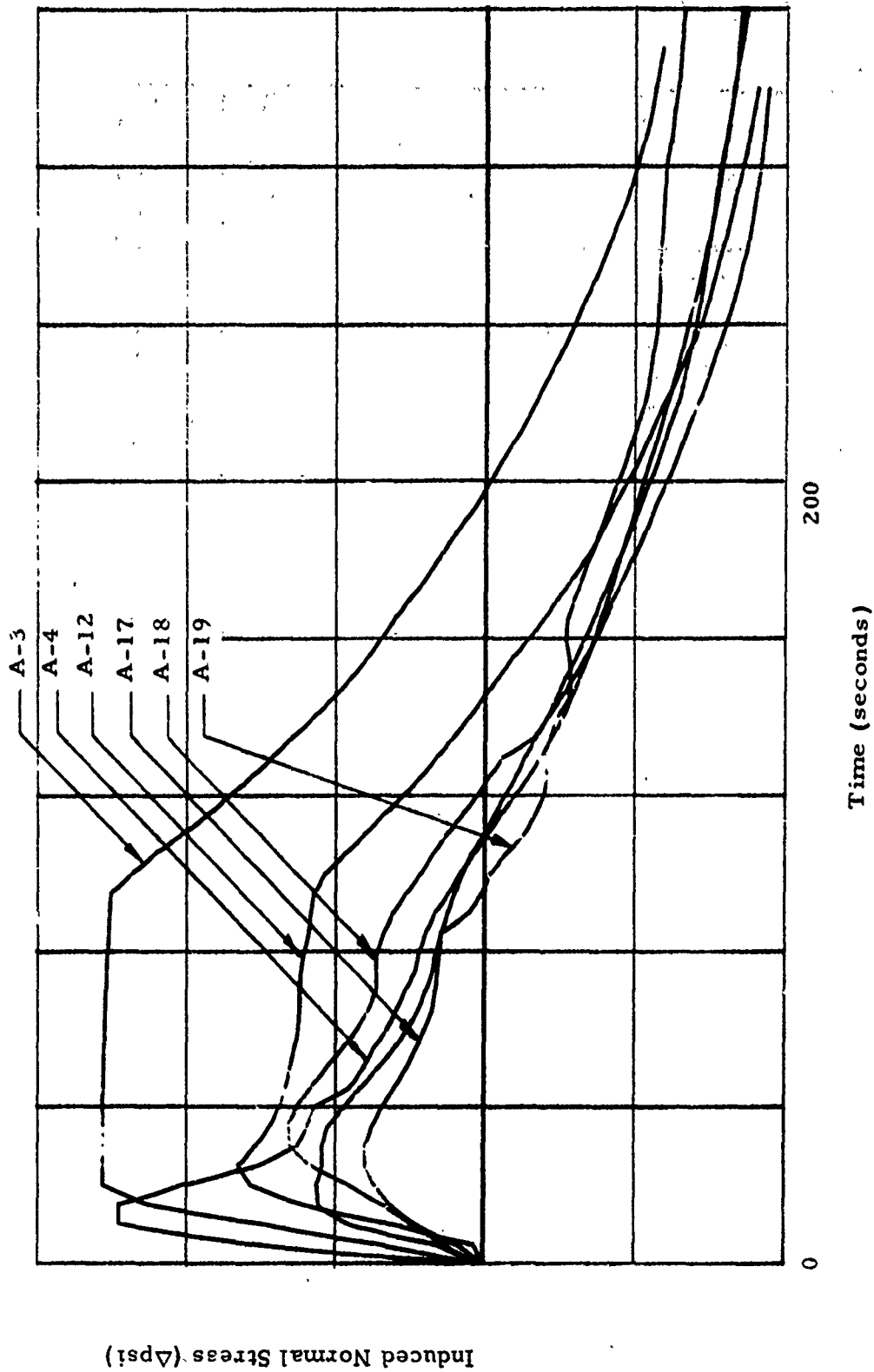
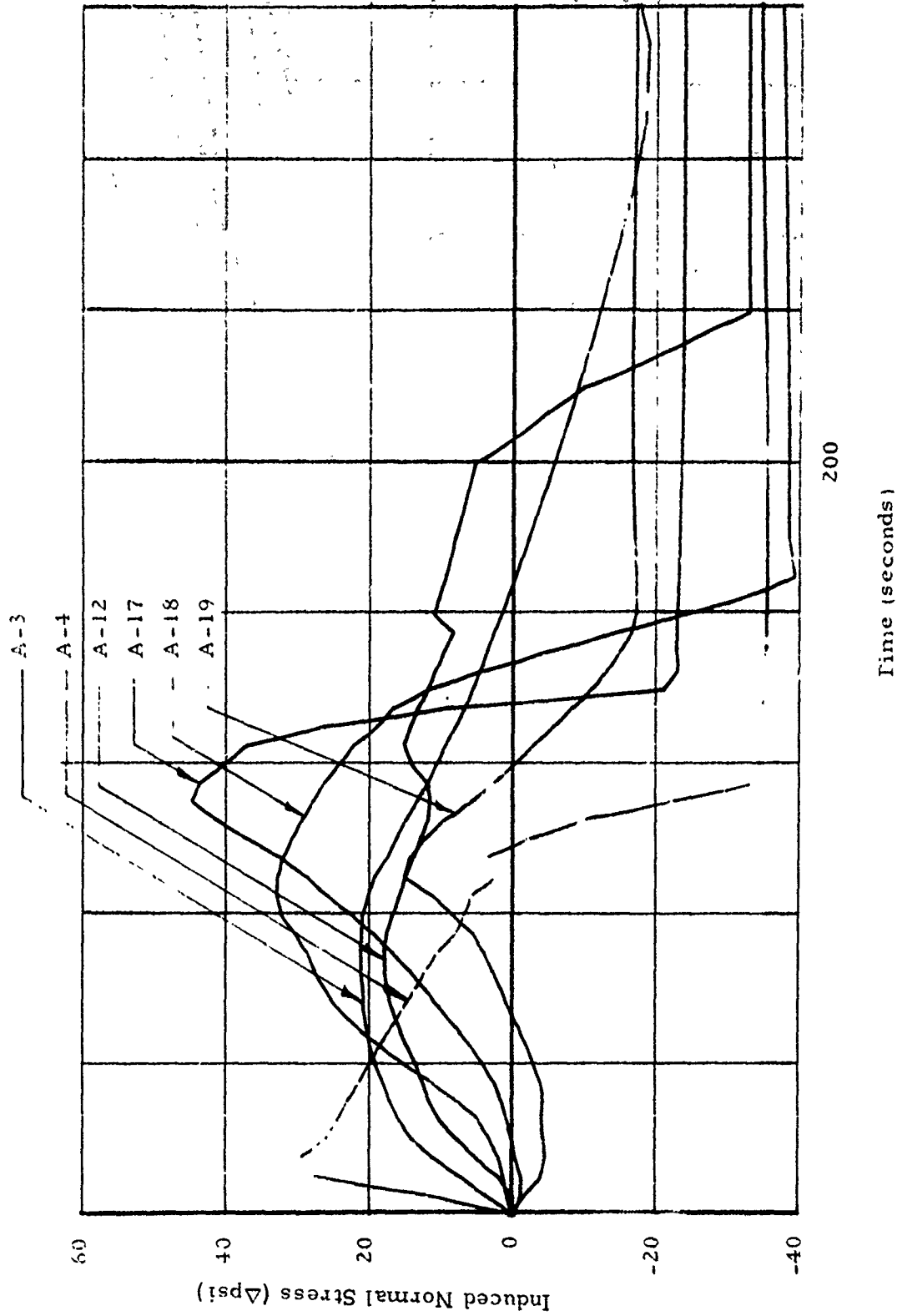


Figure 70. Normal Stress Induced by the SFPI Mission as Measured by N2-42

SFPI Mission Profile A:0 Loading - I:0 - 2  
 Normal Gage #46 Located in the Aft End of the Motor

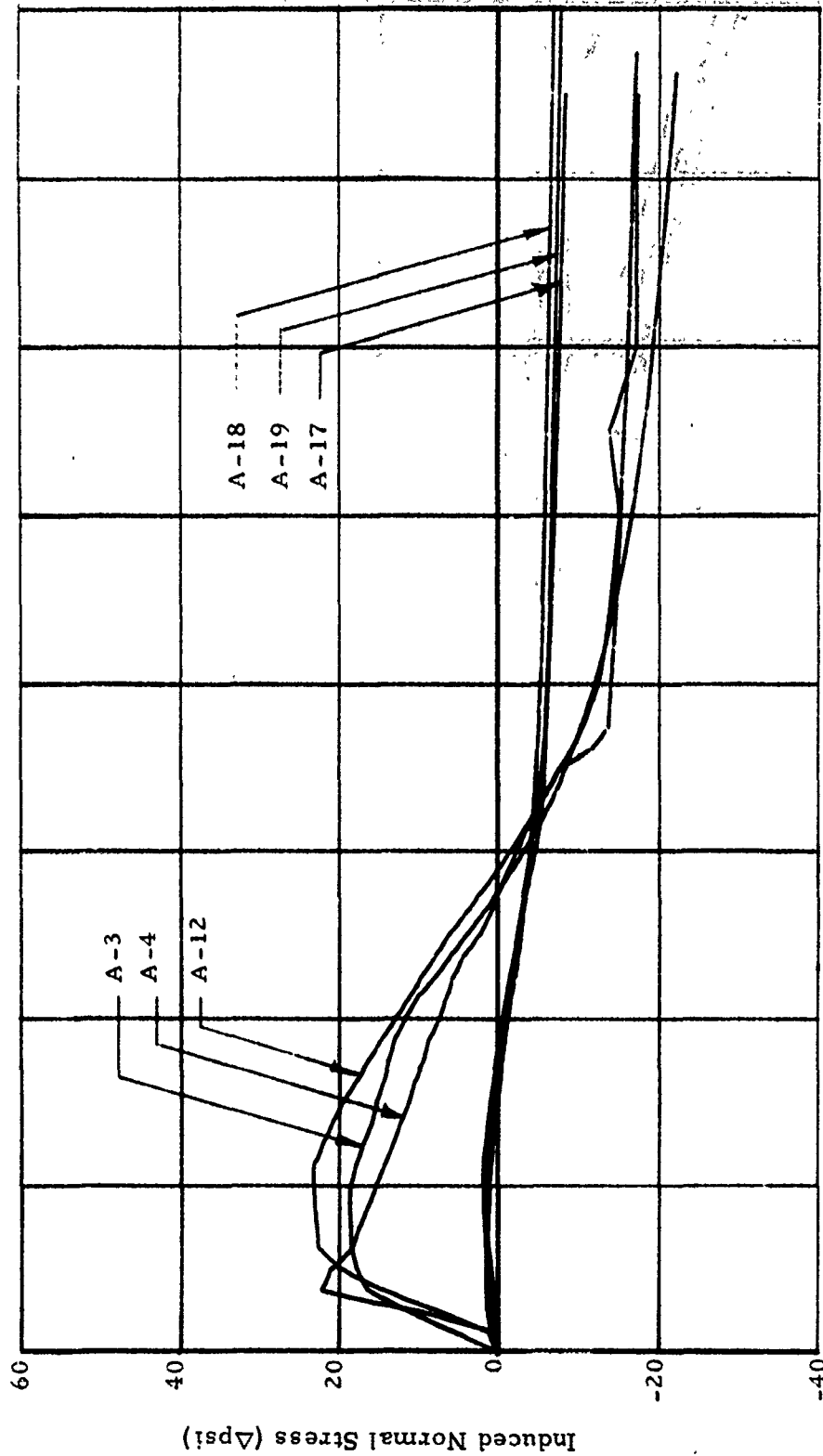


GAC 12/7/73

Figure 71. Normal Stress Induced by the SFPI Mission as Measured by N2-46

SFPI Mission Profile (Acroheating) IM #2

Shear Stress Gage #111 Located in the Aft End of the Motor



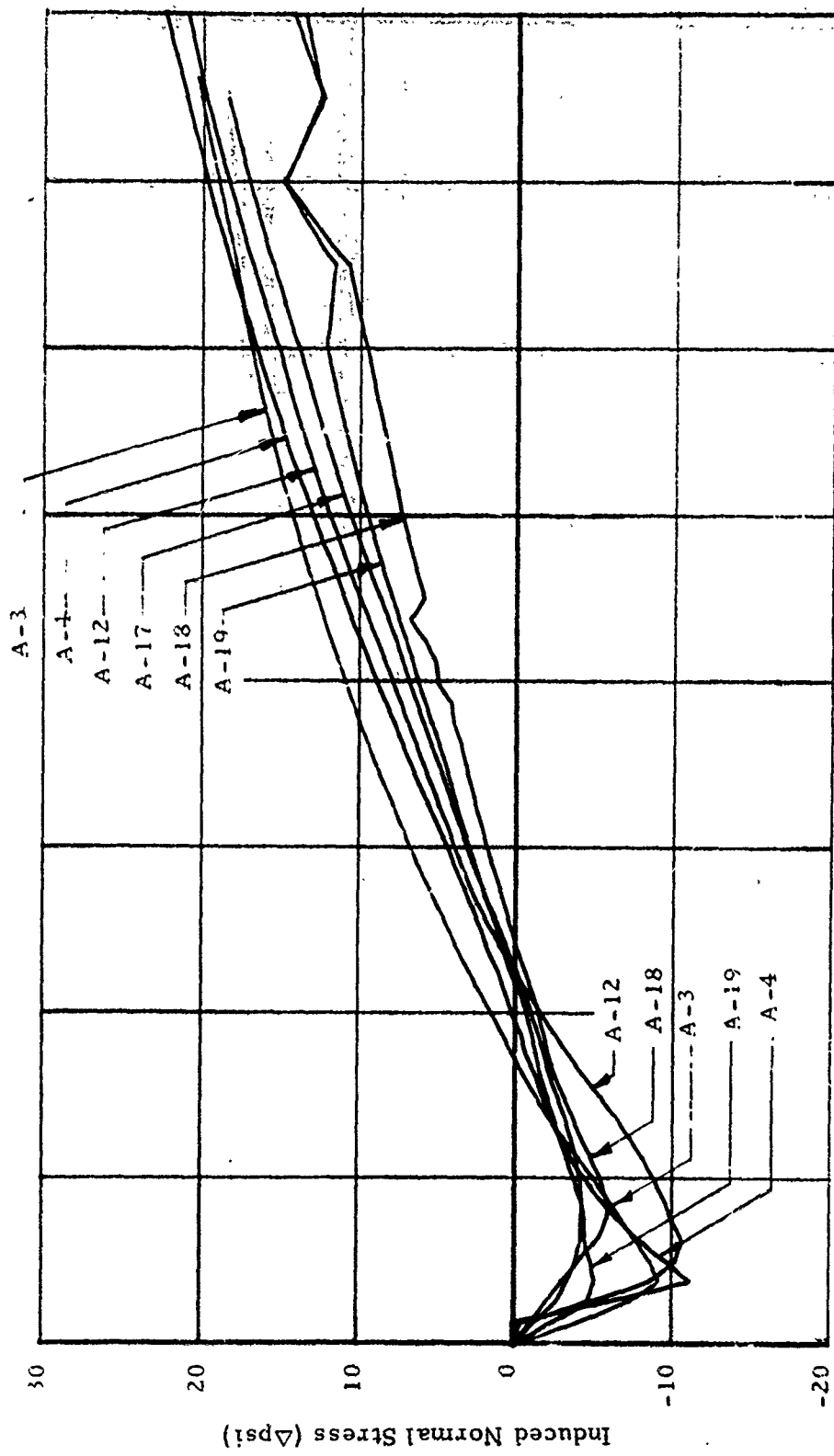
Time (seconds)

GAC 12/7/73

Figure 72. Shear Stress Induced by the SFPI Mission as Measured by S2-111

SFPI Mission Profile (Acrobleating) IM-2

Shear Stress Gage #105 Located in the Head end of the Motor

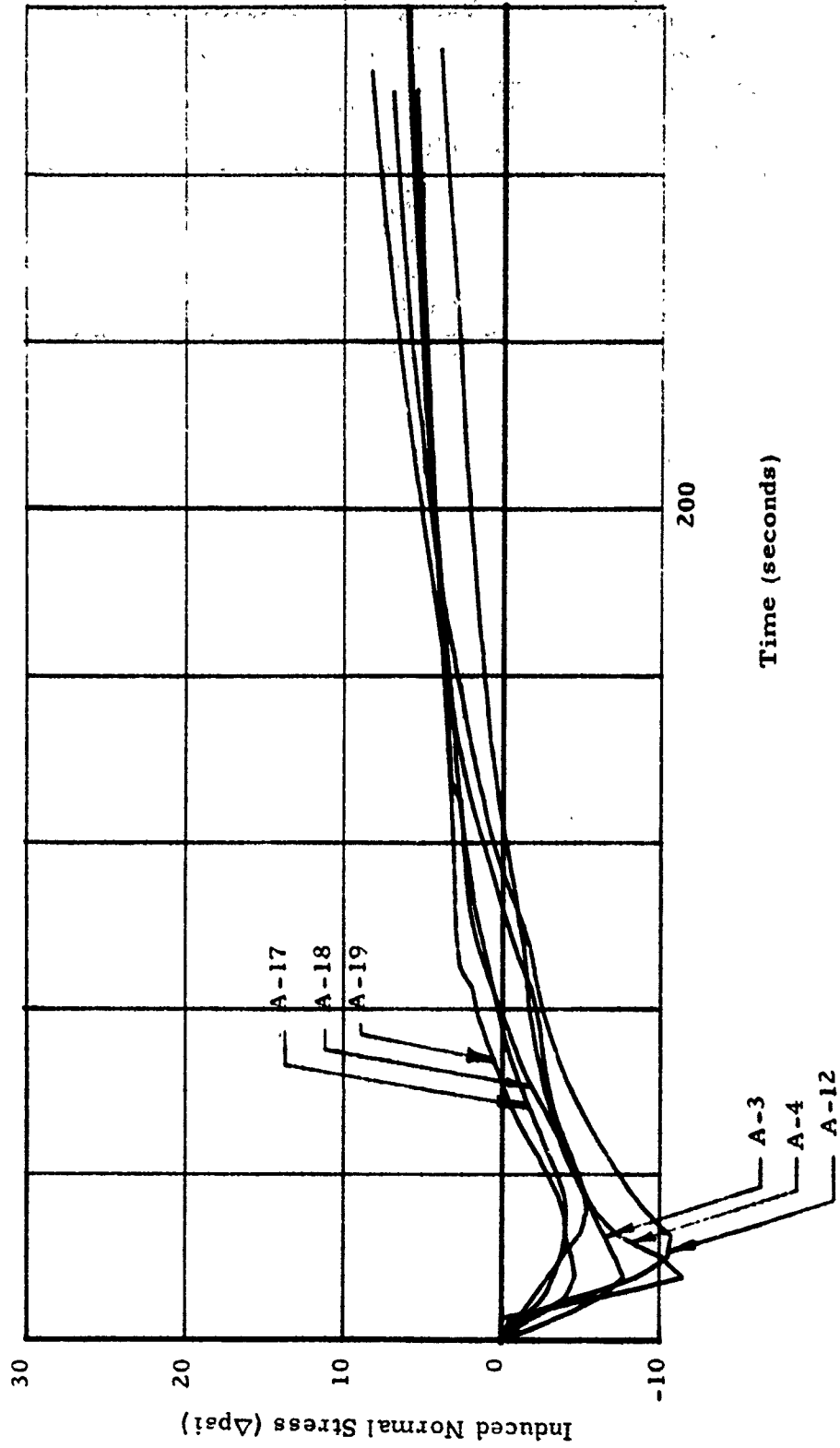


GAC 12/7/73

Figure 73. Shear Stress Induced by the SFPI Mission as Measured by S2-105

SFPI Mission Profile - Aerob heating, IM = 2

Shear Stress Cage #110 Located in the Head End of the Motor.



GAC 12/7/73

Figure 74. Shear Stress Induced by the SFPI Mission as Measured by S2-110

for gage N2-42 which shows nearly a mirror image of gage N2-51. Here again, the output of this gage was off-scale as noted on Tests 3 and 4. The stress at the aft end of the motor (Figure 71) as measured by gage N2-46 shows some reverse trends from the other two. As the unbond failure areas grow in size, the normal stress induced at the aft end is seen to increase, then finally fall to a very minimal response as seen for Test 19. The reason for this became somewhat more apparent as the other data were reviewed. This gage did show the occurrence of two important events. On Test 4, the very rapid stress buildup is terminated in what appears to be a discontinuous manner, followed by what appears to be a normal relaxation rate (normal as compared to Test 3) only to be interrupted again in a discontinuous manner followed by a very high relaxation rate. These two discontinuities on this test must be interpreted as being caused by some degree of unbond occurring. The same phenomena is seen on Test 12 which indicates that unbonding was still occurring or perhaps some rebonding and unbonding occurred as the liner was heated and cooled.

Some of the peculiarities at the aft end as noted above become explainable as shear stress from gage S2-111 presented on Figure 72 is examined. Again we find a similar result on Test 4, that is, the sharp peak in shear stress, but of even more importance was the complete lack of shear on the last three tests. This was construed as meaning that the aft end area was completely unbonded at that time. This information coupled with the observations pertaining to the aft end condition (grain pulled forward and locked in the case) could be used to speculate why the aft end normal stress varies as shown on Figure 71. Since the measured stress is a tensile stress, it would appear that there could be no plausible explanation as to why, if the motor is unbonded, the induced tensile stress could increase as would appear to have happened in Tests 17 and 18. The only possible explanation at the time was that the grain was still bonded at the normal gage location yet unbonded at the shear gage location. The higher induced stress would be an effect of stress concentration near the edge of the unbond. On Test 19 the unbond may have been complete and the response due to the thermal transient within the grain itself. Furthermore, the overall stress level had also decreased to a point showing a stress-free condition.

The head-end shear gages S2-105 shown on Figure 73 and S2-110 shown on Figure 74 provided two important conclusions. First, both showed almost identical initial response measurements for the tests. This in itself was quite refreshing, that is to find good redundant information. The difference in relaxation between the two gages may be due to a nonuniform heating rate over the head of the motor. This is conjecture since the thermocouple associated with S2-110 was broken so a direct comparison was not possible. The second conclusion was the fact that the unbond failure affects the shear and normal stresses in much the same manner.

Because of the early failure experienced in IM #2, only Tests 1, 2, and 3 can be considered as being representative of the motor response to a given loading condition. All the rest of the tests find the motor in some sort

of degraded condition. Examination and use of these data are restricted to analyzing what may be termed "cumulative" failure. That is the obvious conclusion that the unbond area grew in size from test to test. From these data it probably could be projected that continued cycling would result in continued unbonding until the bond stresses were completely relieved. Since the point of failure was identified to have occurred on Test 4 (perhaps instigated by the severity of Test 3), there was little need in continuing the analysis of these data. Therefore, the data obtained on IM #2 were stored as a sort of data bank and their use restricted to appropriate comparisons with the results of similar tests made with IM #3. The data from Tests 1-6 were completely reduced and are presented in Volume II of this report. The only other data reduced from these tests were shown on Figures 69-74.

### IM #3 Aeroheat Test Results

Aeroheat testing of IM #3 consisted of a total of 17 tests. A summary of the test history is shown in Table 10. As seen, the first three tests were conducted for identical test conditions; that is, the DMP-3 mission profile with the motor thermally conditioned to  $-65^{\circ}\text{F}$  prior to the tests. These three tests were made to provide a set of baseline data and to define the repeatability of response of the gages to a given load history. Following these tests, a short series of tests using the HSMH mission profile was conducted. These tests were slightly more severe than the DMP-3, particularly those made from  $-65^{\circ}\text{F}$  (Test 5 and 6). The SFPI series was initiated with one test being made from  $60^{\circ}\text{F}$ . This test was slightly more severe than the HSMH, not in terms of induced stress, but in terms of bond line temperature extremes. The severity was built up gradually on Tests 8-10 with an initial motor temperature of  $-40^{\circ}\text{F}$  being attained. Before proceeding to the most severe SFPI, a DMP-3 test was made to determine if any changes in structural response had been induced by the test history to date. Tests 12-16 were the most severe SFPI series with the final test, Test 17, being another DMP-3 repeat. The program set up for this motor is therefore seen to be much more cautious than that conducted on IM #2. The purpose here was twofold: first, obtain as much structural response data as possible prior to failure, and second, see if an unbond failure would repeat itself for the same test condition. The results of these tests are presented in full in Volume II of this report; however, many will be duplicated here for convenience.

Probably the most appropriate manner in which to consider and review these data are in terms of the thermal gradient first, the normal gages second, shear gages third, and clip gages fourth. Further, the discussion and data shown here will be essentially limited to those tests which were conducted for an initial motor temperature of  $-65^{\circ}\text{F}$ . Significant effects of changing the initial motor temperature will be identified herein; however, the reader is directed to Volume II for specific data.

Typical temperature profile histories for each test condition (i. e. Tests 1, 4-9, 12) are presented on Figures 75-81. These data provide an assessment of the severity of the aeroheat tests. Severity can be examined in two ways. First, the rate of the temperature rise on the case can be interpreted as an indication of induced stress rise. Second, the overall temperature levels reached at the case, liner interface (basically Thermocouple T3-0) and at the propellant-liner interface (Thermocouple T3-1) provide an assessment of potential thermally induced bond system damage. Both of these aspects are important in a review of the data. Another important facet is the excellent repeatability on Tests 3, 11 and 17 as well as Tests 12-16. Since these tests were conducted to examine repeatability of gage output and to provide baseline data, that purpose was well satisfied. Of course, the temperature data show how well the test conditions and thus the induced loads were duplicated.

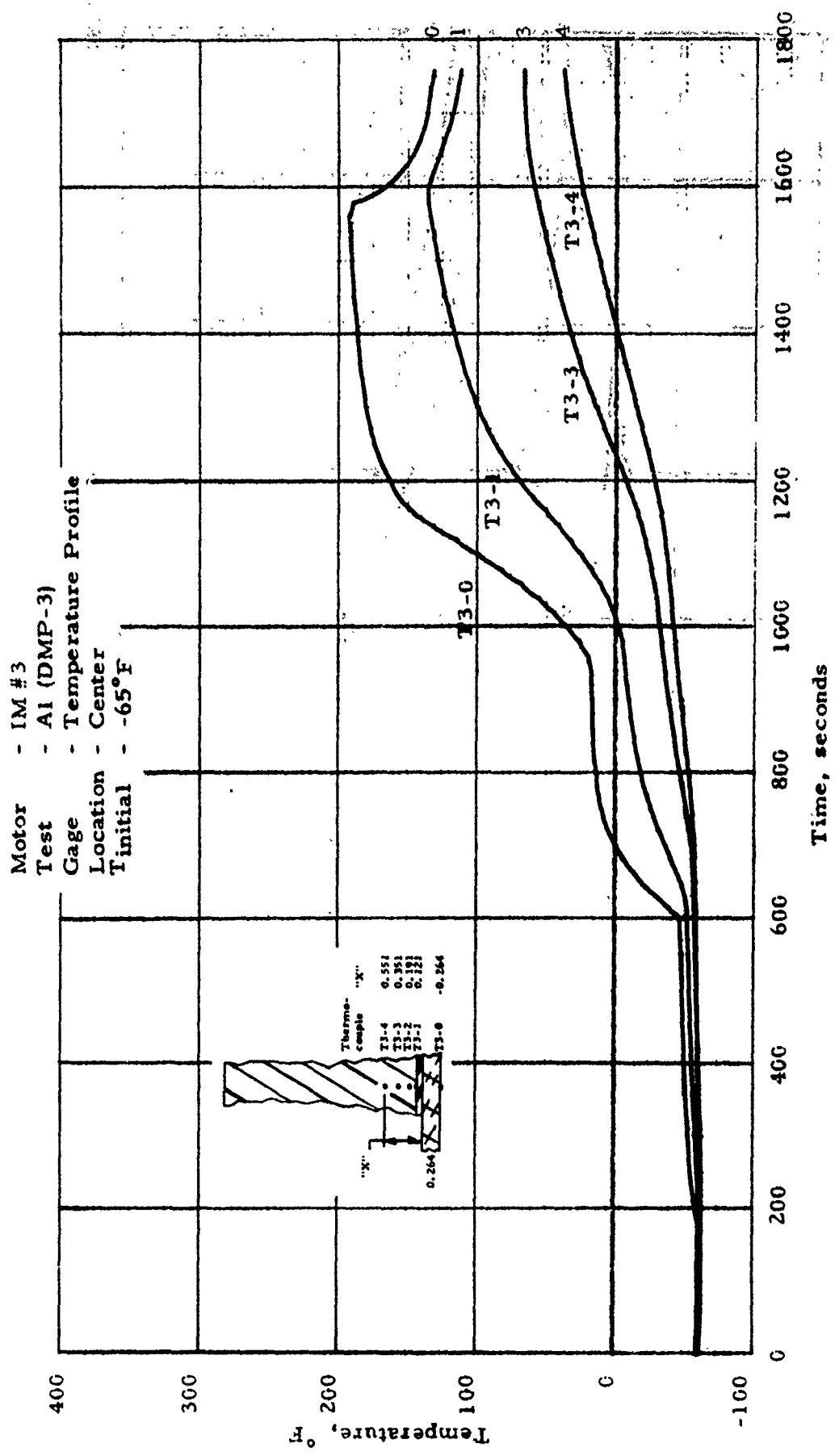


Figure 75 Temperature Profile Histories for Various Aeroheat Loads (Test No. A-1)

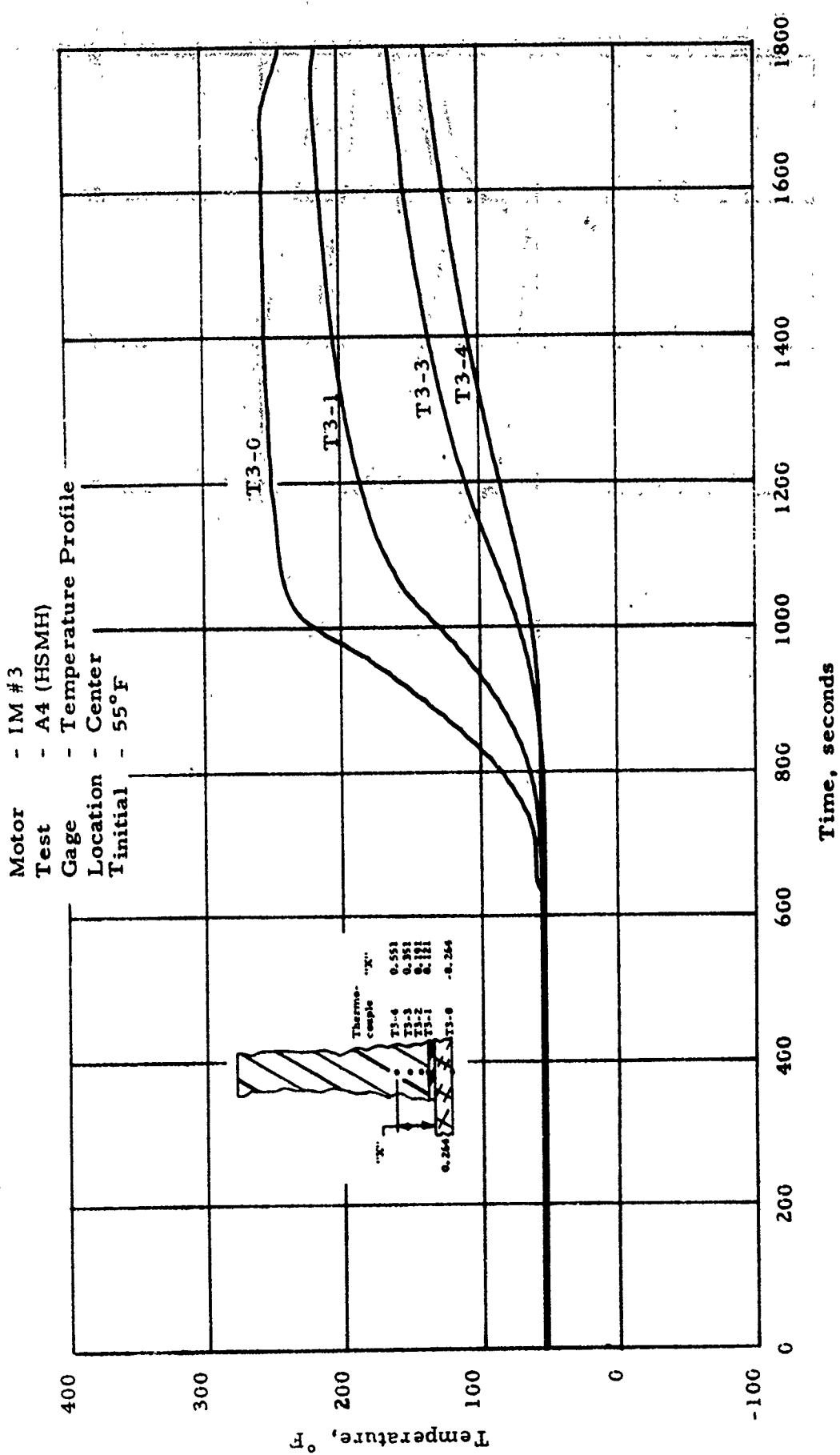


Figure 76 Temperature Profile Histories for Various Aeroheat Loads (Test No. A-4)

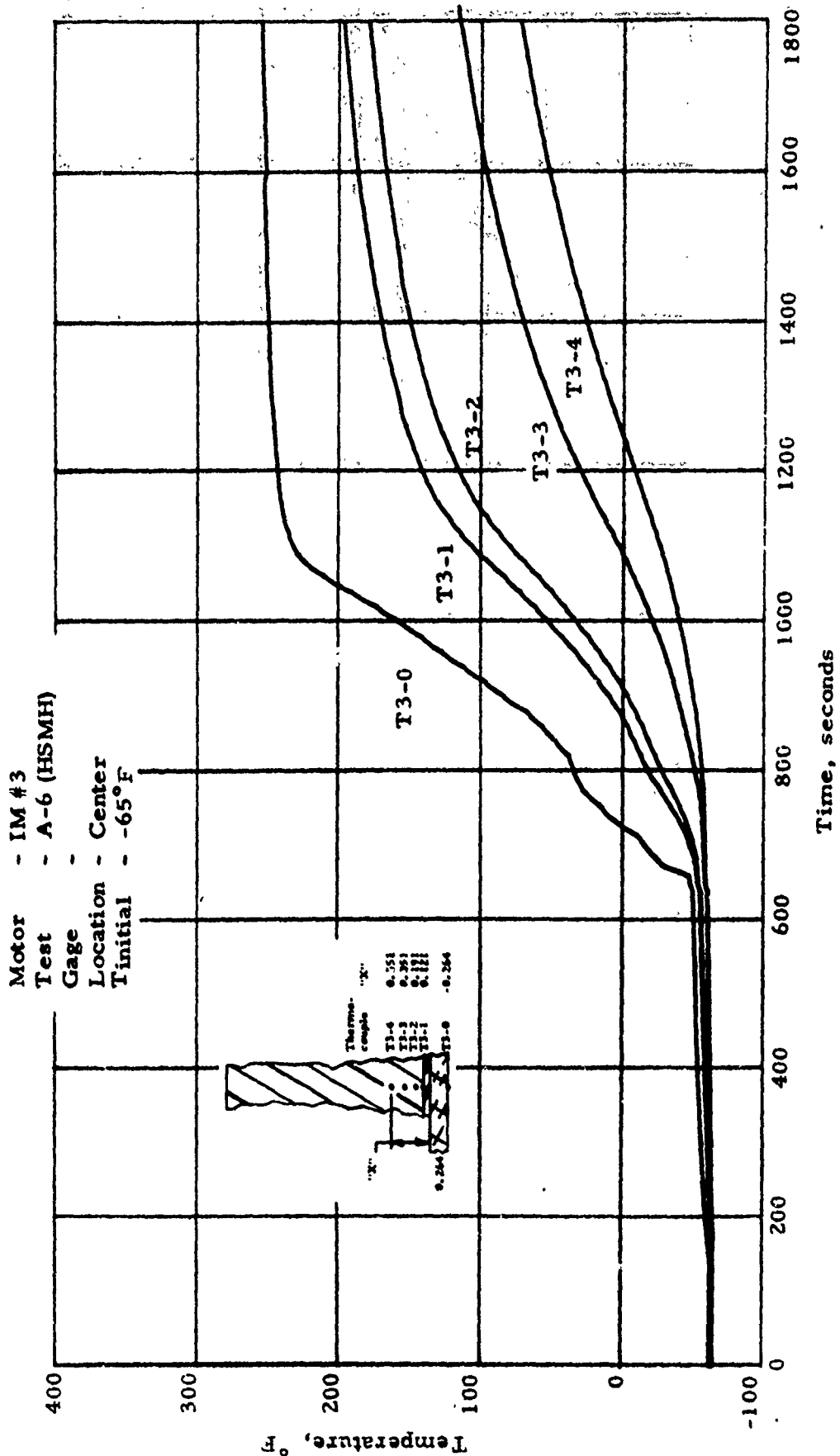


Figure 77 Temperature Profile Histories for Various Aeroheat Loads (Test No. A-6)

Motor - IM #3  
 Test - A7 (SFPI)  
 Gage - Temperature Profile  
 Location - Center  
 T initial - +60°F

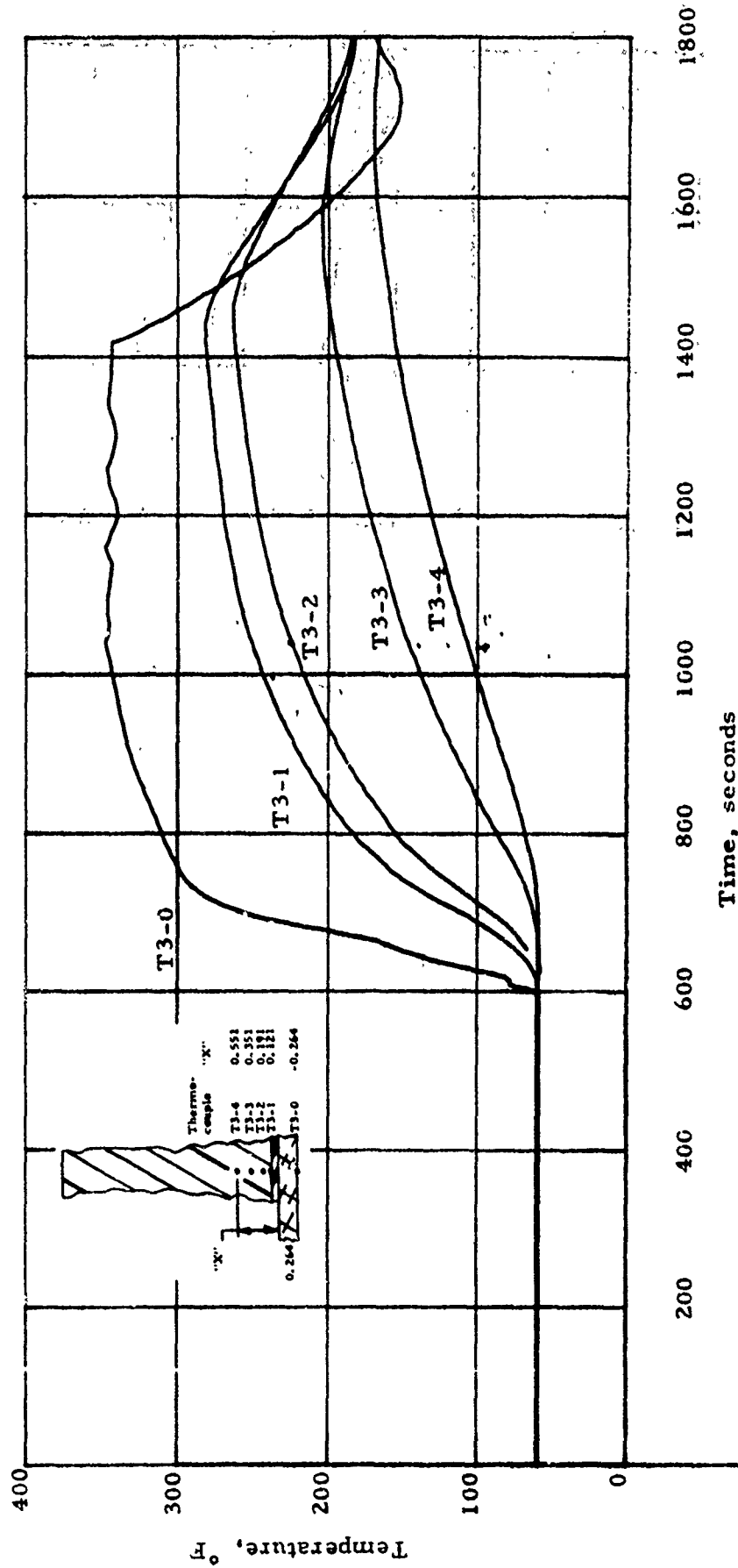


Figure 78 Temperature Profile Histories for Various Aeroheat Loads (Test No. A-7)

Motor - IM #3  
 Test - A8 (SFPI)  
 Gage - Temperature Profile  
 Location - Center  
 T initial - 0°F

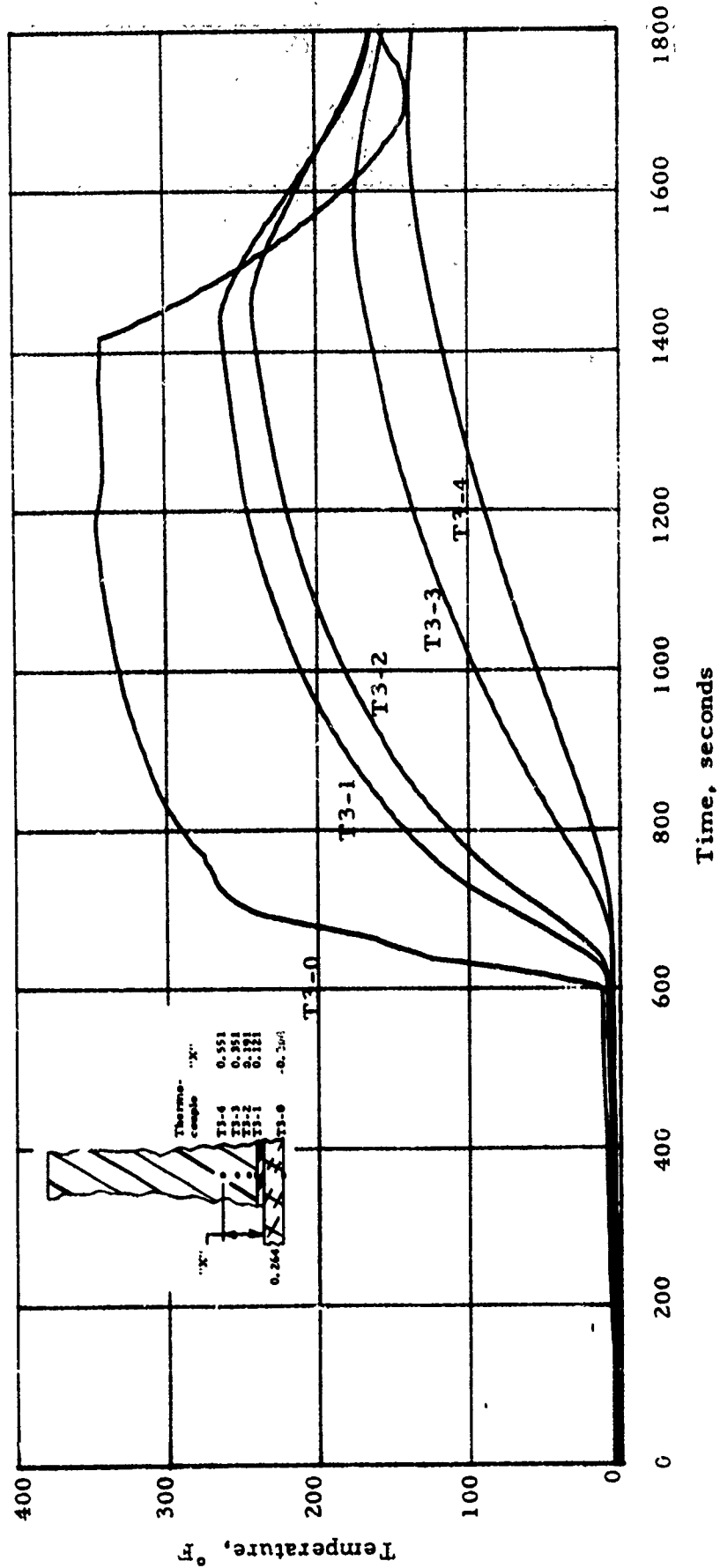
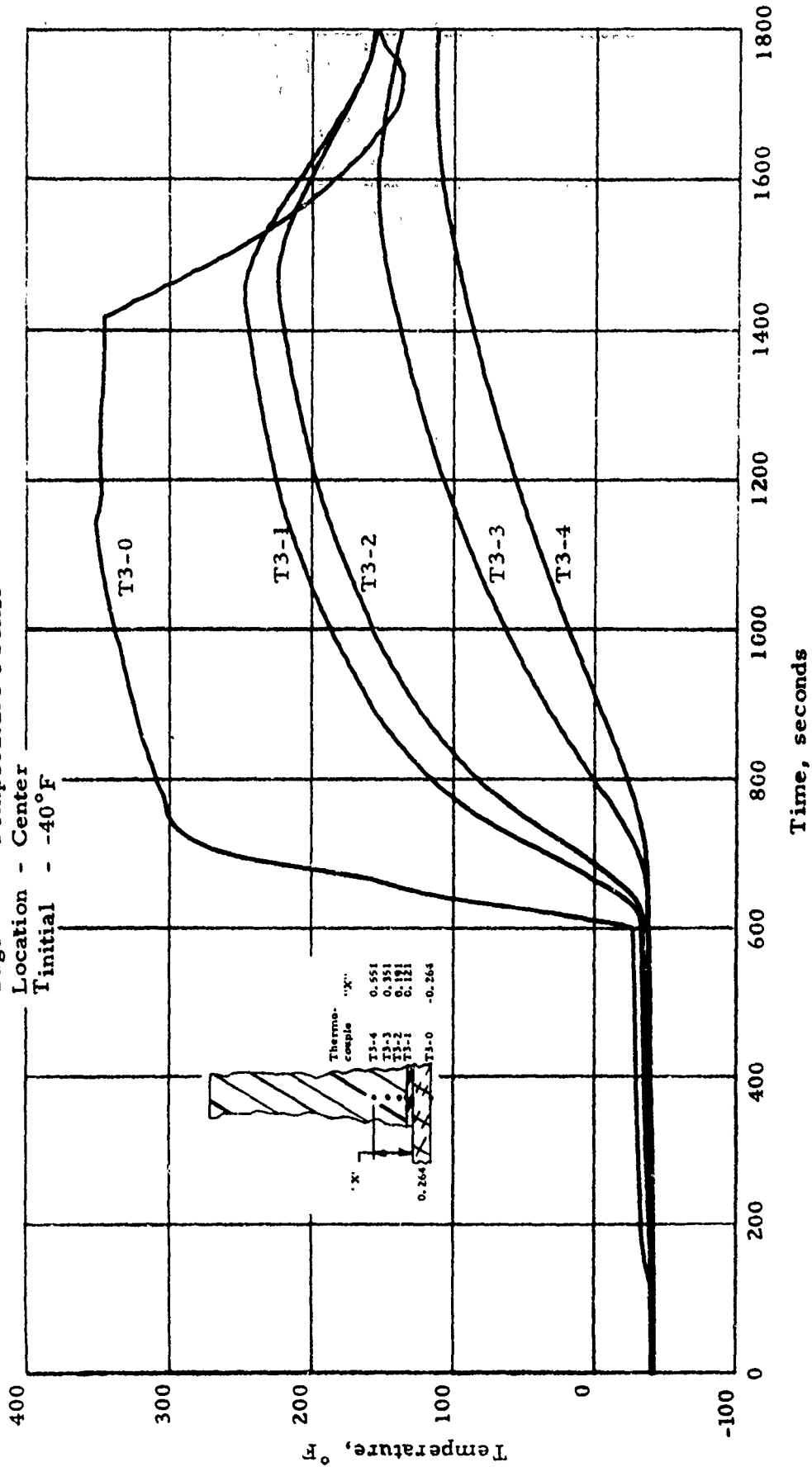


Figure 79 Temperature Profile Histories for Various Aeroheat Loads

Motor - IM #3  
 Test - A9 (SFPI)  
 Cage - Temperature Profile  
 Location - Center  
 T initial - -40°F



Thermo-couple "X"

T3-4	0.551
T3-3	0.351
T3-2	0.121
T3-1	0.121
T3-0	-0.264

Figure 80 Temperature Profile Histories for Various Aeroheat Loads

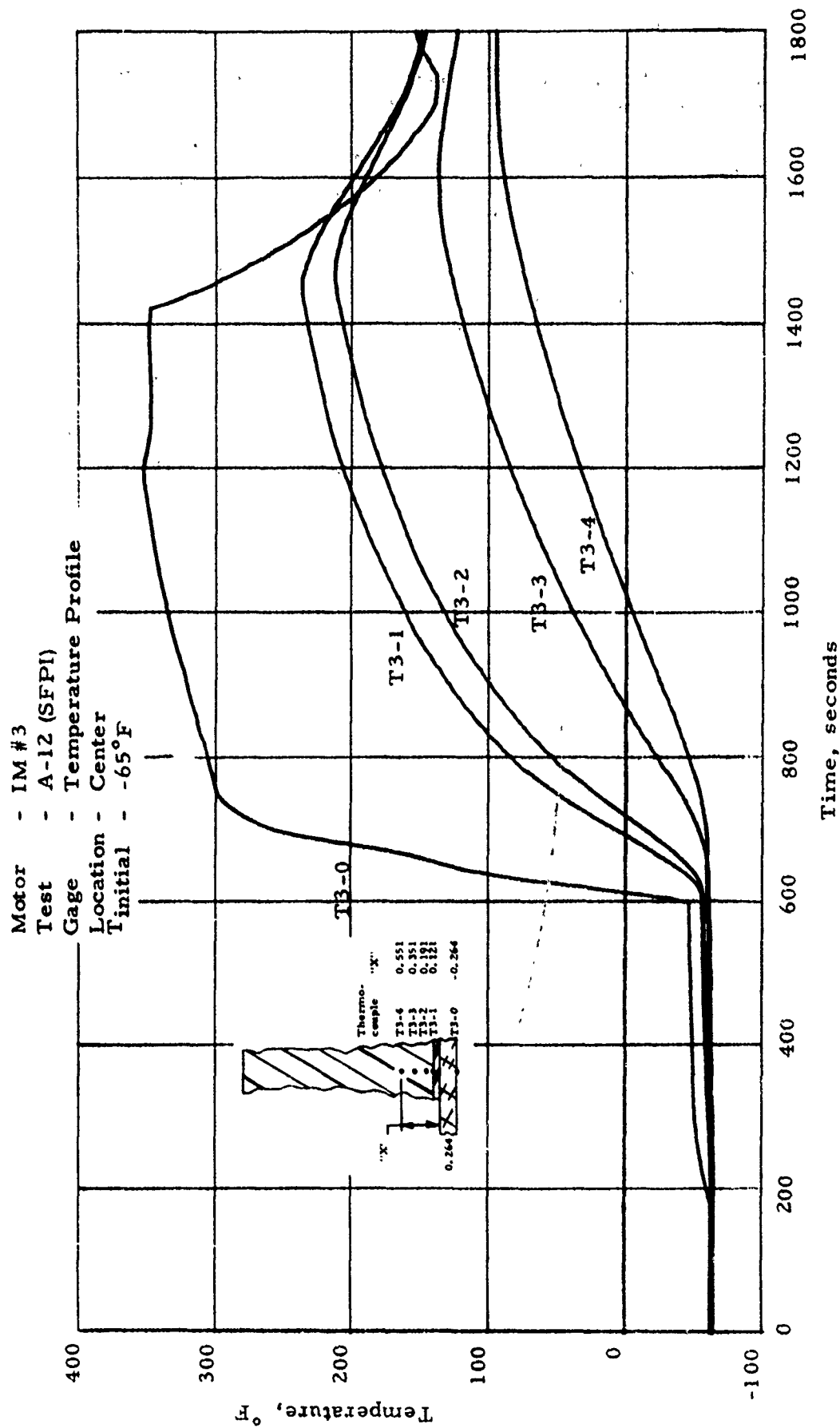


Figure 81 Temperature Profile Histories for Various Aeroheat Loads

One of the most important finds made while reviewing this temperature gradient data was that the time of failure of IM #2 could be pinpointed. Recalling the fact that the unbond failure in IM #2 occurred under the thermocouple slab, the temperature gradient data should be different depending on whether or not an unbond exists. This is particularly true if the expansion of the case during aeroheat is sufficient to actually pull a gap between the liner and the case. Review of the temperature profile data from IM #2 did not, at the time, reveal anything that could be used as concrete evidence of when the unbond occurred. There were differences in the temperature profile histories between Tests A-3 and A-4 on IM #2; however, the differences only seemed to confirm that something, perhaps, unbond occurred in that time period. Although these data are presented in Volume II, they are reproduced here for convenience on Figures 82 and 83 for IM #2 tests A-3 and A-4, respectively. Comparing these data then with the corresponding data from IM #3 (Figure 80), we immediately see the difference in the temperature histories in the grain. The outside case histories are nearly the same so the differences in internal temperatures must be due to the existence of the unbond. Closer inspection on both Figures 82 and 83 show that the temperatures initially increase at much the same rate as those in IM #3, but then suddenly deviated. This deviation can only be caused by a change in the mode of heat transfer through the motor. The heat transfer mode for a fully bonded system is, of course, by conduction. The existence of an unbond in which a gap between the case and liner forms will result in the mode of heat transfer being by radiation which simply reduces the heat transfer rate. The point at which we see this break in the temperature time curve is the point at which unbond occurs. Therefore IM #2 failure occurred early in Test A-3. Since the same phenomena, but to a much lesser extent, is seen to exist on Test A-4, some sort of healing or rebonding must have occurred later in or after Test A-3. This then was destroyed on Test A-4.

Prior to proceeding into a discussion of the gage outputs, a word of explanation is necessary for those who have examined the temperature profile data in Volume II and have some question regarding the odd shape shown for Test A-5. The abrupt decrease beginning at 900 seconds was caused by the necessity to abort the test at that time. After a shutdown of 120 seconds during which the case cooled, the flow was re-established and the test was continued at the same conditions existing when terminated. In comparing the results from Tests 5 and 6, which were to be the same test conditions, data must be restricted to that obtained prior to 900 seconds.

Typical results from the two normal gages located in the center section of the motors are presented on Figures 84-89. Since both gages (N3-43 and N3-47) are located at the same radial and longitudinal positions (differ only in circumferential location) similar results would be expected. This similarity does exist throughout these tests. Upon examination of Figure 84, we can see that these gages compare well over the first three tests (repeatability of each gage is excellent), although there is a tendency of Gage N3-43 to measure a higher stress on the secondary peak than Gage N3-47. This could have been caused by one of a number of reasons from a poor gage to different local

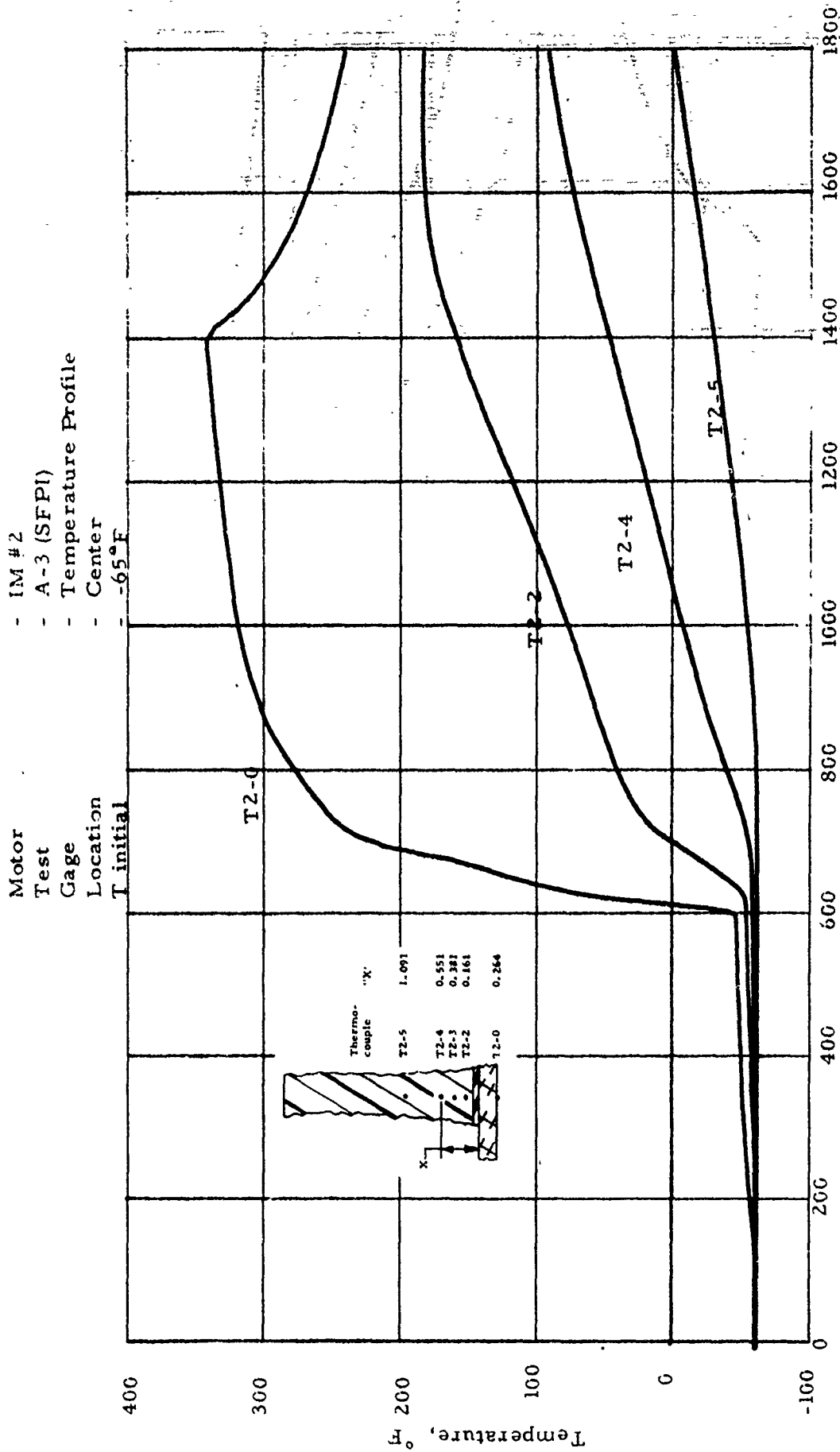
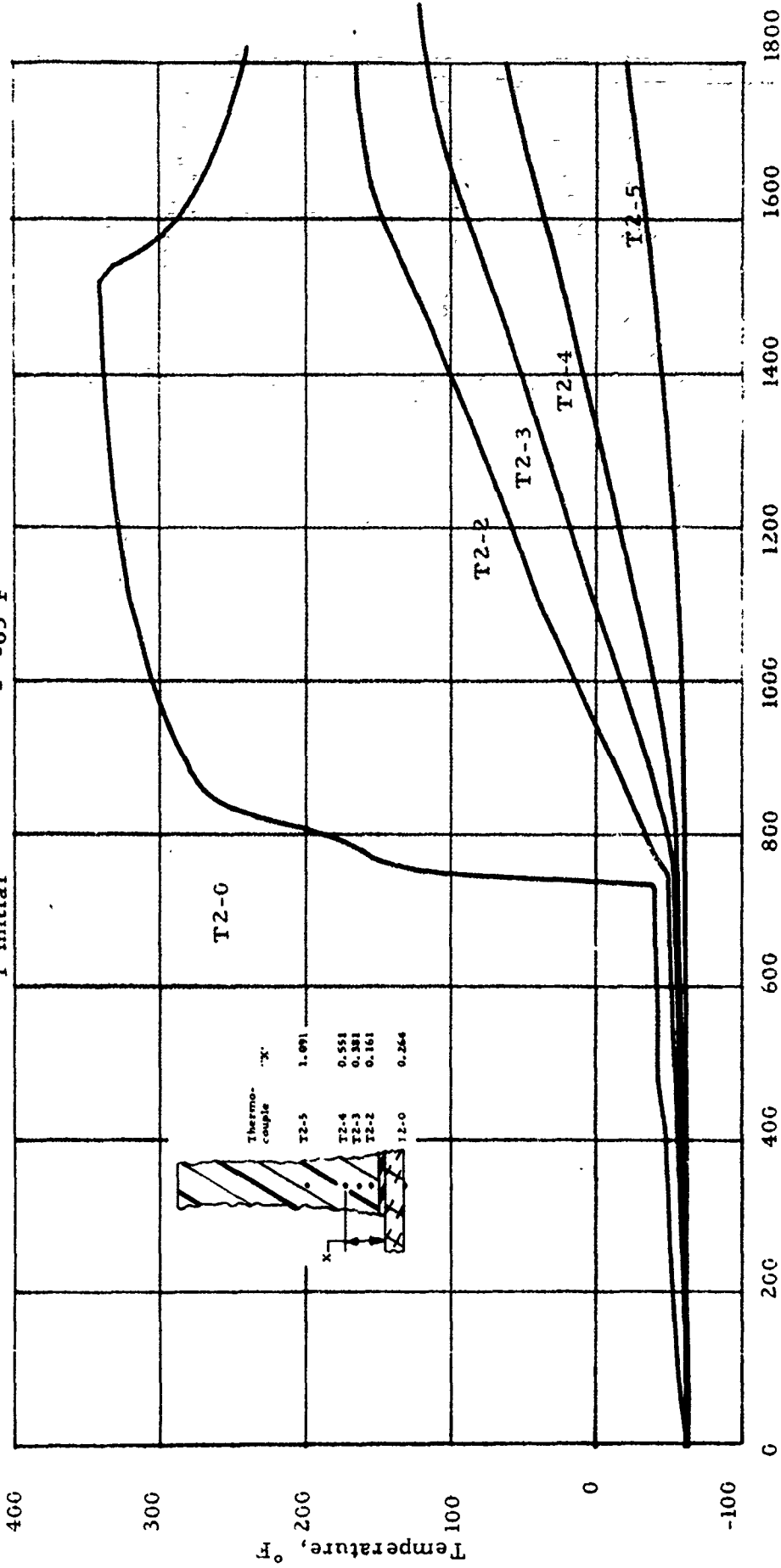


Figure 82 Temperature Profile Histories for Various Aeroheat Loads. Test A-3

- IM #2  
 - A-4 (SFPI)  
 - Temperature Profile  
 - Center  
 - -65°F

Motor  
 Test  
 Gage  
 Location  
 T initial



Time, Seconds

Figure 83 Temperature Profile Histories for Various Aeroheat Loads. Test A-4

Motor - IM #3  
 Test - A-1, A-2, A-3  
 Gage - N3-4, N3-47  
 Location - Center  
 T<sub>initial</sub> - -65°F  
 --- N3-47  
 --- N3-43

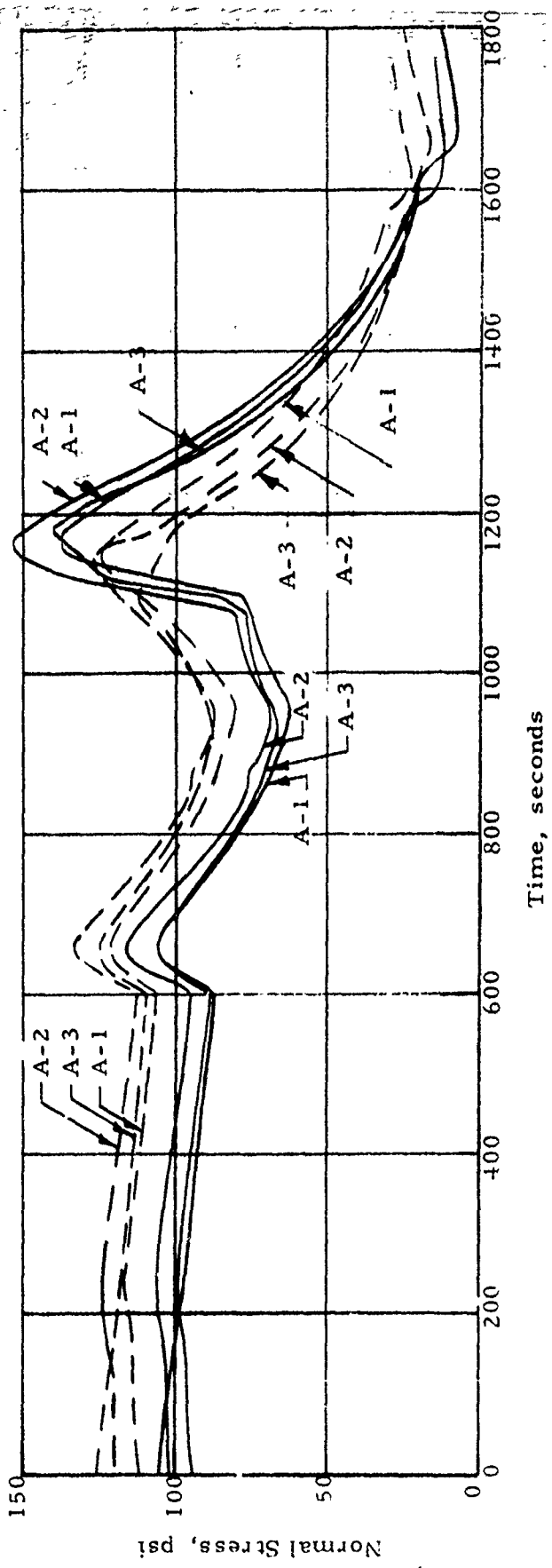


Figure 84. IM #3 Mid Motor Normal Stress, Tests A1 through A-3

--- N3-17

— N3-43

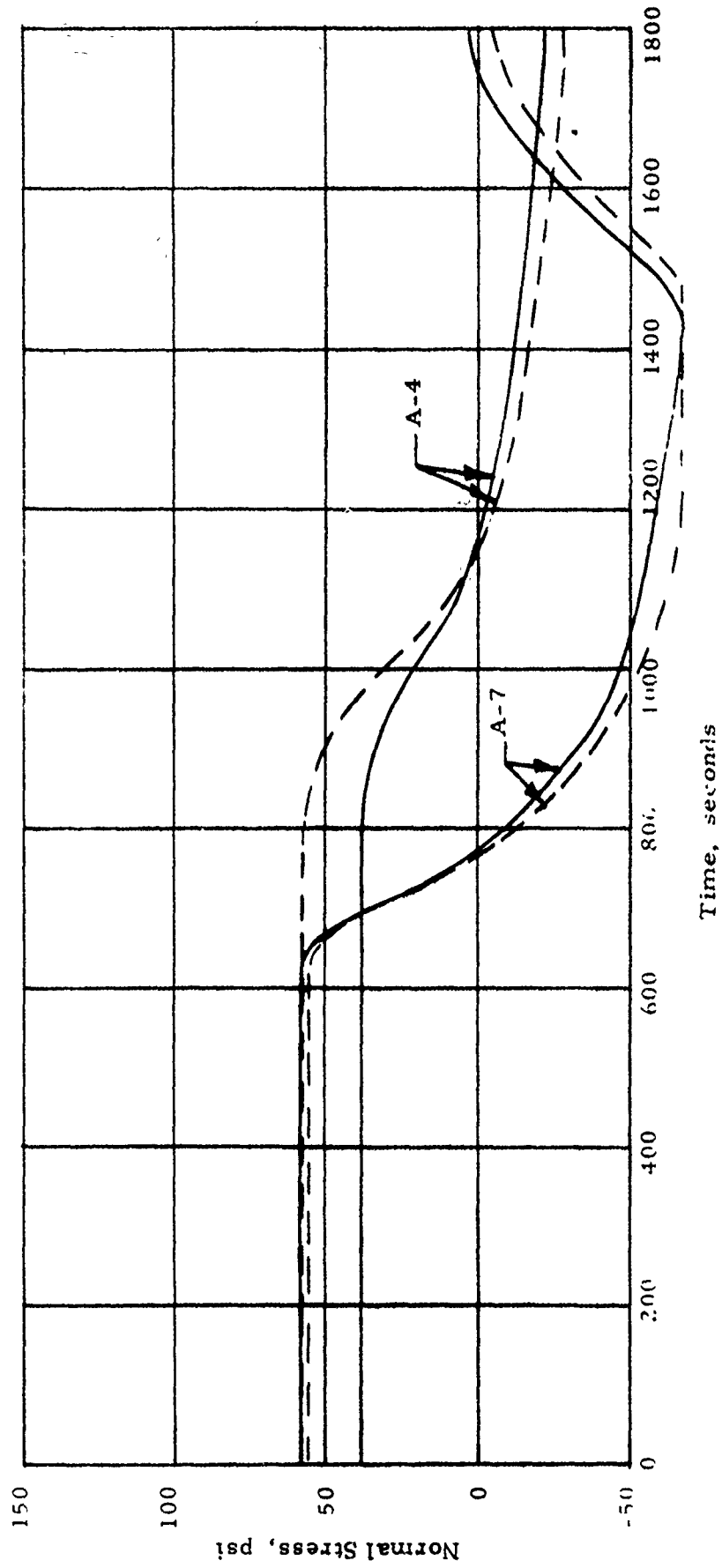


Figure 85. Comparison of HSMH and SFP Test Results at an Initial Motor Temperature of 60°F

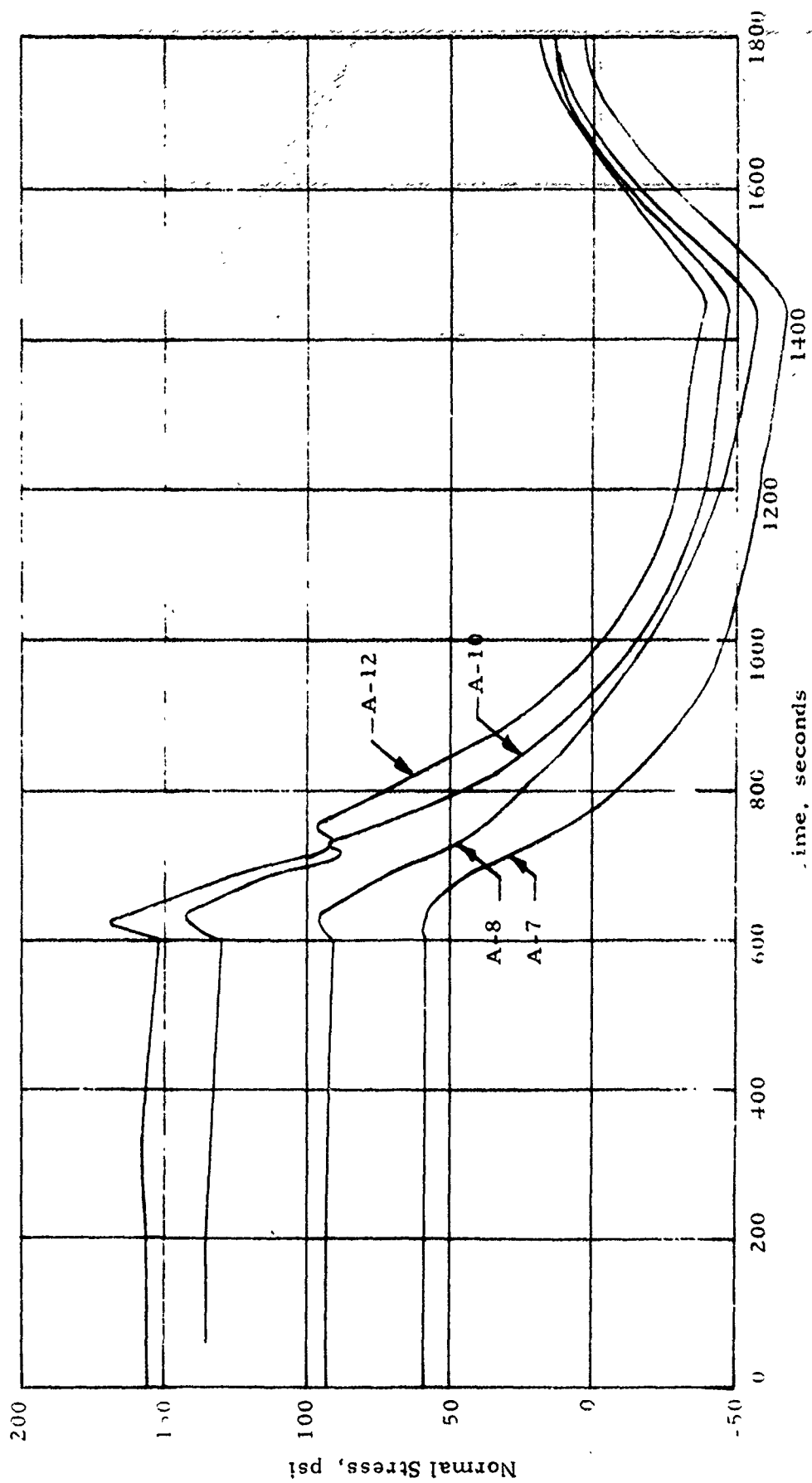


Figure 86. Effect of Decreasing Initial Motor Temperature. --Cage 3-43, SFPI Profile

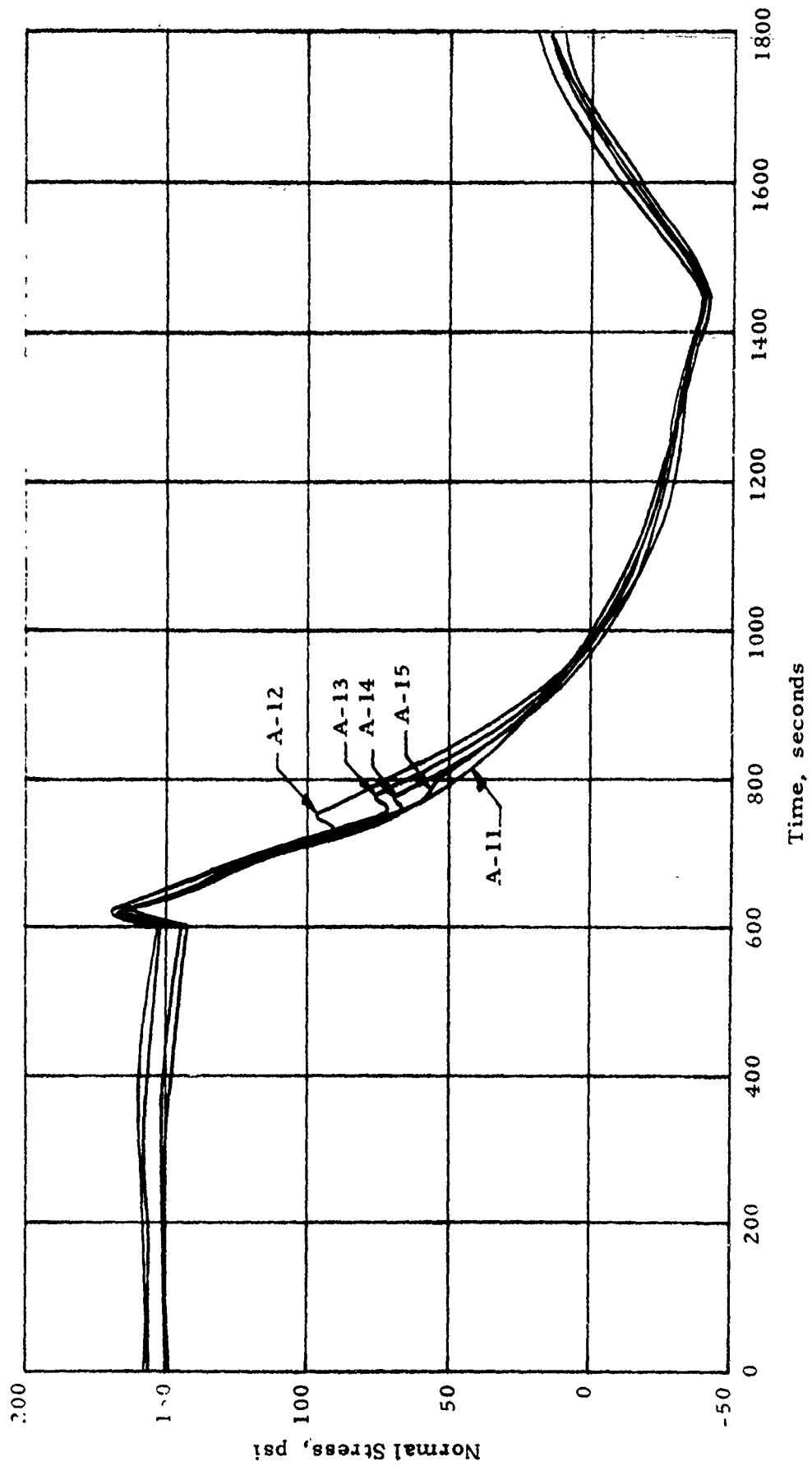


Figure 87. Comparison of Results from Successive SFPI Tests--Gage N3-43

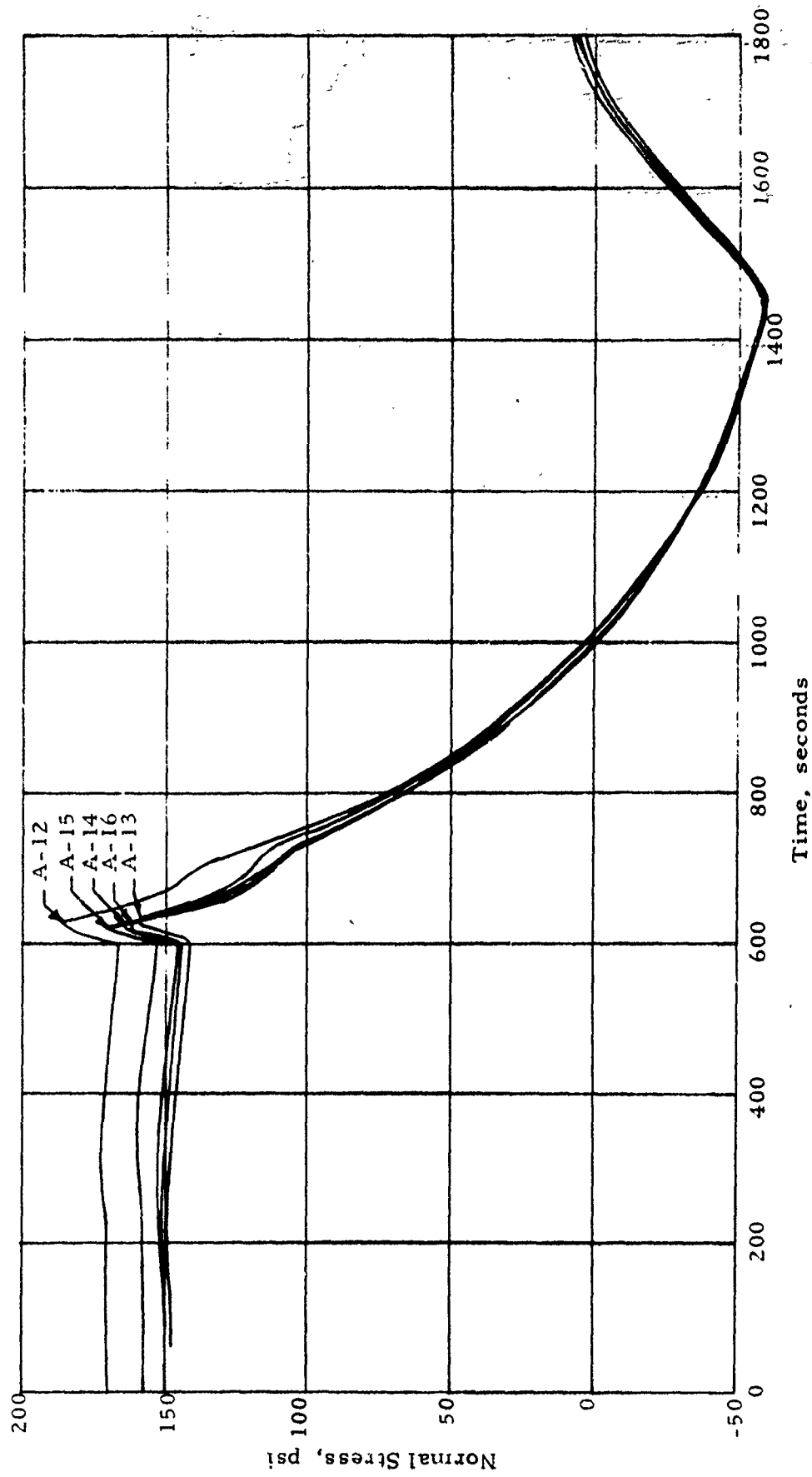


Figure 88. Comparison of Results from Successive SFPI Test--Gage N3-47

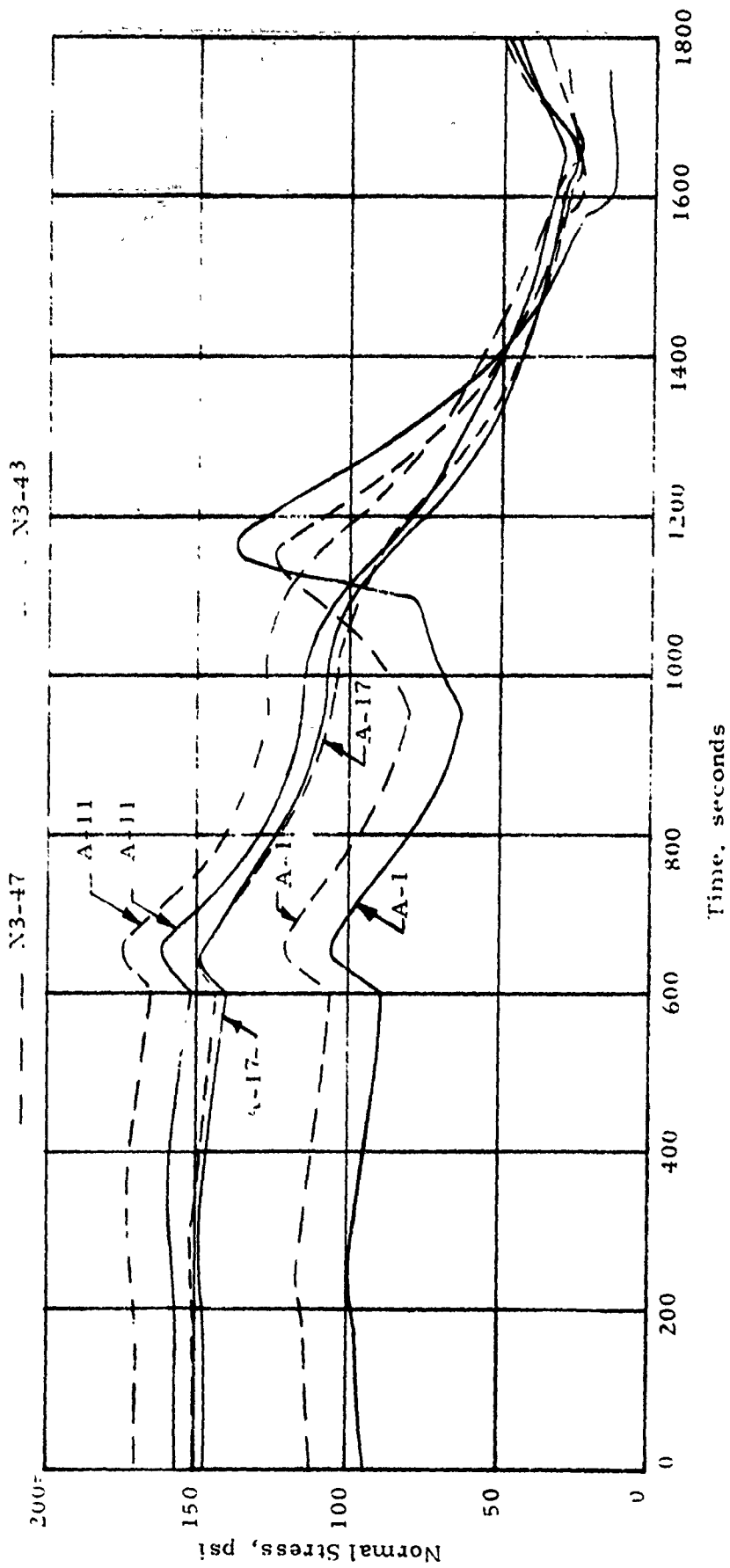


Figure 89. Effect of Aeroheal Testing on DMP-3 Profile Response

grain structure around the gages.

Probably the most surprising data were those obtained on Tests A-4 and A-7. Both of these tests were made from an initial motor temperature of about 60°F. As shown on Figure 85, neither gage indicated any induced stress for either test. This is adverse to what had been theoretically predicted earlier and the results from the aeroheat tests of IM #2. However, at the time these type tests were made on IM #2, the unbond failure had occurred. Daily inspection, both sonic and ultrasonic, did not reveal any unbond in this motor. Therefore, comparing data acquired from IM #2 with IM #3 would not be proper except in terms of showing the effects of unbond on the stress response.

The remaining tests, Tests 8 through 17, as shown in Table 10, are predominantly based on the SFPI mission profile and lower initial motor temperatures. The exceptions are, of course, Tests 11 and 17. Test 11 was conducted to determine if any change in motor response had occurred since Tests 1 through 3 because of the aeroheat cycling. Similarly, the final test (Test 17) was conducted to determine how much additional damage, if any, was done by the SFPI series. The results of the comparison tests will be discussed later.

Typical measured stress levels for the SFPI profiles are shown on Figures 86-88. The effects from repeating five SFPI tests in succession are shown on Figures 87 and 88 for gages N3-43 and N3-47, respectively. Although showing excellent qualities of consistency and repeatability, these data do not adhere rigorously to the claim that severity is related to temperature rise rate. For example, about as much stress was induced during the relatively mild DMP-3 tests (Test 1-3) as was on the SFPI tests. This is completely adverse to the trends noted on IM #2 even after the bond line failure and the results of the initial THVINC studies. As stated previously, the rate of temperature rise on the case can be interpreted as an indication of induced stress rise and the overall temperature level attained as a potential bond system damage mechanism. Therefore, in comparing the results of the gage measurements the temperature profile data need to be consulted to check not only the temperature excursions, but also repeatability of the applied thermal loads in designated replicate tests. An examination of these data contained in Volume II will show that this repeatability is excellent on Tests 12-16. Besides little stress being induced at the -65°F condition, there were only slight increases in stress induced for the different initial motor temperatures.

A review of these data shows that significant changes in structural response occurred as a result of these aeroheat tests. The amount of change can be seen by comparing the results of Tests 1, 2, and 3 with the results of Test 11 and then by comparing both with Test 17. These results from gages N3-43 and N3-47 are shown on Figure 88 for Test A-1, A-11, and A-17. The results of Tests A-1, A-2, and A-3 were compared on Figure 84. Not only has the structural response changed for a dynamic load (aeroheat), but a

rather obvious increase in the stress level under equilibrium conditions can also be noted. Although this increase is easily detectable by inspection of Figures 84 through 89, an attempt was made to provide some type of correlated summary of this effort. This was done by going back to the gage checkout data and defining a baseline stress curve. The baseline curves for each of the four normal gages in this motor are shown on Figures 90 through 93. The curve for each gage has been faired through the data in a rather arbitrary manner. The tendency was to put more reliance in the stress levels measured at a given temperature when that temperature had been achieved by cooling from a higher value. This is, of course, similar to what occurs after each aeroheat test when the motor is re-cooled. Since these curves are used only to normalize the measured stress values from the aeroheat test series, it makes little difference whether the faired curves are statistically correct or incorrect.

The normalized changes in stress in percent are shown on Figure 94 as a function of test number. The manner in which the data were normalized is shown in equation form. The term  $\sigma_{act}$  refers to the stress measured when the motor was equilibrated to  $-65^{\circ}\text{F}$  after the test which is designated by the test number. All data were referenced to the initial state prior to Test 1 as indicated by the equation. The use of the test number as a variable is a manner of convenience; although it does show the change was indeed induced by the aeroheat tests. It is obvious that both normal gages (Gages N3-43 and N3-47), located in center region of the motor, show very nearly the same rate of change and overall change. The aft-end gage (Gage N3-45) shows extreme increases which if IM #2 data were to be believed would indicate local unbonding in that region. The head-end gage shows the opposite effect which could in part be caused by gage location and orientation but more probably from unbonding.

In addition to these past test stress levels changes, differences in the rate of relaxation down from the peak stress levels induced in the aeroheat tests were found. These can be found by very close inspection of all the normal gage data as presented in Volume II, but are far more prominent in the aft-end region. The aeroheat induced stress, as measured by Gage N3-45 for Tests 12 through 16, are shown on Figure 95. Although approximately the same peak stress level was induced for each test, the increase in the rate of relaxation from this peak value with each test is fully discernable. These data indicate that appreciable change in the aft end grain structural response has occurred. These changes can be caused by many things including propellant physical property change. However, as stated before, it was felt that the major cause was due to growth of unbond areas in that region.

The preceding observations have been made based on normal stress gage data only. Considerations of the shear stress and clip gage data should either confirm or deny these observations. Unfortunately only one shear gage (S3-104) was in IM #3 and its reliability is somewhat in question. The reason for these doubts is evident upon examination of response of this gage during gage checkout testing. These data are shown in Appendix A. This examina-

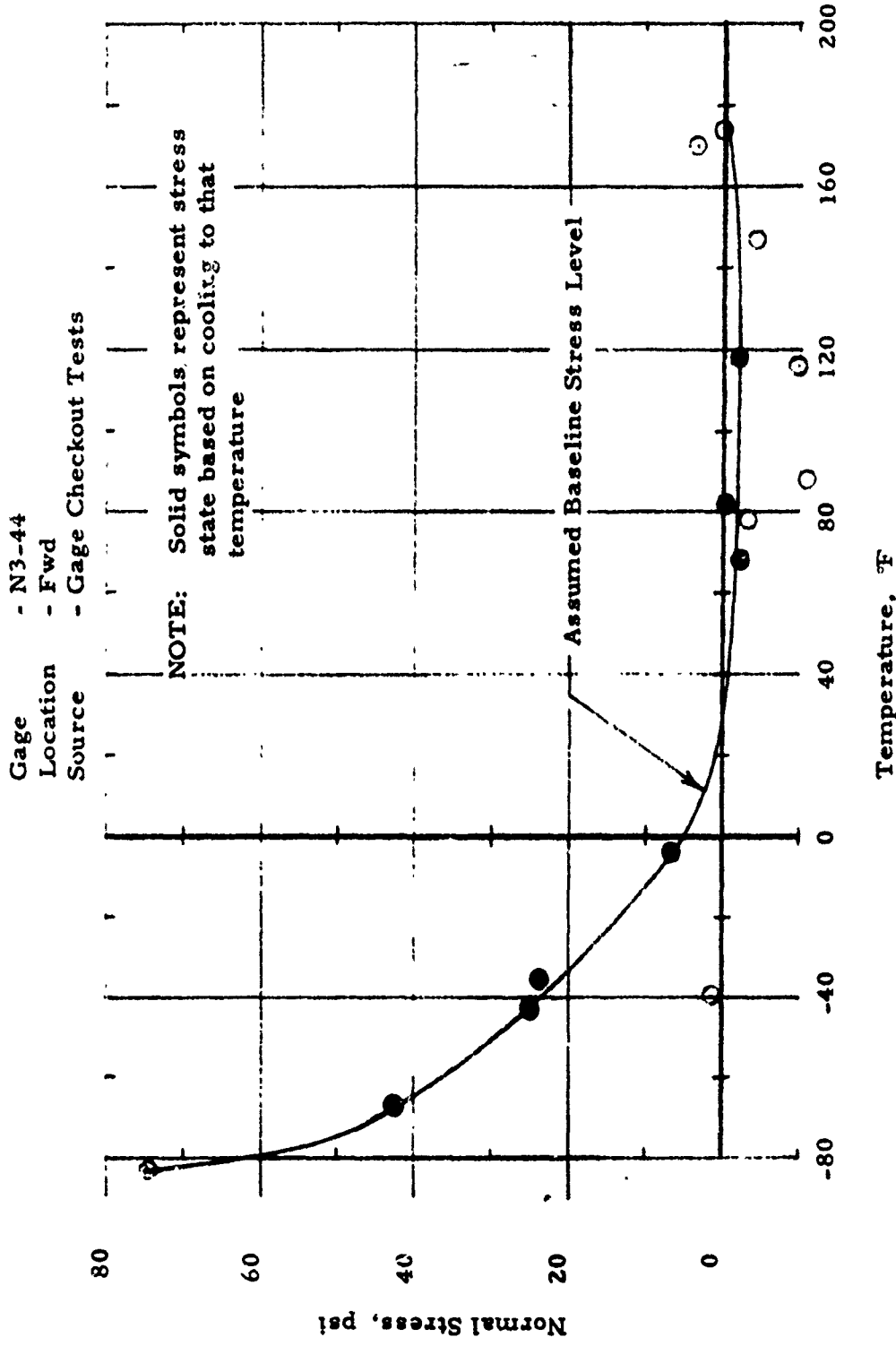


Figure 90. Baseline Stress Data For Gage N3-44

Gage - N3-43  
Location - Center  
Source - Gage Checkout Tests

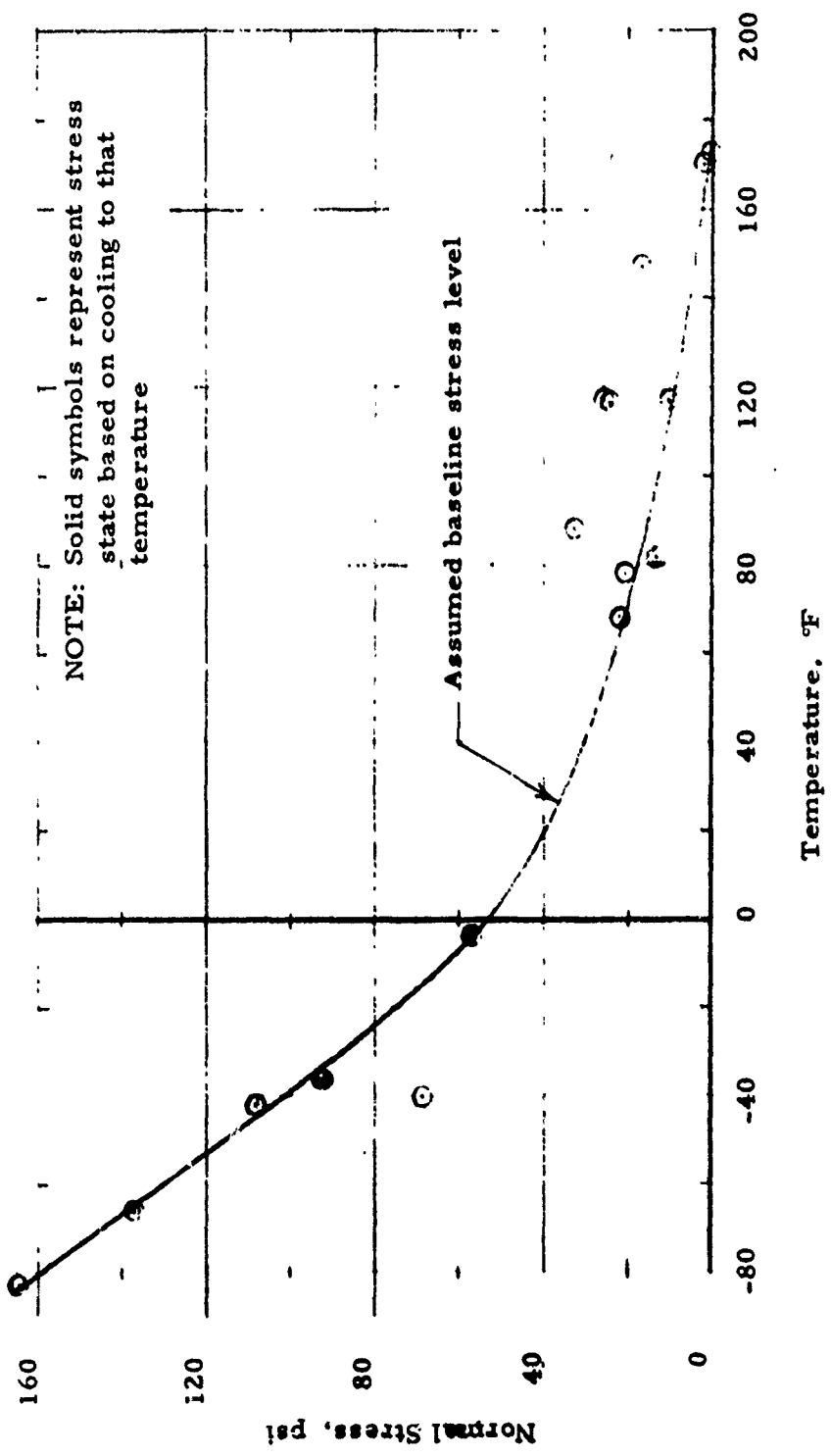


Figure 91. Baseline Stress Data For Gage N3-43

Gage - N3-47  
 Location - Center  
 Source - Gage Checkout Tests

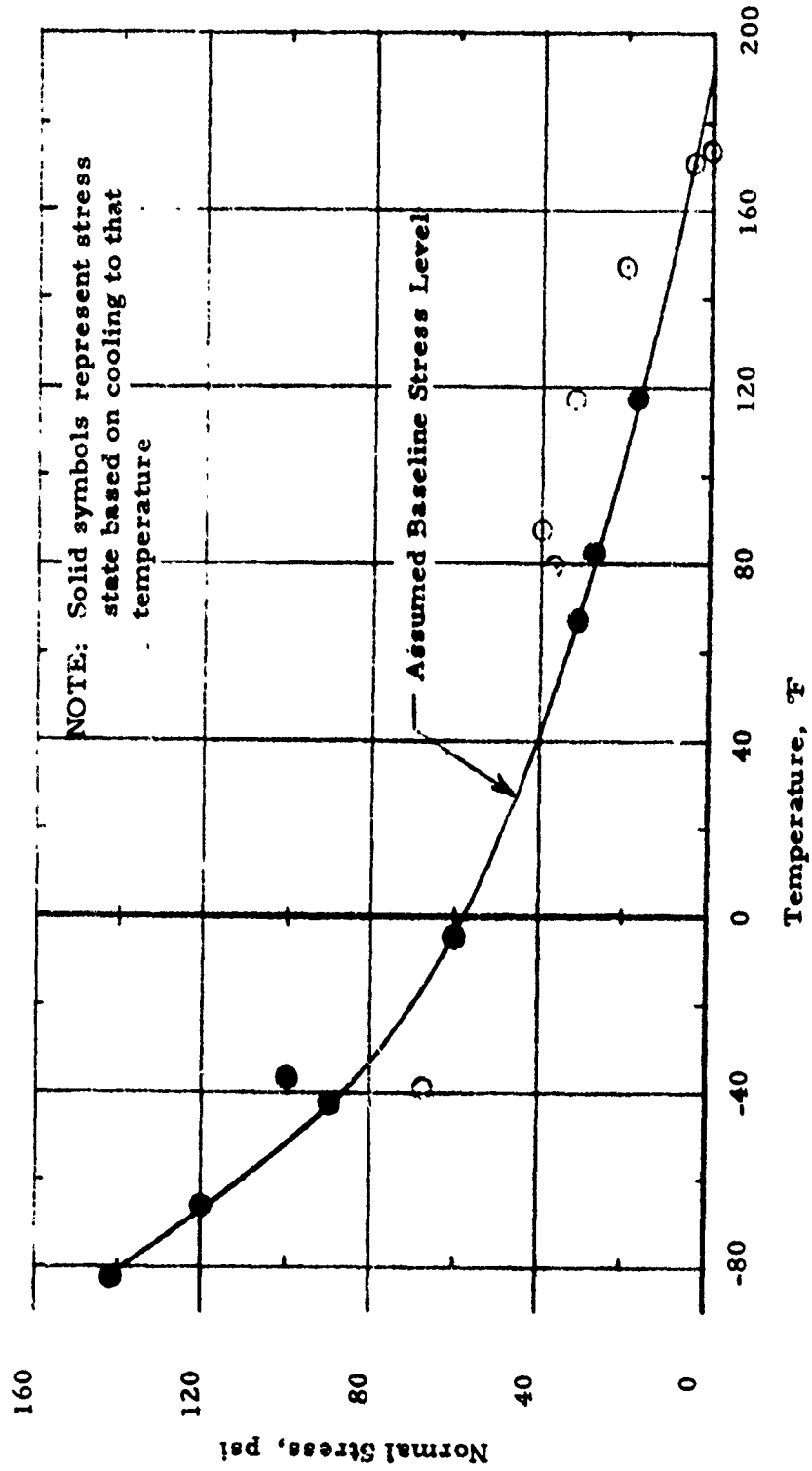


Figure 92. Baseline Stress Data For Gage N3-47

Gage - N3-45  
 Location - Aft  
 Source - Gage Checkout Tests

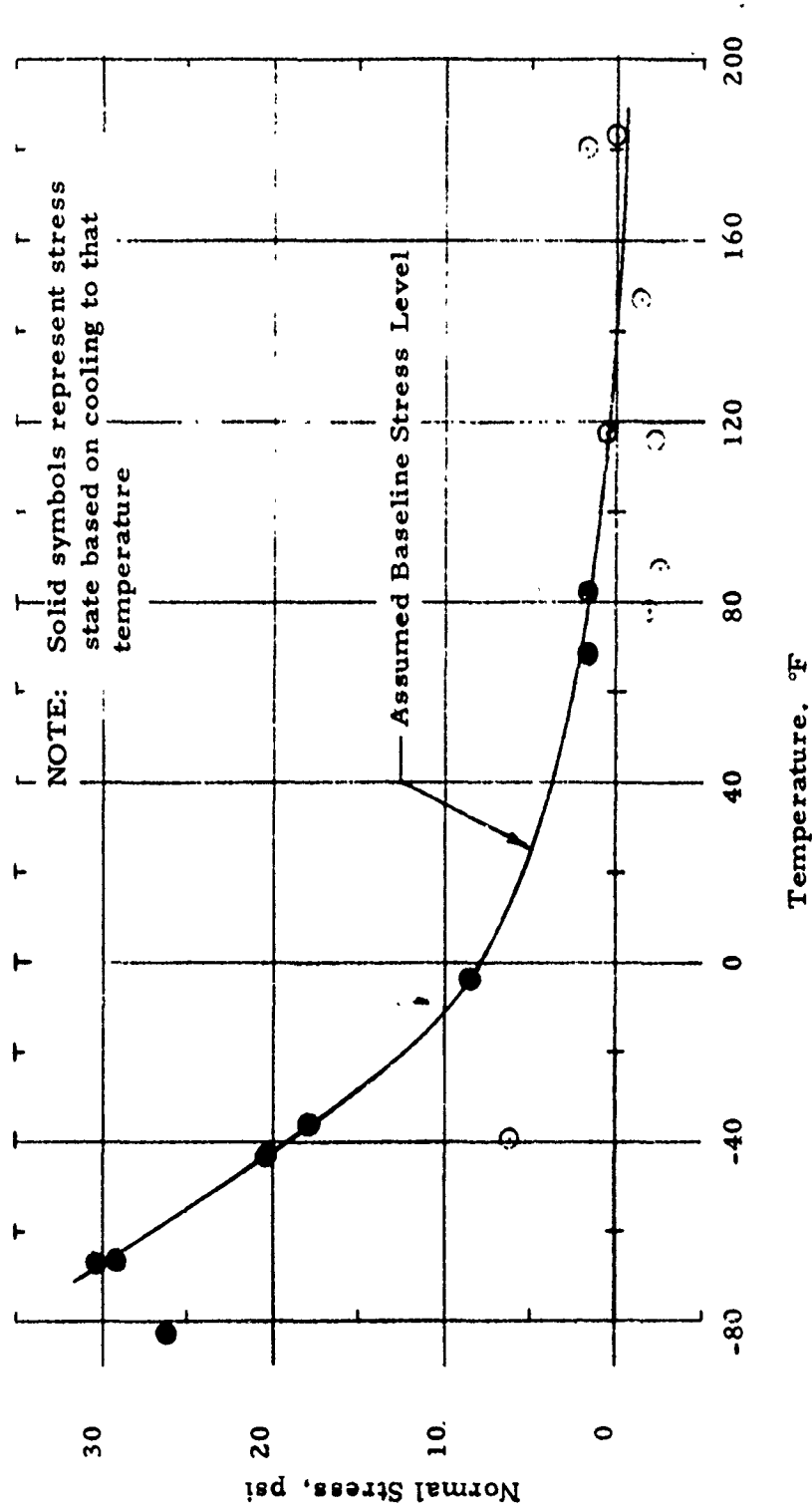


Figure 93. Baseline Stress Data For Gage N3-45

- N3-44 Fwd
- △ N3-43 Center
- N3-47 Center
- ◇ N3-45 Aft

$$\Delta\sigma = (\sigma_{act} - \sigma_{base}) - (\sigma_{act} - \sigma_{base})_{Test A-1}$$

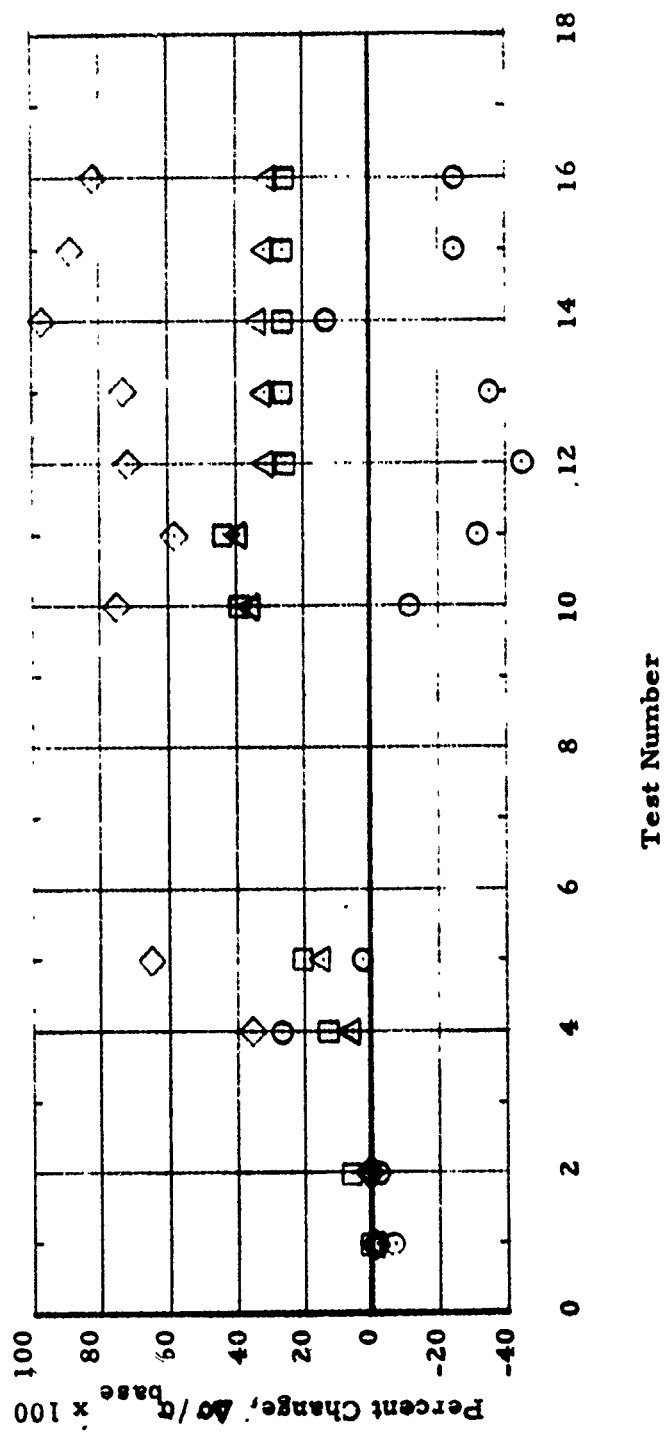


Figure 94. Change in Stress in IM #3 at -65°F Due to Aeroheat Cycling

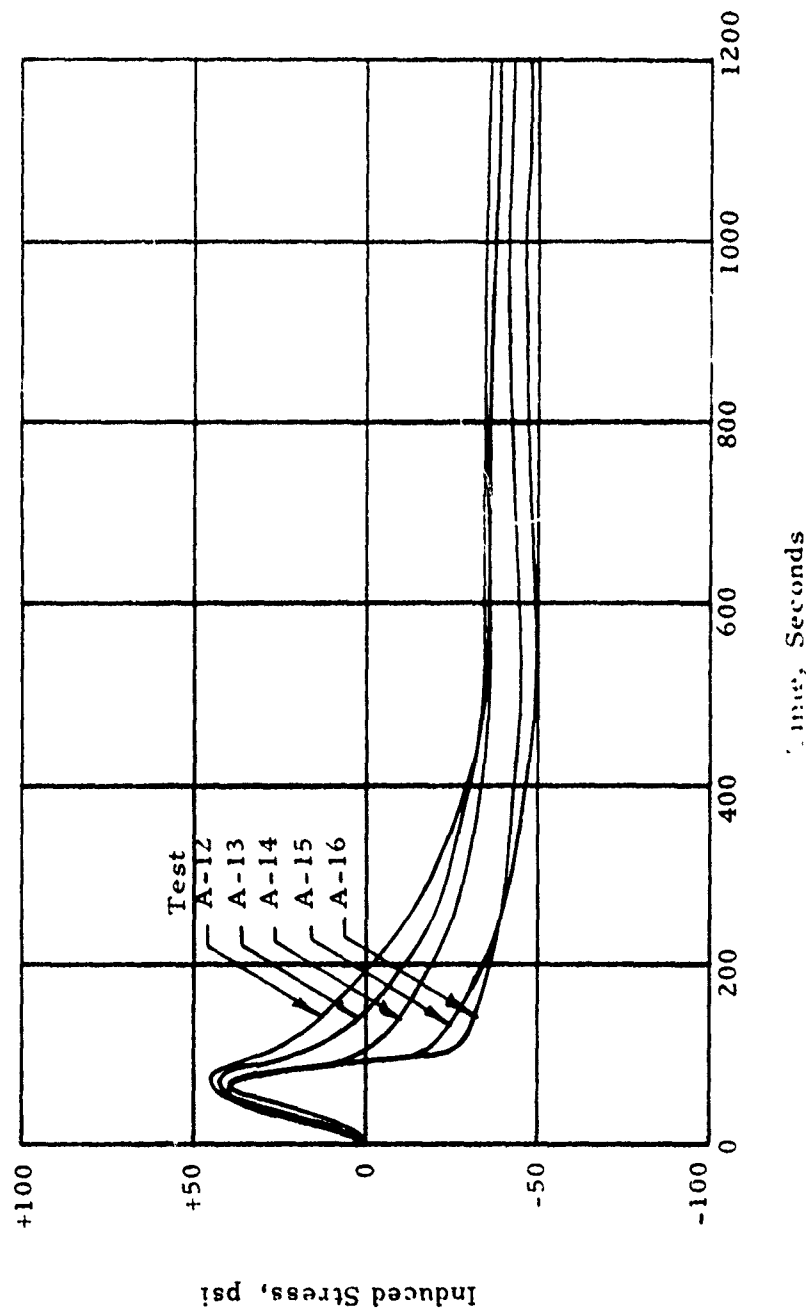


Figure 95. Aft End Motor Stress Relaxation Rate Increase Observed by Gage N3-45

tion will reveal two aspects--poor repeatability and a change in direction of response at low temperature--which must be considered abnormal for a shear gage. Examination of similar shear gage data for the other motors will illustrate these differences. The data produced by this gage during the aeroheat tests show little effect of the aeroheat loads imposed with the exception of the  $-65^{\circ}\text{F}$  initiated SFPI tests. For tests 12-16, a shear stress level of 6 to 8 psi as shown typically on Figure 96 is induced by the aeroheat cycle. Although not shown on Figure 96 relatively good repeatability from test to test was found; furthermore, no change in the shear stress level under  $-65^{\circ}\text{F}$  equilibrium loading is observed. The peculiar aspect is the decay in output after the peak stress levels have been reached. The abrupt change in direction as shown on Figure 96 at approximately 720 seconds indicates a continuation of the same behavior noted in the gage checkout data. The abruptness of the change would seem to indicate a malfunction of one of the semiconductor strain gage elements within the gage. Basically then, the shear gage data can neither be used to confirm nor deny observations made from the normal gage data.

The clip gage data when examined in a manner similar to the normal gage data do show similar results. The bore strain measured under a  $-65^{\circ}\text{F}$  equilibrium load and also induced by aeroheat loads was observed to have changed with the percent difference in bore strain at  $-65^{\circ}\text{F}$  as a function of test numbers is shown on Figure 97. The manner in which the values of percent difference were calculated is illustrated on the figure. The baseline strain was determined in the same manner as was done with the normal stress gage, that is, through use of the gage checkout data. These baseline data are shown on Figures 98, 99 and 100 for clip gages C3-18, C3-19, and C3-20, respectively. The decrease in strain level noted to have accumulated with time or test numbers would indicate either an unbond condition or bore cracking. The very large changes seen at the aft end of grain does indicate considerable unbond which grows with each succeeding test.

Changes in the level of strain induced by aeroheat are illustrated on Figure 101. The data presented are from Gage C3-19 (located near the aft end of the small bore) for the SFPI Tests 12-16. (Similar results were obtained from the other gages.) The decrease in induced strain with each succeeding test is obvious. This decrease correlates well with the reduction in strain at the equilibrium loading condition which confirms a definite degradation in motor structural integrity. Additional evidence for confirmation of this conclusion can be gathered by inspecting all the clip strain data as presented in Volume II.

Because of the non-linearity with temperature and shift in gage output of the clip gages as is evidenced on Figures 98-100, emphasis was placed on determining the correctness of the gage measurements. Basic bore strain clip gage measurements were checked by making comparable bore diameter measurements. The results of these measurements are presented on Figure 102 in terms of bore strain in percent as a function of motor temperature. These measurements were made adjacent to the clip gage C3-19 located

Motor - IM #3  
 Test - A-12 (SFPI)  
 Gage - S3-104  
 Location - Fwd  
 T<sub>initial</sub> - -65°F

Data based on gage output being adjusted to zero (0) reading  
 when motor is equilibrated to a temperature of +170°F.

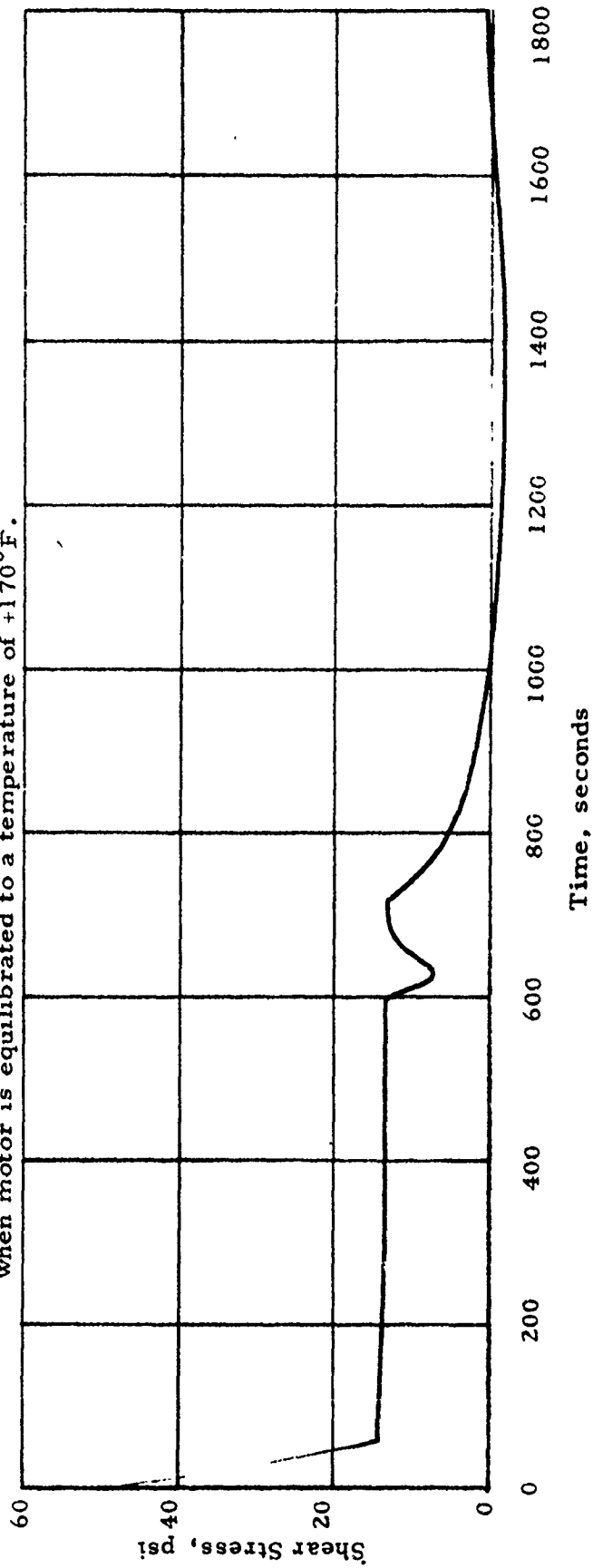


Figure 96 Head End Shear Stress Response to Aeroheat Loads -- Gage S3-104

- C3-18 Forward
- C3-20 Aft
- ◇ C3-19 Aft

$$\Delta = (\xi_{Act} - \xi_{Base}) - (\xi_{Act} - \xi_{Base}@A-1)$$

$$\% \text{ Diff.} = \Delta / \xi_{Base} \times 100 \%$$

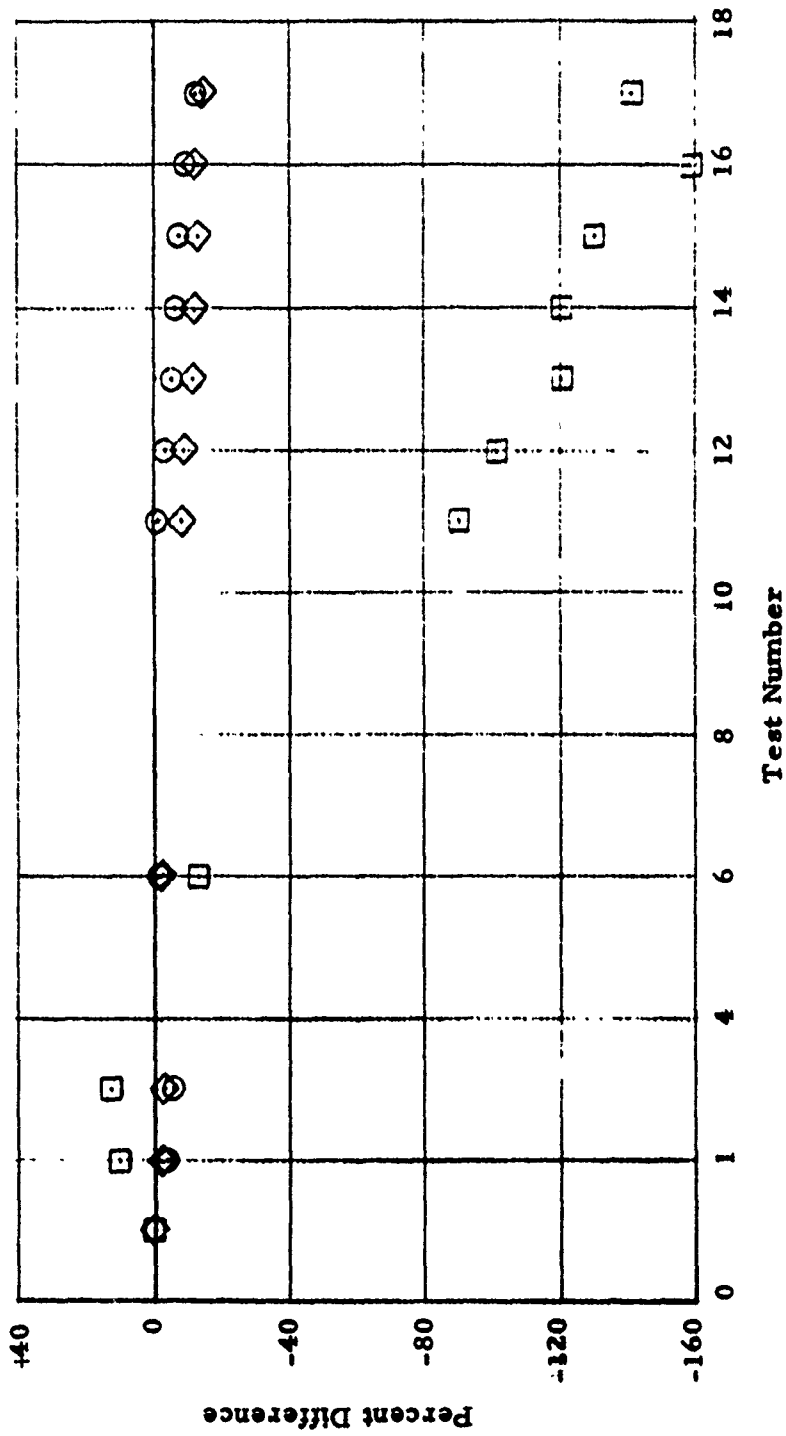


Figure 97. Change in Bore Hoop Strain in IM #3 at -65°F Due to Aeroheat Cycling

Motor - IM #3  
 Gage - C3-18  
 Location - Forward  
 Source - Gage Checkout Tests

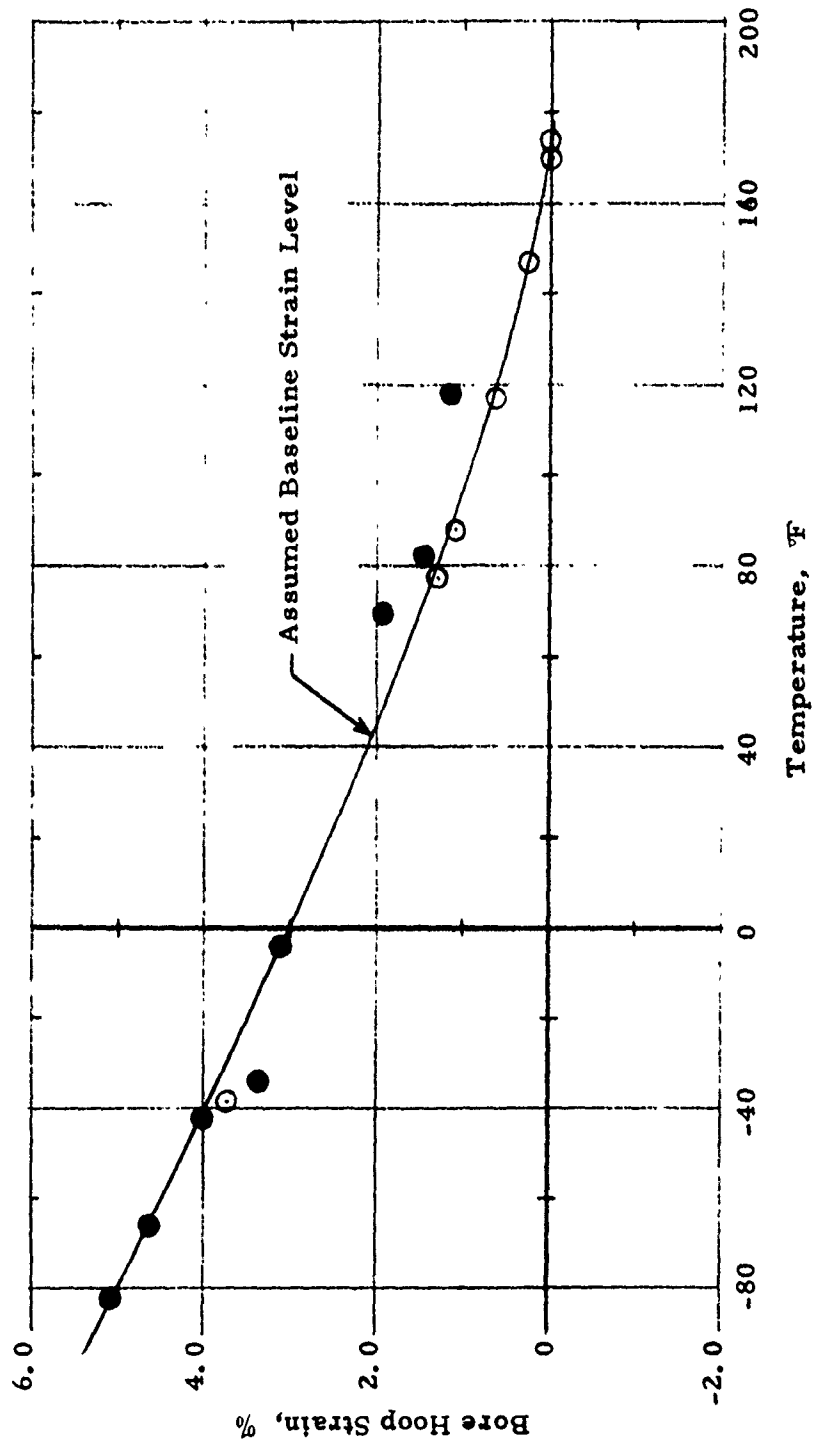
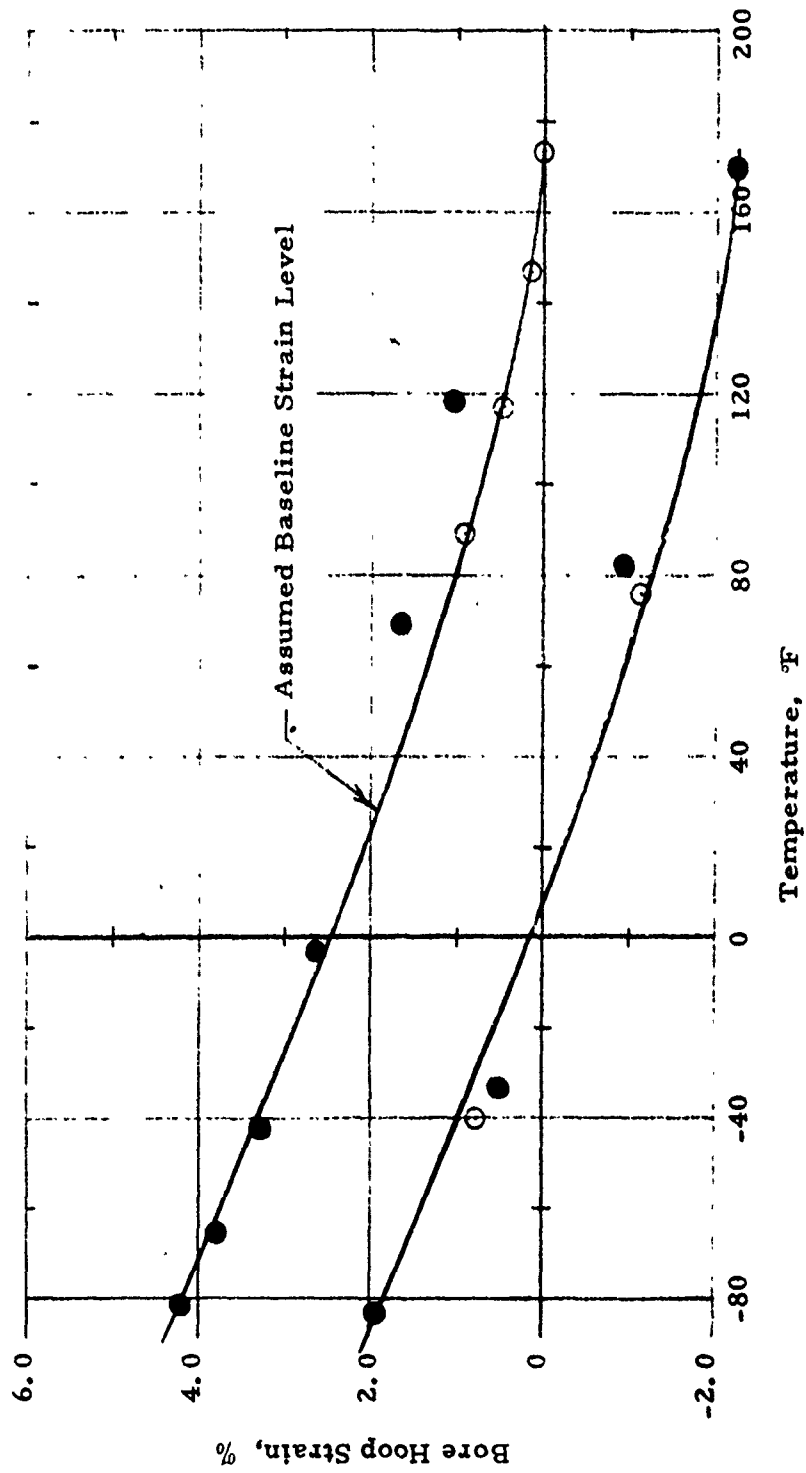


Figure 98. Baseline Bore Strain Data From Gage C3-18

Motor - IM #3  
 Gage - C3-19  
 Location - Aft (small bore)



Motor - IM #3  
 Gage - C3-20  
 Location - Aft

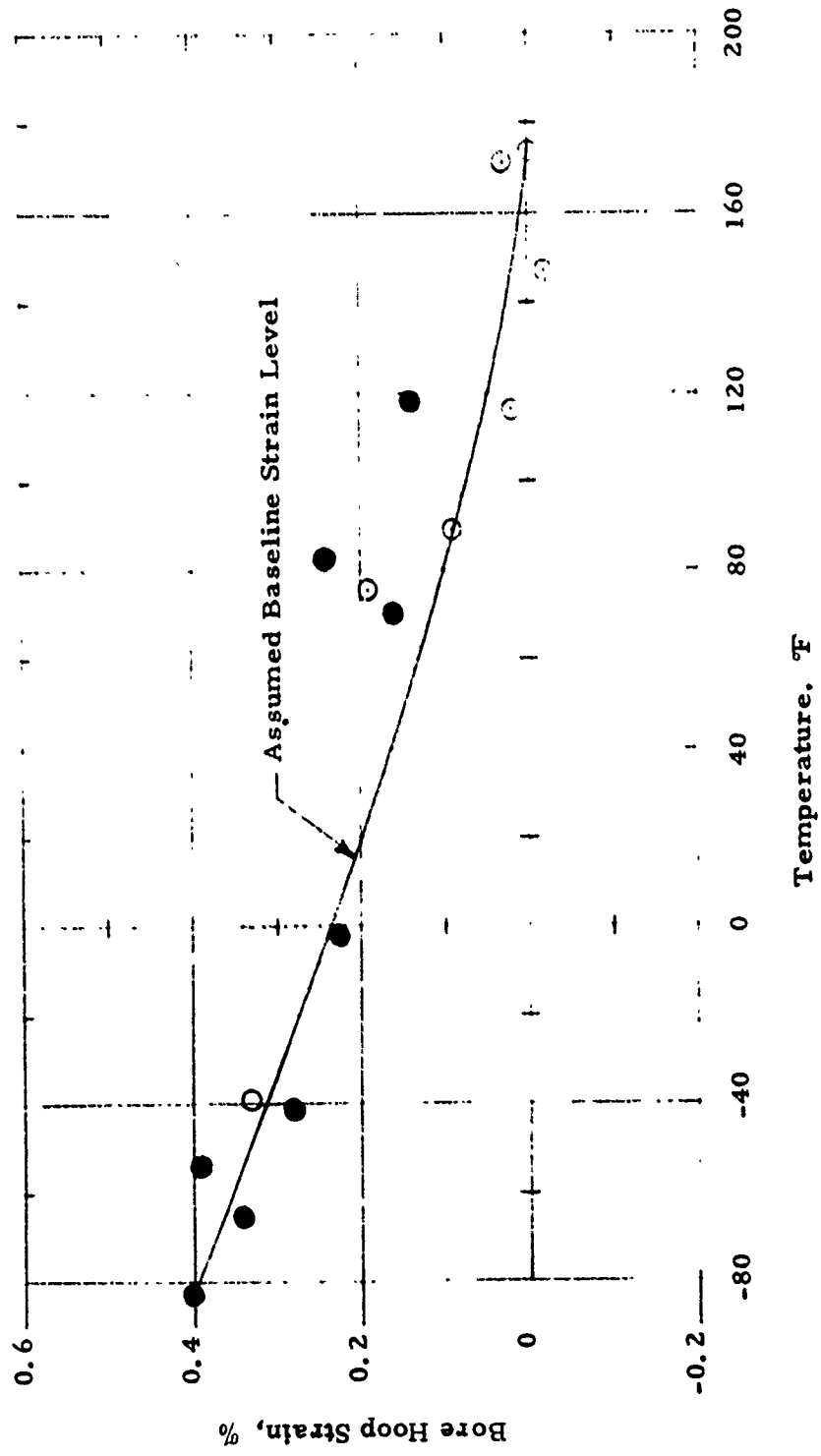


Figure 100. Baseline Bore Strain Data From Gage C3-30

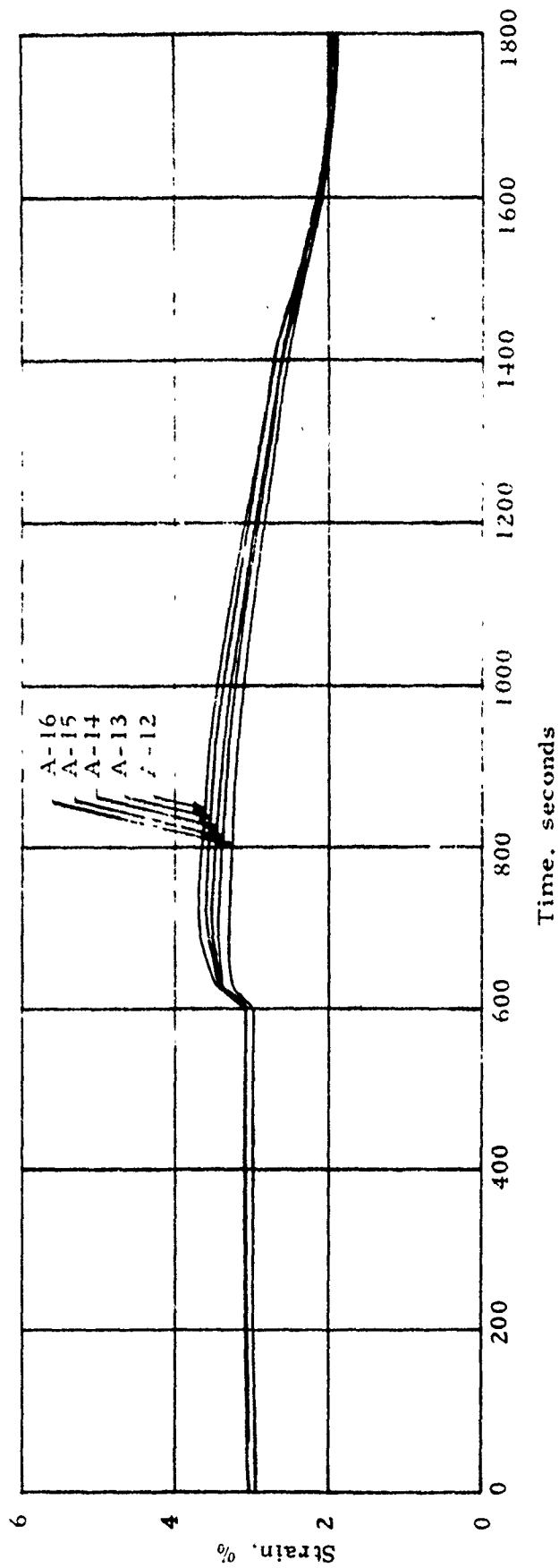


Figure 101. Comparison of Results from Successive SFPI Tests -- Gage C3-19

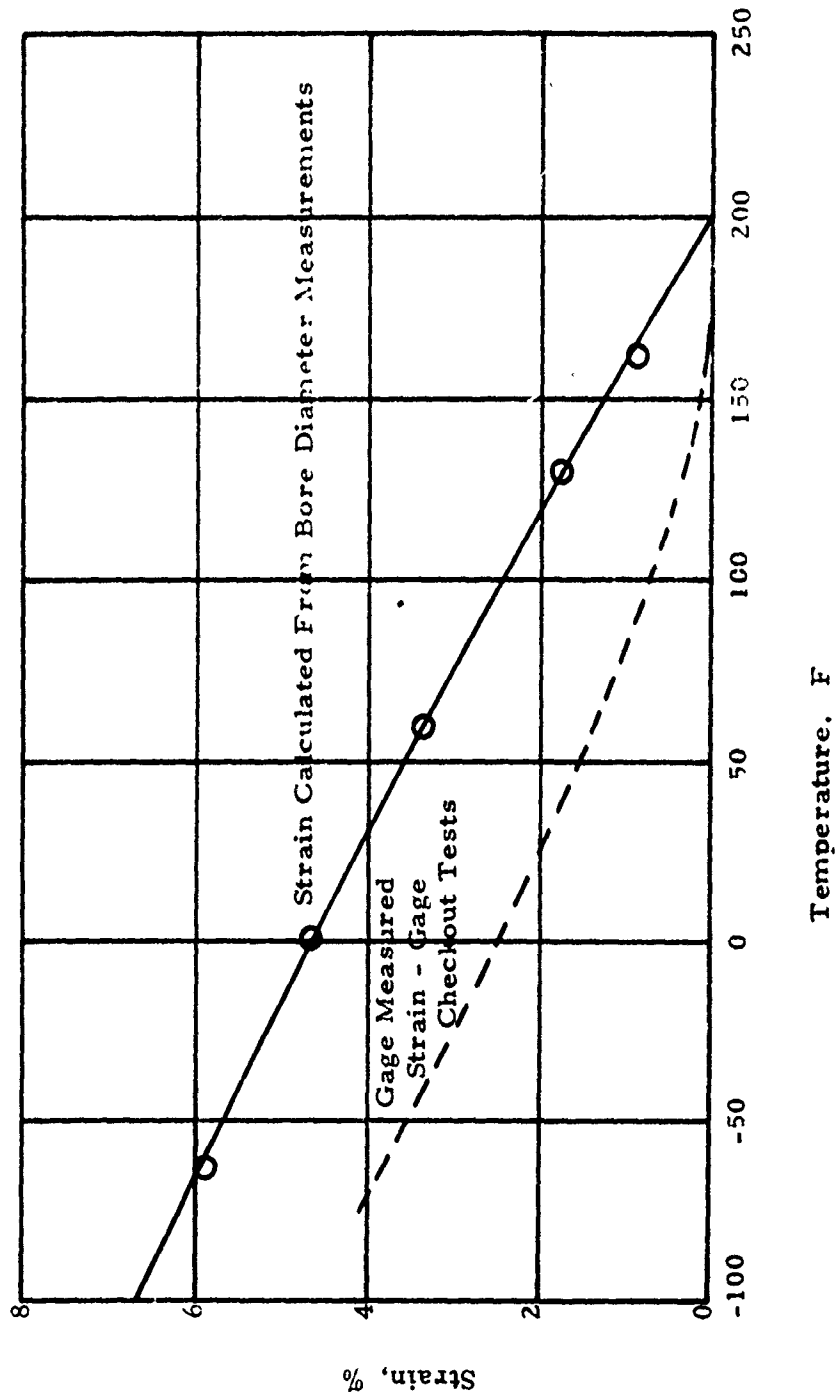


Figure 102. Comparison of Gage Measured Strain With Adjacent Bore Diameter Measurements - Gage C3-13

in the aft portion of the small bore. The output of this gage is also presented on Figure 102 for comparison purposes. The poor agreement is obvious. Much of this is artificial because the gage output has arbitrarily been zeroed out at 170°F. Therefore, a more appropriate comparison is one where the bore diameter measured data are moved downward to intersect zero at 170°F. The major disagreement then appears to be slope, except at the low temperatures. It is obvious that the gage measured a relatively linear phenomenon in a nonlinear manner. Recalibration of two gages removed from IM #2 provided a probable explanation for this nonlinearity effect. These two gages were found to be linear only when they are being strained at levels of 2 percent or better. The gage sensitivity (mv/ $\mu$ in) increased at lower strain levels. Since the gage data are reduced based on a fixed value of sensitivity, the effect of an increase such as this would result in showing relatively little strain change at the low strain levels resulting in a curvature in the gage data at the higher temperatures. Therefore, the accuracy of the clip gage data are questionable in terms of actual strain levels. However, at the lower temperatures in the data in terms of differences resulting from some other loading such as the strain induced by aeroheat, would, of course, be accurate. Also, the use of the gages to define changes in the structure at low temperature as a result of repeated loading would be appropriate. The clip gages are then thought to provide accurate data only when used as reference instruments at low temperatures.

Checks on the sensitivity of the normal gages in IM #3 were made prior to the simulation tests. This was accomplished by using a vacuum pump and reducing motor cavity by approximately 5 psi. The gage output reduced in terms of sensitivity (mv/psi) was then compared to that measured during gage checkout tests. Basically, a change in sensitivity was found in the gages located in the center portion of the motors. Little change was found in head-end and aft-end gages. Complete results of these pressurization tests are presented and discussed in the section entitled Motor Dissection and Propellant Property Testing.

At no time during this series of tests were any sign of bond failure detectable by sonic and ultrasonic inspection or was bore failure detectable by visual inspection. Movement of the aft face of the grain was detected; however, after Tests 15, 16, and 17. In subsequent visual inspection of the bore, and then only under diffuse light, a pattern of bore cracks was observed. These cracks were approximately 1 to 2 inches long and ran in the longitudinal direction. These cracks existed in the mid-section of the small bore and covered an area approximately 8 inches long by 10 inches in circumference (approximately 75 percent of the bore circumference). The patterns and location of these cracks in the bore had the typical appearance of fatigue cracking. Evaluations of the bore strain gage results indicated strain reduction (motor thermally equilibrated at -65°F) over the previous 5 tests. This tends to correlate with a corresponding slight decrease in measured stress level in the previous 5 tests as can be inferred from Figure 93. This strain and stress relief as measured could indicate when cracking first began.

## IM #1 Results

Aeroheat testing of IM #1 consisted of a total of twelve tests as delineated in Table 10. These 12 tests, together with the 17 made on IM #3 and the 21 made on IM #2, total 50 aeroheat tests conducted on instrumented motors during this program. As shown in Table 10, the test series conducted was made using the DMP-3 mission in conjunction with an initial motor temperature of  $-65^{\circ}\text{F}$  as the baseline test condition. This test series was very similar to that conducted on IM #3 with the last eight tests being identical. No usable data were obtained from Test 11 because of the gage power supply being accidentally disconnected. A complete series of graphs documenting these data is contained in Volume II.

Instrumented motor IM #1, was based on the Maverick grain configuration. Since the web fraction of this motor is only 0.365 as compared to 0.569 for IM #2 and IM #3, much lower bond line stress and core strain levels were expected on the other tests. However, this was not borne out by the results of the gage checkout tests as shown in Appendix A. Inspection of these gage checkout normal stress data show the same order of magnitude for all motors. The strain levels are lower as anticipated. In general, the data obtained in this series of tests exhibit the trends found in IM #3. The two gages located in the center portion of the motor are found to disagree to some extent. The stress level as measured by Gage N1-49 appeared to become less sensitive to mission type as the test series progresses. This is illustrated on Figure 103 when the output of this gage is compared for Tests A-1, A-10, and A-11. Tests A-1 and A-11 are the DMP-3 type, while Test A-10 was a SFPI type. The other gage located in the center of the motor, N1-40, shows entirely different response characteristics for Test A-1 as shown on Figure 104. Unfortunately the output of this gage increased to such a point that it went off scale on the SFPI tests and the last DMP-3 (A-12) and comparisons are not possible. For Test A-1, however, the response of N1-40 is much consistent with results from the other motors. The output from N1-49 is on the other hand not consistent and probably indicates a bad gage. As stated, in many aspects the results of the IM #1 tests and the IM #3 tests are quite similar. Both show that very rapid relaxation occurs after a stress rise; both show a tendency to go into compression near the end of the test; and both show an increase in stress level as the testing is continued.

The changes in measured level for each normal gage as the testing progressed are presented on Figure 105. As shown, some deviations are found. Two gages, N1-40 (as mentioned above) and N1-50, went off scale. The last on-scale measurement made with these gages are shown. That is, N1-50 was completely off scale in the positive direction after Test 8. Gage N1-40 was off scale in the positive direction after Test 9. These data seem to be completely reversed from those measured on IM #3. That is, the head-end gage increased output in this motor whereas it decreased in the IM #3 tests. The aft-end gage is completely reversed also. The center gages in IM #3 compared well with each other as they both increased. Here we see N1-49 decrease while N1-40 increases to such a point that it went off scale.

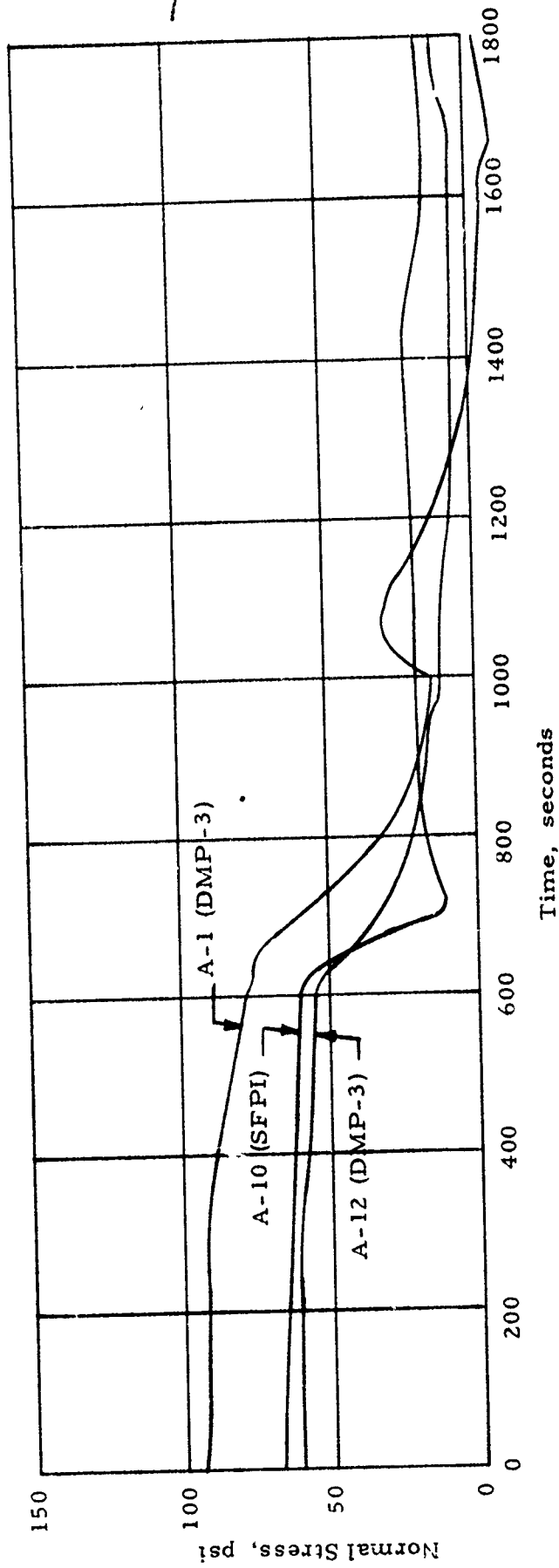


Figure 103. Change in Gage NI-49 Response for Various Tests

Motor - IM-1  
 Test - A-1 (DMP-1)  
 Gage - N1-40  
 Location - Center  
 T<sub>initial</sub> - -65 F

Data based on gage output being adjusted to zero (0) reading  
 when motor is equilibrated to a temperature of +170°F

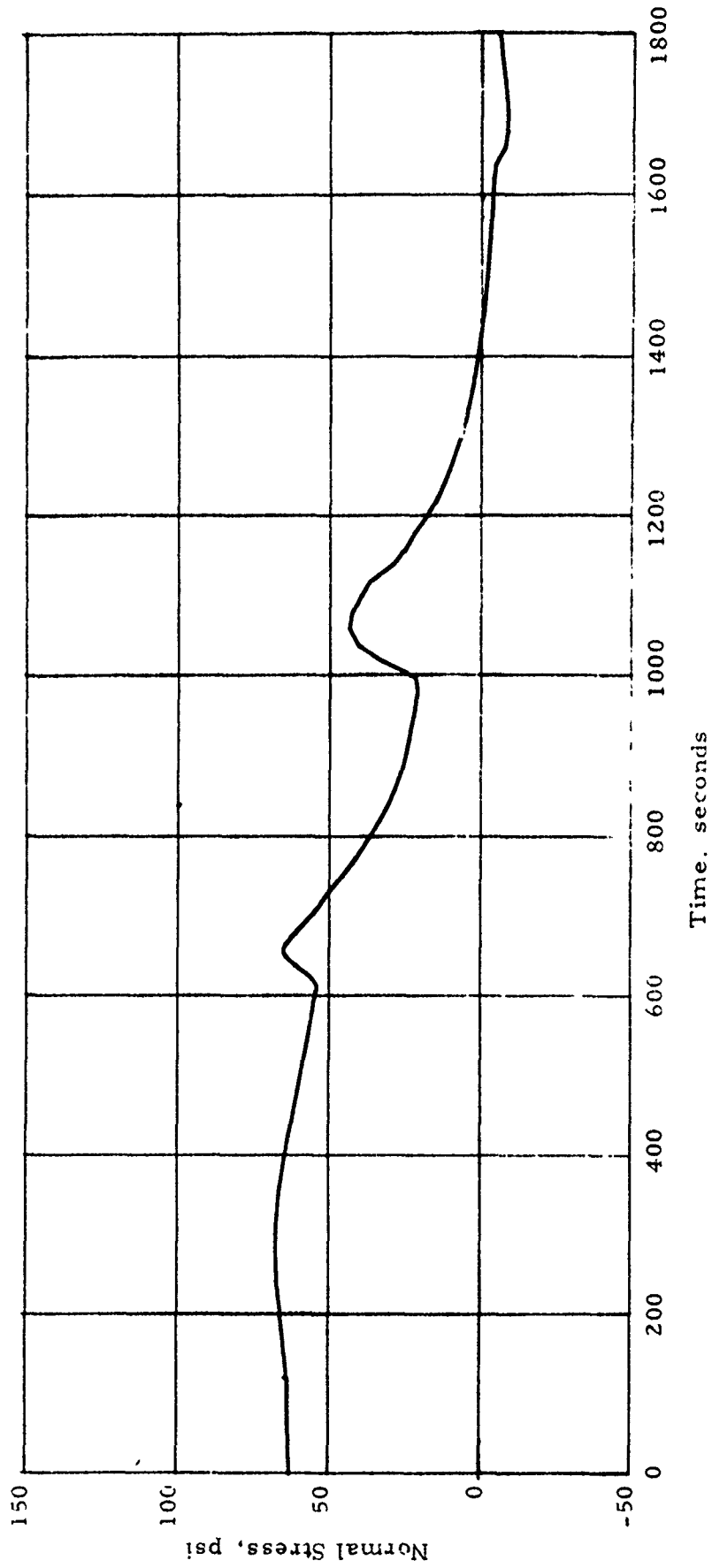


Figure 104 Mid Motor Stress Response to Aerobheat Loads - Gage N1-40 (Test No. A-1)

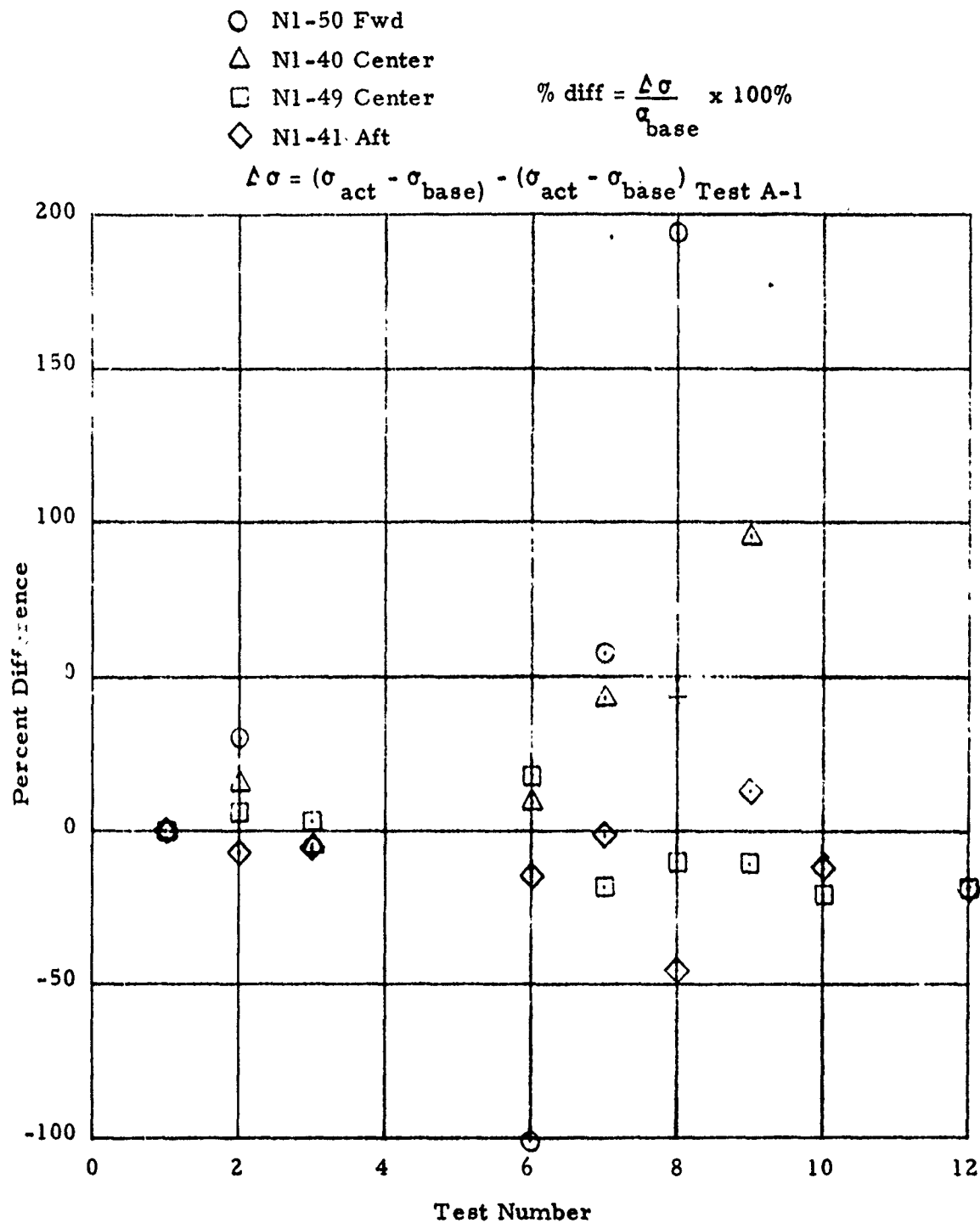


Figure 105. Change in Measured Stress in IM #1 at -65°F Due to Aeroheating Cycling

Probably the greatest difference between IM #3 and IM #1 normal gage results is in consistency. IM #3 results were very consistent while the converse is true of IM #1. The only rational explanation for this inconsistency must be based on the gages themselves.

Only one shear gage (S1-109) was in this motor and the results from it indicate little if any change in output over the test series for an equilibrium load. Repeatability in measured induced stress over the SFPI series is good. These data, while perhaps open to question in terms of accuracy, are consistent and do not show any signs which could be interpreted in terms of an unbond failure in the head end. Therefore, they cannot be used to confirm the changes in N1-50 as being motor structural degradation.

The clip gages also do not show any gross changes over the test series. These data were correlated in the same manner as those in IM #3 and the normal gages of IM #1 presented in Figure 104 with only a few percent change noted. This correlation has not been presented herein since nothing there could be related to motor degradation and failure is evident. This can easily be seen by a cursory inspection of these clip gage data shown in Volume II. The strain rise induced by the aeroheat loads are also consistent although not large. The maximum induced amount is only about 0.2 percent or about 3 millivolts. This is probably just about the accuracy of the system which limits the results to qualitative observations. In this vein, a comparison between the bore strain levels induced on IM #1 as compared to IM #3 for the SFPI profiles show that the CP motors had an induced strain about five times greater than the star configuration. Unfortunately this ratio cannot be estimated from gage data for the equilibrium loads because of the inability of a clip gage to measure absolute strain. It can only measure strain difference between various loading conditions. In order to obtain an actual value of strain, the actual strain must be known at some reference temperature with gage then provide the differences as temperature is changed.

## Aeroheat Simulation Testing

The basic purpose of this effort was to devise an equilibrium temperature cycle which would reproduce the maximum stress and strain levels encountered in the aeroheating tests. This was originally planned to be accomplished in four distinct steps or subtasks. First, the aeroheat data were to be analyzed and correlated. Based on these correlations, a basic simulation cycle would be tested with a previously unused instrumented motor. Upon satisfactory simulation of the aeroheat cycles tested in Task 3, a failure schedule was to be defined which would simulate the stress and strain levels induced when the first motor was failed by aeroheating. This schedule would first be postulated based on the basic simulation testing then confirmed by an actual test cycle. Verification of this failure cycle would be accomplished under Task 5. Inasmuch as all three motors were subjected to aeroheat testing which resulted in two different failures (unbond on IM #2 and bore crackin on IM #3), the basic assumption of simple failure, assumed when initially visualizing this program, was found to be nonexistent. Thus, the effort in Task 4 had to be altered to comply with both the number and state of the instrumented motors available and the knowledge gained to date. These alterations are noted in the following discussions.

An obvious result of the analyses of the aeroheat data was to find that the aeroheat induced stress and strains were short duration phenomena and a function of initial motor temperature. It was also obvious that these data could not be reproduced through equilibrium temperature cycling. The reason for this is based on consideration of the failure mode itself. Failure induced by cooling occurs at a relatively low stress level. That is, the load is generally applied quite slowly so that a relatively long-term modulus exists. In aeroheating, the load is applied quickly with corresponding higher stress. In visualizing this phenomenon on the failure boundary curve, an equilibrium cycle would produce a failure by exceeding strain endurance and/or the right hand boundary. The aeroheat cycle on the other hand would penetrate the top of the curve as seen on Figure 106. Thus it is obvious that the aeroheat failure mode could not be simulated by equilibrium cooling. However, it was thought that the aeroheat cycle might be approximated by rapid cooling and heating in the conditioning box and still force a high stress type failure. However, this is only an approximation since real time cannot be simulated. Aeroheat can only be simulated through simulation of proper heating rates as a function of real time.

Since real time could not be simulated in the conditioning box, it was decided to establish a simulated cycle which could possibly produce a similar stress level as a function of temperature without an appreciable compromise on the strain level. To do this, selected aeroheat data from IM #1 and IM #3 were replotted as a function of local temperature. These data were then compared for similarity with the gage checkout data (Appendix A). The general result of this comparison is shown schematically on Figure 106. The deviation would, of course, indicate the severity of the aeroheat cycle.

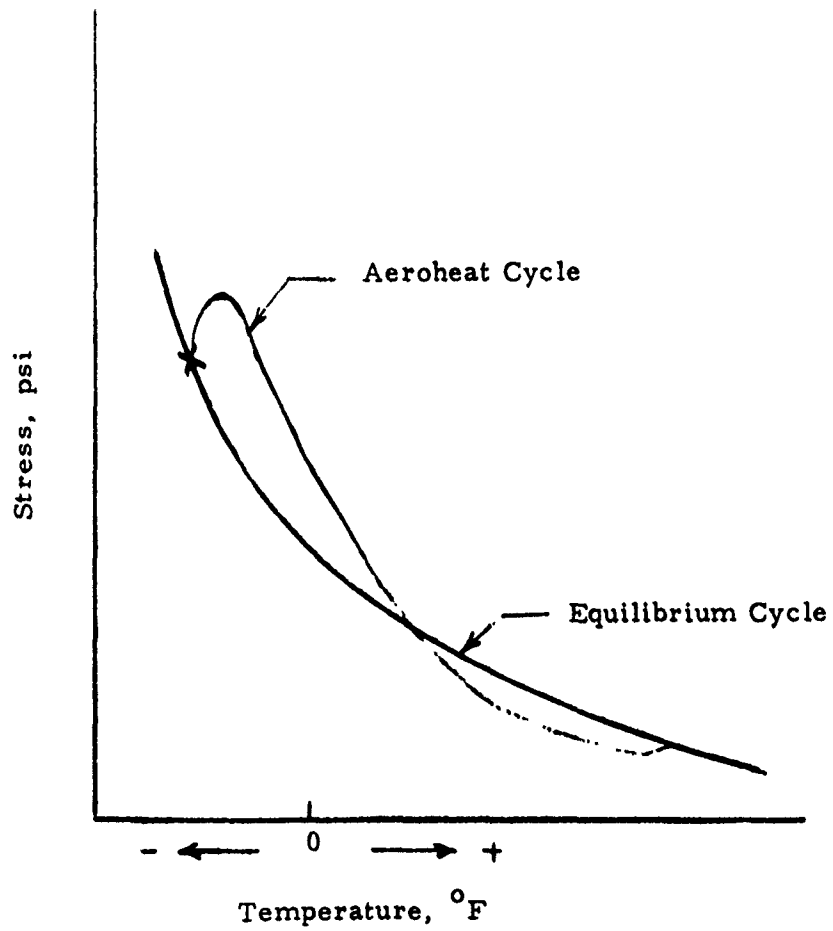


Figure 106. Difference in Stress Levels Between Aeroheat and Equilibrium Cycles

Inasmuch as the purpose here was to define a failure schedule, the most severe cycle that could possibly be produced in the conditioning box was postulated. Even then little hope was held for achieving a failure distribution from the seven motors to be tested because of the inability to fail either UM #1 or UM #2. Basically the cycle consisted of conditioning the motors to  $-65^{\circ}\text{F}$ . Next we wanted to further shrink the grain as much as possible without inducing any significant increase in bore strain. The rationale here was to provide as much movement of the case as possible during initial exposure to high temperature in an attempt to maximize induced stress. Therefore, the first step in the approximation was to rapidly cool the motor from  $-65$  for some period of time. This period of time was set at 90 minutes which corresponded with attaining no more than about 10 degrees decrease in bore temperature but as much as a 25 degree decrease in case temperature. From this point the box was heated rapidly by circulating raw steam (low flow rate) in the box for 30 minutes after which heating was decreased to normal box operation.

This cycle was tested with both IM #1 and IM #3 in the box at the same time. A comparison of the output of selected gages between the last aeroheat test and the simulation tests provide reasonable agreement as shown on Figure 107. Since many of the stress gages in IM #1, were off scale during the aeroheat tests and since IM #3 had undergone some temperature cycling subsequent to its aeroheat tests which had induced apparent bore cracking and unbond, these comparisons can only be considered as qualitative. Since this cycle provides a reasonable approximation of a moderate aeroheat cycle, testing of the seven uninstrumented motors was initiated. The fact that the instrumented motors were already damaged but still had the capability of acting as analogues to signal cumulative effects from this cycling warranted these inclusions in the testing.

The uninstrumented motors chosen for these tests were reject production motors; rejected solely for voids in the starpoints. They had been stored at ambient since manufacture and were approximately one year old. The motors were from four different mixes and had strain capabilities at  $-75^{\circ}\text{F}$  from a low of 14 percent to a high of 49 percent.

A total of 19 tests was conducted on these motors without apparent damage. Complete sonic and X-ray inspections made after culmination of the test program did not show any defects or differences from the X-rays made after production.

The instrumented motors were removed from this test series after the twelfth test and dissected. The change in gage output under equilibrium conditions are shown for both motors on Figures 108-111. The percent change in outputs of the normal and clip gages in IM#3 are shown on Figures 107 and 108 respectively. Also shown on these figures is the temperature levels that the motor cases were subjected to during this time period. The basic difference between these curves and those presented earlier are (1) the data are shown as a function of real time instead of test number, and (2) the complete test history is shown from the first aeroheat to the last simulation test. Similar

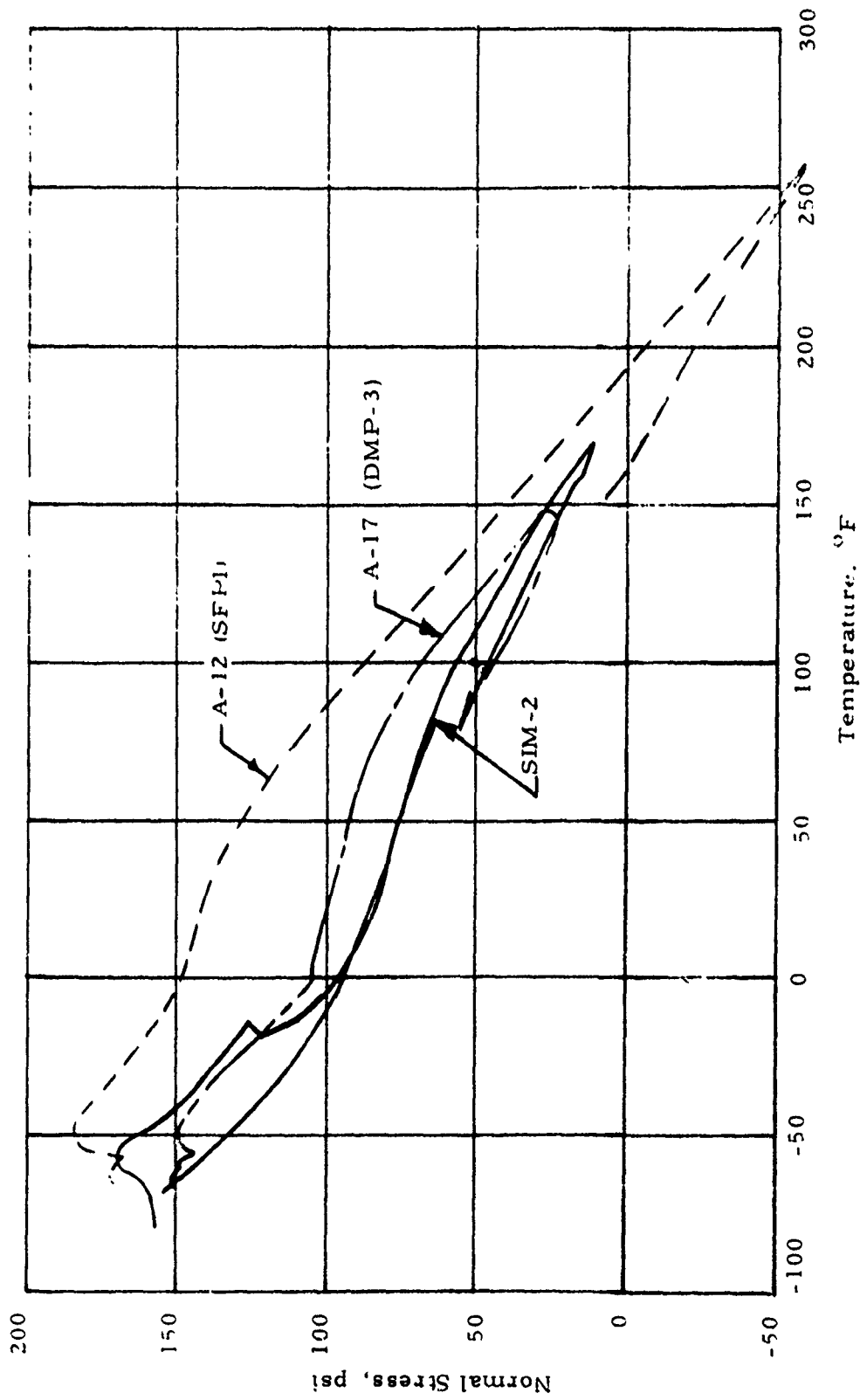


Figure 107. Comparison Between Aeroheat and Simulation Cycle for Gage N3-47.

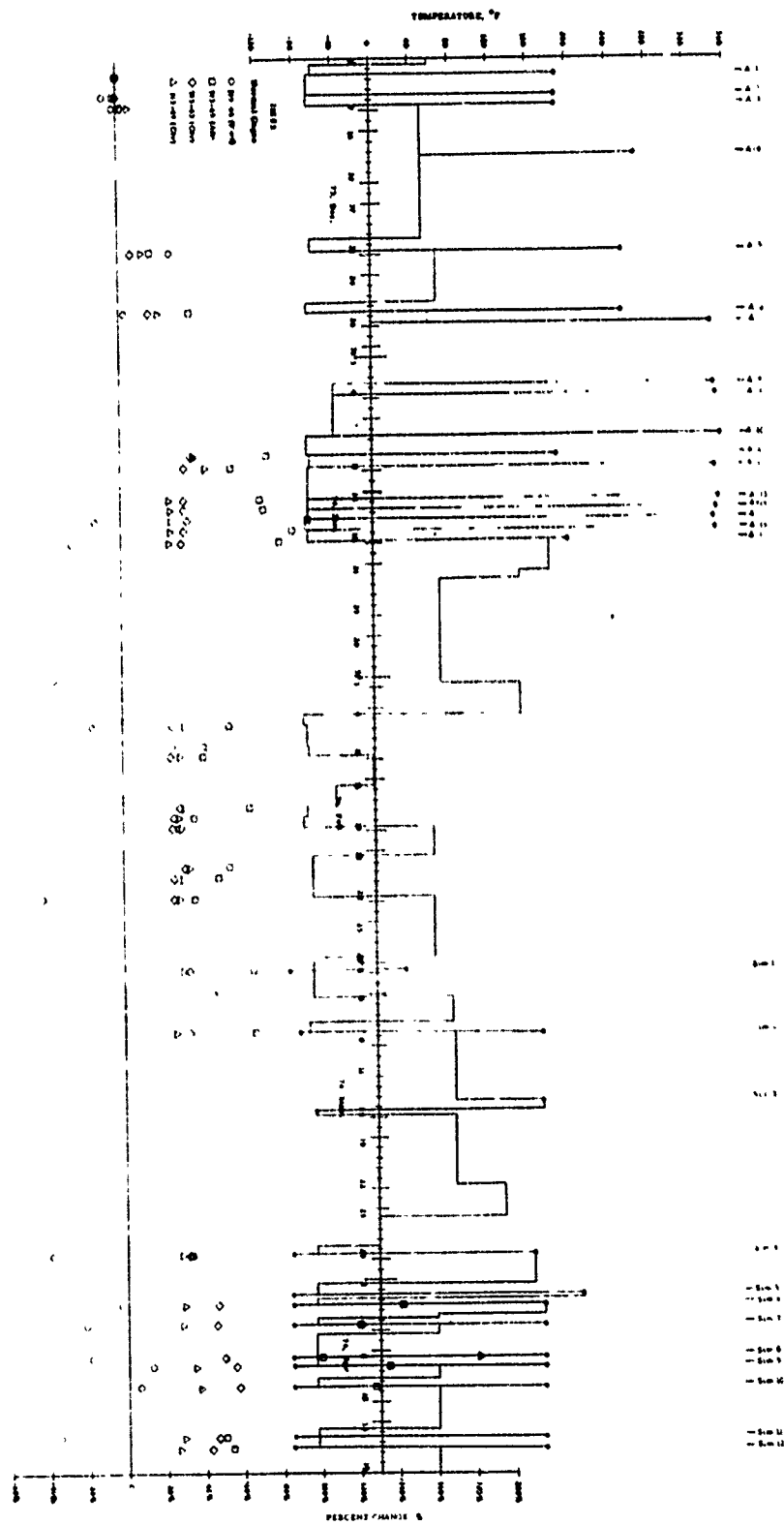


Figure 108. History of IM#3 Normal Gage Response Changes at -65°F.

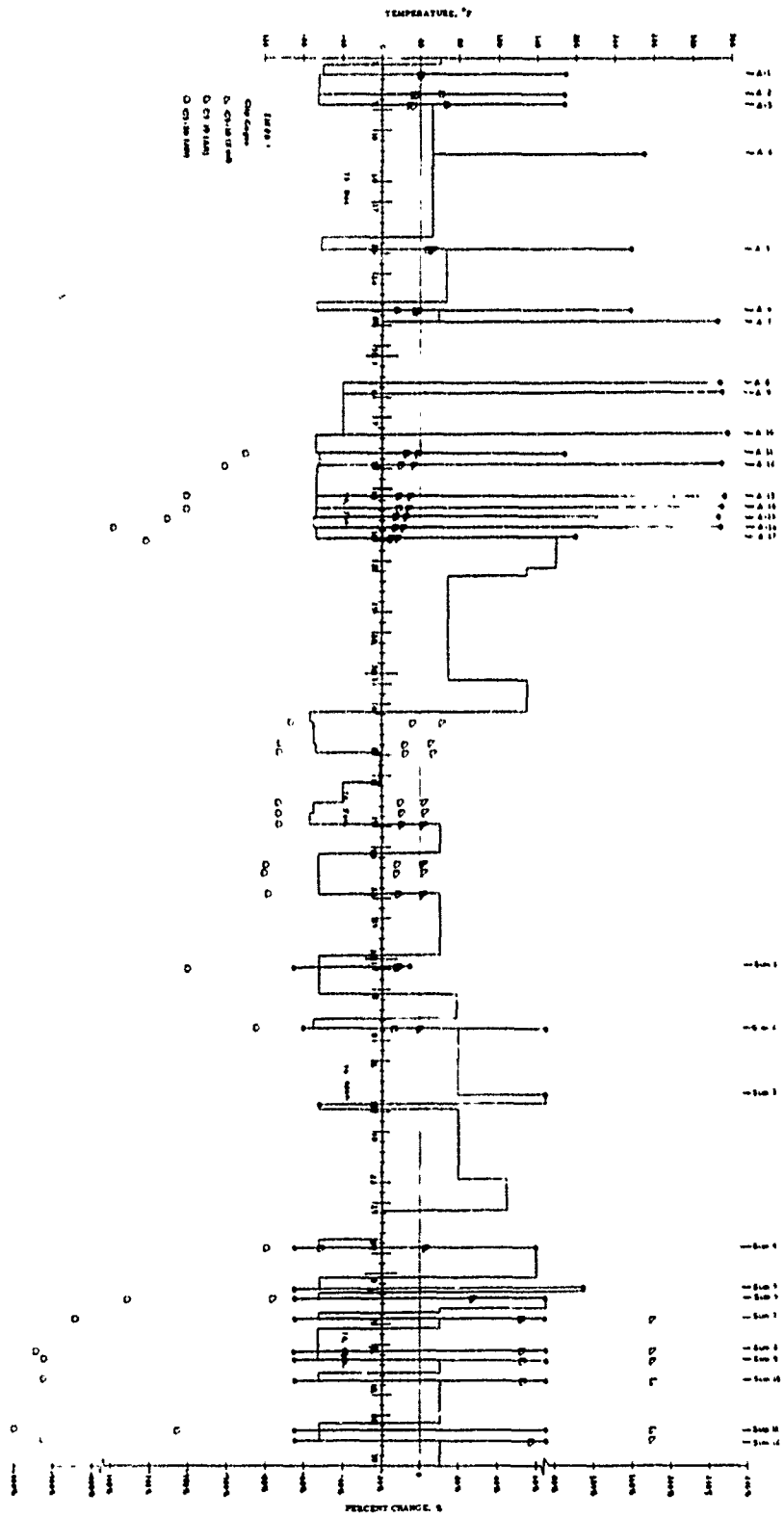


Figure 109. History of IM#3 Clip Gage Response Changes at -65°F.

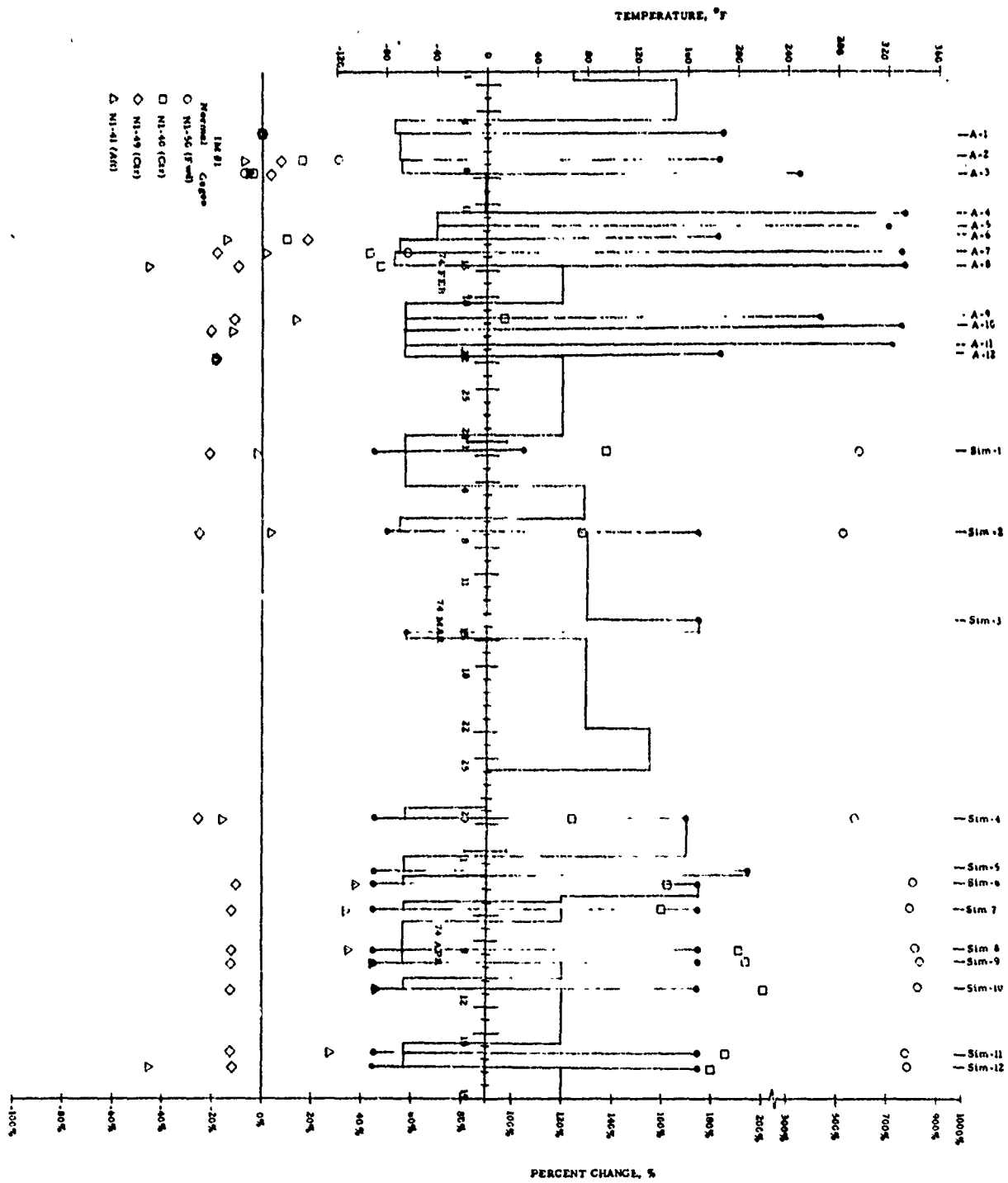


Figure 110. History of IM#1 Normal Gage Response Changes at -65°F.

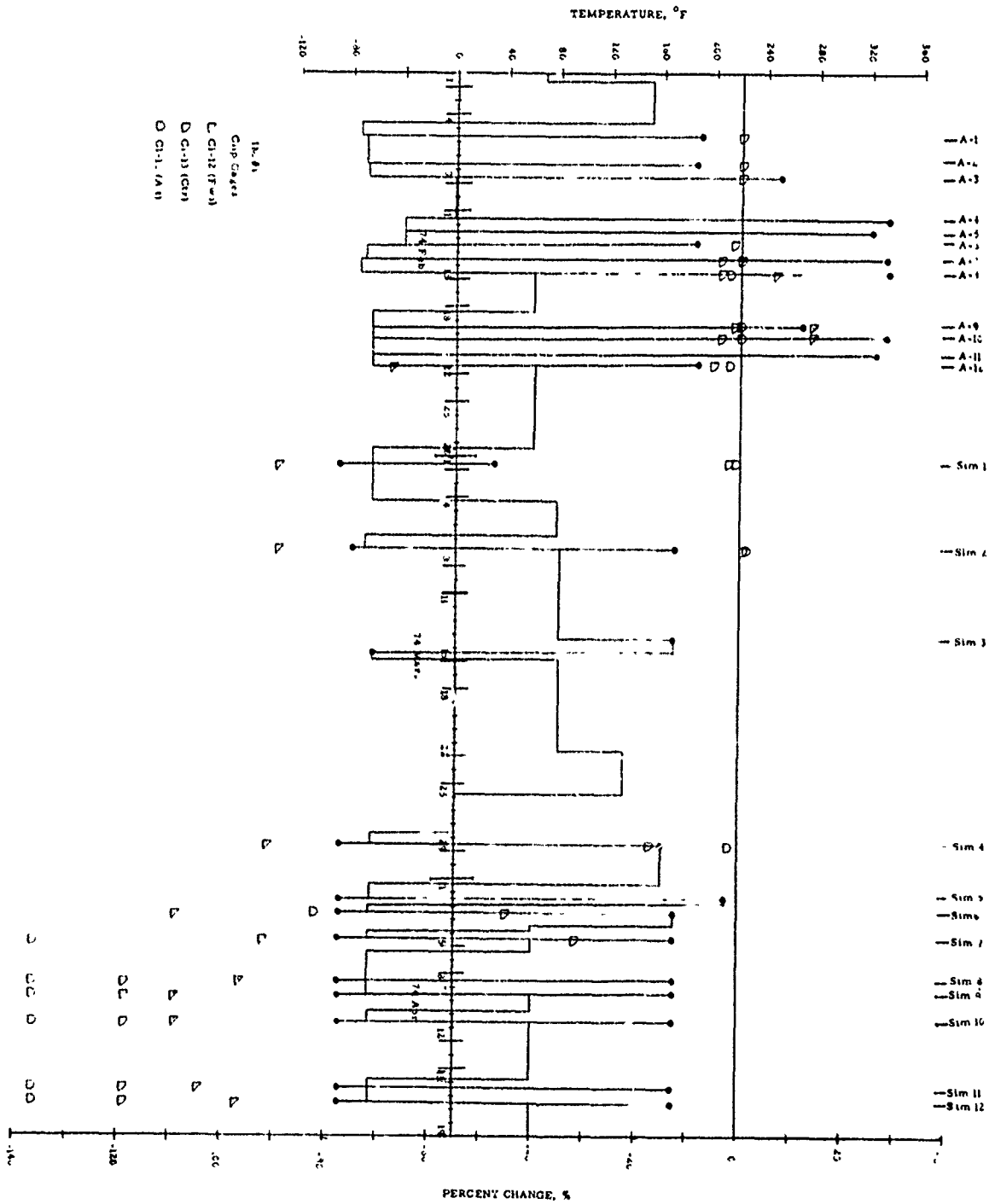


Figure 111. History of IM#1 Clip Gage Response Changes at -65°F.

data are shown for IM #1 on Figures 110 and 111. One of the most interesting aspects of these data is the tendency to move toward zero change after the motor is taken to cure temperature (170°F) as if some healing was occurring. Considerable changes are seen to occur near the end of the simulation tests which could indicate significant degradation of the motor. Significant degradation was found, at least, in terms of the bore cracking of IM #3. How much of this was caused by the load cycle and how much by other means such as water damage (Bore became frosted in IM #3 during bore diameter measurements) is not known. The results of the dissection discussed in the next section indicates that much of these changes are due to changes within the gages themselves.

## MOTOR DISSECTION AND PROPELLANT PROPERTY TESTING

In addition to UM #1 which was dissected to determine the state of the liner, all three instrumented motors were dissected. All four motors were dissected in the same manner. This involved cutting the motors into four segments by remote lathe operation as shown on Figure 112. The lathe was used to cut through the aluminum case only. The propellant grain was then severed using a butcher knife as shown on Figure 113. A photograph of IM #1 in the lathe after the head end had been removed is shown on Figure 114. Marks locating the other two cuts to be made on that motor can be noted. Propellant was then cut from the center two segments and delivered to the lab for preparation of specimens for physical testing. Each center segment was approximately four inches long and covered the position of the motor exposed during aeroheat testing.

### IM #2 Dissection and Propellant Testing

Prior to dissection of the motors, the condition of the grain termination region was examined. In IM #2, a massive area of visual unbond was noted over the aft end of the motor. This visual unbond area (liner to case) extended from a point about 45 degrees or about half way around the motor. At a point about 315 degrees, a gap of approximately 1/16 of an inch was found between the case and the liner, indicating a slump due to weight since the motor was always maintained in the same position. A section of propellant was removed at this point (315 degrees) to determine how far the unbond extended forward. The unbond was found to extend 3-1/4 inches forward. Another curious fact was that the propellant grain had moved forward in the case by as much as 1/2 inch at the bottom (180 degrees) and 1/4 inch at the top (0 degrees). Of course, this movement indicates that the liner is unbonded the entire way around the aft end. Photographs made of this motor after dissection are presented on Figures 115 and 116. The movement of the grain up into the case can be seen at the far edge of the aft section on Figure 115. Looking directly into the aft section, Figure 116, the gap between the liner and case can be noted on both sides of the area where propellant had been removed. The cleanness of the case exposed by propellant removal is also quite evident. Since a gap appears at the top coupled with maximum forward movement at the bottom, it appears that the grain had cocked within the case which was relieved to some extent by the unbond in the forward area. Also cocking of the grain would force it tight against the case on one side giving the illusion of excellent bonding at that point.

### IM #2 Propellant Testing

Samples of TP-L8006 propellant were removed from segments 2 and 3 of the dissected motor. The propellant section removed from segment 2 was extracted from the unbond area and had liner intact. Segment 3 was just aft of segment 2 but in a fully bonded area; thus liner could not be removed intact with the propellant. Both segments saw the same temperature history during the

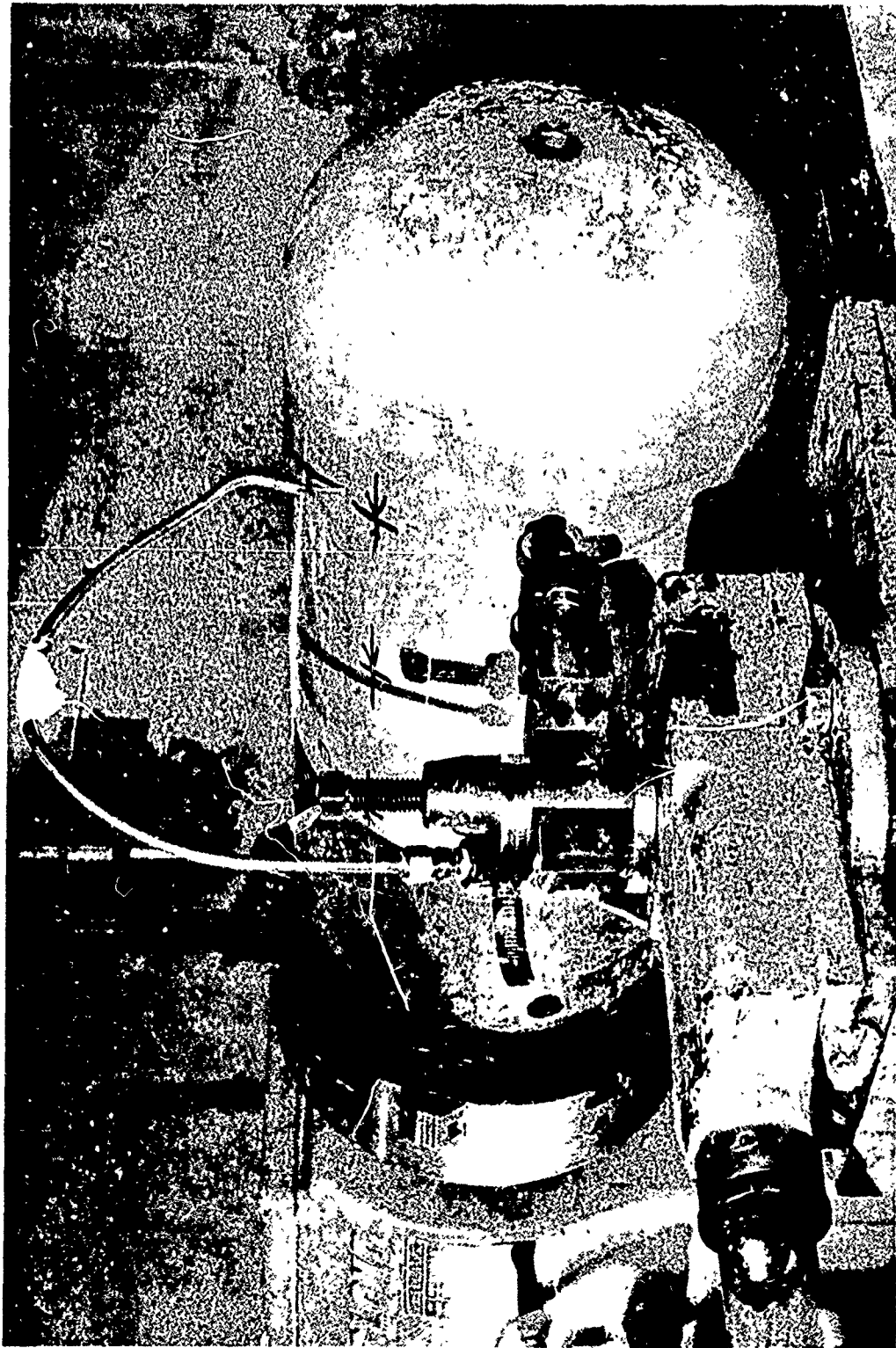


Figure 112. Motor in Lathe



Figure 113. Propellant Grain Being Severed Using Butcher Knife



Figure 114. IM #1 With Head End Removed



Figure 115. IM #2 After Dissection

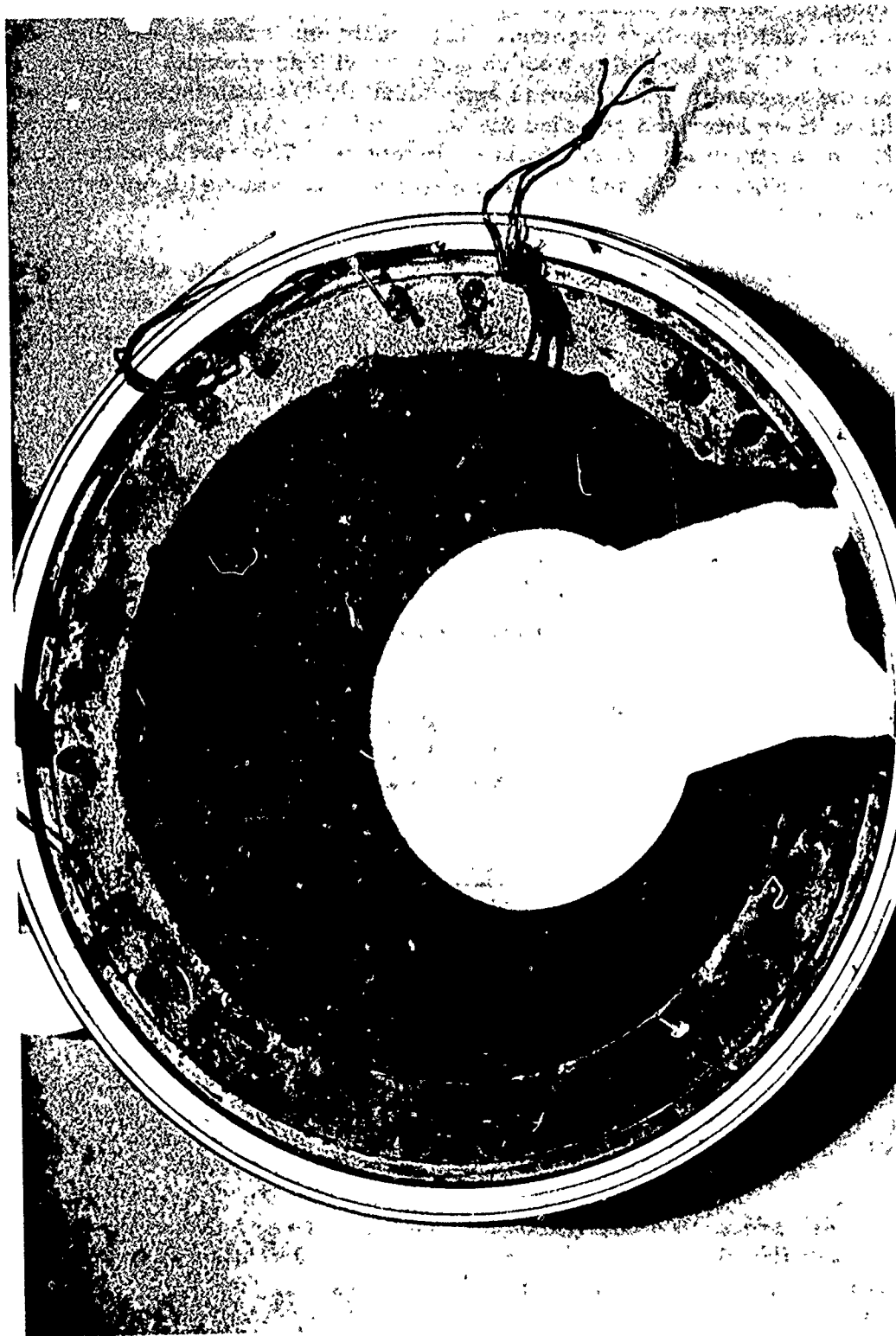


Figure 116. IM #2 After Dissection (Aft Section)

aeroheat testing. Uniaxial tensile properties were measured using specimens extracted from each propellant segment. The specimens utilized were approximately 1/4" x 1/4" x 2" bonded to wooden end tabs with an epoxide. Specimens were cut in the longitudinal direction in approximately 1/4-inch increments from the propellant/liner interface and also the bore surface. All tests were conducted at 77°F and a strain rate of 2.0 inches per minute. The results of these tests are presented in Figures 117 and 118 for the specimens removed from segments 2 and 3, respectively.

Tests were also conducted with TP-L8006 propellant, Mix L-434, to determine the correlation of tensile properties obtained with 2-inch end bonded specimens and the standard JANNAF plastic gauge specimens. The results of these tests are as follows:

<u>Specimen Type</u>	<u>Modulus, psi</u>	<u>Stress, psi</u>	<u>Strain at Max. Stress, in/in</u>
2-inch end bonded	1880	96	0.324
JANNAF Plastic Gauge	1223	100	0.396

These values represent an average of eight tests with the end bonded and nine tests with the JANNAF specimens.

These tests were conducted so that an assessment could be made of any change in tensile properties that occurred during the thermal conditioning of the SALE motors. The nominal JANNAF plastic gauge tensile properties of the unaged propellant loaded into Motor IM #2 are:

<u>Modulus, psi</u>	<u>Stress, psi</u>	<u>Strain at Max. Stress</u>
1480	104	0.38

Based on the tensile specimen correlation factors obtained from testing Mix L-434, the projected unaged tensile properties of the propellant from 2-inch end bonded specimens are as follows:

<u>Modulus, psi</u>	<u>Stress, psi</u>	<u>Strain at Max. Stress</u>
2275	100	0.311

Comparing these properties with those obtained from the samples removed from the motor shows that the thermal conditioning caused a decrease in strain, an increase in modulus, and little or no change in stress.

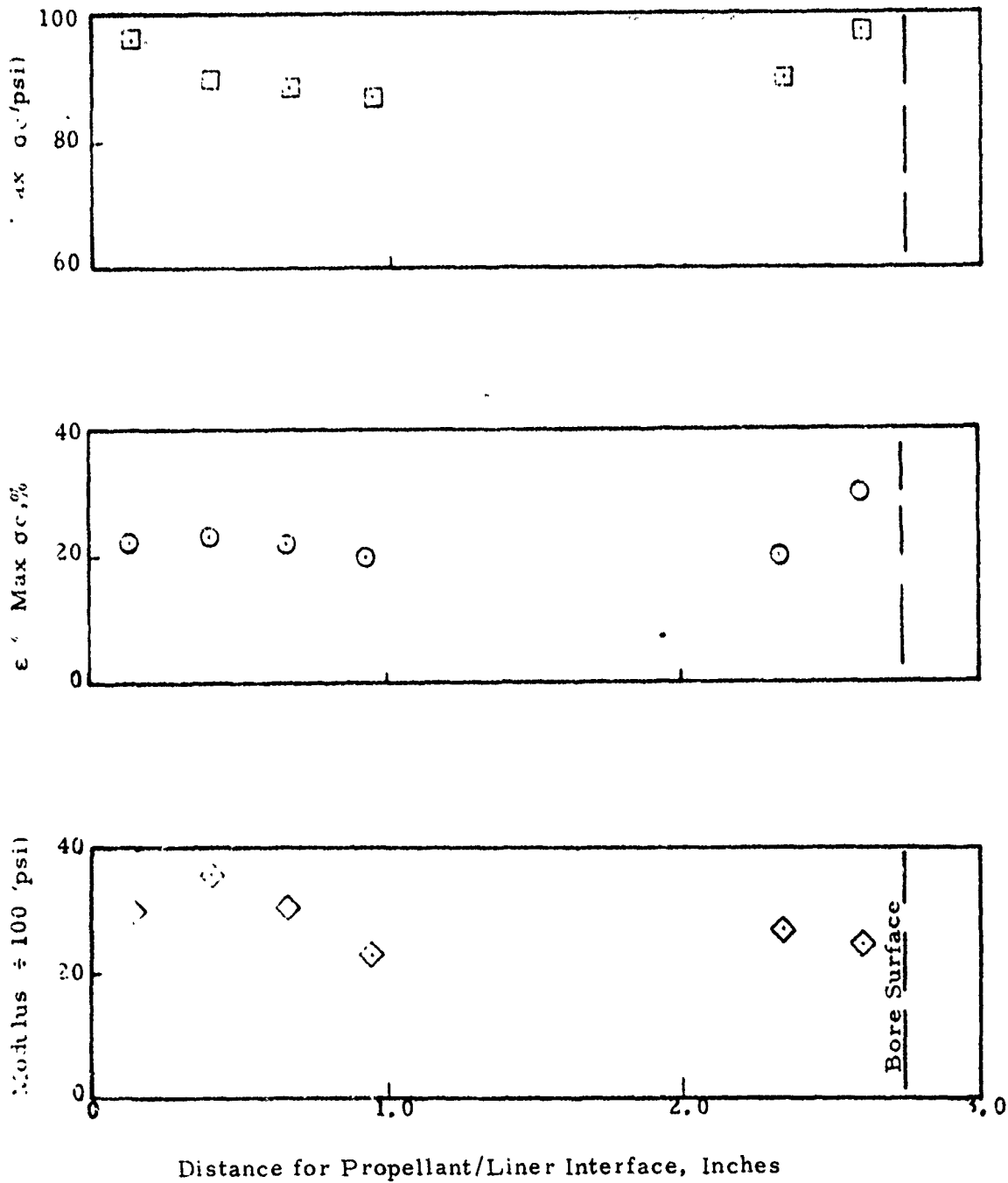


Figure 117. TP-L8006 Propellant Removed from SALE IM #2, Segment 2

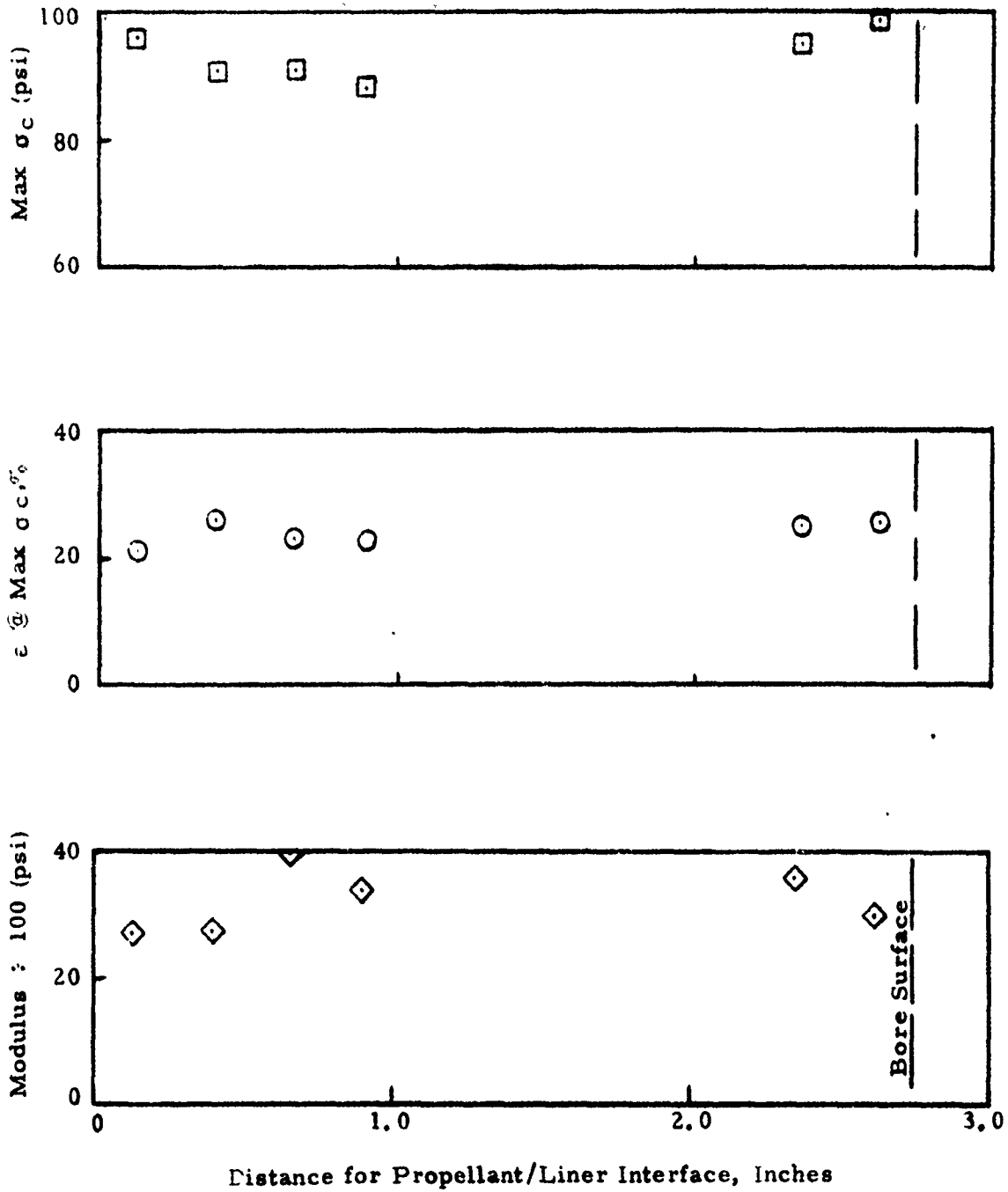


Figure 118. TP-L8006 Propellant Removed from SALE IM #2, Segment 3

## IM #1 & 3 Dissection and Propellant Testing

Dissection of IM #1 and #3 was accomplished after the physical properties of IM #2 had been measured. Both these motors exhibited similar but not nearly as extensive grain termination liner-to-case unbonds as IM #2. The cut interface between Sections 1 and 2 of IM #1 is shown on Figure 119. Considerable ammonium perchlorate leaching is evident on and in the valleys of the starpoint caused by water damage which occurred during simulation testing. The segments of IM #3 are shown on Figure 120. The cracking of the surface in the transition section is evident. This cracking was, of course, much more severe in small bore as clearly shown on Figure 121 which is a photograph of Section 2. The largest of these cracks extended approximately 0.1 inch below the propellant surface. Most of the cracks were less than 0.05 inch in depth. These cracks were very unusual in appearance and were not considered typical of a bore crack due to low temperature storage.

The surface of the bore was very much like that of a structural member which had been tested with a brittle coating applied to the surface. All of the cracks on the surface were perpendicular to the direction of principal stress. The most unusual features of the bore surface were the large number of cracks and shallow depth of the cracks.

Hardness measurements were made on the propellant taken from IM #3 to determine if there was a gradient in propellant properties. The measured Shore "A" hardness readings, after 10 seconds of penetration, are shown in Table 11. These recordings show that the propellant hardness is higher on the surface. From these measurements, it appears that there is a very thin region on the surface where the propellant is considerably harder.

The tensile properties were determined from the dissected IM #3 motor by using the minithin specimen developed by Briggs and Hart.<sup>(1)</sup> These specimens were 0.125-inch thick and were tested at a cross-head speed of 1.0-inch per minute to approximate the strain rate in a standard JANNIF specimen tested at 2.0 inches per minute. The results of these tests are shown on Figures 122 and 123. The plot of maximum stress versus radius (Figure 122) shows that the propellant had a higher tensile strength near the inner bore and near the case wall. From this gradient in maximum stress, lower values for the strain at maximum stress would be expected near the bore surface and the case wall. Although the gradient in tensile properties was not as obvious from the strain at maximum stress measurements as it was for the maximum stress measurement, a definite gradient can be seen from the results shown in Figure 123. From the

---

1. Briggs, W. E. and Hart, W. D., "A Special Miniature Specimen for Evaluating Propellant", JANNAF Mechanical Behavior Working Group 8th Meeting 1969, Vol. I, Nov. 1969, China Lake, California.

TABLE 11

HARDNESS MEASUREMENTS FROM IM#3, SECTION #3 (U)

TP-L8006 Propellant  
 Mix L-198  
 Shore "A" Hardness  
 at 10 Seconds

<u>Distance From Bore Surface</u>	<u>Shore "A"</u>		
Surface	50	52	48
0.125	40	40	40
0.250	39	35	35
0.375	39	38	37
0.500	38	39	37
0.625	37	39	38
0.750	37	39	38
0.875	38	35	37
1.000	35	35	36
1.125	35	35	34
1.250	36	35	37
1.375	35	36	36
1.500	38	37	35
1.625	35	34	37



Figure 119. Cut Interface Between Sections 1 and 2 of IM #1



Figure 120. Segments of IM #3

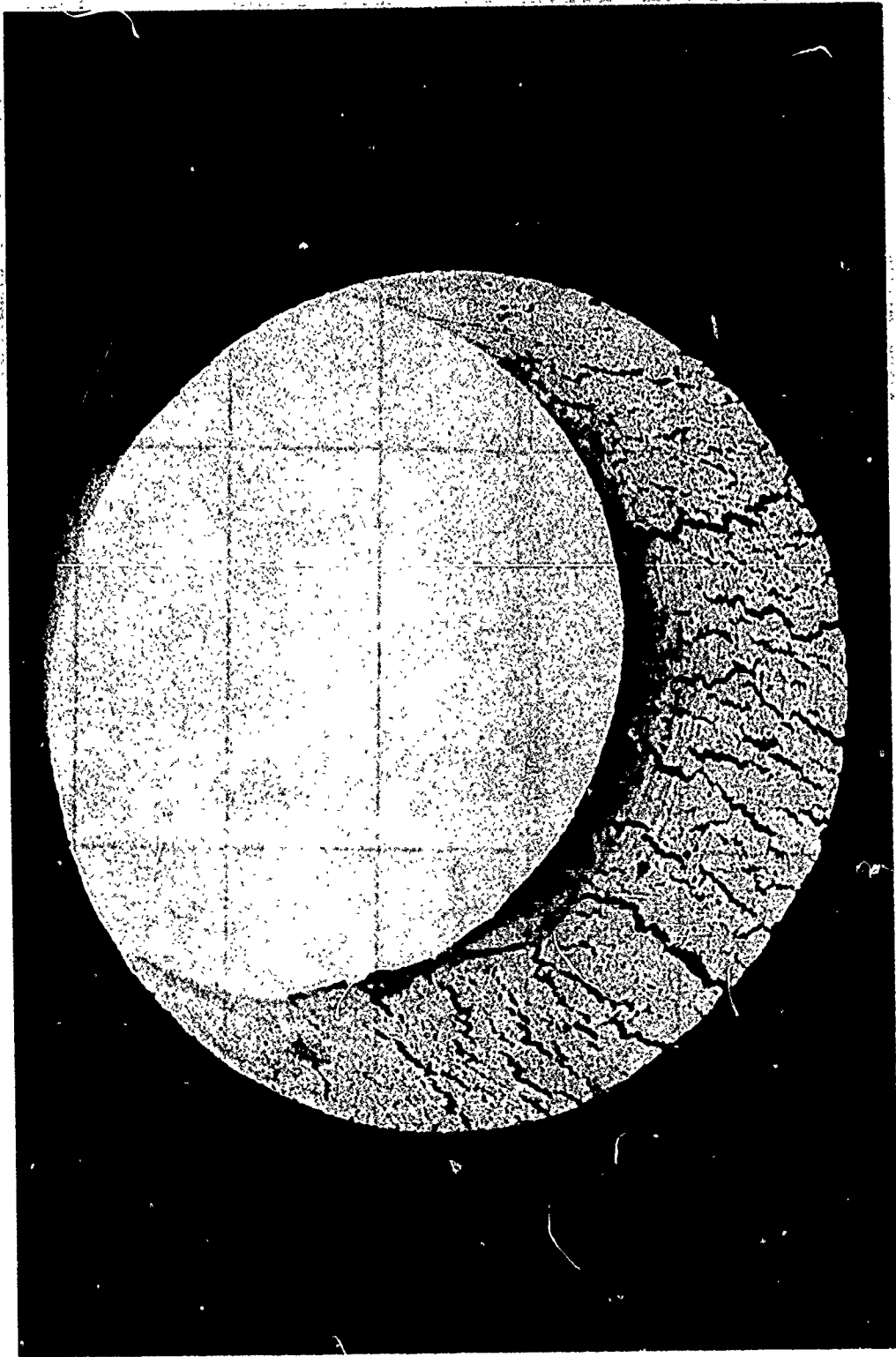


Figure 121. Cracking in IM #3

Motor IM #3  
 TP-L8006 Propellant  
 Mix L-198  
 "C" Die End Bonded Specimens  
 77°F Test Temperature  
 1.0 in/min Cross-head Speed

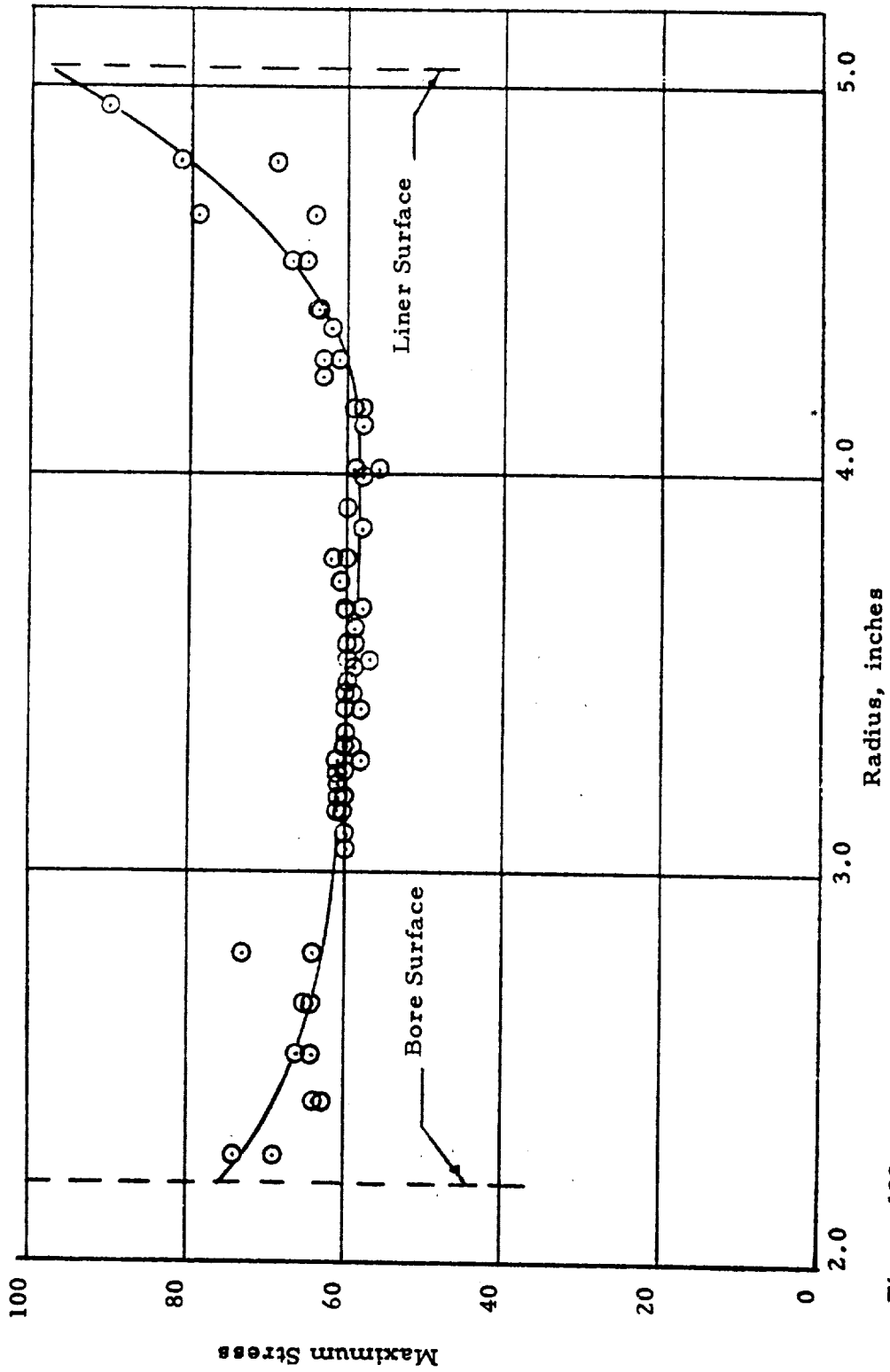


Figure 122. Maximum Stress Versus Radius, Motor IM #3

Motor IM #3  
 TP-L8006 Propellant  
 Mix L-198  
 "C" Die End Bonded Specimens  
 77°F Test Temperature  
 1.0 in/min Cross-head Speed

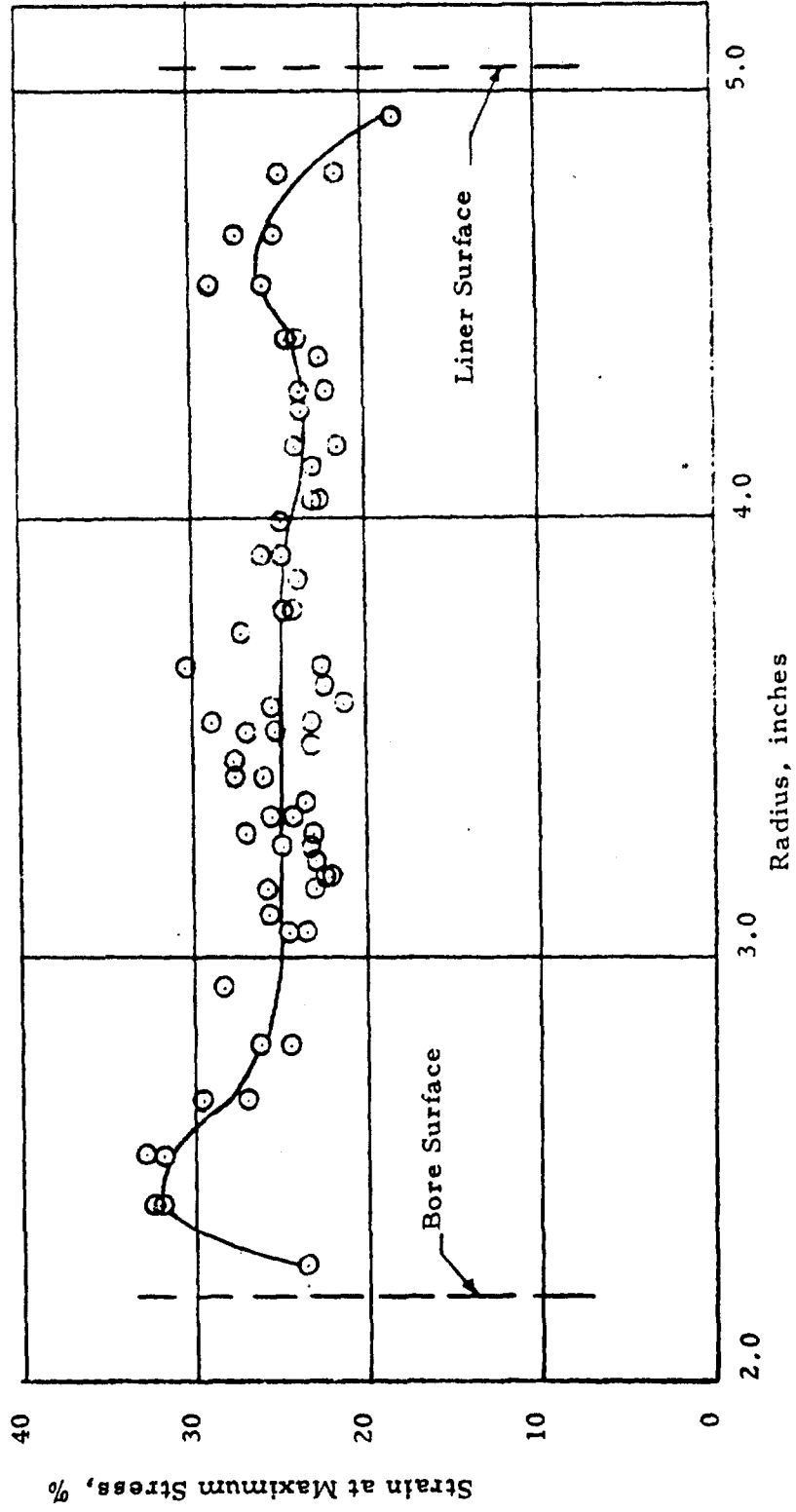


Figure 123. Strain at Maximum Stress Versus Radius, Motor IM #3

limited measurements which were taken near the bore surface and the case wall, it appeared that there was a large loss in strain capacity in these areas.

The loss in strain capacity near the bore surface could account for the large number of cracks which developed on bore surface of IM #3. Because of the thin thickness of the region on the surface which degraded, it was not possible to accurately characterize the propellant in this region. One hypothesis is that the propellant became embrittled in a thin layer on the surface, perhaps 0.005 to 0.025-inch thick, and cracked on aeroheat cycling because of the loss in strain capability. Upon subsequent step temperature cycling, the surface was subjected to excessive moisture condensation which caused further propagation of the surface cracks. This hypothesis agrees with visual observation of the motor. After completion of the aeroheat cycles, the surface cracks were only hairline cracks. After the step-temperature cycling, the cracks are substantially larger.

Gel fraction measurements were made on propellant removed from IM #3 to determine changes in this quantity. Gel fraction provides an indication of the degree of cure or crosslinking of the binder. Consequently, an increase in gel fraction generally indicates an increase in the tensile strength and tensile modulus. A loss in strain capability is generally observed with an increase in gel fraction.

The results of the gel fraction tests indicated that the propellant near the inner bore and the liner surface was cured to a greater degree than the propellant at the mid-grain. The results of these tests are summarized below.

<u>Location</u>	<u>Gel Fraction</u>
Inner Bore (0.1" of surface)	0.39
Sub-Surface (0.1-0.2" below surface)	0.46
Mid-Grain	0.22
Liner Surface (within 0.1" of liner surface)	0.38

The gel fraction measured from the propellant near the mid-grain was about nominal for TP-L8006 propellant, but was considerably lower than that measured near the bore and liner surfaces. Therefore, a higher tensile strength would be expected from the propellant near the inner bore and the liner surface. These results agree with the tensile test data obtained from this motor. A very limited testing program was performed on this IM #1 since a rather extensive examination of Motor IM#3 revealed no large changes in the propellant properties after aeroheat cycling except very near the propellant surface.

### Uninstrumented Motor Propellant Testing

Propellant from the star points was also removed from one of the uninstrumented motors being subjected to the simulation testing. This motor identified as Mix L-205, Charge 23, had two star points removed and propellant properties measured in March 1973. This motor was stored at ambient between that time and when it was employed in the simulation tests in March 1974. Upon completion of these tests in May 1974, two additional star points were removed. Specimens were cut through the thickness direction of the star points with a JANNAF specimen die. This resulted in tensile specimens which were 3/4-inch thick. Previous experience with measuring tensile properties from a Maverick motor in this manner indicated that the motor propellant properties were lower than the carton propellant properties. This difference in properties was attributed to the thicker specimen and damage to the specimen as it was removed from the die cutter. Previously, differences in measured properties from 3/4-inch thick and 1/2-inch thick JANNAF specimens had been observed when the samples were cut from the same carton. Consequently, the specimens from IM#1 were tested at -75°F for the purpose of comparing the propellant properties before and after aeroheat cycling since the specimens tested before aeroheat cycling were tested at -75°F. These results are shown below.

#### TENSILE PROPERTIES OF PROPELLANT BEFORE AEROHEAT SIMULATION CYCLING

Propellant: TP-L8006  
Mix No.: L-205 Chg. 23  
Test Temp.: -75°F

<u>Modulus</u>	<u>Ult. Strain</u>	<u>Strain at Max. Corrected Stress</u>	<u>Max. Corrected Stress</u>
	<u>%</u>	<u>%</u>	<u>psi</u>
19440	20.0	8.1	940
23980	20.2	6.7	910
18600	21.3	14.6	940
18300	24.0	21.8	923
17900	26.4	25.2	906
<u>17100</u>	<u>17.5</u>	<u>11.3</u>	<u>908</u>
19200	21.5	14.6	920

NOTE: JANNAF specimens cut from starpoints.

TENSILE PROPERTIES OF IM#1 PROPELLANT  
AFTER STORAGE AND AEROHEAT SIMULATION CYCLING (Cont'd)

Propellant: TP-L8006  
 Mix Number: L-205 Chg. 23  
 Test Temp.: -75°F

<u>Modulus</u> psi	<u>Ult. Strain</u> %	<u>Strain at Max. Corrected Stress</u> %	<u>Max. Corrected Stress</u> psi
86700	2.7	2.5	965
33200	8.6	7.2	990
35000	5.3	5.1	940
<u>40200</u>	<u>5.2</u>	<u>4.7</u>	<u>970</u>
48800	5.4	4.9	966

NOTE: JANNAF specimens cut from starpoints.

From the above results, it will be noted that there is an appreciable decrease in strain capacity after aeroheat simulation cycling. Also, the initial tangent modulus is approximately twice as large after storage and simulation cycling. These results are consistent with the results obtained from IM#3.

Gage Recovery and Recalibration

Cutting the motors into four segments made recovery of the normal gages a relatively simple task. Gage recovery had not been planned during the conception of this program because of the difficulty encountered in the earlier STV programs. Because of some of the erratic reading that had been observed from a few gages during the aeroheat tests, it was decided to make an attempt to recover the normal gages. This was done initially on IM#2 when gage N2-48 was recovered. This gage had produced quite erratic readings since early in the gage checkout testing. The reason for the behavior had been conjectured to be unbond between the liner and case under the gage, or unbond of the liner from the surface of the gage. The interest in recovering this gage was to determine whether either of these arguments were valid. Actually in the final analysis, neither were and the cause was found to be unbond of the gage element from the diaphragm. Inasmuch as the attempt at recovery of gage N2-48 proved successful, it was then decided to recover all the normal gages.

The gages were cut from the motors still embedded in the liner with propellant still bonded to the surface. This propellant was removed by hand trimming and peeling away from the liner. This left a piece of liner with the gage in place encapsulated in the hemispherical shape dome of liner. The dome was carefully cut into by knife to bare the edge of the gage. The liner was then peeled from the front and back surface of the gage and its condition noted in terms of softness, observable contamination, and bond appearance. The gages

were then taken to Leeming and Associates where they were recalibrated using the same bridge completion circuits that were used in the aeroheat tests.

The results of the recalibration are presented along with comparable factory calibrations, gage checkout data, and motor pressurization grouped for each motor IM#1, IM#2, and IM#3 in Tables 12, 13, and 14, respectively. The visual condition of the gage and surrounding material observed during dissection is also noted on each table. In general the gages located in the center portion of the motor suffered the most deterioration. The bonds were poorer and the liner adjacent to the gages was softer. The head end and aft end gages showed maximum variation although they did undergo some change. The data presented for these gages will be much more representative of what actually occurs in the motor during aeroheat. Much of the changes in gage output observed during testing discussed in the previous section can be attributed to unbonding. Of course, an obvious exception is N1-50 which underwent considerable change. The reason for the changes can probably be attributed to chemical attack by the potting material. The basic effect was an increase in the resistance of the outside semiconductor, which would occur if the semiconductor was etched. It is obvious that both the inside and outside elements underwent the same temperature history; therefore, the only difference between the environments of these two elements is the potting material (liner) on the outside. It is obvious, however, that temperature accelerated the effect since the gages located in the center of the motors where they were exposed to high temperature (250°F as compared to 150°F at the ends) suffered the most deterioration. Placing one of the gage elements on the outside of the diaphragm is obviously a design fault and should be corrected in future gage designs. Apparently this design evolved after the STV program and is common to all GFE supplied gages.

TABLE 12  
SUMMARY OF GAGE CALIBRATIONS  
FOR GAGES IN IM #1

GAGE & LOCATION	EVENT	DATE	GAGE OUTPUT, MV		GAGE SENSITIVITY MV/PSI		REMARKS
			T=170°	T=-65°	T=170°	T=80°	
NI-50 Fwd	F/E	2/15/73	0.49	-1.00	0.7776	0.7683	Liner under gage removed clean from case. Good bond on back side of gage, bond on front side satisfactory. Liner surrounding gage not nearly as soft as in the center gages. White filmy material along one edge of gage.
	PIC	3/16/73	5.0	18.25	---	---	
	GCO	6/73	21.0	44.0	---	---	
	Press	7/30/73	---	24-25.5	---	≈0.84	
	PDC	3/25/74	---	107**	---	≈0.20**	
NI-40 Center	PDC	6/7/74	57.4	152.7	.457	.523	Liner material soft-very soft on surface gage. Bond very poor on back side--almost unbonded--bond good on edges and fairly good on diaphragm side. A minute quantity of uncured material was seen near lead-gage junction on backside.
	F/E	1/19/73	0.60*	5.65	0.7678*	0.7657	
	PIC	3/16/73	2.9	-9.66	---	---	
	GCO	6/73	18	65	---	---	
	Press	7/30/73	---	23.5*	---	1.057	
NI-49 Center	Press	3/25/74	---	65**	---	1.826**	Back side completely uncured or reverted (sticky) foreign material found on back. Consisting of a sliver of some material approximately 1/8 inch in diameter, by 3-4 mils thick. This object is glued to the gage by a material that looks or is tacky like rubber cement. There is another piece of this material under this one bonded on the surface.
	PDC	6/7/74	31.1	80	≈1.89	2.323	
	F/E	2/15/73	+3.33	+0.21	0.7337	0.7307	
	PIC	3/16/73	-1.1	-38.36	---	---	
	GCO	6/73	1	24	---	---	
NI-41 Aft	Press	7/30/73	---	7	---	0.7123	Liner under gage removed clean from case. Good bond on both sides of gage, liner surrounding gage not nearly as soft as in the center gages.
	Press	3/25/74	---	5.5**	---	0.6072**	
	PDC	6/7/74	14.1	17.4	0.770	0.763	
	F/E	1/19/73	2.74*	4.77	0.8454*	0.8269	
	PIC	3/16/73	-3.1	-25.14	---	---	
NI-50 Fwd	GCO	6/73	6	34	---	---	Liner under gage removed clean from case. Good bond on both sides of gage, liner surrounding gage not nearly as soft as in the center gages.
	Press	7/30/73	---	11	---	0.7167	
	Press	3/25/74	---	19**	---	0.8051**	
	PDC	6/7/74	30.6	21.2	0.860	0.881	
	F/E	1/19/73	2.74*	4.77	0.8454*	0.8269	

\* T = 150°F  
\*\* T = 60°F

F/E  
PIC  
GCO  
Press  
PDC

Factory  
Post Gage Installation Calibration  
Gage Checkout - Motor Loaded  
Pressurization - Motor Loaded  
Post Dissection Calibration

TABLE 13  
SUMMARY OF GAGE CALIBRATIONS  
FOR GAGES IN IM #2

GAGE & LOCATION	EVENT	DATE	GAGE OUTPUT, MV		GAGE SENSITIVITY MV/PSI		REMARKS
			T=170°	T=80°	T=170°	T=80°	
N2-42 Fwd	F/E	1/19/73	2.24*	1.48	0.740*	0.733	Liner under gage removed clean from case. Poor bond on back of gage. Good bond on front. Seems to have picked up dirt or solder off end of strain gage. No sign of any reversion or extreme softness notes on center gage of IM#1 and IM#3.
	PIC	3/16/73	-2.1	-5.0	---	---	
	GCO	6/73	13	43	---	---	
	Press	8/73	23	38**	0.59	0.60	
	Press	8/73	---	---	---	0.56**	
	PDC	8/73	---	---	---	0.63	
N2-48 Center	F/E	1/19/73	0.58*	-0.19	0.7176*	0.7184	Fairly good bond over gage--liner somewhat soft on gage.
	PIC	3/16/73	4.6	-0.4	---	---	
	GCO	6/73	33	26	---	---	
	Press	8/73	25	66	2.30	1.73	
	Press	8/73	---	73	---	2.4	
	PDC	6/17/74	+35.6	+65	0.770	.458	
N2-51 Center	F/E	1/19/73	0.44	-1.34	0.7933	0.7871	Bond on gage a little weaker than those on the ends. Liner also a little softer about the gage.
	PIC	3/16/73	5.3	2.3	---	---	
	GCO	6/73	33	27	---	---	
	Press	8/73	34	30	0.733	0.742	
	Press	8/73	---	26	---	0.659	
	PDC	6/7/74	+45.4	40.4	0.787	0.812	
N2-46 Aft	F/E	1/19/73	0.16*	-1.46	0.7274*	0.7309	Liner under gage removed clean from case. Poor bond on back of gage. Good bond on front. Seems to have picked up dirt or solder off end of strain gage. No sign of any reversion or extreme softness notes on center gage of IM#1 and IM#3.
	PIC	3/16/73	-0.8	-6.6	---	---	
	GCO	6/73	19	15	---	---	
	Press	8/73	26	22	0.717	0.650	
	Press	8/73	---	26	---	0.70	
	PDC	8/73	---	---	---	---	

F/E  
PIC  
GCO  
Press  
PDC

Factory  
Post Gage Installation  
Gage Checkout - Motor Loaded  
Pressurization - Motor Loaded  
Post Dissection Calibration

\*T = 150°F  
\*\*T = -40°F

TABLE 14  
SUMMARY OF GAGE CALIBRATIONS  
FOR GAGES IN IM #3

GAGE & LOCATION	EVENT	DATE	GAGE OUTPUT, MV		GAGE SENSITIVITY MV/PSI		REMARKS
			T=170°	T=80°	T=170°	T=80°	
N3-44 Fwd	F/E	1/19/73	0.22*	-0.24	0.8017*	0.7997	Liner under gage removed clean from case. Good bond over gage-liner on gage not as soft as center gages.
	PIC	3/16/73	-2.9	-3.69	---	---	
	GCO	6/73	-67	-70	---	---	
	Press	7/30/73	---	-64	---	0.6329	
	Press	3/25/74	-54**	-60.2***	0.6666	0.6579***	
	PDC	6/7/74	-55.6	-60	0.767	0.781	
N3-43 Center	F/E	1/19/73	1.86*	1.09	0.7655*	0.7636	Liner material soft-very soft on surface gage. Bond very poor on back side--almost unbonded--bond good on edges and fairly good on diaphragm side. A minute quantity of uncured material was seen near lead-gage junction on backside.
	PIC	3/16/73	0.2	-2.1	---	---	
	GCO	6/73	57	70	---	---	
	Press	7/30/73	---	72.5	---	0.7168	
	Press	3/25/74	90.1**	106.5***	0.4762	0.5556***	
	PDC	6/7/74	81.1	123	0.492	0.4	
N3-47 Center	F/E	1/19/73	3.02*	-1.48	0.7068	0.7110	Same appeared as N3-43 including the uncured region.
	PIC	3/16/73	-1.6	-3.0	---	---	
	GCO	6/73	42	60	---	---	
	Press	7/30/73	---	66	---	0.7290	
	Press	3/25/74	---	84.8***	---	0.4444***	
	PDC	6/7/74	82.3	123.2	0.4	0.410	
N3-45 Aft	F/E	1/19/73	1.61*	-0.68	0.7488*	0.7297	Great deal of porosity in liner between gage and wall. Very poor bond on back surface. Bond on front surface good. Leads are so short; may not be able to do anything. A piece of white filmy material found on front surface near edge.
	PIC	3/16/73	-5.2	-1.7	---	---	
	GCO	6/73	1	3	---	---	
	Press	7/30/73	---	---	---	---	
	Press	3/25/74	24.8**	24.2***	0.7299	0.7143***	
	PDC	6/7/74	59.5	63.7	0.786	0.776	

\*T = 150°F  
\*\*T = 130°F  
\*\*\*T = 60°F

F/E Factory  
PIC Post Gage Installation  
GCO Gage Checkout - Motor Loaded  
Press Pressurization - Motor Loaded  
PDC Post Dissection Calibration

## INTERPRETATION OF DATA

Interpretation of data requires consideration of each aspect that could induce errors or shifts in those data. In this case, the basic correlation of the data showed considerable changes in gage output as a function of aeroheat testing. Two motors geometrically the same were found to have apparent differences in bondline stresses. Liner to case unbond and propellant bore cracking occurred which would influence these data. The propellant itself was seen to age and finally the gages were found to have changed calibration which apparently occurred as a function of the testing. When these aspects are considered, it becomes obvious that the usefulness of the data is more qualitative than quantitative. This assumes that although the magnitude of the reduced stress values are known to be in error the measured trends are correct. It is obvious that part of the gage change noted was due to unbond and or bore cracking and part to gage aging. These are the aspects that effect the interpretation of data in terms of both structural response and failure characteristics. There is another aspect, however, that can provide a consistent basis for interpretation, and that is theory. Of course, if theory was all that good, there would be little need in conducting the test program. The use of both theory and data, although each have their inaccuracies and limitation, can provide an interpretation which provides a better insight into the effect of aeroheating on a solid rocket motor.

The prediction of the stress and strain state in a solid propellant rocket motor exposed to an aeroheat environment is a very difficult problem due to the fact that the solution is a function of time and temperature. To add to the complexity of the problem, the propellant and liner are thermal viscoelastic materials which implies that their properties change with time and temperature. Therefore, it is necessary to have good material properties, physical as well as thermal, that are determined as a function of time and temperature. The next ingredient necessary for the prediction is to have a thermal-viscoelastic-two dimensional finite element computer code such as THVINC. THVINC is a first generation viscoelastic code based on linear constitutive relations to predict stress fields in propellant during transient thermal conditions. There is a school of thought, however, that propellant under such conditions is a highly non-linear viscoelastic material. If this is true then THVINC predictions would become more inaccurate as the rate of thermal change increased.

In order to establish the sensitivities of various input parameters to the aeroheat induced stress in a motor, a parametric study was conducted. Since the study was a parametric study, the simple plane strain version of THVINC was used. The nodal point grid and finite element model set up for this study are shown on Figures 124 and 125, respectively. This model assumed the motor to be an infinite cylinder by requiring zero axial displacement boundary condition. The plane strain model was felt to be relatively realistic because IM #2 and IM #3 have CP grain configurations with gages in the CP section of the motor. Another governing factor in the selection of a simple model is that a thermal viscoelastic solution in 2-D is computationally

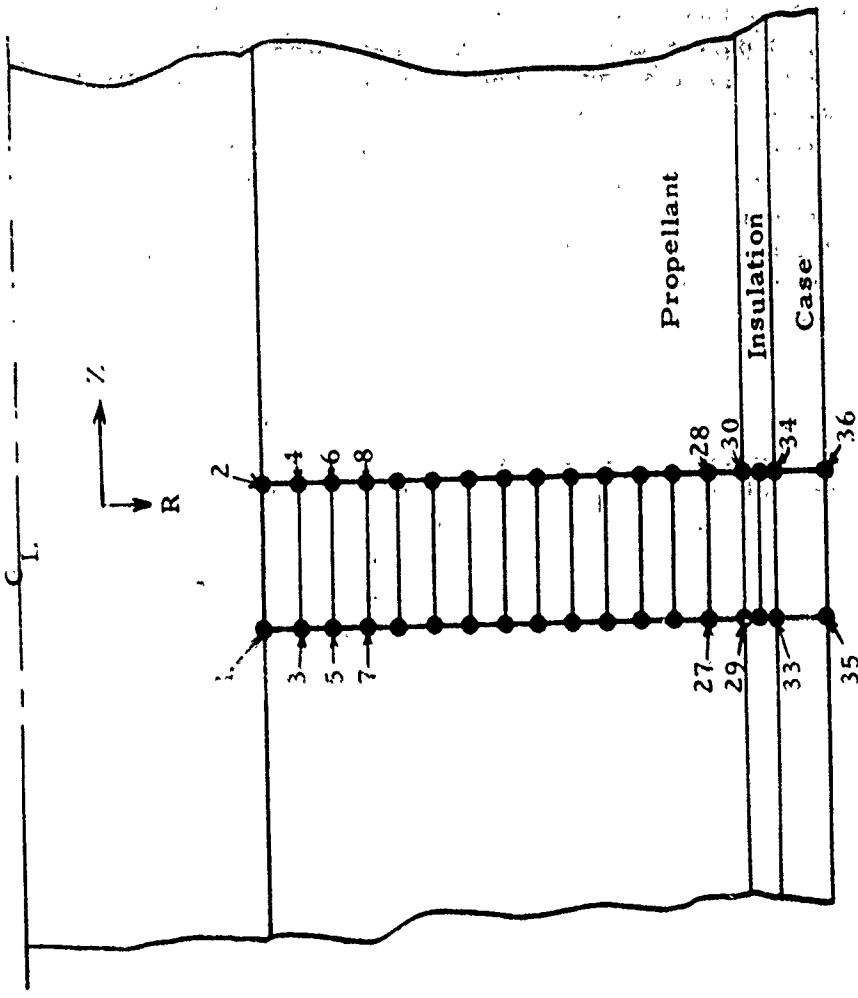


Figure 124. Nodal Point Modeling of Problem (one dimensional) THVINC

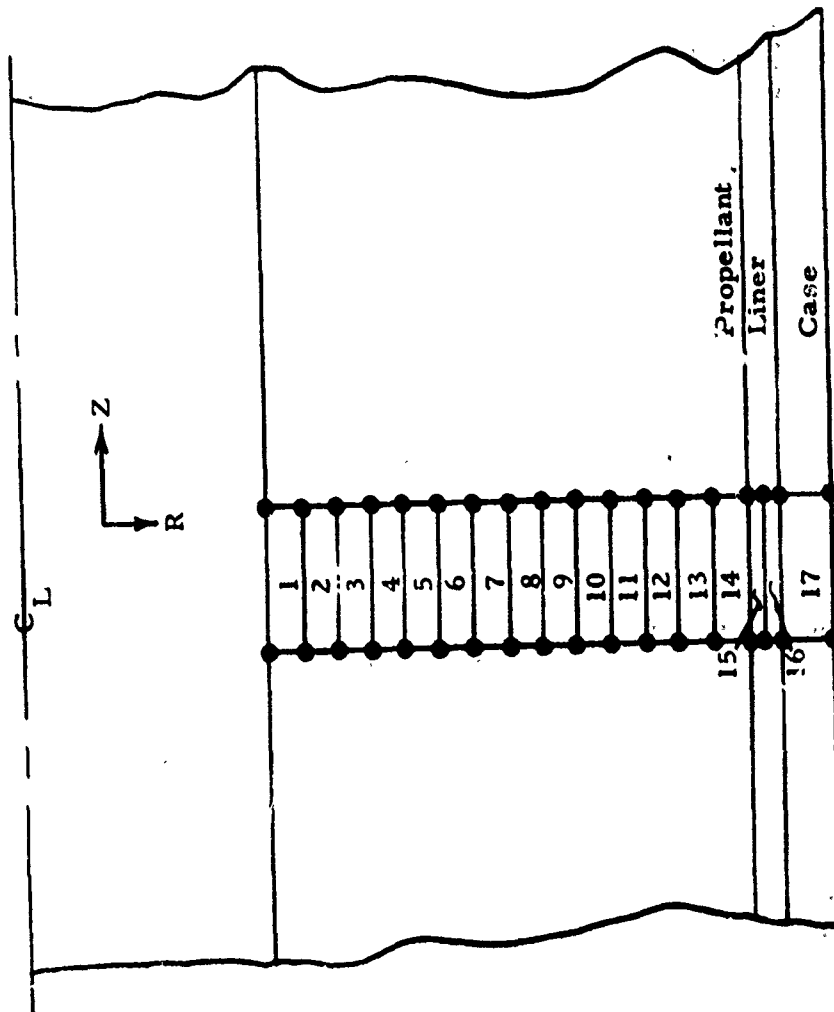


Figure 125 Element Modeling for Problem: (one dimensional) THVINC

expensive. The expense is directly related to the number of time steps taken and the number of elements in the model.

The stress fields produced are a function of the relaxation modulus of the viscoelastic materials involved. THVINC uses a viscoelastic shear modulus represented by an nth term exponential series which is obtained by fitting a Prony series to the relaxation modulus curve. In addition it is necessary to have the  $a_T$  curve (William-Landel-Ferry equation), WLF, to account for the temperature shift of the material. The viscoelastic shear modulus in THVINC is represented by an nth term exponential series

$$G(\xi) = G_0 + \sum_{i=1}^n G_i e^{-\xi/\lambda_i}$$

where the reduced time  $\xi$  is related to the real time through

$$\xi(t) = \int_0^t \omega(T) dt'$$

where  $\omega(T) = \frac{1}{a_T}$

and  $a_T = \frac{C_1 (T - T_s)}{C_2 + (T - T_s)}$  (WLF equation)

and  $T_s$  = reference temperature

The four propellant relaxation modulus curves used in this study are presented in Figure 126. Two of the curves are established from physical test data and two curves are just arbitrary curves to provide a broader evaluation. The results of THVINC using these four different curves are presented in Figures 127 and 128. Figure 127 shows a comparison between the calculated radial stress or normal stress at the bondline for a DMP-3 aeroheat mission on IM #2 and actual gage data. Figure 128 shows the THVINC prediction of the hoop stress at the inner bore. It is obvious after studying the two figures that the relaxation modulus does indeed have a substantial effect on the analysis results. There is about a 60 psi deviation between the two extremes of the bondline stress and about 160 psi deviation for the hoop stress at the inner bore. In these calculations the modulus of the liner is assumed to be the same as the propellant.

Later in the program the instrumented motors were dissected and the aged propellant relaxation modulus was determined. The aged and unaged modulus curves are presented in Figure 129. As is evident the propellant modulus has changed after experiencing the aeroheat cycles. It appears that the propellant has become softer at the longer times or higher temperature and somewhat harder at short time and low temperature. A comparison between the effects on radial stress at the bondline and the hoop stress at the

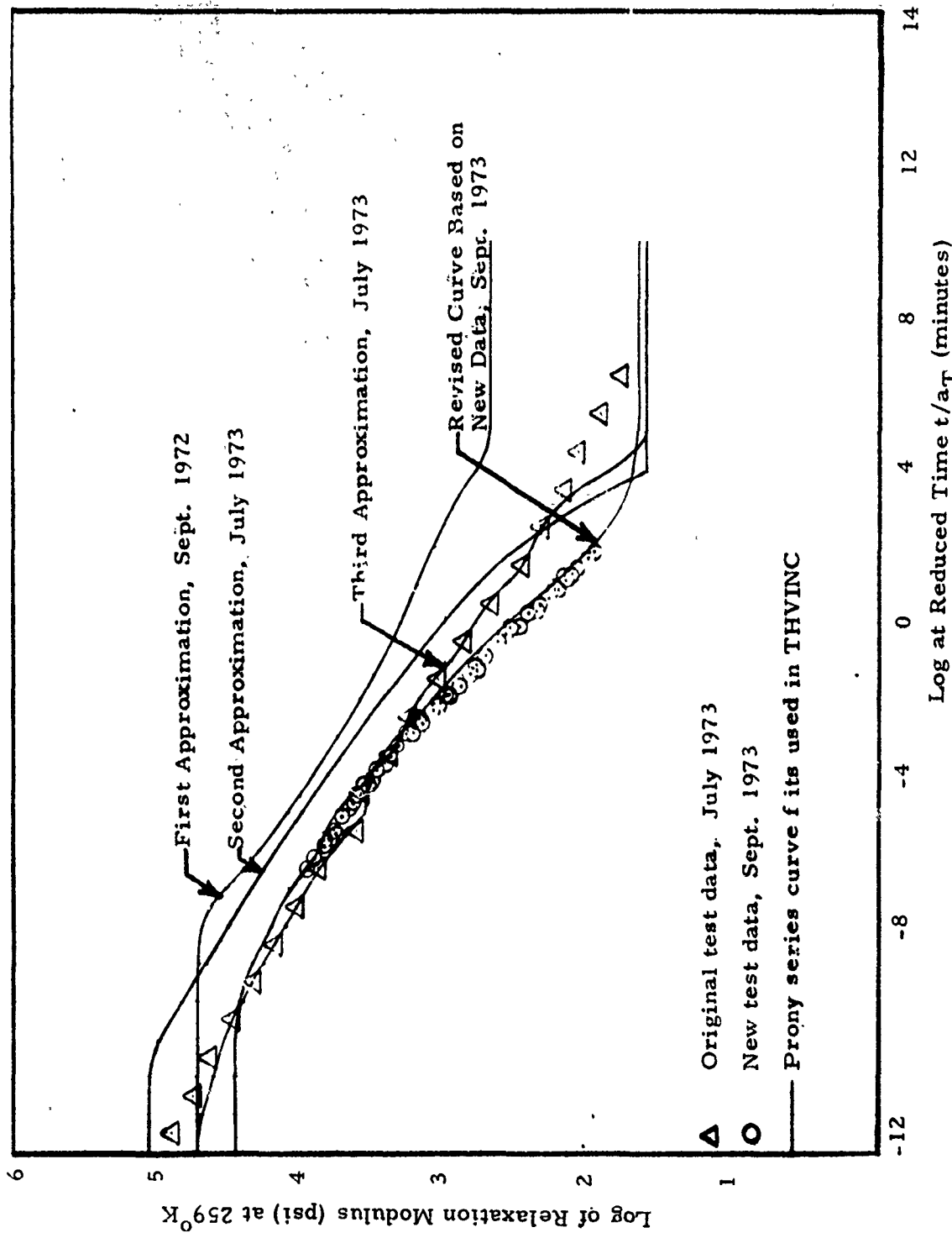


Figure 126. Relaxation Modulus Curve, TP-L8006 Propellant

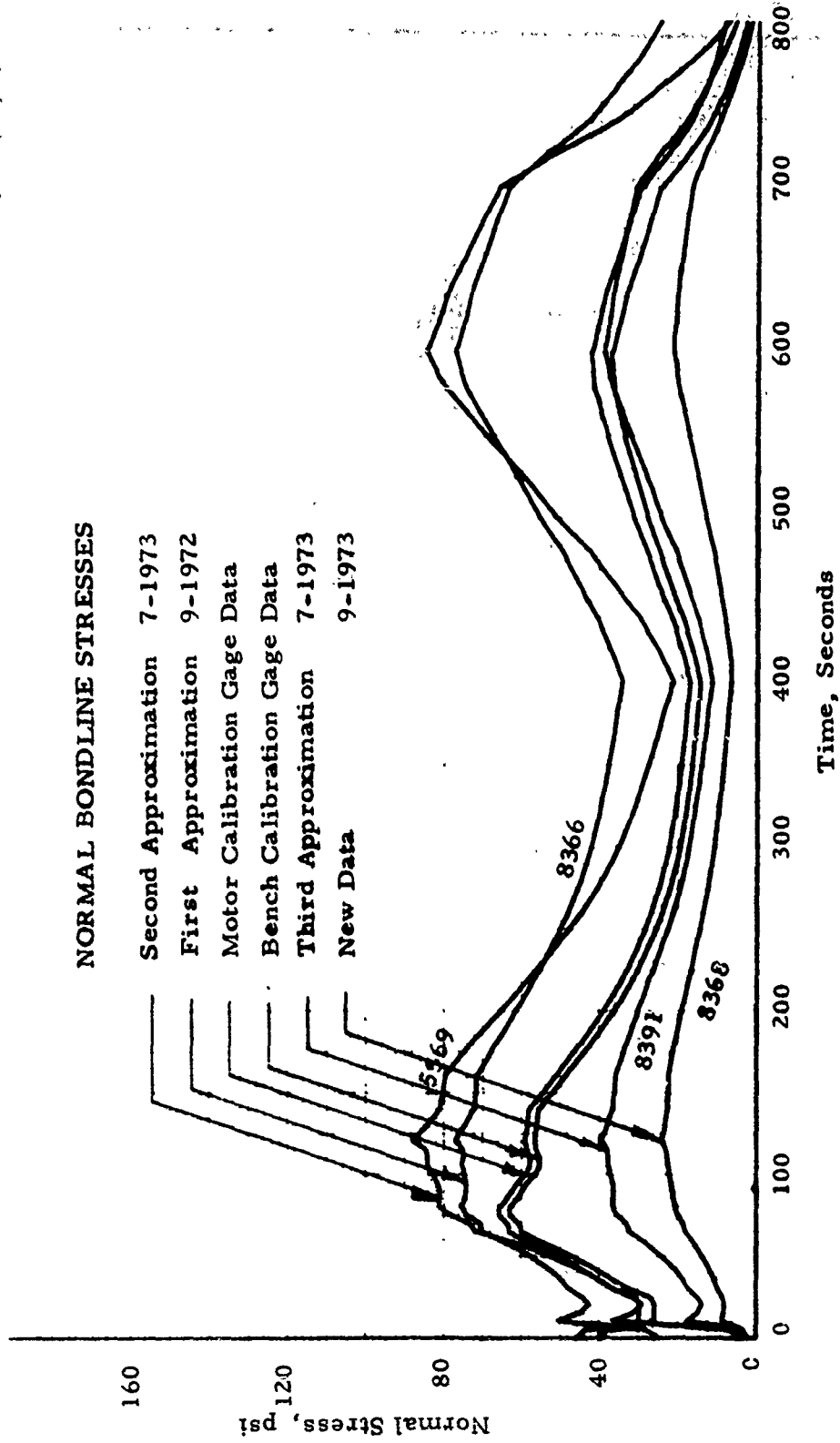


Figure 127 Calculated and Measured Normal Stresses N2-51 for Aeroheat DMP-3, A-1, IM #2, Using Different Modulus Curves

HOOP BORE STRESSES

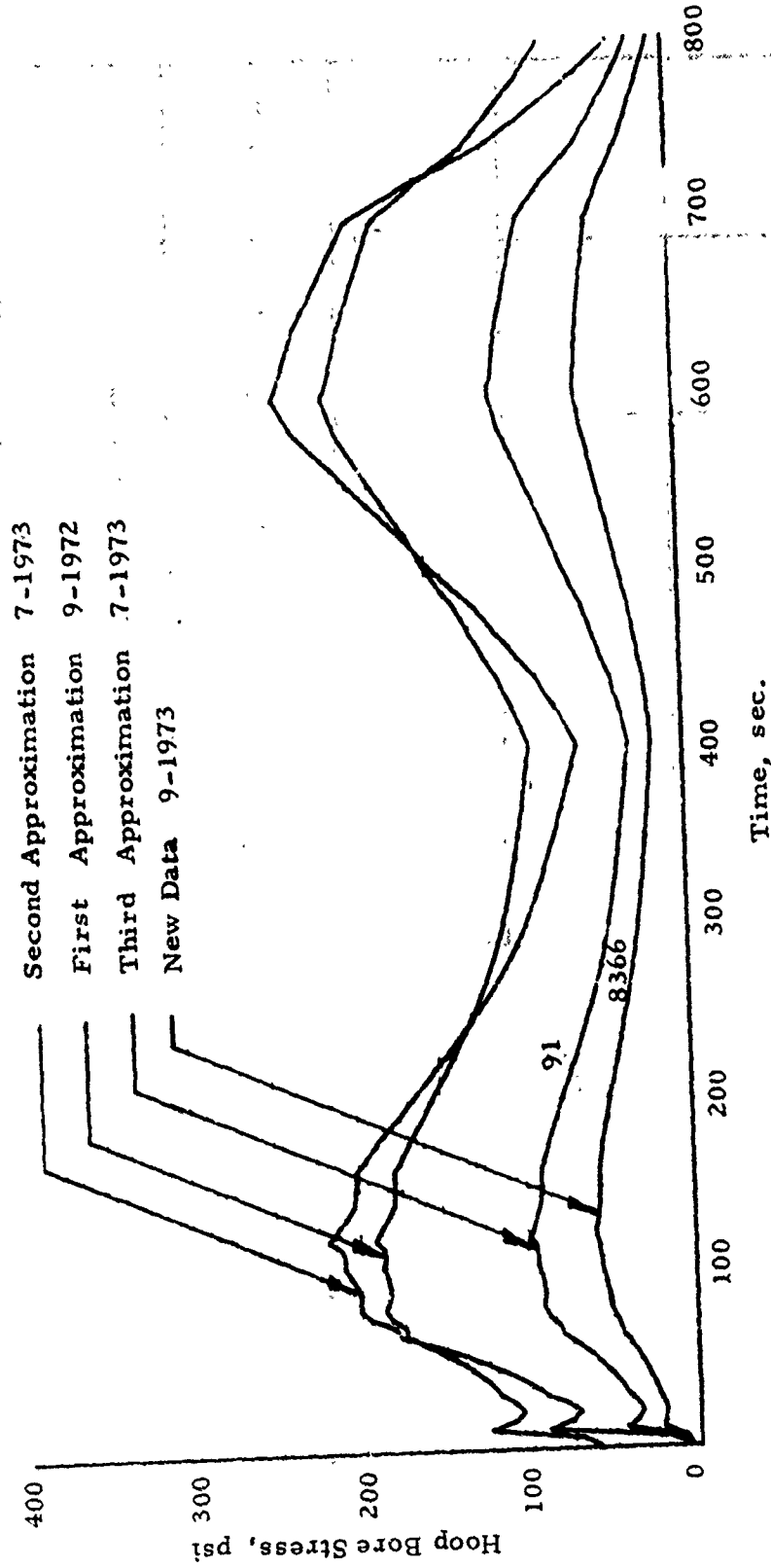


Figure 128. THERMVINC Results Using Different Modulus Curves for Aeroheat DMP-3, A-1, IM #2.

$$\log a_T = \frac{C_1 (T - T_s)}{C_2 + (T - T_s)} \quad \text{where } C_1 = 5.280$$

$$C_2 = 166.583$$

$$T_s = 298^{\circ}\text{K}$$

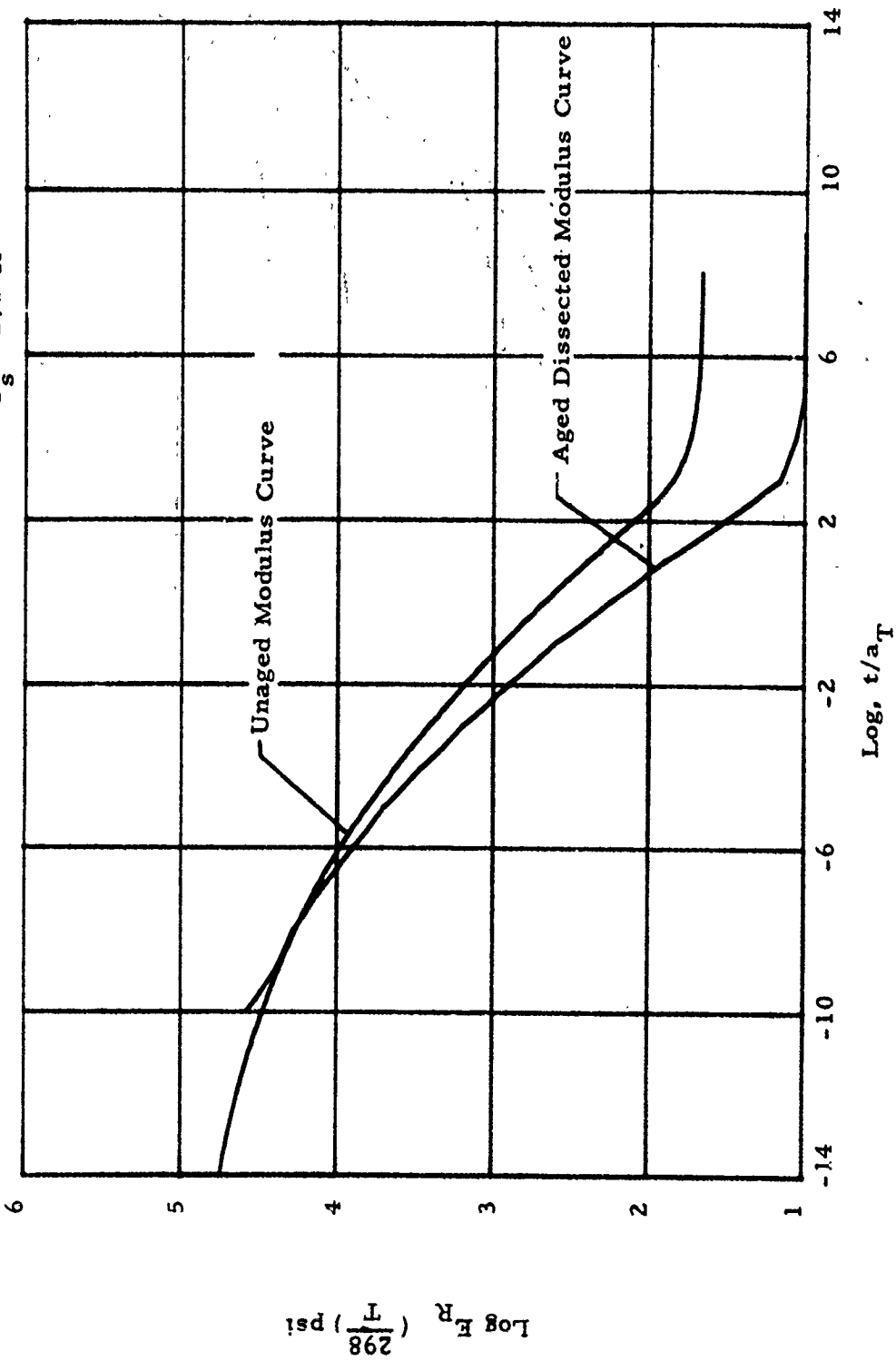


Figure 129. Relaxation Modulus Curve for Aged and Unaged TP-L8006 Propellant

inner bore produced by use of the aged and unaged modulus for a DMP-3 mission are presented on Figures 130 and 131 respectively. It is evident that for this mission the effect is small, representing 5 psi at the bondline and 15 psi at the bore. Again, the modulus of the liner is assumed to be the same as the modulus of the propellant. This aspect in itself was felt to provide a considerable effect; therefore, the effect of varying liner modulus and thickness was investigated. Relaxation modulus data were available for two materials, TL-H706A liner and TP-H727B filler material, which should have similar properties to the polysulfide liner. Unfortunately the polysulfide liner had not been fully characterized, thus the need for using the other data. The relaxation modulus data for each of these materials are shown on Figure 132.

The effect the use of the various moduli in different combinations have on the calculated results are shown for a SFPI mission (Test A-12 on IM #3) in Figures 133 and 134. The effect on bondline normal stress is shown on Figure 133 & bore hoop stress on Figure 134. At the bondline the deviation at the extremes is 25 psi; however, at the inner bore the deviation is 50 psi.

The effect of varying liner thickness on bondline normal stress and bore hoop stress are shown for the DMP-3 mission on Figures 135 and 136 respectively. These calculations are based on using the TL-H706A modulus data for the liner--felt to be the most representative--and the aged propellant modulus. The selection of a thickness of 1.0 inch was based on the desire to examine gross effects. It should be recalled that the normal gages were encapsulated in liner material with about 0.25 inch of the material being between the gage and the case. It is interesting to note that one of the effects of a thicker liner is to show the curve skewing downward with increasing time. This effect is quite similar to that seen in gage data. This could indicate that gage encapsulation in the liner material induced errors in response because the relaxation in the encapsulant was faster than the surrounding propellant. The deviation at the two extremes in terms of response is only 10 psi at the bondline and 22 psi at the inner bore. However, it should be noted that this deviation will increase with the hotter SFPI aeroheat mission profiles. The importance of the liner properties and thickness is obvious by the significant sensitivity that they have on the induced stress field. This was further confirmed when a calculation was made in which the coefficient of thermal expansion of the liner was doubled resulting in a decrease in bondline stress of 10 percent.

As a further check on the ability of THVINC to accurately predict temperature histories, comparisons between the predicted temperature gradient and measured gradient were made at different times. These comparisons are shown on Figure 137. The calculations were based on inputting into THVINC the case temperature-time history as shown in Figure 138 forcing the program to calculate the temperature profiles. As shown, the agreement is good, considering an average value of thermal conductivity was used. However, THVINC was not normally input in this manner. Since thermal conductivity as a function of temperature data was not available, the measured temperature gradient was used as input temperatures in the THVINC analysis.

Motor - IM #3  
 Test - A-1 (DMP-3)  
 T<sub>initial</sub> - -65°F

THVINC prediction based on measured temperature gradient.

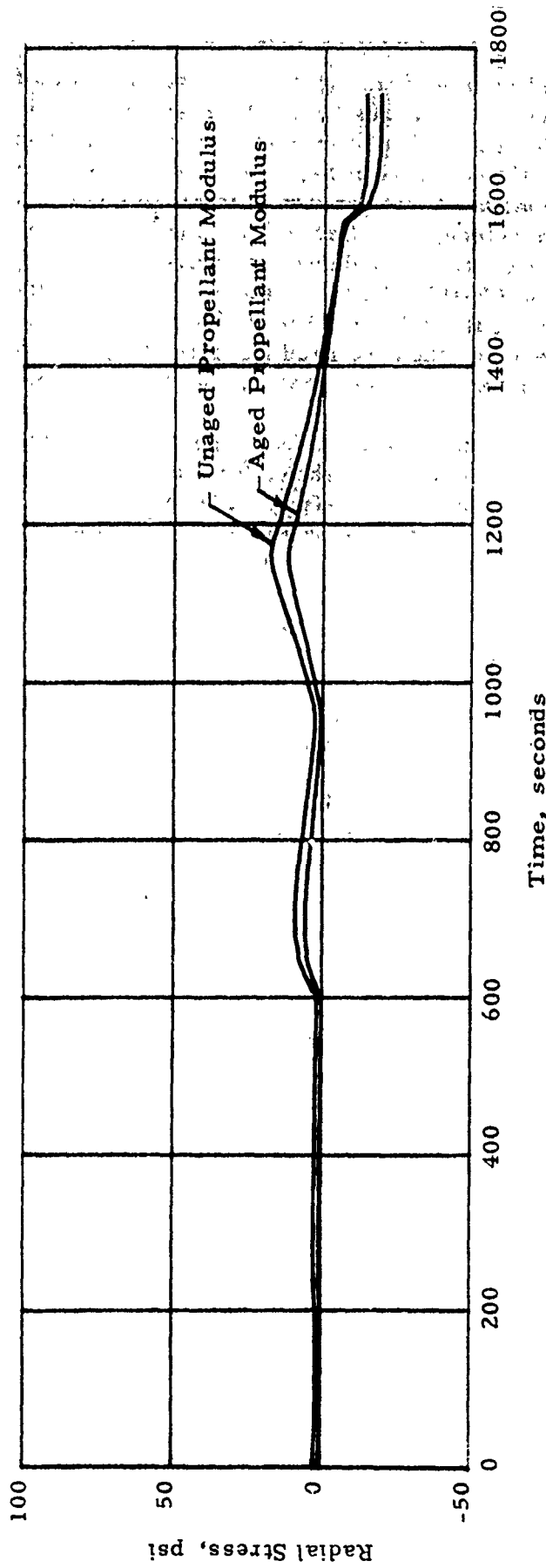


Figure 130. THVINC Prediction of Radial Stress at the Bondline for DMP-3 Aeroheat Mission With Aged and Unaged Propellant

Motor - IM #3  
 Test - A-1 (DMP-3)  
 T<sub>initial</sub> - -65°F

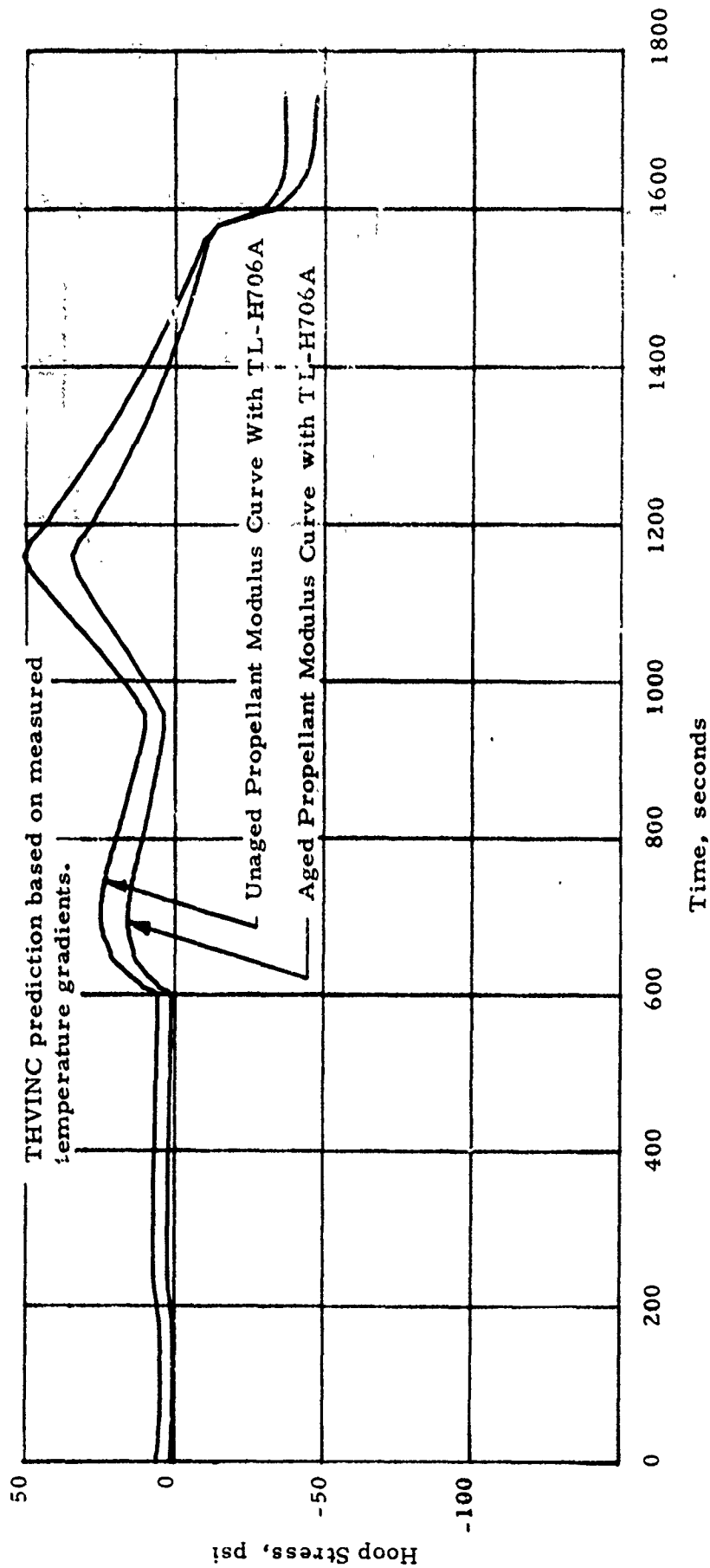


Figure 131. THVINC Prediction of Hoop Stress at the Inner Bore for DMP-3 Aeroheat Mission With Aged and Unaged Propellant

$$\log a_T = \frac{C_1 (T - T_s)}{C_2 + (T - T_s)}, \text{ where } C_1 = 8.86$$

$$C_2 = 101.6$$

$$T_s = 250^\circ\text{K}$$

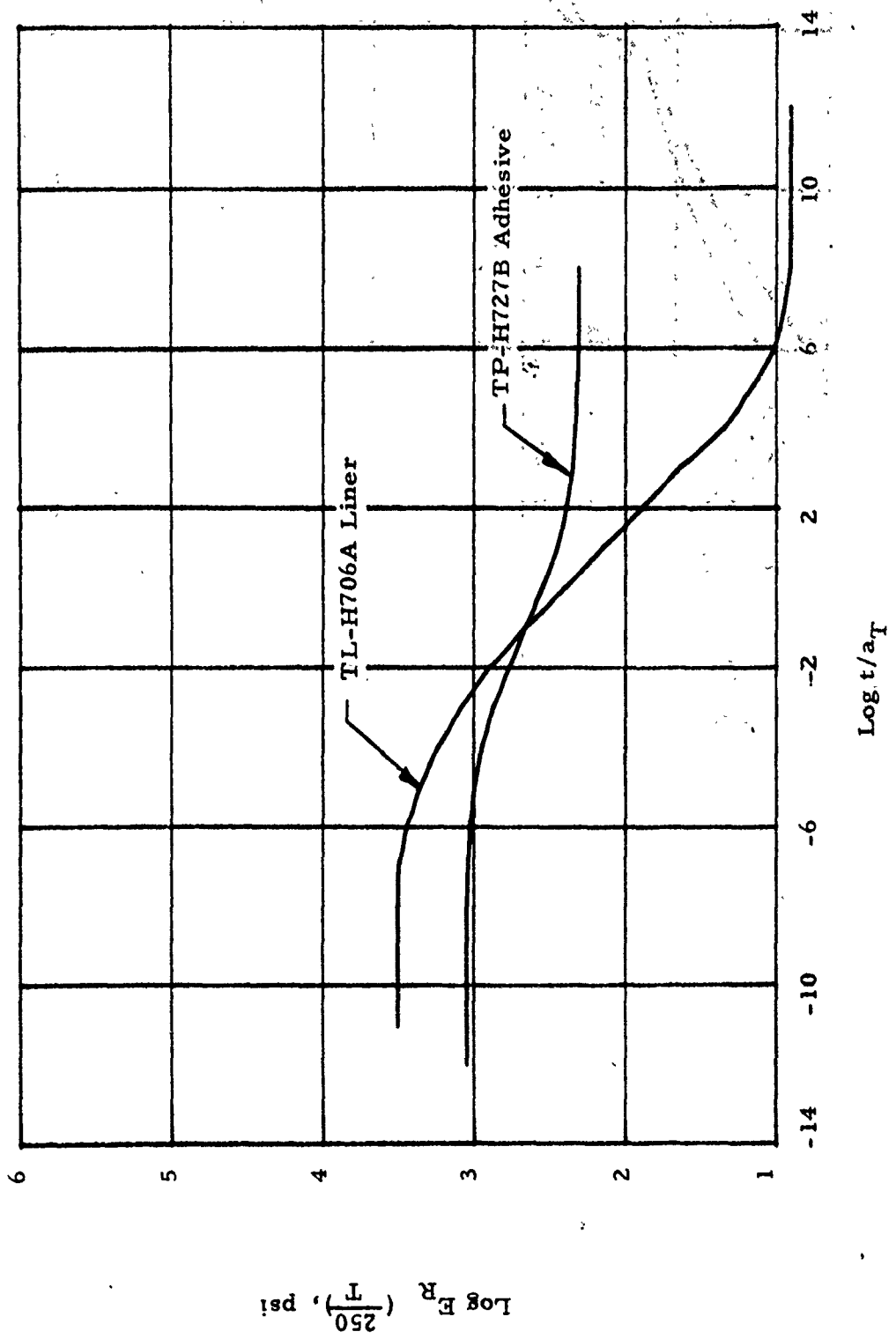


Figure 132. Relaxation Modulus Curve for TL-H706A Liner and TA-H727B Adhesive

Motor - IM #3  
 Test - A-12 (SFPI)  
 T<sub>initial</sub> - -65°F

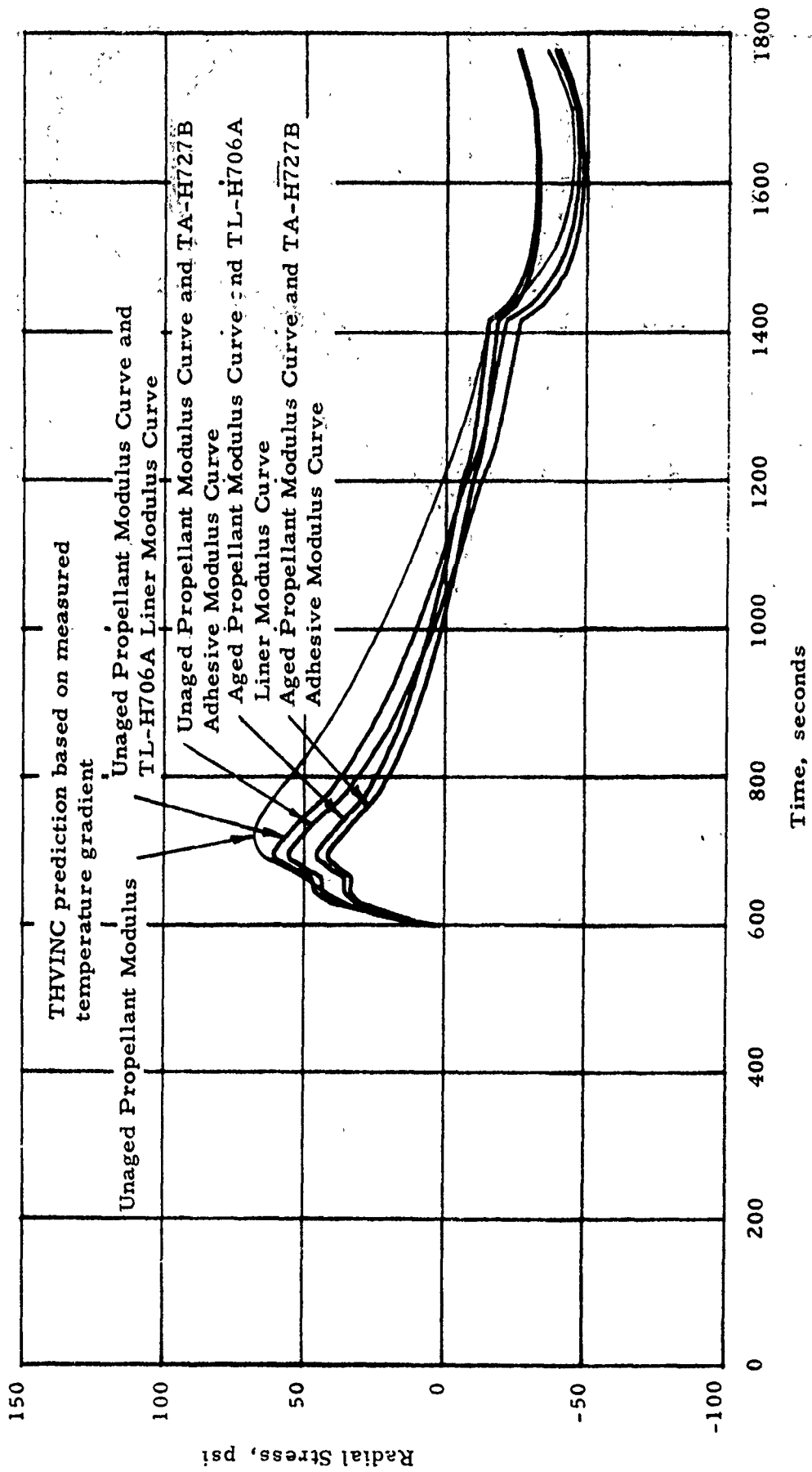


Figure 133. THVINC Prediction of Radial Stress at the Bondline for the SFPI Aeroheat Mission Using Different Modulus Curves

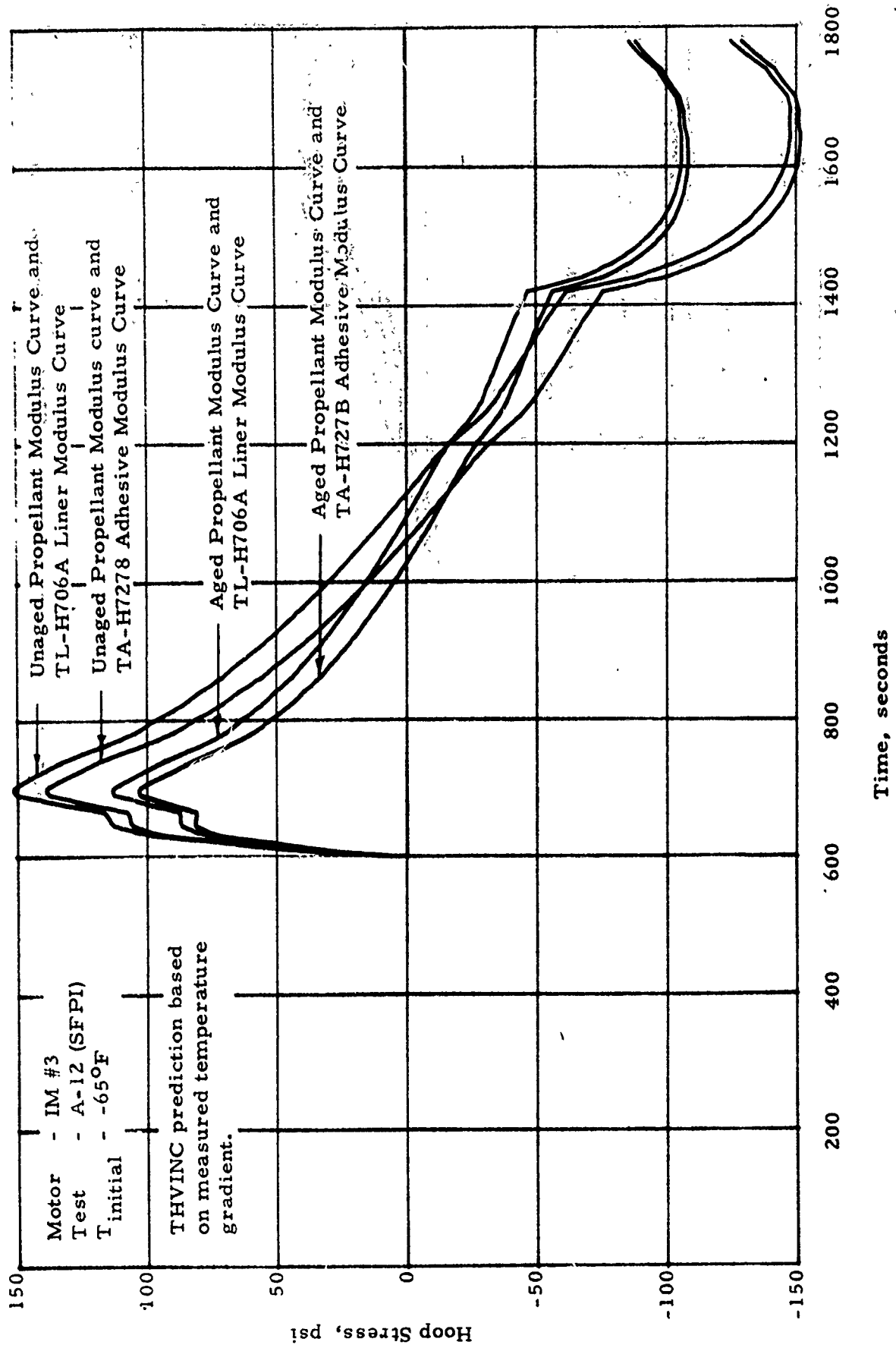


Figure 134. THVINC Prediction of Hoop Stress at the Inner Bore for the SFPI Aeroheat Mission Using Different Modulus Curves

Motor - IM #3  
Test - A-1 (DMP-3)  
T<sub>initial</sub> - -65°F

THVINC Prediction Based on Measured Temperature Gradient

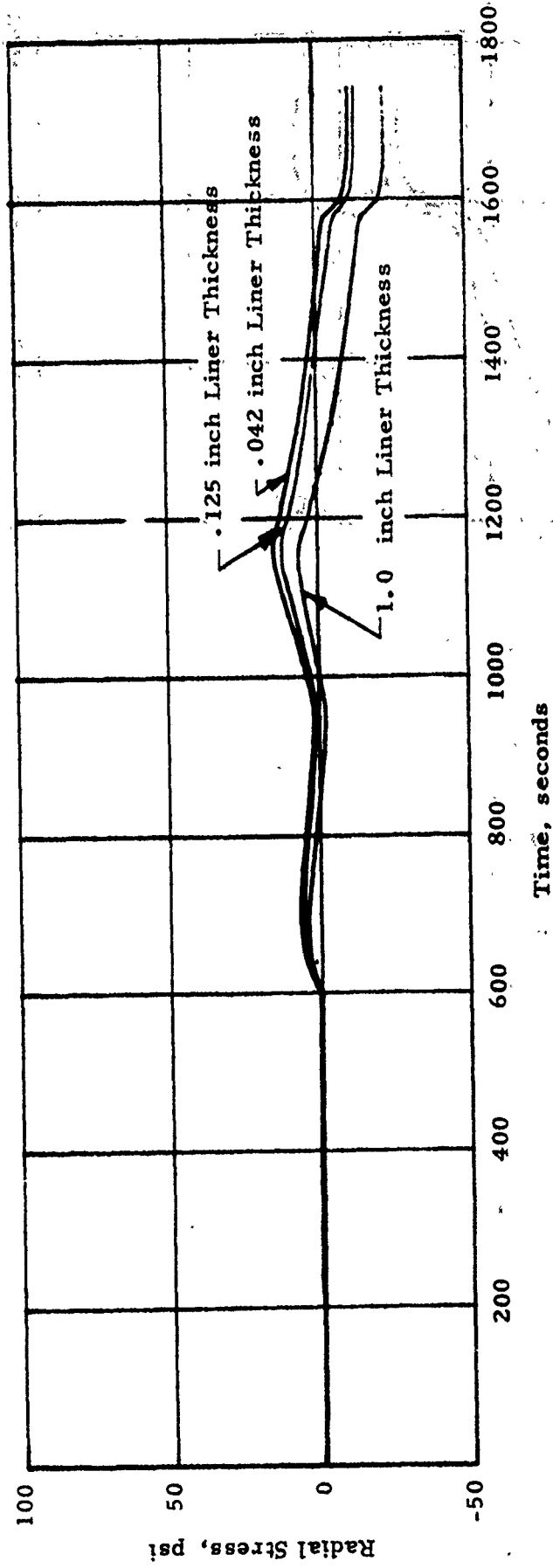


Figure 135. THVINC Prediction of Radial Stress at the Bondline for DMP-3-Aeroheat-Mission With Different Liner Thicknesses

Motor - IM #3  
 Test - A-1 (DMP-3)  
 T<sub>initial</sub> - -65°F

THVINC Prediction Based on Measured Temperature Gradients

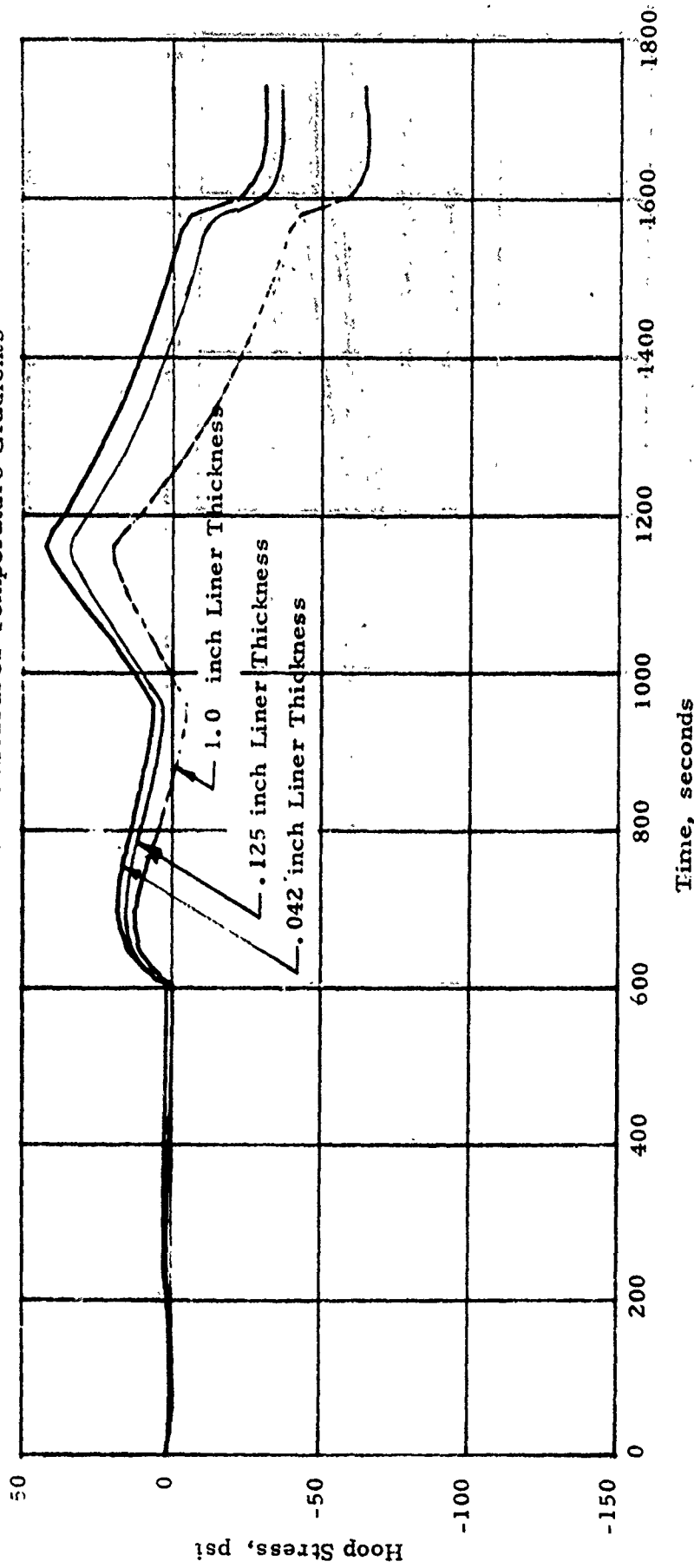


Figure 136. THVINC Prediction of Hoop Stress at the Inner Bore for DMP-3 Aeroheat Mission With Different Liner Thickness

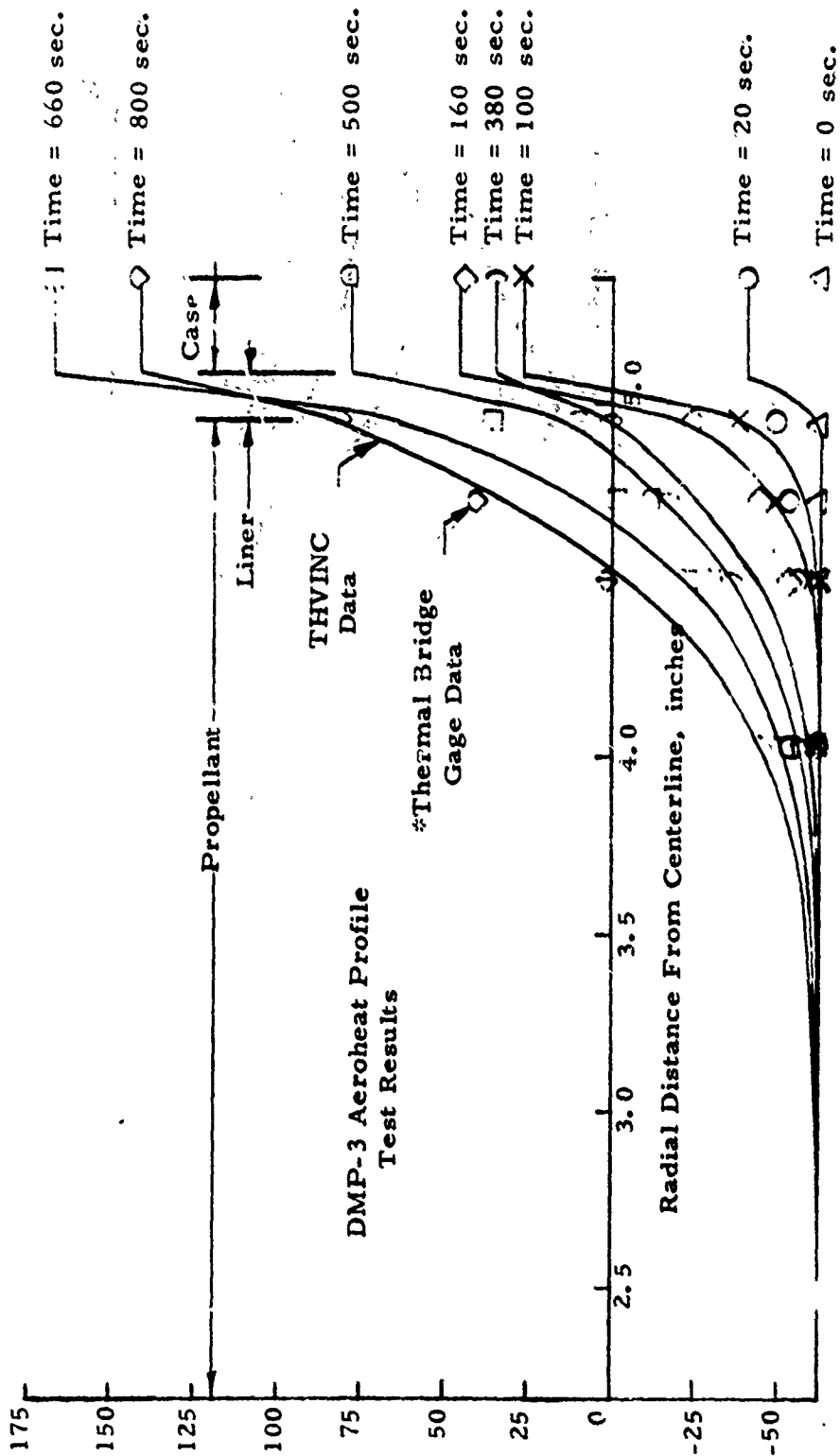


Figure 157. Comparison of THVINC Predictions and Aeroheat Results

Motor - IM #2  
 Test - A-1 (DMP-3)  
 Gage - Temperature Profile  
 Location - Center  
 T Initial - -65°F

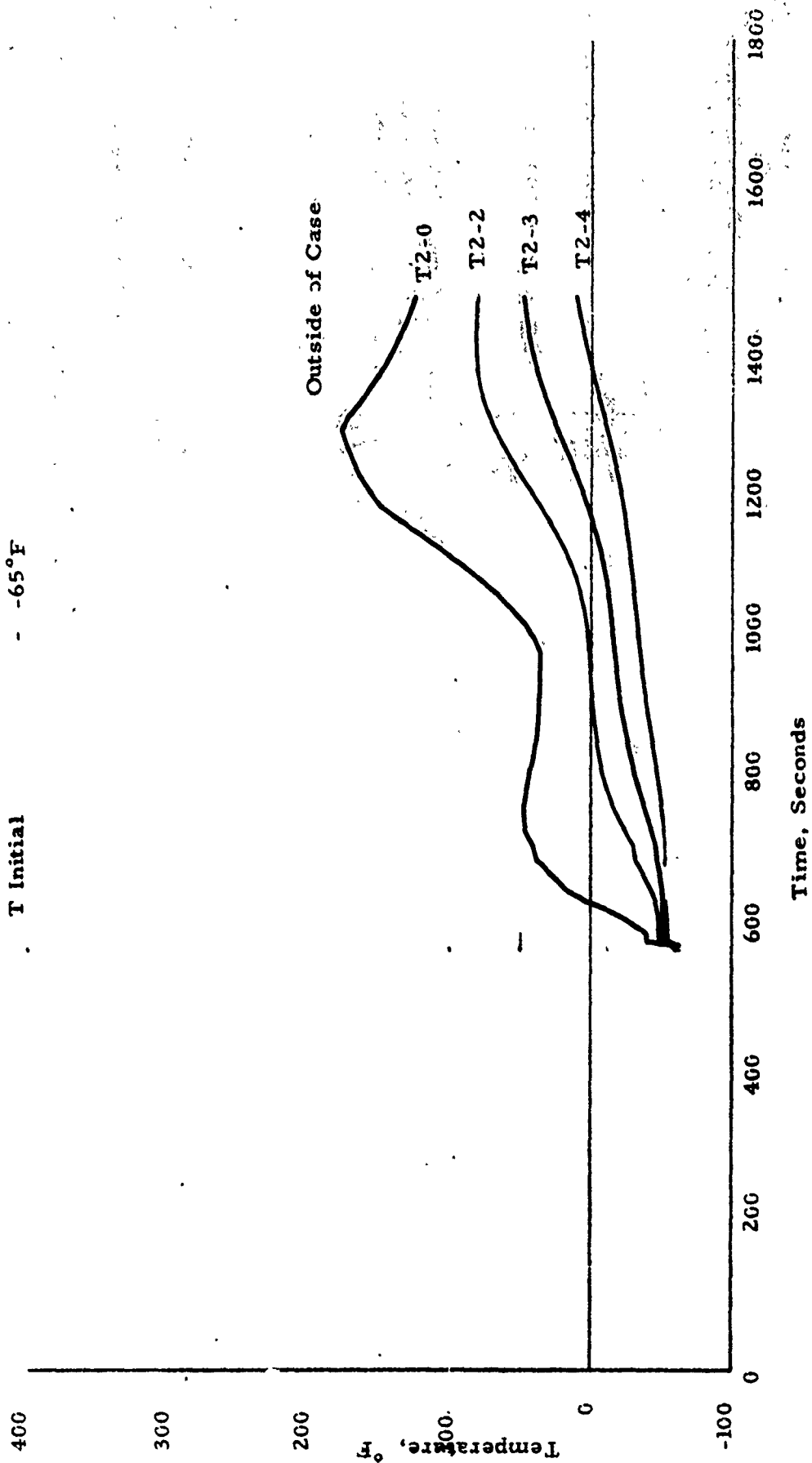


Figure 138. Temperature Profile Histories for Various Aeroheat Loads. Test A-1

This method insured that the heat load was properly being applied. The thermocouple slab data were punched out in card form from the data reduction program for input to THVINC. This procedure required that THVINC be set up on the same time step basis as the data were acquired.

Since IM #2 and IM #3 were finite circular cylinders, an axisymmetric finite element THVINC analysis was performed to establish the end effects. The mathematical element model is shown in Figure 139. This model is relatively coarse due to the computational expense of a viscoelastic analysis. However, it is adequate in comparing gage data at the bondline due to the smaller bondline elements. To establish the realistic temperature profile along the length of the motor, a quadratic curve fit of temperature data on the exterior of the case was established at a given time. From this calculation an equation as a function of axial distance and radial distance was formed. An overall complete temperature profile was generated as a function of time based on projecting the measured radial profile in the axial direction for use as input for THVINC. The THVINC axisymmetric analysis was performed using the A-12, SFPI, aeroheat temperature shown on Figure 140 obtained from the thermocouple slab. A comparison between the plane strain and axisymmetric analysis is shown on Figure 141. Figures 142 through 146 show the axisymmetric results at the same location as the bondline normal and shear gages in the forward, center, and aft end of the motor. The analysis did not completely account for the thermal shielding at the forward and aft end of the motor by the aeroheat hardware which effects the axial growth of the case during an aeroheat test. Also, the brackets that hold the motor in the aeroheat fixtures were not considered. A comparison stress measured by head end gages N3-44 and N2-42 with the THVINC radial stress calculation are shown in Figure 147. Since the gages are on the forward dome, the measurement will be a normal stress as opposed to radial. A geometrical correction shows that at a test time of 700 seconds the calculated normal stress is 41 psi when the radial stress is 34 psi. The normal stress lies between the maximum principal and the radial stress.

When solving transient problem or problems that are a function of time, the nonlinearity of propellant should be considered due to the deviation of measured and calculated stress values. This aspect has been studied and reported by Farris and Schapery<sup>1</sup>. It is interesting to note from the data they present in that report that a large deviation between linear and non-linear theory exist for slow temperature changes while better agreement was found for rapid temperature changes. The nonlinear theory agrees with experimental results for both conditions and shows much faster stress rise rates and relaxation rates. These are interesting data and the nonlinear

---

<sup>1</sup>"Development of a Solid Rocket Propellant Nonlinear Viscoelastic Constitutive Theory", AFRPL-TR-73-50, by Dr. R. J. Farris, Aerojet and Dr. R. A. Schapery, Texas A&M.

Motor - IM #2, IM #3

- Element Number 30 Head End Gage Location
- Element Number 94 Center Gage Location
- Element Number 174 Aft End Gage Location
- Element Number 137 Strain Gage Location
- Element Number 169 Strain Gage Location

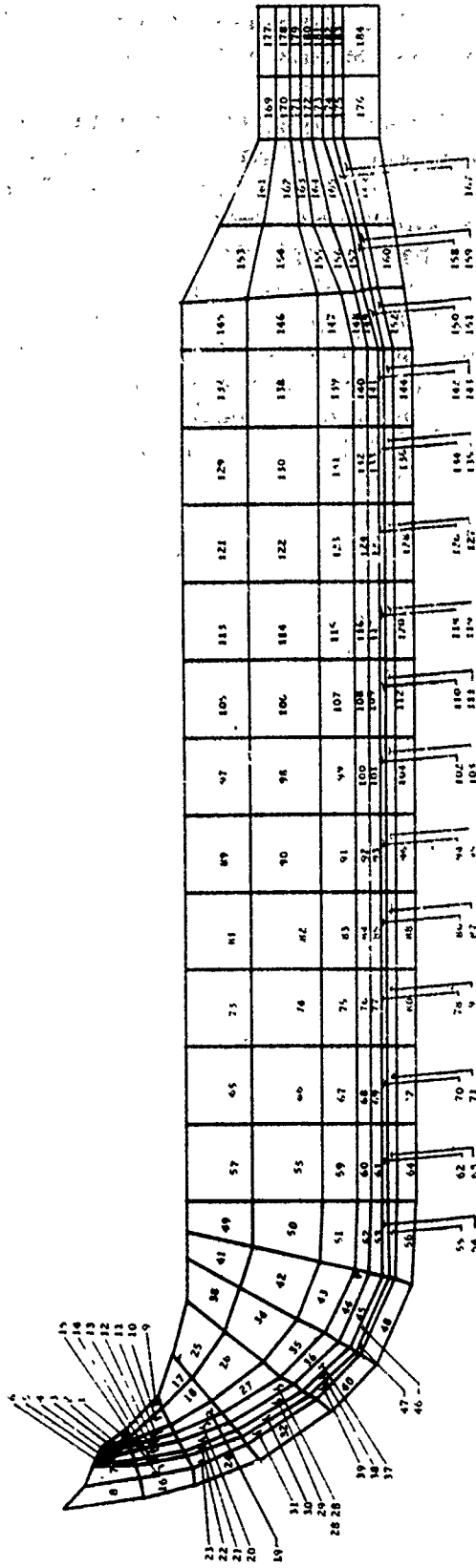


Figure 139. THVINC Axisymmetric Mathematical Element Model

Motor - IM #3  
 Test - A-12 (SFPI)  
 Gage - Temperature Profile  
 Location - Center  
 T<sub>initial</sub> - -65°F

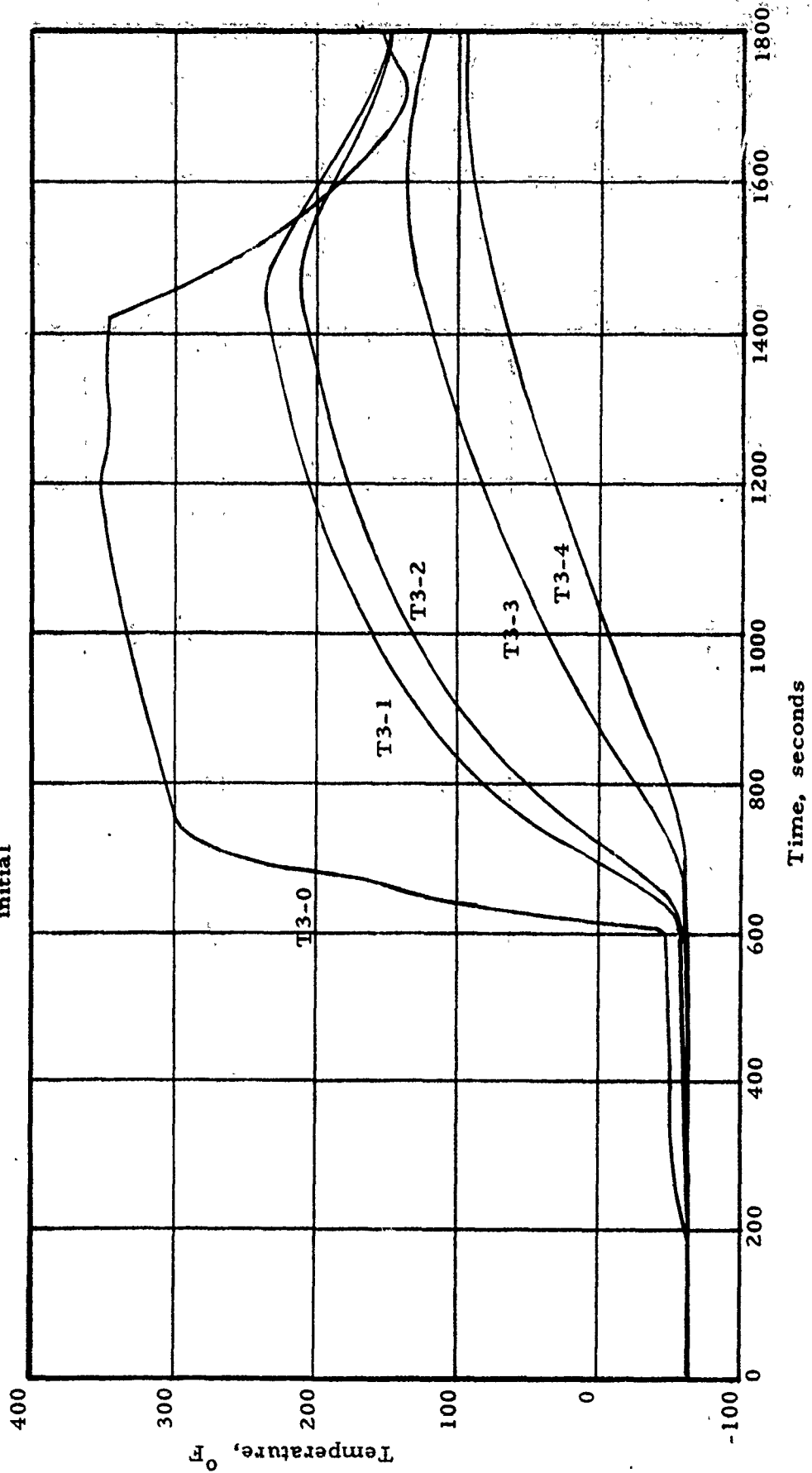


Figure 140. Temperature Profile Histories for Various Aeroheat Loads

Motor - IM #3  
 Test - A-12  
 T initial - -65°F

THVINC Prediction based on Measured Temperature Gradients

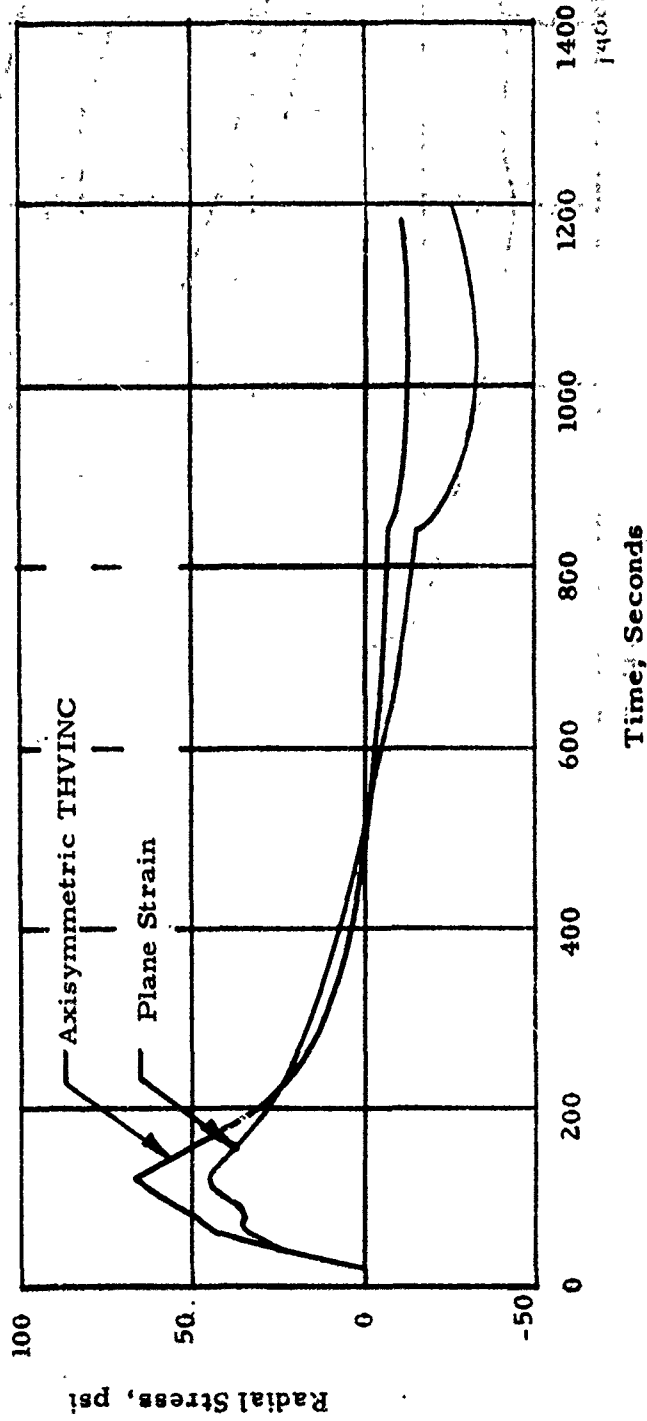


Figure 14. THVINC Prediction of Radial Stress at the Bondline for SFPI Aeroheat Mission.

MOTOR - IM#3  
 TEST - A-12  
 INITIAL - -65°F  
 2-DIMENSIONAL

THVINC PREDICTION BASED ON MEASURED TEMPERATURE GRADIENT

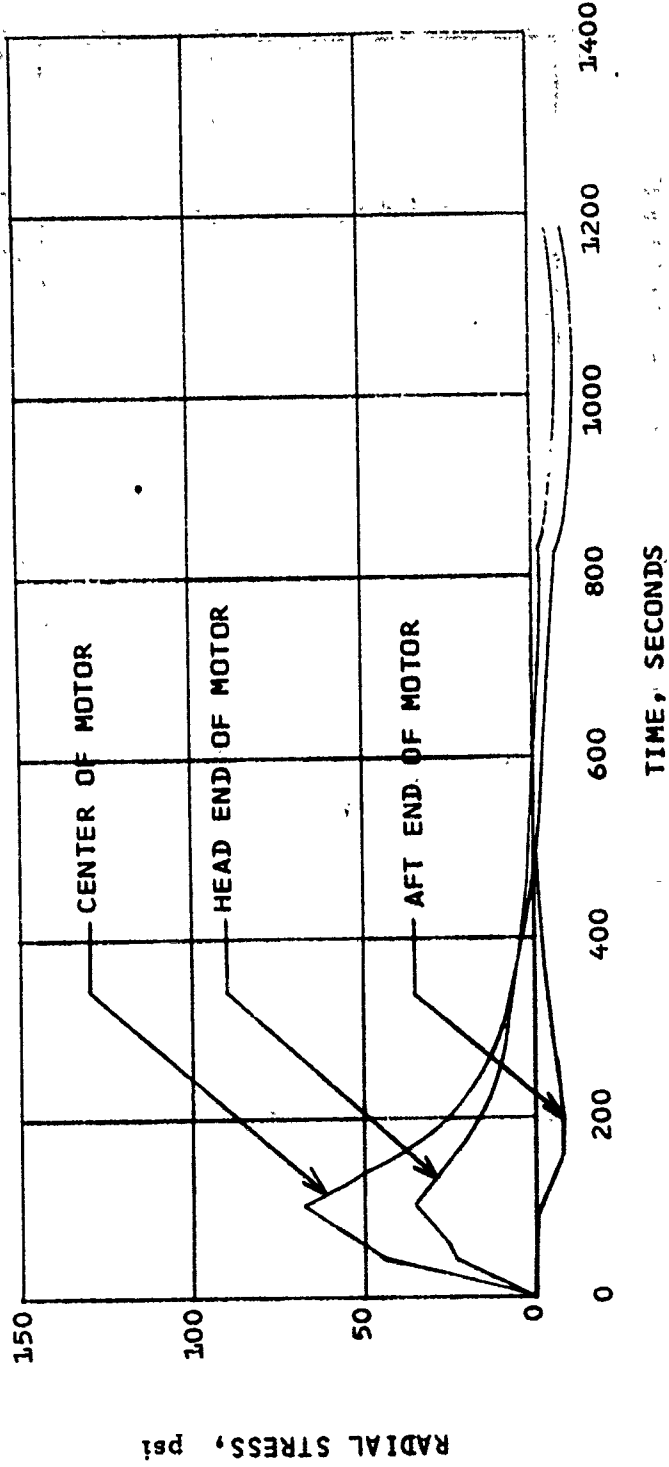


Figure 142. THVINC PREDICTION OF RADIAL STRESS AT THE BONDLINE FOR SFPI AEROHEAT MISSION

MOTOR - IM#3  
 TEST - A-12  
 INITIAL - -65°F  
 2-DIMENSIONAL

THVINC PREDICTION BASED ON MEASURED TEMPERATURE GRADIENT

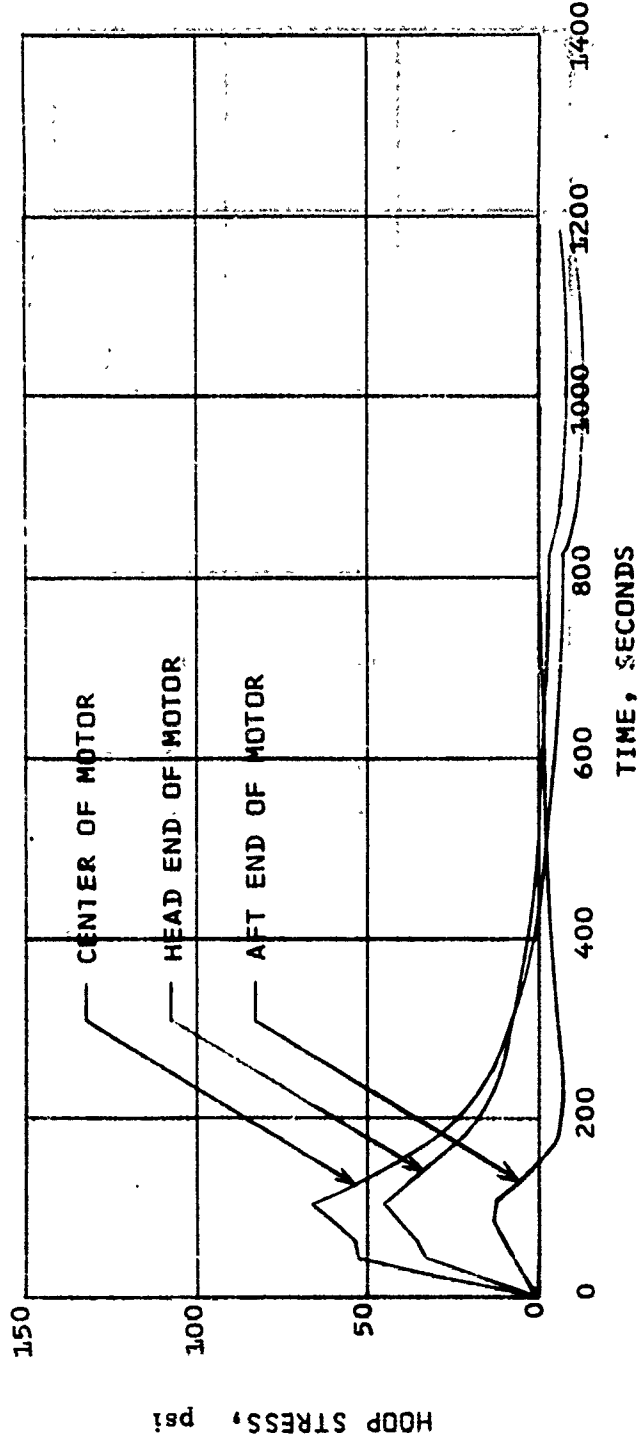


Figure 143. THVINC PREDICTION OF HOOP STRESS AT THE BONDLINE FOR SFPI AEROHEAT MISSION

MOTOR - IM#3  
 TEST - A-12  
 INITIAL - -64°F  
 2-DIMENSIONAL

THVINC PREDICTION BASED ON MEASURED TEMPERATURE GRADIENT

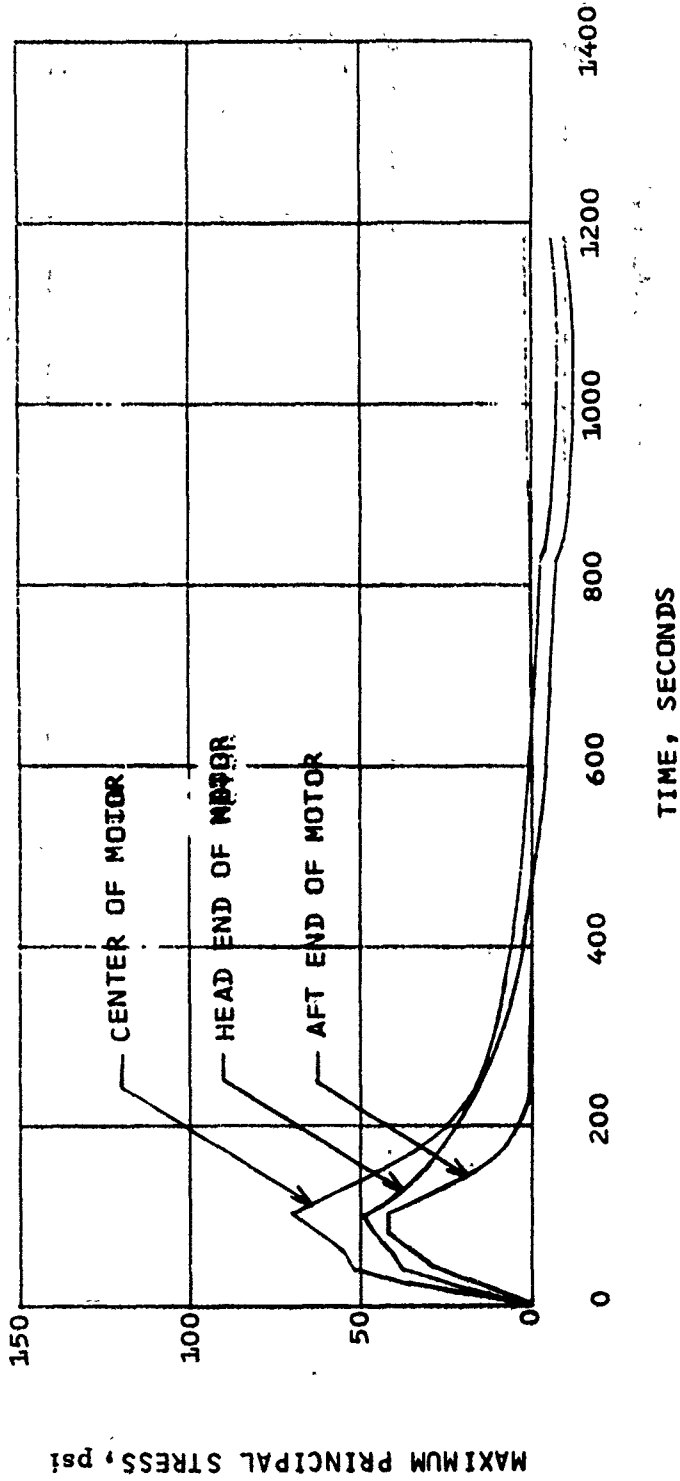


Figure 144. THVINC PREDICTION OF MAXIMUM PRINCIPAL STRESS AT THE BONDLINE FOR SFPI AEROHEAT MISSION.

MOTOR - IM#3  
 TEST - A-12  
 T INITIAL - 65°F  
 2-DIMENSIONAL

THVINC PREDICTION BASED ON MEASURED TEMPERATURE GRADIENT

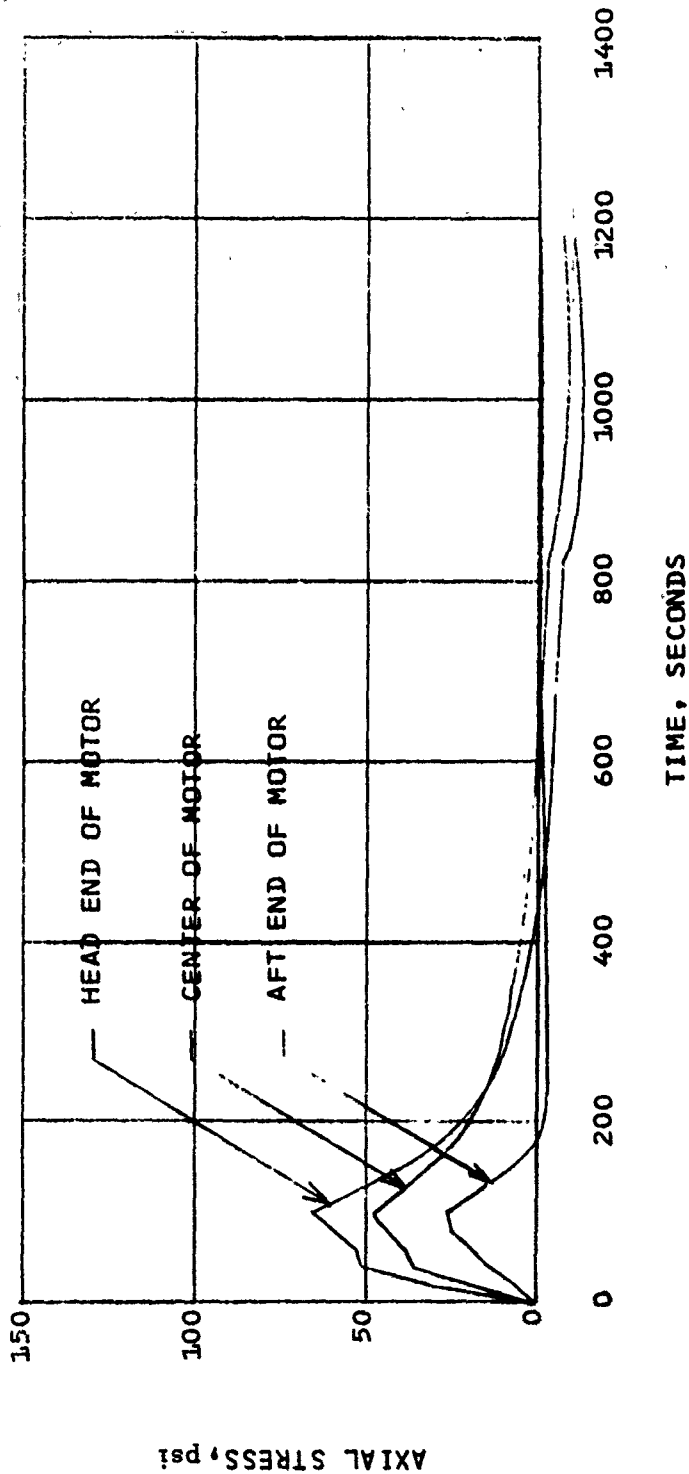


Figure 145. THVINC PREDICTION OF AXIAL STRESS AT THE BONDLINE FOR SFPI AEROHEAT MISSION

MOTOR - IM#3  
 TEST - A-12  
 T INITIAL - -65°F  
 2-DIMENSIONAL

THVINC PREDICTION BASED ON MEASURED TEMPERATURE GRADIENT

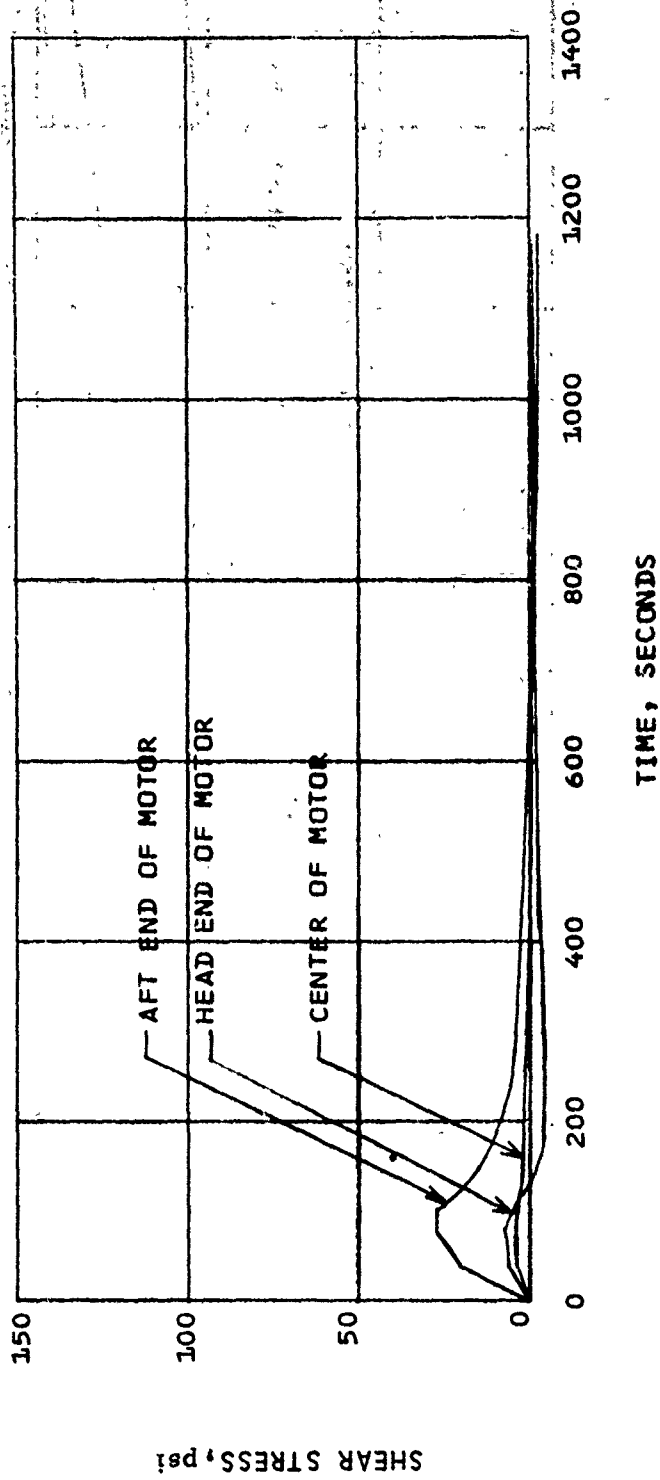


Figure 146. THVINC PREDICTION OF SHEAR STRESS AT THE BONDLINE FOR SFPI AEROHEAT MISSION

Motor IM #3, IM #2  
 Test A-12, A-3 (SFPI)  
 Initial -65  
 Gage N3-44, N2-42  
 Location Forward

Data based on gage output being adjusted to zero (0) reading when motor is equilibrated to a temperature of 170°F.

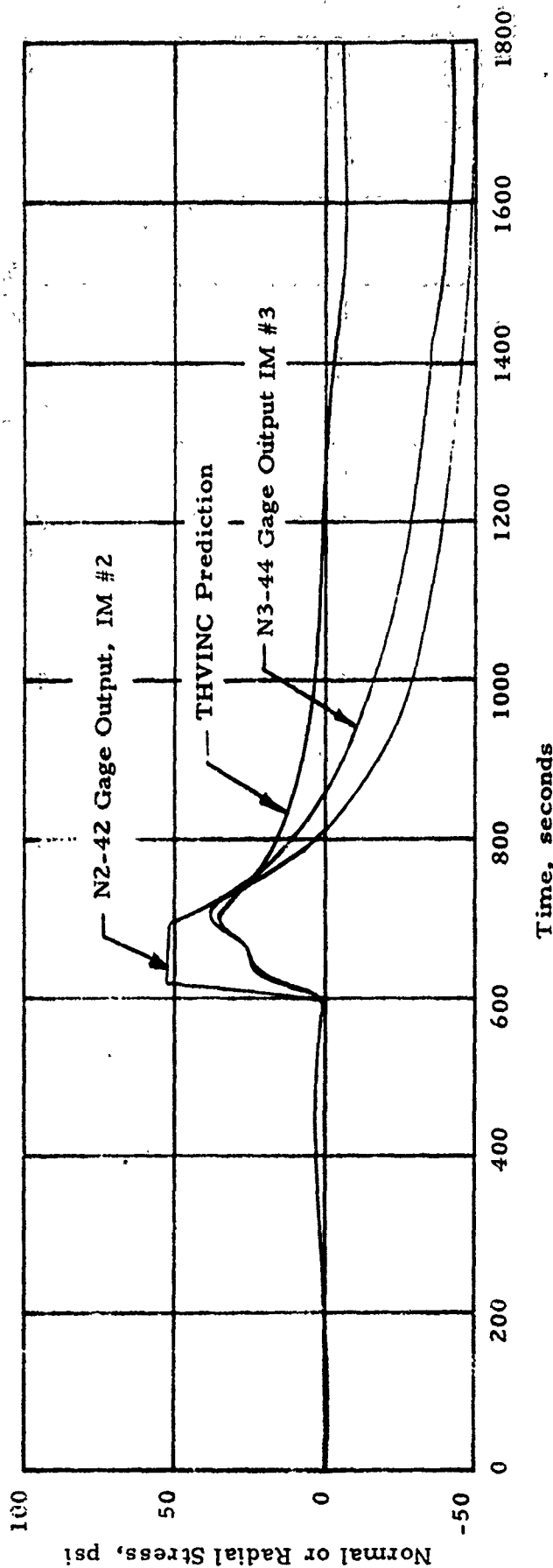


Figure 147. Head End Normal Stress Gage Output and Axisymmetric THVINC Results at the Bondline

effects may well be the reason for the rapid rise and relaxation seen in SALE data and the tendency for a linear theory like THVINC to underpredict.

In general, the parametric study showed that propellant and liner relaxation modulus curves, thermal conductivity as a function of temperature, coefficient of thermal expansion as a function of temperature, modeling of the problem, liner thicknesses, accurate boundary condition and the possibility of nonlinearity of propellant can induce significant deviations in the solution. These possible sources of error must be considered when comparing the measured data to the predictions. The errors caused by shifts in gage calibration in the measured data, and the effects of grain deterioration such as bore cracking all tend, coupled with the limitation in the theoretical analyses, to deny valid comparison. For instance, an example of the effect the bore cracking had on strain measurements is illustrated on Figure 148. Here, the measured strain induced by aeroheat is seen to decrease as the initial motor temperature is decreased; whereas, it should increase in the manner that is shown theoretically. Whether or not the difference shown between theory and experiment at 0°F is caused by the bore already having deteriorated is not known. Corresponding bondline normal stresses for the test are shown on Figure 149 as a matter of interest and to show the sensitivity of initial grain temperature. (In making these comparisons it must be remembered that both the experimental data and theoretical calculations were referenced to 170°F which was not the strain free temperature) these same predictions are repeated on Figure 150 where they are shown in comparison with data from IM #2 and IM #3. The IM #2 data (N2-51) is comparable to Test A-12 of IM #3 since both were SFPI missions initiated from -65°F. The most obvious difference is in the initial stress levels. THVINC which uses an equilibrium modulus value for the initial calculation shows the initial stress level to be essentially zero. Part of the differences in the others are due to the initial temperature differences. Another obvious difference between experiment and theory is in the relaxation rate after the peak stress level has been reached. It was postulated that perhaps part of this was due to the seemingly high initial stress level. A THVINC calculation was made assuming a prestressed condition and it can be seen from the code that the relaxation would be a factor from the higher stress state is basically confirmed.

A better comparison between theory and experiment would be based on the initial DMP-3 tests. Both gage aging and grain deterioration effects would be minimum there. Such a comparison is shown on Figure 151. In general, we find similar trends with the gages showing higher induced stress on the second peak than theory. It is again interesting to see the downward skew in the gage curves which was seen in the parametric study to be a function of liner thickness. In this figure, the data is presented in terms of induced stress for easier comparison.

Since the gage data is known to be in error due to chemical aging, the only alternative is to consider that the analysis is more accurate in describing this type of loading condition. However, it is important to have some reliable test data to verify the analysis. It should be noted that in the comparison

Motor - IM #3  
 Test - A-8, A-9  
 T<sub>initial</sub> - A-8 (0°F), A-9 (-40°F), A-12 (-65°F)

THVINC prediction based on measured temperature gradient.

--- Measured Strain-Superimposed on Theory

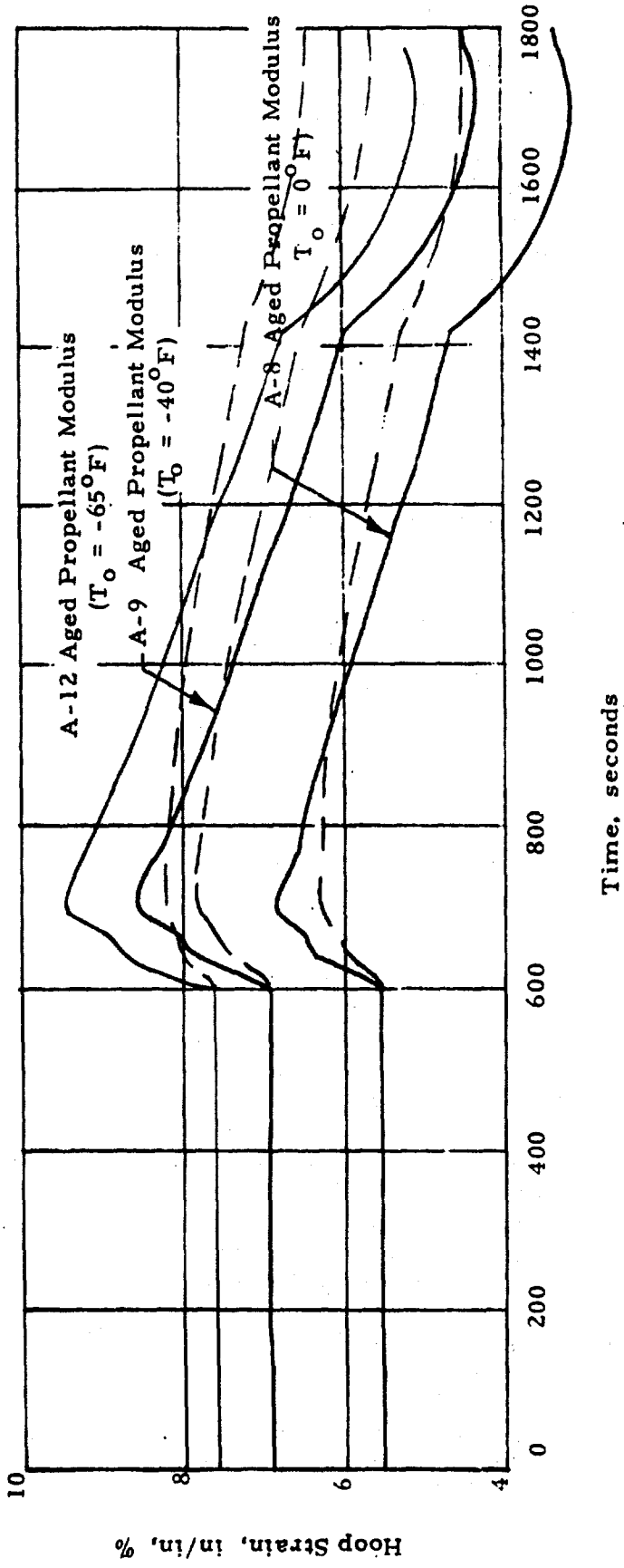


Figure 148. THVINC Prediction of Hoop Strain at the Inner Bore for SFPI Aeroheat Mission

Motor - IM #3  
 Test - A-8, A-9  
 T<sub>initial</sub> - A-8 (0°F), A-9 (-40°F), A-12 (-65°F)

THVINC prediction based on measured temperature gradient.

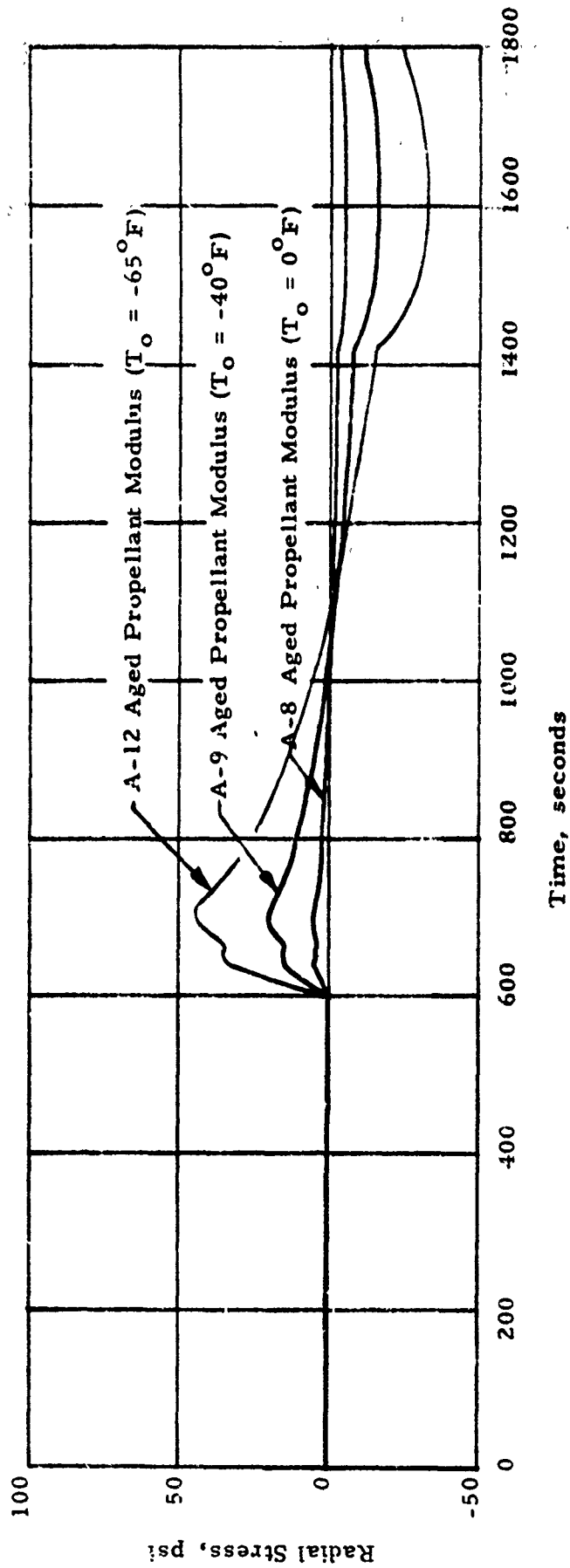
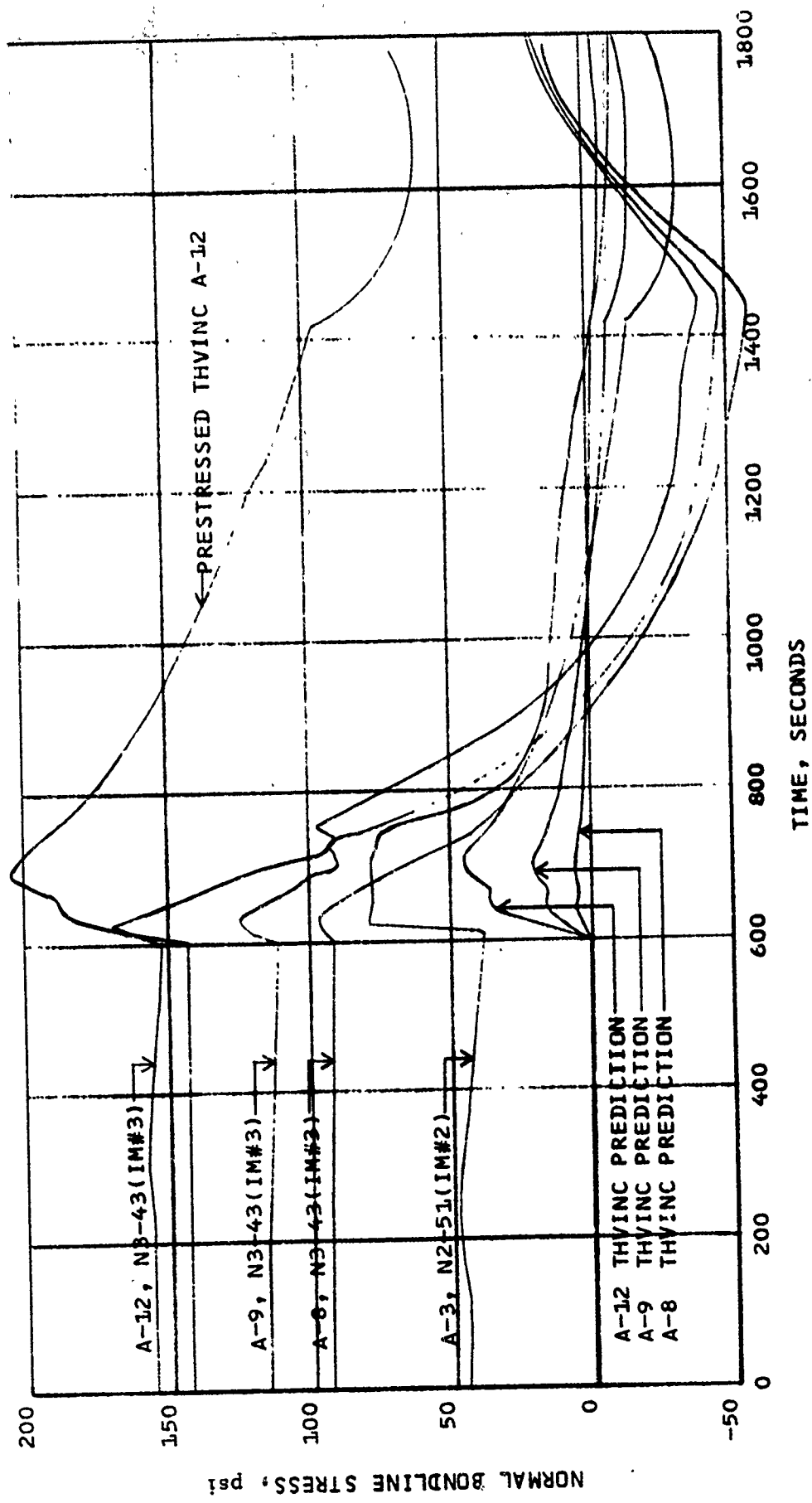


Figure 149. THVINC Prediction of Radial Stress at the Bondline for SFPI Aeroheat Mission

MOTOR - IM#2 AND IM#3  
 TEST - A-3, A-8, A-9, A-12  
 INITIAL - A-3(-65°F), A-8(0°F), A-9(-40°F), A-12(-65°F)

GAGE - N2-51, N3-51  
 LOCATION - CENTER OF MOTOR



COMPARISON BETWEEN NORMAL GAGE DATA AND THVINC PREDICTION  
 FOR A SFPI AEROHEAT MISSION WITH IM#2 AND IM#3

FIGURE 150.

MOTOR - IM #2 AND IM #3  
 TEST - DMP-3  
 GAGE - N2-51, N3-43, N3-47  
 LOCATION - CENTER  
 TINITIAL - -65°F

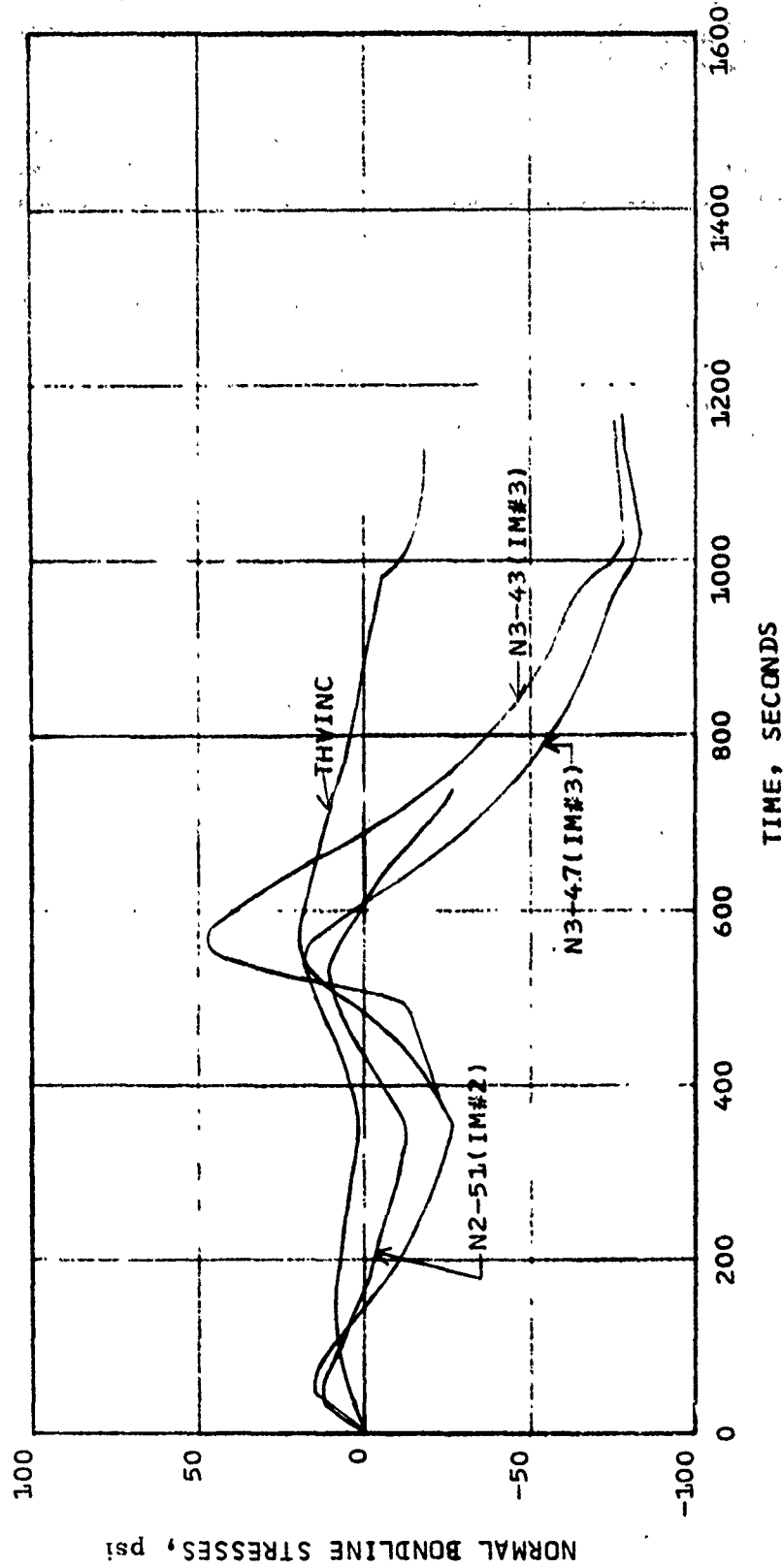


FIGURE 151. COMPARISON BETWEEN NORMAL STRESS GAGE DATA AND THVINC.  
 PREDICTIONS FOR TEST A-2, IM#2, AND TEST A-1, IM#3, DMP-3  
 AEROHEAT MISSION

of gage output and analysis in the forward end of IM #2 and IM #3, the results were very favorable as presented in Figure 145 except for the prestress phenomena. This information does give additional confidence in the analysis, since the normal stress gages in the head end of IM #2 and IM #3 were not severely chemically-aged because they did not experience the extreme temperature gradients as did the other gages.

Interpretation of the data is quite difficult because everything has aged or changed. The gages have chemically aged, their zero points have shifted, and their sensitivity have changed. The theory which is sensitive to physical and thermal material properties as was discussed previously, modeling, liner modulus, liner thickness, conductivity as a function of time, and the coefficient of thermal expansion as a function of time could be in error. Of course, the possibility of the propellant post curing, hardening, shift in stress free temperature and nonlinearity give added accumulation in error to calculated results which makes a precise interpretation of the data out of the question. However, since the analysis and the gage data do path the same (increase and decrease at the same time), gives this some confidence that the analysis can describe aeroheating environments with the actual magnitudes of the stresses being questionable. At this point, it has been concluded that the gages have aged sufficiently especially in the center of the motor to discredit their measurements in terms of magnitudes. It can be concluded from the theory that an air launch environment imposed on a solid propellant rocket motor does create a high stress state on the propellant grain. The severity of the stress state is dependent on the aeroheat mission profile, grain configuration, and failure properties of the propellant. In the design of air launch motors, the aeroheat environment should be investigated from a structural standpoint to verify the design. Of course, with additional insulation in a design the stress would greatly be reduced for a given aeroheat load. The areas that seem to be potential modes of failure are grain termination, inner bores, and bondline areas.

The effects of propellant aging in the data cover several areas such as relaxation modulus shift, post curing, hardening, and surface effects. The relaxation modulus shift does have some effect of the state of stress in the motor. However, the age modulus from the dissected motor could only be obtained from the center of the web. The most worked propellant from the aeroheat cycling was at the bondline and at the inner bore. Therefore, just using the determined aged modulus, the change only created small changes in the stress levels. The post cure and handling of the propellant could explain some of the high prestress reading of the gage output. Of course, the measured prestress values are affected by the gage aging also.

The effects of failure in the instrumented motor will cause changes in gage output. Especially the case-to-liner unbonding in the center of the motor and at grain termination. After the unbonding occurs, the gage response is changed in magnitude but more noticeably in rate of increase or decay of stresses. The bore cracking or crazing should lower the gage output at the bondline. It would be the same as lowering the web fraction of the motor to the depth of the deepest crack.

PROGRAM EVALUATION -  
CONCLUSIONS AND RECOMMENDATIONS

AEROHEAT SIMULATION METHODS AND PROCEDURES

An interesting exercise at the conclusion of an experimental program, especially one in which new techniques have been applied, is to evaluate the methods and procedures used, particularly in respect to their effectiveness for obtaining the desired results. One particular aspect that merits such consideration is the methods used in simulating the air launch environment. The blow down type aeroheat facility, the separate conditioning chamber, and even the basis of simulation are all aspects that might be evaluated. Alternate methods of simulation as well as the exactness of simulation are in themselves an important topic for consideration. Such a discussion attacks the question as to whether the structural loads induced by the aeroheat environment can be successfully duplicated by simple equilibrium temperature cycling. What about the measurement of the structural response to these simulated loads? A discussion of the worth of the instrumentation devices and techniques used for making these measurements is indeed merited.

In considering the simulation of the aeroheat portion of the air launch environment, one must recognize that exact simulation of the structural loads requires exact simulation of the real time thermal history. The motor in captive flight is aeroheated at a rate which is a function of the aircraft velocity, altitude and flight path. The mode of attachment of the missile to the aircraft usually assures that the heating rate over the motor will be non-uniform with the degree of non-uniformity being a function of mission. In this study, the flight heating parameters such as heat transfer coefficient ( $h$ ) and adiabatic wall temperature ( $T_{aw}$ ) were based on simple one-dimensional flat plate calculations and no allowance were made for non-uniformity over the motor. The basis for obtaining a true simulation of the thermal loads in the motor is simply duplicating the temperature history of the motor case. In general, one would like to control the case temperature history by duplicating both the heat transfer coefficient and the adiabatic wall temperature such as done in this study; however, this may not always be possible and other methods must be used. In all cases, the same basic criteria holds which on a simple one dimensional, quasi-steady basis is that

$$\dot{q} = h (T_{aw} - T_w)$$

where  $\dot{q}$  - instantaneous heating rate  
 $h$  - heat transfer coefficient  
 $T_{aw}$  - adiabatic wall temperature  
 $T_w$  - case wall temperature

for flight then

$$\dot{q}_f = h_f (T_{aw_f} - T_{w_f})$$

and simulation

$$\dot{q}_s = h_s (T_{aw_s} - T_{w_s})$$

since the condition for a true simulation is

$$T_{w_s} = T_{w_f}$$

at any given real time, then

$$(\dot{q}_s/h_s) - T_{aw_s} = (\dot{q}_f/h_f) - T_{aw_f}$$

Therefore, it is obvious that the correct wall temperature can be forced by manipulating the heat transfer coefficient and adiabatic wall temperature if they both cannot be fully simulated as done in the aeroheat facility used in the program. A common technique for simulating an heating environment is the use of banks of radiation lamps. Here the heat transfer coefficient is a constant and the wall temperature is controlled by varying the lamp intensity. Since the mode of heating is radiative, the heating rate is quite sensitive to temperature change varying as a function of the temperature to the fourth power. This type facility has the advantage of being controlled electrically and thus providing very fast response to desired changes in temperature. Relatively simple thermocouple initiated feedback control loops can be used to program a desired temperature time history.

Another method of simulation is to encase the motor in a cocoon and recirculate hot air over the motor. The procedure is a hybrid between the blowdown aeroheat facility and the radiative lamps. The mode of heat transfer is convective with the heat transfer coefficient being near constant and the wall temperature history being controlled by changing the air temperature. The major disadvantage of this method is that the response to changing temperature is much slower than either of the other two methods. This is an excellent method, however, when one has a very slow changing, long-duration-type flight profile to simulate.

Other methods would include several which rely on the conductive mode of heat transfer. For example, spray baths of some hot liquid such as oil or water could be made to work but would be quite messy particularly using instrumented motors. Heating coils circulating hot water could be wrapped around the motor. Electrical heating cable could also be used; however, this would be considered very risky from a safety standpoint besides the possibility of picking up the sixty cycles on the instrumentation if instrumented motors were being used.

Any evaluation of the aeroheat facility with respect to its usefulness as a device for simulating the air launch environment must be done on the basis of its intended use. In a program such as this which centers around studying the aeroheat phenomena through the use of instrumented motors, this type of facility

and simulation

$$\dot{q}_s = h_s (T_{aw_s} - T_{w_s})$$

since the condition for a true simulation is

$$T_{w_s} = T_{w_f}$$

at any given real time, then

$$(\dot{q}_s / h_s) - T_{aw_s} = (\dot{q}_f / h_f) - T_{aw_f}$$

Therefore, it is obvious that the correct wall temperature can be forced by manipulating the heat transfer coefficient and adiabatic wall temperature if they both cannot be fully simulated as done in the aeroheat facility used in the program. A common technique for simulating an heating environment is the use of banks of radiation lamps. Here the heat transfer coefficient is a constant and the wall temperature is controlled by varying the lamp intensity. Since the mode of heating is radiative, the heating rate is quite sensitive to temperature change varying as a function of the temperature to the fourth power. This type facility has the advantage of being controlled electrically and thus providing very fast response to desired changes in temperature. Relatively simple thermocouple initiated feedback control loops can be used to program a desired temperature time history.

Another method of simulation is to encase the motor in a cocoon and recirculate hot air over the motor. The procedure is a hybrid between the blowdown aeroheat facility and the radiative lamps. The mode of heat transfer is convective with the heat transfer coefficient being near constant and the wall temperature history being controlled by changing the air temperature. The major disadvantage of this method is that the response to changing temperature is much slower than either of the other two methods. This is an excellent method, however, when one has a very slow changing, long-duration-type flight profile to simulate.

Other methods would include several which rely on the conductive mode of heat transfer. For example, spray baths of some hot liquid such as oil or water could be made to work but would be quite messy particularly using instrumented motors. Heating coils circulating hot water could be wrapped around the motor. Electrical heating cable could also be used; however, this would be considered very risky from a safety standpoint besides the possibility of picking up the sixty cycles on the instrumentation if instrumented motors were being used.

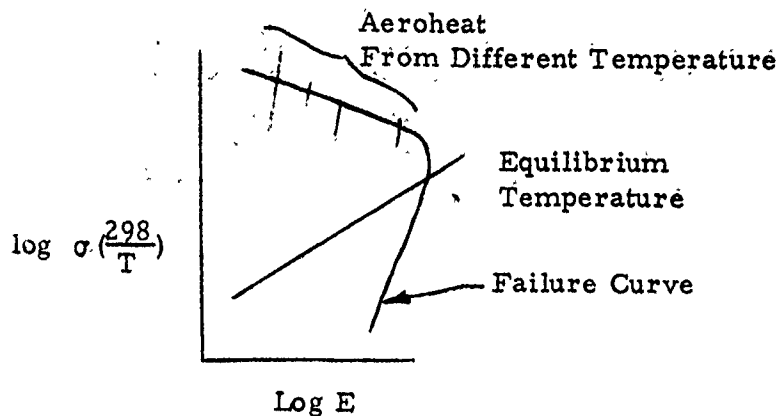
Any evaluation of the aeroheat facility with respect to its usefulness as a device for simulating the air launch environment must be done on the basis of its intended use. In a program such as this which centers around studying the aeroheat phenomena through the use of instrumented motors, this type of facility

excels. This facility has all the necessary equipment in terms of air storage tankage, valving and piping, heating and cooling, and data acquisition to be efficiently utilized and provides an excellent capability for simulation of various short duration, high performance, aeroheat missions. However this facility does have its limitations, with duration being one. Long duration missions are generally characterized by constant flight conditions and can well be simulated in the conditioning box. There is a potential limitation in the inability to vibrate simultaneously with aeroheating. Vibration is an important part of the air launch environment and a true simulation of the environment would of necessity include the combined effects. Inasmuch as the SALE program addressed only the aeroheat aspect of the air launch environment, the lack of vibrational capability cannot be considered a facility limitation.

Various methods of simulating the aeroheat environment to achieve true temperature-time histories have been discussed; however, suppose that a true simulation cannot be made. What then is the effect of the mismatch? Can an equilibrium cycle be derived which permits duplication of the peak aeroheat stress and strain levels? The answers to both these questions became relatively obvious during the early part of the program under the mission severity evaluation phase. The levels of stress and strain induced by aeroheat as shown previously in this report are direct functions of the heating rate and the thermal and physical properties of the materials involved. In general, the faster the case is heated, the higher the value of peak stress induced. However, this peak level is controlled by propellant relaxation which, of course, is faster at the higher temperatures. In other words, the faster the case is heated the faster the case expands which loads the propellant at some rate. While this is occurring heat is being transferred into the grain raising the temperature causing the stress to relax faster. The faster the heat is conducted into the grain the quicker the stress will relax. The peak level attained becomes a compromise between expansion rate of the case and the thermal conductivity of the propellant. As materials are changed, or thickness of materials changed, the stress and strain levels induced for a given aeroheat mission will also change. While all this occurs in the vicinity of the case/liner/propellant interfaces, the inner bore of a CP motor is essentially unchanged thermally or physically except for the induced increase in strain. By the time the bore begins to heat, the stress level has relaxed significantly--possibly to a level below that existing prior to the aeroheat.

What this means in terms of aeroheat mission simulation is that the stress and strain fields in a motor are unique to the heating condition. Mismatches in heating rate can result in under tests or over tests. Fortunately, the problem is not as bad as it appears since the magnitude of the mismatch in stresses and strains can be approximated using THVINC. This allows one to evaluate his simulation technique in view of his requirements. Further THVINC results which have been confirmed phenomenologically by the results of this program can be used to show that aeroheat stress strain fields cannot be reproduced

through equilibrium temperature cycling. This might be illustrated as follows:



The paths established by plotting the log of the normalized stress against the log of the strain for a given aeroheat cycle initiated from different equilibrium temperatures can be seen to be considerably different than the equilibrium temperature path. It can be seen that any attempt to match the peak aeroheat cycle stress by further cooldown of the motor to a lower equilibrium temperature results in a gross mismatch in strain. Failures produced by the equilibrium cooldown would not be representative of the aeroheat type failure.

In order to reproduce the stress and strain levels induced by aeroheat and/or reproduce the failure mechanisms, the simulation test method must accurately represent the real time aeroheat environment. This conclusion is based on the interrelationship between the heating rate and stress/strain level in the motor. Inasmuch as each mission represents a different heating rate, it may be possible to generalize or categorize missions with corresponding heating rates. Now it would be possible to specify a certain number of cycles at a given heating rate that a motor must be able to endure. Specification of the heating rate in terms of degree F per second, duration, and initial case temperature would permit rapid assessment of present simulation capability and define what added capability is necessary. This would be advantageous in surveillance programs where a simulation method unique to the motor under surveillance could easily be set up on a semipermanent basis.

#### AEROHEAT FAILURE CRITERIA

Perhaps the most important objective of this program was to establish failure criteria for the Maverick motor under aeroheating conditions. Initially, the bond region was considered as the most likely site for a failure to occur since aeroheating could be thought of as pulling, by thermal expansion, the case from the grain. Results of the THVINC calculation made in the mission severity analysis showed, however, that this would not be the case. Of course,

THVINC was useful in showing only the structural response to the different aero-heat loads and cannot predict the degree of degradation of the physical properties in the bond region as a result of high temperature cycling. The results of that analysis did show that the most likely failure would occur in the bore region from overstress. These results also showed that extreme overtesting had to be done if there was to be any hope of achieving this failure. The calculations in themselves assumed over test since the bare motor case was exposed directly to aeroheat as opposed to assuming some effective insulation as is the case for the real Maverick system. Even with the gross overtesting the results of the uninstrumented motor tests were disappointing. They showed that failure could not be achieved on the Maverick motor from aeroheating. The reason for the apparent insensitivity to failure was probably due to two things: first, the web fraction of the motor was small resulting in low bore strain levels at equilibrium condition; second the liner which was 0.060 inch thick apparently, because of its good plasticity at low temperature, absorbs most of the strain induced by the case expansion. Therefore, it appeared that the program would be limited to a study of the structural response from the aeroheat loading.

With the results of the uninstrumented motor tests having no failures, the instrumented motor tests were begun. Needless to say, the unbond failure on IM #2 was a considerable surprise--particularly when this failure occurred on the first SFPI test. Granted the web fraction of C. P. motors was greater resulting in a higher bond stress than the Maverick design; however, the difference in bond stresses should not have been enough to have caused the failure. Continued cycling of that motor resulted in unbond occurring between liner and case extending forward from the aft end of the motor. This same aft end unbond was found on the other two instrumented motors after being subjected to the SFPI aeroheat. Therefore, all three instrumented motors, including IM #1 with the Maverick grain configuration showed an aft end unbond failure which did not occur on either uninstrumented motor. The gages did indicate a reason for aft end unbond by showing that both high normal and shear stresses are induced there by aeroheat. Further the gages were found to be useful for detecting the beginning of unbond and monitoring its growth. This was done by observing a decrease with repeated testing of the induced and equilibrium values of shear stress and bore hoop strain at the aft end. The reason for the aft end unbond could be rationalized as being caused by shear induced from the aeroheat. While this is undoubtedly so, it must also be pointed out that it is doubtful if this stress was high enough to have caused an unbond unless the initial bond was extremely weak. Thus a failure was induced by aeroheat that should not have existed and did not exist on motors (UM #1 and UM #2) with a normal bond capability.

The reason for the poor bond on these motors is not known. Apparently the cases were contaminated prior to lining in some manner which resulted in spotty bonding of the liner to the case. The spotty nature of the bond was found during dissection where in some locations the liner could be removed cleanly from the case while in other locations the liner would tear before it would peel

from the case. The unbond under the thermocouple slab in IM #2 appeared to be one of those locations where the initial bond was extremely weak. This failure like the aft end unbond failures should not have and would not have existed with a good liner to case bond system. About the only cause for contamination that can be eliminated is contamination occurring during instrumentation. The cases were lined prior to gage installation and any contamination that may have occurred would have effected the propellant to liner bond. The propellant to liner bond did appear good in the vicinity of the gages when it inspected during gage recovery.

The most notable motor failure in this program was the bore cracking which occurred in IM #3. There is no doubt that the early unbond in IM #2 played a major role in negating any bore cracking in that motor. There is no way to tell how much stress relief occurred at the surface of the bore because of the aft end unbond on IM #3. The bore failure was induced by aeroheating but compromised by unbonding; therefore, one is left with a confused picture of the effects of repeated aeroheat cycling on failure development. Basically, the motor that exhibited the least unbond had the bore cracks which does confirm to a sense that bore cracking would be the predominate failure mode in aeroheat applications assuming, of course, an adequate bond system.

In considering the aspect of cycle life of the motor, one might develop two conclusions. First, the cycle life, in terms of the number of aeroheat cycles the motor can withstand without failure, of the Maverick motor is indefinite. In other words, it appears, based on the uninstrumented motor tests, that the Maverick motor cannot fail from the aeroheat loads. This considers that the thirty-seven tests that UM #2 was subjected to are such gross overtests as to be equivalent in terms of severity to probably hundreds of typical Maverick aeroheat missions. Of course, any adverse effects due to vibration must be considered in the final assessment of cycle life. The second conclusion is that the CP analogues of the Maverick do have a finite cycle life when subjected to these aeroheat missions. Inasmuch as the CP grains (IM #2 and IM #3) were designed to have the same bore strain as existed in the fillets of star points of Maverick grain, one would have expected cracking to have occurred in the fillets of the Maverick grain. There was some degree of crazing noted in some of the uninstrumented motors as well as in IM #1; however, this was barely visible to the naked eye. There was no crazing in the fillets of UM #2. Since the bore cracking was induced by aeroheating in the CP motors, and no effect was noted on the Maverick configuration, there is some question as to the validity of the design of the CP motors as analogue for the star configurations. The design of the CP's were based on equilibrium conditions to match bore strains which result, of course, in a mismatch of bondline stress. This condition of higher bondline stress at equilibrium in the CP's would result when aeroheated in much higher bore stresses and strains being induced than would have otherwise occurred. This trend was noted when making some sensitivity studies

using THVINC which confirms the value of such a computer code. What then constituted an analogue for an equilibrium condition, is not an analogue under transient thermal conditions. This is an important consideration on propellant and motor development studies.

In considering the application of these results to other motors, the above discussion is most appropriate. The data obtained in this program are unique to the motors tested. The data reflects the unbond failure and the bore cracking as well as being compromised by gage instabilities. Therefore, there is no direct application of these data possible to other motors or systems. There are, however, aspects of these data that may be considered and extended to other motors. The above point on the analogue motor is one. Another would be the judicious use of a program such as THVINC to provide indications of stress and strain levels for the transient thermal conditions under question. In terms of failure, the results of this program show that the most probable failure mode is bore cracking although unbond cannot be ruled out. The most probable failure sites are regions of high bore hoop stress and high bondline shear stress. Examinations of these sites with THVINC and plotting the path on a failure boundary plot will provide an idea of the safety margin.

## CONCLUSIONS

Some of the main points of the program have been summarized and some conclusions drawn in the preceding discussion. The intent here will be to delineate pertinent conclusions as a function of topic area. Topic areas which are covered include Aeroheat Environment and Simulation, Motor Instrumentation and Data Acquisition, Structural Response Analysis, Failure Criteria, and Program Evaluation. Comments are included where appropriate.

### Aeroheat Environment and Simulation

- o True simulation of an aeroheat mission requires the case temperature-time history to be accurately duplicated.
- o Severity in terms of maximum stresses and strains induced is a direct function of the rate of increase of case temperature.
- o The Thiokol aeroheat facility through plagued during the early phases of testing by compressor problems proved to be quite versatile in being able to simulate a wide variety of missions and quite reproducible when repeating missions.
- o The method of installing the motor in the aeroheat test section worked well. The time from when the conditioning box was

opened to when the motor was installed, personnel cleared, and controls set averaged approximately four minutes. A ten minute duration was standardized in the test program to allow for contingencies and still permit test to test duplication. This ten minute time period was exceeded in only three tests out of the hundred conducted.

#### Motor Instrumentation and Data Acquisition

- o The use of embedded gages did not have any adverse effect on motor manufacture. Of course, routing of the lead wires must be compatible with tooling.
- o The GFE gages used in this program were of poor quality which compromised the results of the program. The normal gages exhibited both zero and sensitivity shifts which occurred during the test program. Out of nine shear gages furnished only three one in IM #1 and two in IM #3, seemed to perform normally. The output of the clip gages after installation in the motor appeared to be non-linear. This is adverse to the factory calibration, therefore it may be due to the installation procedure. In the future, every effort should be made to minimize any possibility of material incompatibility.
- o The success of an instrumented motor test program can lie in the frequency at which data is acquired. It is better to have an excess of data points by more frequent acquisition than to try to rationalize what happened if a rapid shift in gage output occurs.
- o Gage calibration both in terms of gage response at various motor temperatures (gage checkout tests) and motor cavity pressurization are necessary for interpreting the gage data in terms of potential damage cumulation.
- o The thermocouple slabs installed prior to casting provided the most consistent data obtained. Since such small thermocouple wire (0.005 in. diameter) was used, they were not visible in the motor X-rays, but the base of the slab was. Fortunately, the slabs had been X-rayed prior to installation and exact location of junctions within the slabs could be found. To overcome the potential problem of not being able to precisely locate thermocouple junctions, embedding lead shots for reference markers when fabricating the slabs is highly recommended.

- o The use of thermocouples installed in the vicinity of the gages to provide a reference temperature measurement for data reduction purposes is unacceptable for aeroheat testing. The reason for this is the large radial thermal gradient that exists and the thermocouple junction may not be at the same radial location as the gage.

#### Structural Response Analyses

- o The structural response of a motor to aeroheat thermal loads can be evaluated on a relative basis by use of THVINC. The accuracy of the calculation is a function of both the thermal and physical properties input as well as the rate of loading. This latter effect would be due to the non-linearities of the system which become more pronounced as rate of loading is increased.
- o Measurement of the structural response of these motors for the various aeroheat missions was compromised by both gage inadequacies and motor failures. Unfortunately the degree of gage aging at any given time is not known. The beginning of failure can usually be established for each motor. Consequently comparisons between motors (IM #2 and IM #3) must be limited to the first few DMP-3 tests. In general, both motors exhibited similar trends, but different magnitudes of induced stresses.
- o Design of CP analogue motors for star configurations for transient thermal testing should be done based on simulating the induced stress and strain path as opposed to equilibrium strain values. An analogue under equilibrium conditions may not be such in transient environments.
- o Comparisons of gage data with THVINC results cannot be made without full consideration of the inadequacies in both the experimental and analytical results. The trends predicted by THVINC were confirmed by the gage data; however, magnitudes cannot be confirmed because of the zero shifts in the gage data. The usefulness of the comparisons is, of course, in developing a physical interpretation of the aeroheat phenomena.

#### Failure Criteria

- o The most probable failure mode due to aeroheating a CP motor is bore cracking although unbond cannot be ruled out.
- o The most probable failure sites are regions of high bore hoop stress and high bond line shear stress.

- o Potential failure sites can be tentatively identified by conducting a THVINC analysis of the motor for the candidate missions. Plotting the induced stress against the induced strain on a failure boundary plot will provide a basis for establishing margin of safety.
- o The unbond failures that occurred in the instrumented motors were aeroheat induced; however, they should not and would not have existed with a good liner to case bond system.
- o The initiation of failure (e. g. bore surface cracks, or unbond) as well as the development of the failure over a massive region can be detected with the embedded gages. However, since the changes in gage output are quite subtle as opposed to being abrupt, it may not be possible, as it was not here, to interpret this data immediately as reflecting initiation of failure.

#### Program

- o Aeroheat is an important consideration in air launch motor design. The results of this program show that very significant stress levels can be induced by aeroheating. Prompt consideration of the problem during design can lead to a motor properly insulated to minimize the effects of aeroheat.
- o Satisfaction of the overall objectives of this program was compromised somewhat by the gage problems. However, recovery of the gages which was over and above the scope of the program provided a positive assessment of gage aging which until this time had been postulated, but never proved.
- o Much valuable information can be obtained from an instrumented motor program. There are, however, various do's and don'ts. The importance of periodic pressurization of the loaded grain when equilibrated at preselected temperature is considered a must.
- o Although unbond and bore cracking was induced in the CP analogue motors by aeroheating, there appears to be no way of failing a Maverick motor during captive flight.

## RECOMMENDATIONS

There are basically two types of recommendations that can be offered based on the results of this program. The first considers the current instrumented motor programs while the second considers what should be undertaken in the future. Recommendations which may be helpful on current programs entail the use and interpretation of gage data are as follows:

- o The current practice in instrumenting motors is to pressurize motor cases to 30-50 psi at different temperatures prior to loading to provide a final check on normal gage sensitivity and establish reference zeros for all gages as a function of temperature. This process should be repeated after core removal at least at ambient temperatures. This provides baseline data for subsequent comparisons.
- o Periodically the instrumented motor should be pressurized at the same conditions as the baseline to determine if the response is the same. Changes in response can be caused by either gage aging or propellant aging. If gage aging is suspected, the data can be reduced based on sensitivities derived from these pressurization data.
- o Record data in a manner that a complete history can be constructed. Propellant relaxation phenomena differs little from unbond or bore cracking with respect to gage readings.

Based on the results of this program and consideration of the overall air launch environment, the following recommendations are offered:

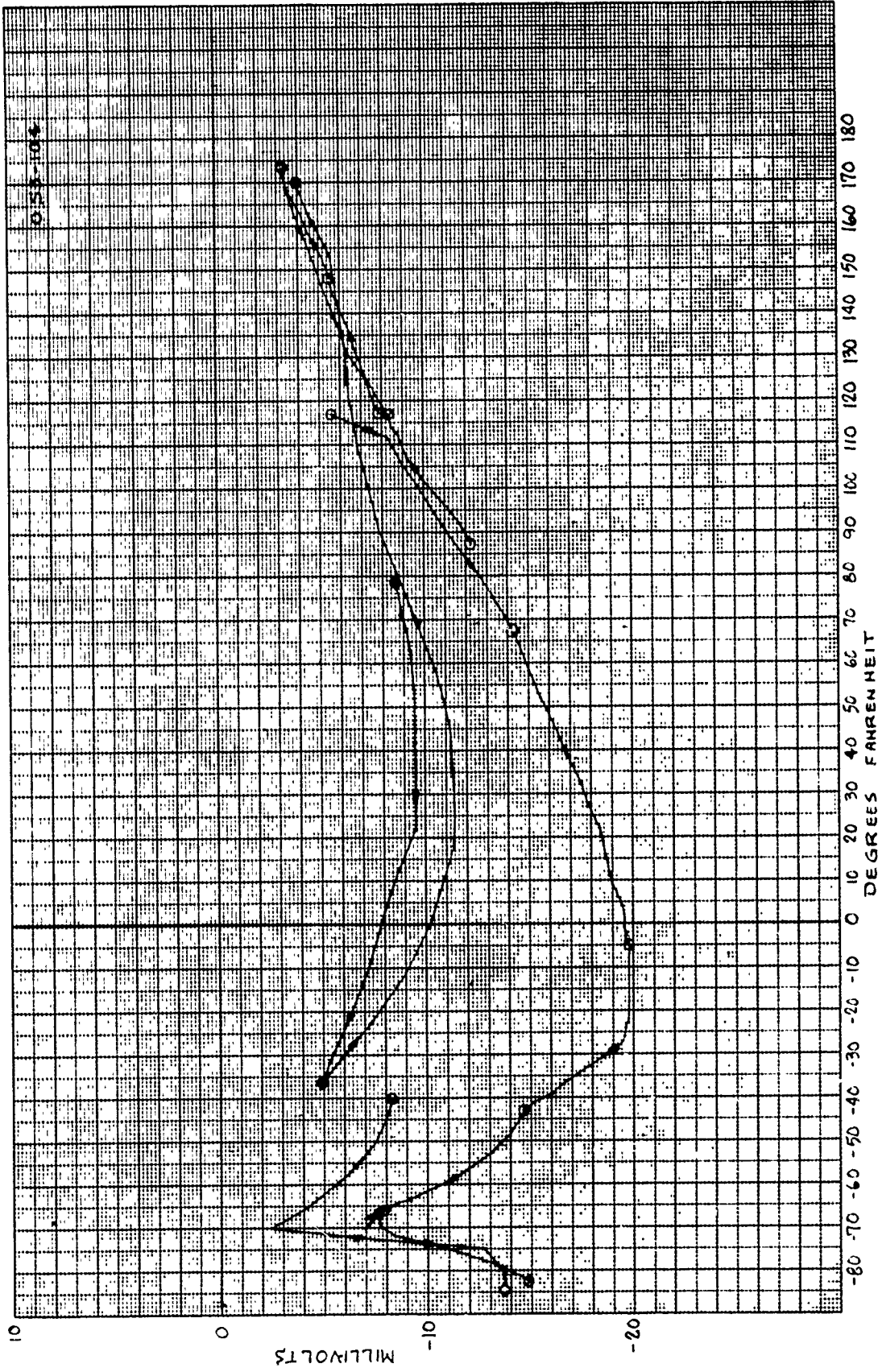
- o The use of instrumented motors for accessing the structural and failure response of air launch motors to the air launch environment should be continued despite the problems encountered with gage aging in this program.
- o The interaction between gage and surrounding propellant should be reexamined now with advent of new 2-D and 3-D stress codes. The differences in interaction phenomena between equilibrium and dynamic loading conditions should be examined in particular.
- o Calibration techniques now in use consider only equilibrium one-dimensional load. The effects of non-uniform and dynamic loads should be investigated and appropriate calibration techniques developed.
- o Surveillance programs for air launch motors should incorporate thermal cycling tests with both the rate of change of temperature and temperature levels selected to reasonably simulate the expected flight environment.

## REFERENCES

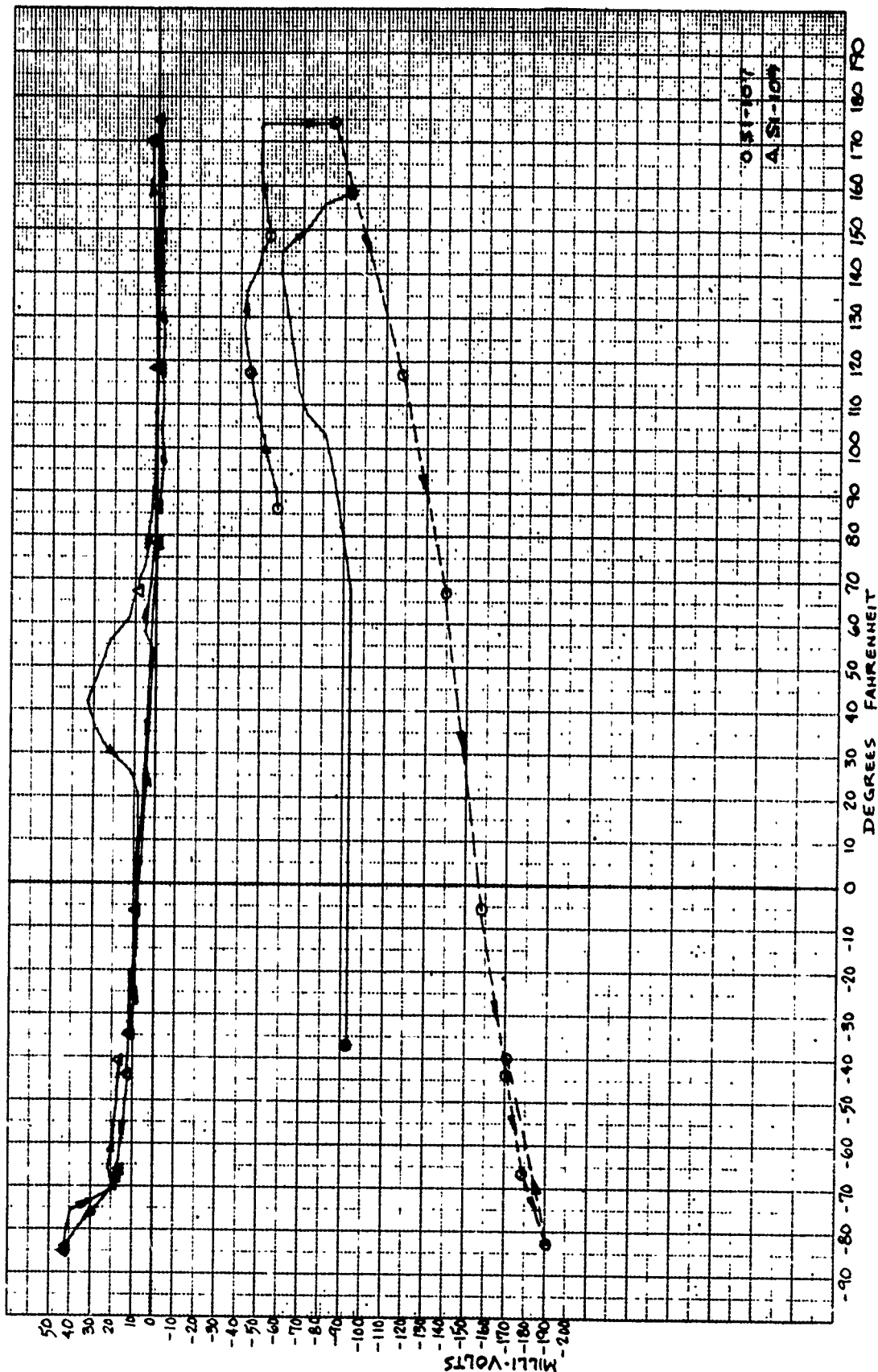
1. ----- "Severe Environmental Air Launched Study (SEALS)," (U) Raytheon Company, AFRPL-TR-69-205, November 1969, Confidential (no classified information extracted or reproduced from this report is contained herein.)
2. ----- "Predicted Flight Environment for a Test Store Carried on a F-111", General Dynamics/Convair FZM-5761, 23 August 1971.
3. Schmidt, J. S., "Turbulent Skin-Friction and Heat Transfer Parameters for a Flat Plate at High Hypersonic Speeds in Terms of Free-Stream Flow Properties", NASA TN-O-869, May 1961.
4. Eckert, E. R. G., "Survey of Heat Transfer at High Speeds", WADC Technical Report 54-70, April 1954.
5. Leeming, H., et al, "Final Report: Solid Propellant Structural Test Vehicle Program", AFRPL-TR-72-29, April 1972.

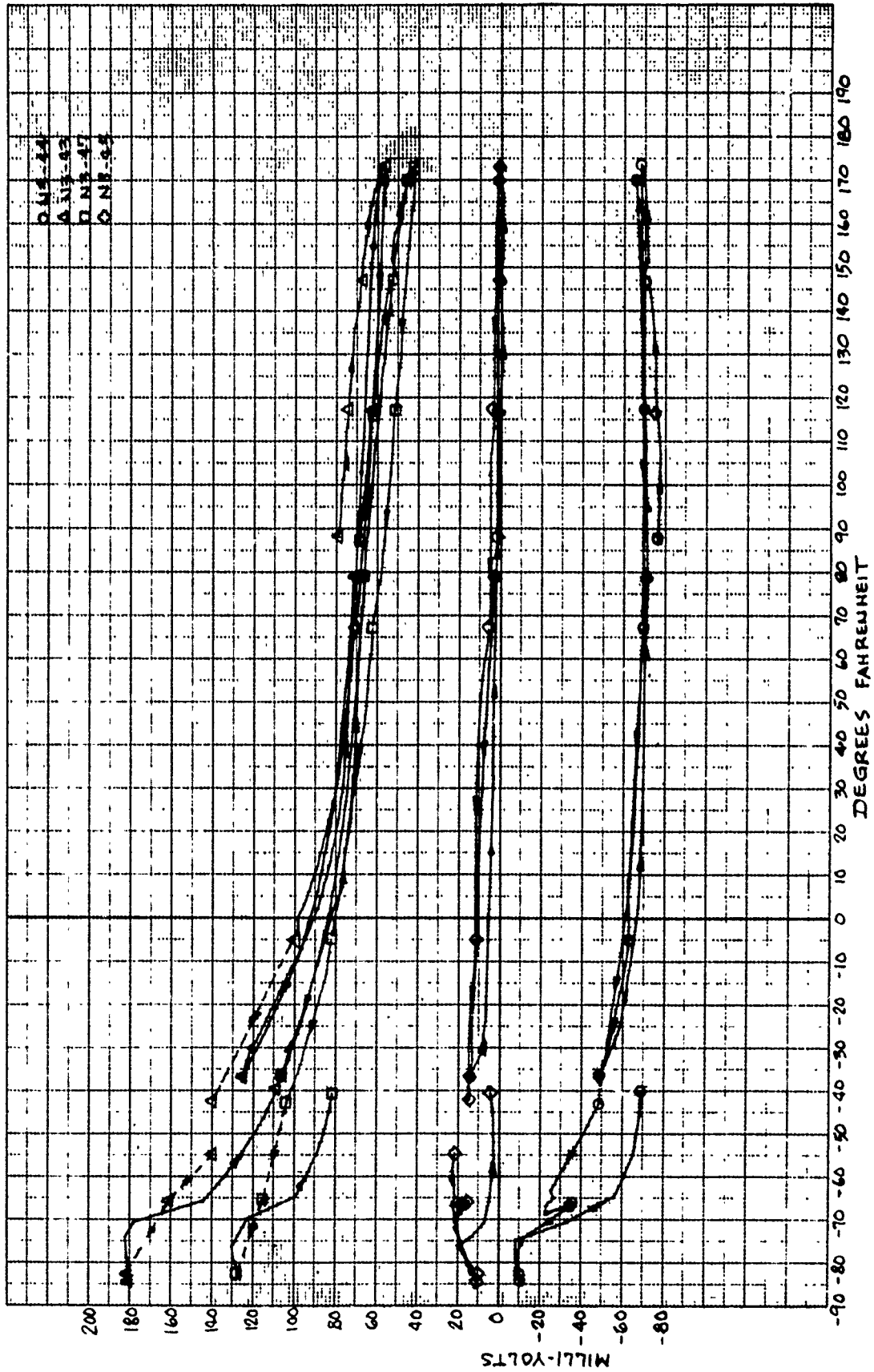
APPENDIX A

GAGE RESPONSE

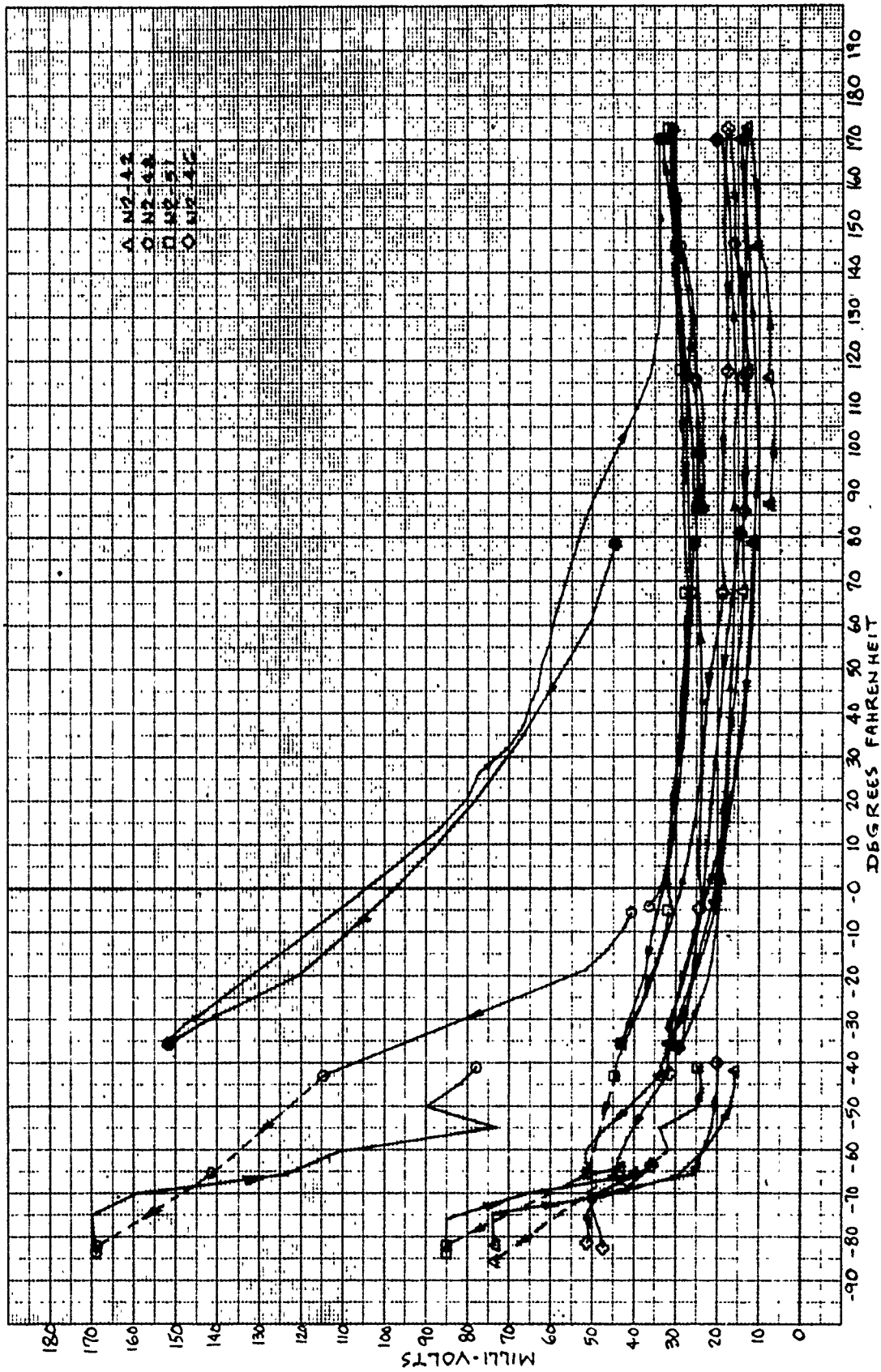


A-2

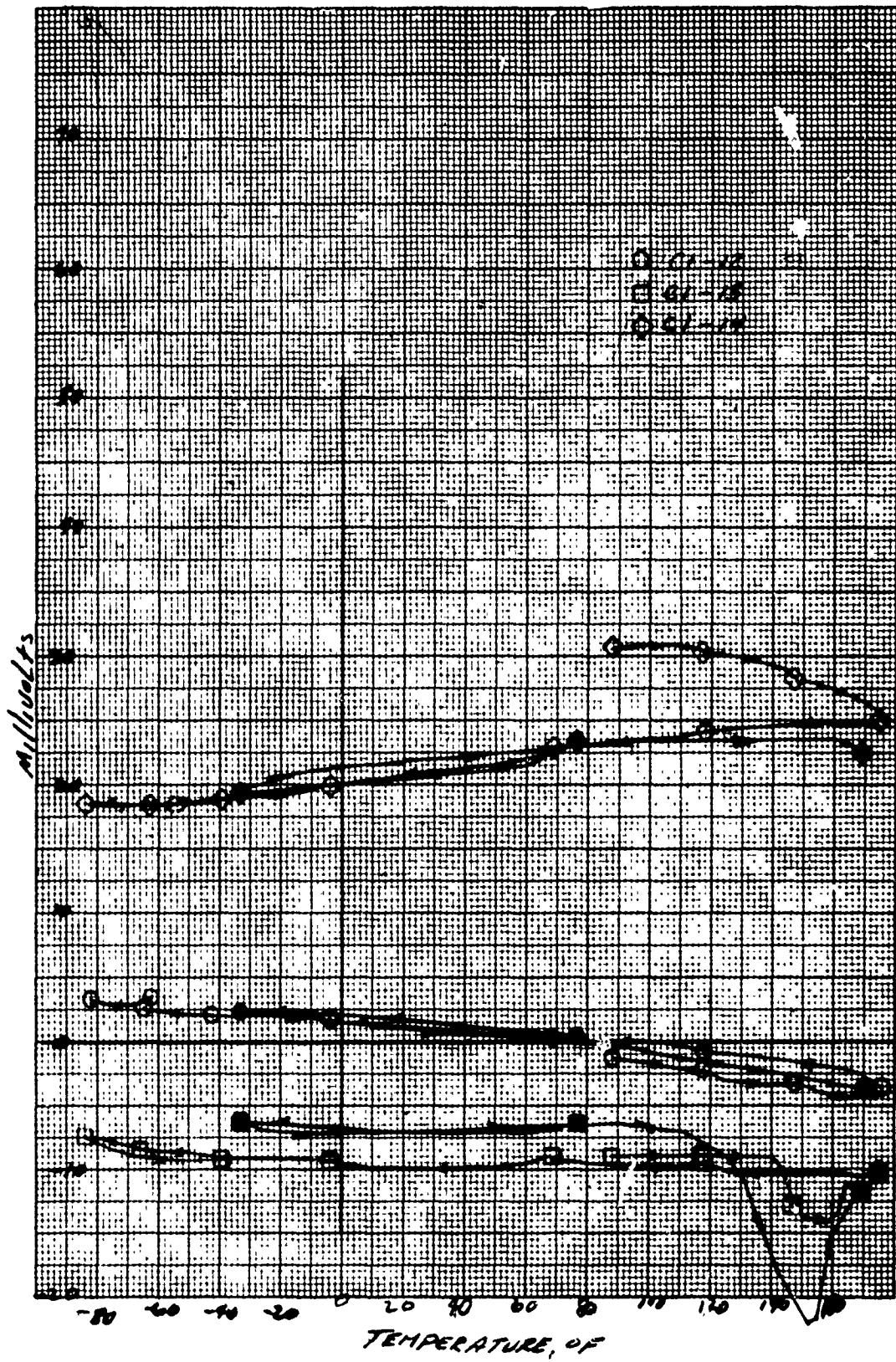


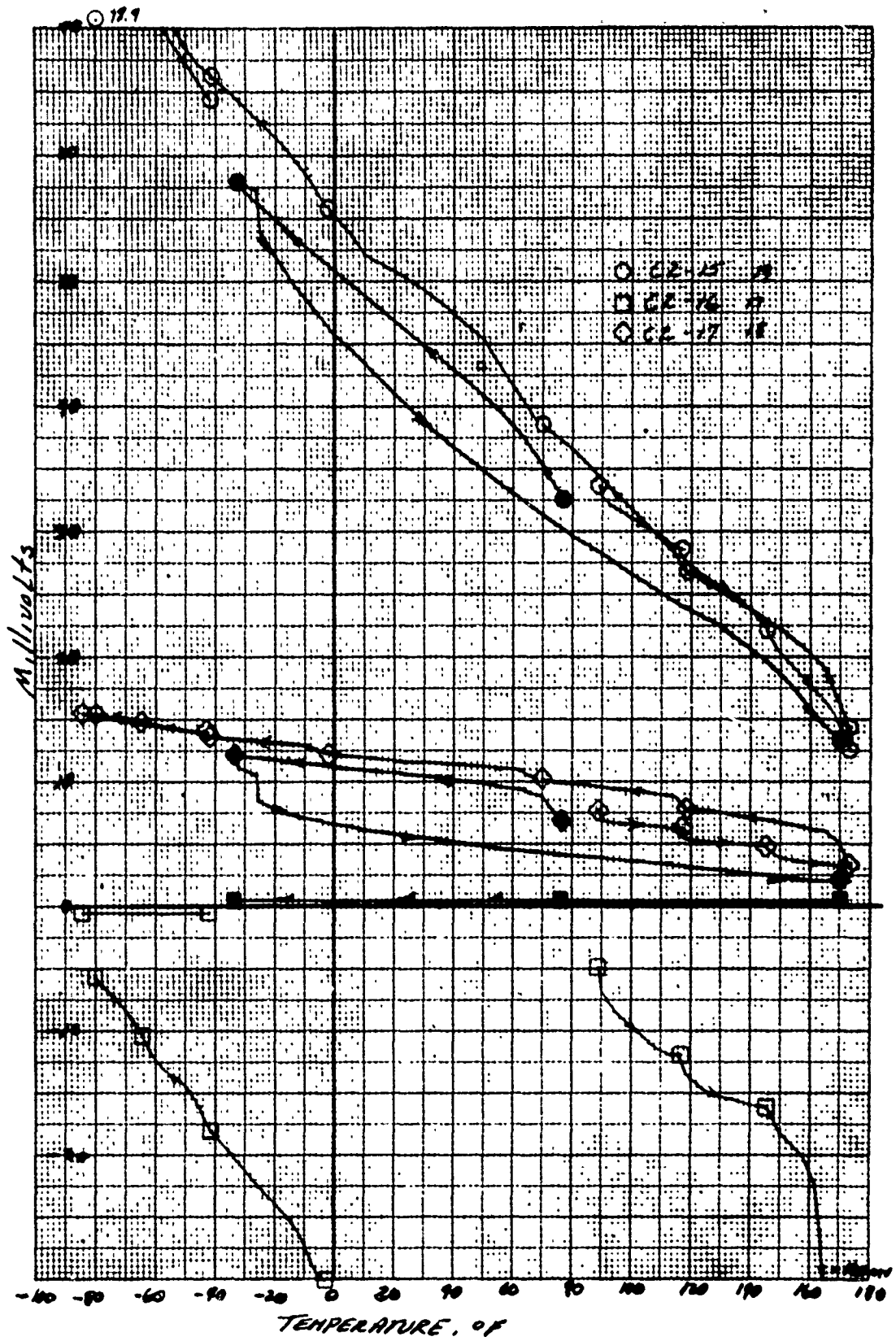


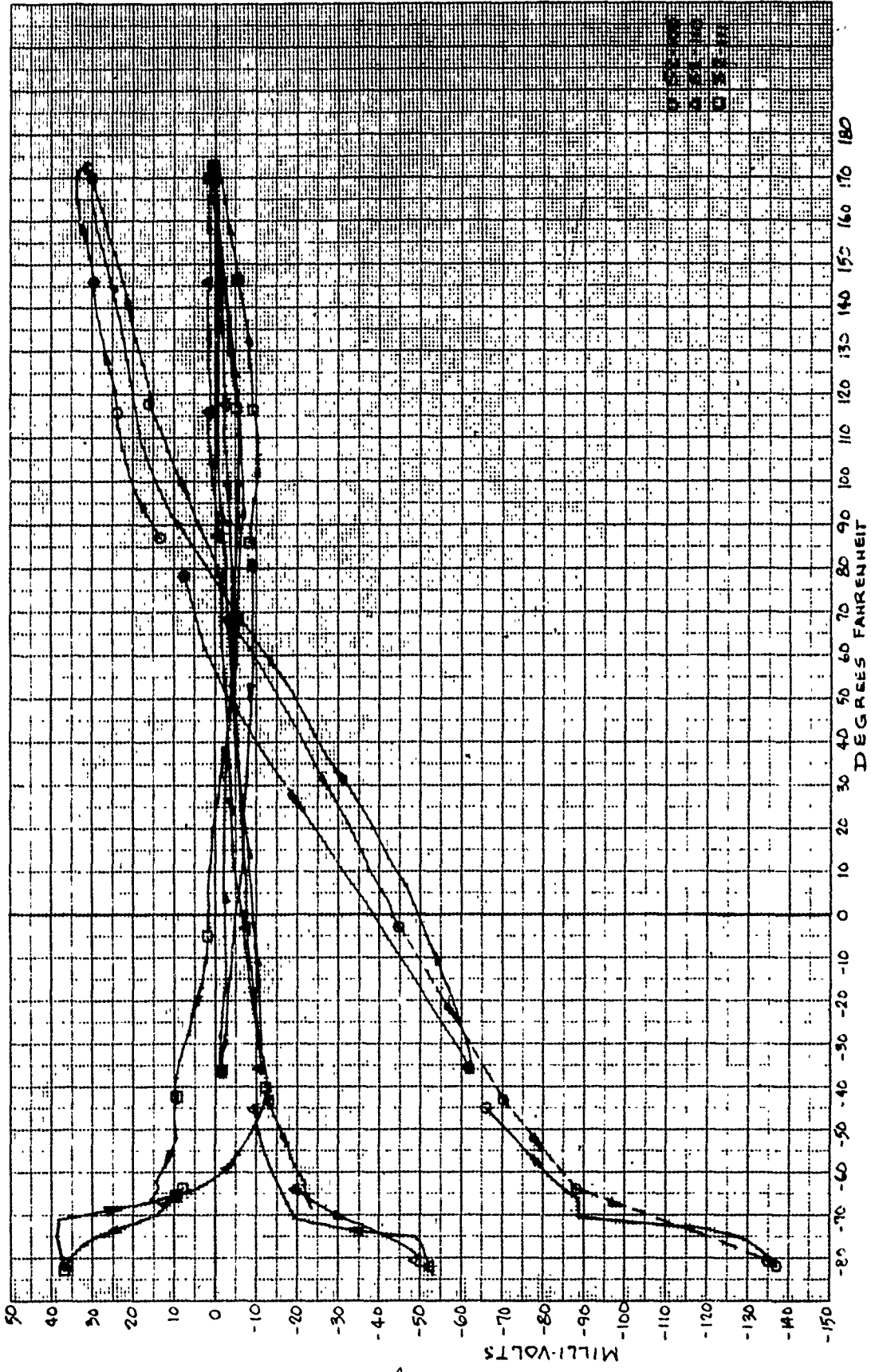
A-4



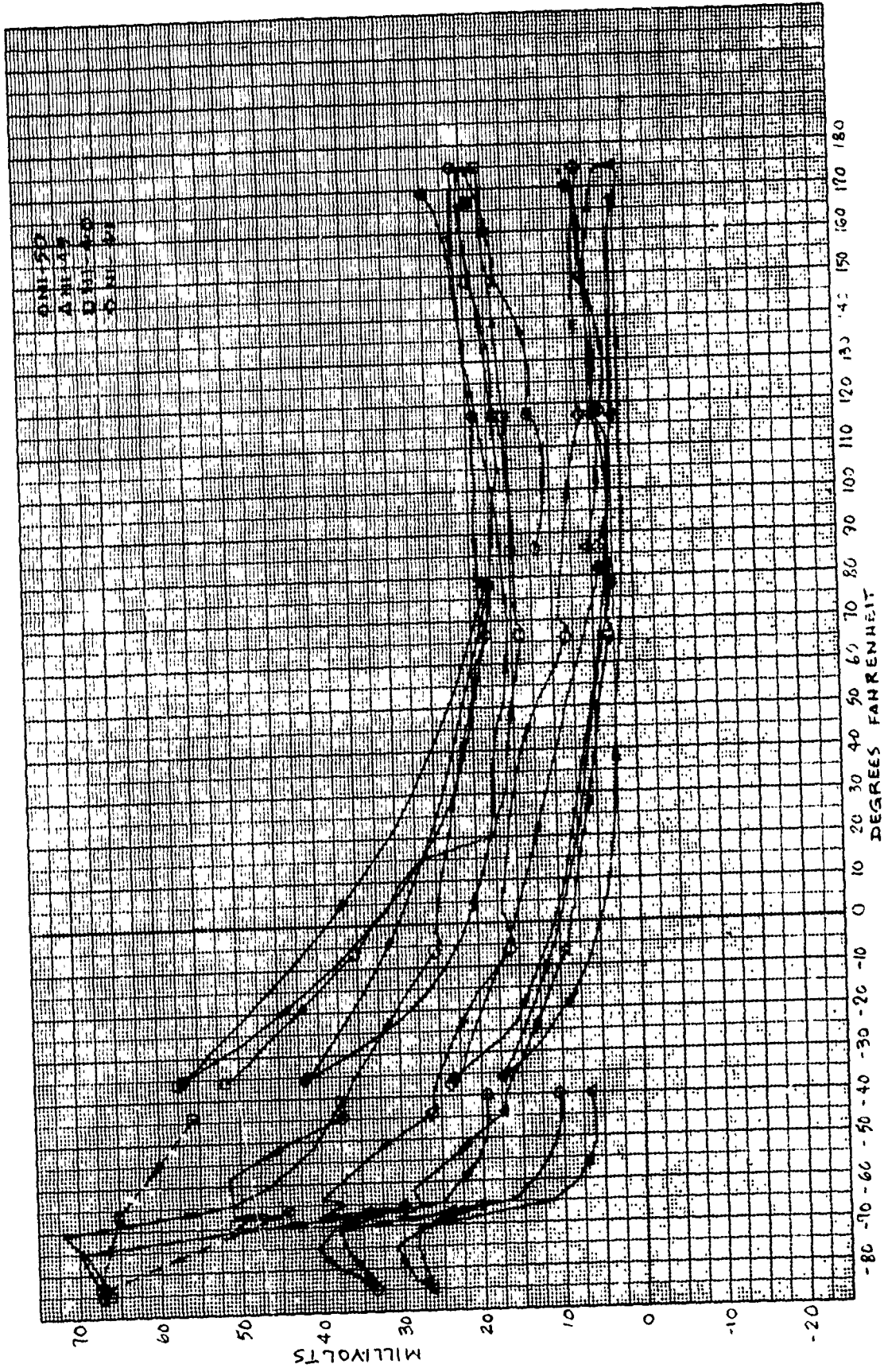
▲ N2-A2  
 ○ N2-42  
 □ N2-51  
 ◇ N2-47







A.8



A-9

